UNIVERSITÄT
BAYREUTH

Dissertation

Reducing Electron Self-Interaction via Orbital-Dependent Functionals in Density Functional Theory

Rían Ránall Nioclás Richter

Reducing Electron Self-Interaction via Orbital-Dependent Functionals in Density Functional Theory

Von der Universität Bayreuth
zur Erlangung des Grades eines
Doktors der Naturwissenschaften (Dr. rer. nat.)
genehmigte Abhandlung

von

Rían Ránall Nioclás Richter

aus Bayreuth

1. Gutachter: Prof. Dr. Stephan Kümmel
2. Gutachter: Prof. Dr. Johannes Margraf

Tag der Einreichung: 5. Mai 2025
Tag des Kolloquiums: 28. Juli 2025

Abstract

The continuous increase in energy consumption worldwide, together with the problematic environmental and climate impact of traditional power plants that burn fossil fuels in limited supply, make a shift to renewable energy sources inevitable. Among these sources, solar power holds great potential as a sustainable solution to meet our growing energy demand. Since nature has optimized the use of solar light through photosynthesis, gaining a deeper understanding of the natural processes could provide valuable insights for improving the design of human-engineered solar cells. In addition to the experimental investigation of natural model systems and materials relevant for technical applications, a key focus lies on improving the theoretical description of central physical processes, including charge-transfer excitations and electronic properties such as the band gap.

Density functional theory (DFT), together with its time-dependent formulation (TDDFT), has become a widely used framework for calculating electronic properties of organic molecules as well as solids due to its favorable ratio between accuracy and computational cost. In particular, its real-space and real-time implementation is highly parallelizable, enabling efficient simulations of large-scale molecular systems. Its predictive power, however, fundamentally depends on the approximations employed for the exchange-correlation (xc) energy and the corresponding xc potential. Frequently used (semi-)local xc functionals, like the local density approximation (LDA) or generalized gradient approximations (GGAs), exhibit well-known limitations, such as underestimating band gaps in solids and failing to describe charge-transfer processes in molecules accurately. These limitations result from shortcomings inherent in (semi-)local functionals, including their inability to account for nonlocal effects and their insufficient correction of the nonlocal self-interaction error of the Hartree term, which describes the average classical electron-electron interaction. Although functionals that partly include Fock exchange, like range-separated hybrids, can address these issues, they come at high computational costs, making them impractical for the application to large systems. Meta-generalized gradient approximations (meta-GGAs) offer a promising solution because, in addition to the electron density, they depend on the kinetic energy density and can exhibit nonlocal features similar to Fock exchange while maintaining the computational cost of semilocal functionals. This property has been shown to improve the description of band gaps in solids and, therefore, raises the hope of enhancing the accuracy in describing charge-transfer excitations in organic molecules within TDDFT.

However, meta-GGAs cannot be straightforwardly used in TDDFT, as their dependence on the kinetic energy density introduces a gauge dependence. To address this issue, a previously proposed current-density correction of the kinetic energy density is adapted in this thesis to apply meta-GGA functionals within TDDFT. Subsequently, the performance of meta-GGAs in describing charge-transfer excitations is investigated using two different organic model systems. The results demonstrate that the current-density correction can significantly influence the excitation spectrum obtained with meta-GGAs. Additionally, despite some improvement in the description of charge-transfer excitations with the meta-GGA functional TASK, it remains insufficient to resolve the fundamental charge-transfer problem of (semi-)local xc functionals. This limitation can be attributed

to the persistent self-interaction error of the Hartree term when using meta-GGA exchange functionals and the incorrect asymptotic behavior of the meta-GGA potential.

To address these shortcomings, this thesis revisits the Perdew-Zunger self-interaction correction (PZ-SIC), which eliminates the (one-electron) self-interaction error and restores the correct asymptotic behavior of the xc potential. Subsequently, the PZ-SIC is extended to systems with non-integer particle numbers to examine the extent to which the straight-line condition, a measure for the correction of the many-electron self-interaction error, can be fulfilled. Based on previous approaches in the literature, an algorithm for efficiently calculating the PZ-SIC ground state of various systems is developed as well. Calculations for a small test set show that applying the algorithm to the LDA and the GGA functional PBE is straightforward. However, calculating the PZ-SIC ground state using meta-GGA functionals leads to numerical challenges. These challenges are addressed by introducing a construction principle for meta-GGAs that ensures numerical stability within the PZ-SIC framework. While PZ-SIC calculations for small molecules lead to an improved description of the straight-line condition relative to uncorrected xc functionals, they also reveal signs of an overcorrection.

To mitigate the overcorrection of the full PZ-SIC while maintaining the correct asymptotic behavior of the xc potential, a new strategy based on a range-separation approach combining the PZ-SIC and the LDA functional is introduced. Within this approach, a range-separation parameter can control the specific range at which the self-interaction correction is applied. Using this approach on a test set of small molecules shows that the range-separation parameter can be tuned to closely satisfy the straight-line condition.

Kurzfassung

Der stetige Anstieg des weltweiten Energieverbrauchs sowie die negativen Folgen herkömmlicher, mit fossilen Brennstoffen betriebener Kraftwerke auf Umwelt und Klima machen einen Wandel hin zu erneuerbaren Energiequellen unausweichlich. Unter den umweltfreundlichen Alternativen bietet vor allem die Solarenergie großes Potenzial, unseren wachsenden Energiebedarf bedienen zu können. Die Natur hat sich die Sonnenenergie durch die Photosynthese schon früh zunutze gemacht und im Laufe der Evolution perfektioniert. Ein detailliertes Verständnis dieses natürlichen Prozesses könnte daher wertvolle Erkenntnisse für die Weiterentwicklung technischer Solarzellen liefern. Neben der experimentellen Untersuchung natürlicher Modellsysteme und geeigneter Materialien für technische Anwendungen ist insbesondere eine verbesserte theoretische Beschreibung zentraler physikalischer Prozesse, wie Ladungstransferanregungen, sowie elektronischer Materialeigenschaften, wie der Bandlücke, von wesentlicher Bedeutung.

Aufgrund ihrer guten Balance zwischen Vorhersagekraft und Rechenaufwand ist die Dichtefunktionaltheorie (DFT), einschließlich der zeitabhängigen Dichtefunktionaltheorie (TDDFT), zu einer weitverbreiteten Methode zur Berechnung elektronischer Eigenschaften von organischen Molekülen und Festkörpern geworden. Besonders die Propagationsmethode auf einem Realraumgitter ist hochgradig parallelisierbar und erlaubt die Simulation großskaliger molekularer Systeme, wobei die Genauigkeit der Ergebnisse wesentlich vom verwendeten Funktional zur Näherung der Austauschkorrelationsenergie (xc-Funktional) und des dazugehörigen Potentials (xc-Potential) abhängt. Allerdings zeigen häufig verwendete (semi-)lokale xc-Funktionale, wie die lokale Dichtenäherung (LDA) oder verallgemeinerte Gradientennäherungen (GGAs) bekannte Schwächen. Beispiele dafür sind die Unterschätzung von Bandlücken in Festkörpern sowie die fehlerhafte Beschreibung von Ladungstransferprozessen in Molekülen. Diese Defizite resultieren aus dem Fehlen von nichtlokalen Eigenschaften sowie der unzureichenden Korrektur des nichtlokalen Selbstwechselwirkungsfehlers des Hartree-Terms, der die mittlere klassische Wechselwirkung der Elektronen untereinander beschreibt. Funktionale, die einen Anteil an Fock-Austausch enthalten, wie reichweitenseparierte Hybridfunktionale, können diese Probleme größtenteils beheben, sind aber für die Anwendung auf große Systeme oft zu rechenintensiv. Meta-GGAs bieten eine vielversprechende Alternative, da sie zusätzlich zur Elektronendichte noch von der kinetischen Energiedichte abhängen und somit unter Beibehaltung des Rechenaufwands semilokaler Funktionale ähnliche nichtlokale Eigenschaften wie das Fock-Austauschfunktional aufweisen können. Dies verbessert die Beschreibung von Bandlücken von Festkörpern und weckt deshalb die Hoffnung auf eine genauere Beschreibung von Ladungstransferanregungen in organischen Molekülen innerhalb der TDDFT.

Meta-GGA Funktionale können jedoch nicht direkt in der TDDFT eingesetzt werden, da ihre Abhängigkeit von der kinetischen Energiedichte eine Eichvarianz zur Folge hat. Um dieses Problem zu lösen, wird in dieser Arbeit eine bereits vorgeschlagene Stromdichtekorrektur der kinetischen Energiedichte für die Anwendung von meta-GGA Funktionalen in der TDDFT übernommen. Anschließend wird die Vorhersagekraft der meta-GGAs bei der Beschreibung von Ladungstransferanregungen an zwei organischen

Modellsystemen untersucht. Die Ergebnisse zeigen, dass die Stromdichtekorrektur das mit meta-GGAs berechnete Anregungsspektrum erheblich beeinflussen kann. Trotz einer gewissen Verbesserung in der Beschreibung von Ladungstransferanregungen durch das meta-GGA TASK, kann diese Korrektur das fundamentale Problem der fehlerhaften Beschreibung von Ladungstransferanregungen durch (semi-)lokale Funktionale nicht beheben. Dies lässt sich auf den verbleibenden Selbstwechselwirkungsfehler des Hartree-Terms und das falsche asymptotische Verhalten des meta-GGA Potentials zurückführen.

Als Ansatz diese Defizite zu beheben, wird die Perdew-Zunger Selbstwechselwirkungskorrektur (PZ-SIC) aufgegriffen, die den (Ein-Elektronen-)Selbstwechselwirkungsfehler eliminiert und das korrekte asymptotische Verhalten des xc-Potentials wiederherstellt. Anschließend wird die PZ-SIC auf Systeme mit nicht-ganzzahligen Teilchenzahlen erweitert, um zu prüfen, inwieweit die sog. *straight-line condition*, ein Maß für die Korrektur des Vielteilchenselbstwechselwirkungsfehlers, erfüllt werden kann. Aufbauend auf bisherigen Methoden in der Literatur wird schließlich ein Algorithmus entwickelt, der eine effiziente Berechnung des PZ-SIC-Grundzustands ermöglicht. Während sich bei der Anwendung des PZ-SIC-Algorithmus in Kombination mit dem LDA bzw. PBE Funktional jeweils die Berechnungen der Grundzustände für einen Satz von Testsystemen problemlos durchführen lassen, treten bei der Anwendung des Algorithmus in Verbindung mit meta-GGAs numerische Herausforderungen auf, die jedoch durch die Einführung eines speziellen Konstruktionsprinzips überwunden werden können. Die Ergebnisse für kleine Modellsysteme zeigen, dass die PZ-SIC die straight-line condition zwar besser erfüllt als unkorrigierte xc-Funktionale, aber Anzeichen einer Überkorrektur aufweist.

Um die Überkorrektur durch die volle PZ-SIC zu mildern und gleichzeitig das korrekte asymptotische Verhalten des xc-Potentials zu bewahren, wird eine neue Selbstwechselwirkungskorrekturmethode eingeführt, die die PZ-SIC mit dem LDA Funktional auf Grundlage eines Reichweitenseparationsansatzes kombiniert. Hierbei wird durch einen Skalierungsparameter die Reichweite, in der die Selbstwechselwirkungskorrektur auf das i. A. (semi-)lokale Funktional wirkt, eingestellt. Die Anwendung eines solchen Ansatzes auf den Testsatz kleiner Moleküle zeigt, dass der Skalierungsparameter so gewählt werden kann, dass die straight-line condition in hohem Maße erfüllt ist.

Contents

Chapter 1

Introduction

The ongoing use of traditional power plants that use fossil fuels is problematic, not only because these energy sources are finite, but also primarily due to their negative environmental impacts as their combustion emits greenhouse gases that drive climate change [MR80]. Therefore, we are facing the problem that we have to reduce the severe environmental impact of our increasing energy consumption. One form of energy that is particularly promising in fulfilling these needs is solar energy. The process of using this form of energy has long been optimized by nature, and its efficiency can still not be matched by modern human-designed solar cells. In order to improve existing technologies, it is beneficial to reach a better understanding of the underlying processes of solar energy harvesting in organic model systems [SŞS12; Cor+19; LZ20]. In addition to the experimental investigation of natural model systems and materials suitable for technical applications, a key focus lies on an enhanced theoretical understanding of central physical processes, including charge-transfer (CT) excitations, and electronic properties, such as the band gap.

Computational methods that are suitable for investigating the electronic structure of large-scale organic systems must, on the one hand, be efficient enough to handle several hundred or even thousands of electrons but, on the other hand, accurate enough to predict the physical properties of different materials or molecules outside the initially tested model systems. One theoretical framework that can meet these requirements is density functional theory (DFT) with its time-dependent expansion (TDDFT). Its ground-state theory of many-body quantum mechanics, originally developed by Hohenberg and Kohn [HK64], reduces the computational cost enormously by using the electron density as the main quantity instead of the many-body wave function within Schrödinger's formulation [Sch26]. Later, it was made broadly applicable by the Kohn-Sham formulation [KS65], which introduces an auxiliary system of noninteracting particles described by single-particle orbitals.

The predictive power of DFT fundamentally depends on the approximations used to describe exchange-correlation (xc) effects. The physical properties calculated using (semi-)local approximations, such as the local density approximation (LDA) [HK64] and generalized gradient approximations (GGAs) [Bec86; Per+92; PBE96], often show reasonable agreement with experimental results for many systems [Par20]. However, these approximations exhibit significant shortcomings as they typically underestimate the band gap of solids [PL83; GSS86] and fail to describe CT processes accurately, which manifests in systematically underestimating CT excitation energies within TDDFT [Toz03; DWH03; DH04; Mai05; KK08; Mai17; Küm17; Sch+19; Keh+20]. These limitations of (semi-)local xc approximations, which lead to overly delocalized electrons are discussed in detail in Chapter 3: because such approximations depend (semi-)locally on the electron density, they inherently lack nonlocal features and cannot correct the self-interaction error introduced by the Hartree term, which describes the average classical

electron-electron interaction. Although range-separated hybrid functionals can address these issues [SKB09; Kro+12; AS14; Küm17], their partial dependence on Fock exchange significantly increases computational costs. This is because Fock exchange involves numerous Coulomb integrals, thereby making their practical application increasingly expensive for large systems. Consequently, there is a need for xc approximations that integrate the advantages of range-separated hybrids with the efficiency of semilocal functionals.

Meta-generalized gradient approximations (meta-GGAs), introduced in Chapter 4, might fulfill this requirement, as they depend not only on the electron density but also on the kinetic energy density and can, therefore, exhibit nonlocal features while maintaining the computational cost of semilocal functionals. This characteristic of meta-GGAs has led to an enhanced description of band gaps [AK19; Bor+20; KBM23; Leb+23; LAK24], raising the hope that they could also improve the accuracy of CT excitations in TDDFT. However, applying meta-GGA functionals in TDDFT is not straightforward because their dependence on the kinetic energy density introduces a gauge dependence [Tao05; BF12]. Chapter 5 addresses this issue. It explores the influence of applying a previously proposed current-density correction of the kinetic energy density [Bec02; Tao05] when using meta-GGA functionals within TDDFT for various model systems. Chapter 5 further examines the performance of meta-GGAs at the description of CT excitations in TDDFT, using two model systems as benchmarks. The results of this investigation are also presented in Ref. [Ric+23].

Although the results of Chapter 5 indicate a somewhat improved description of CT excitations using the meta-GGA TASK [AK19; Ric+23], it becomes evident that meta-GGAs cannot resolve the CT problem inherent to semilocal xc functionals. This limitation can be attributed to the persistent inability of meta-GGA exchange functionals to fully correct the self-interaction error introduced by the Hartree term and the incorrect asymptotic behavior of the xc potential. To address these shortcomings, Chapter 6 revisits the Perdew-Zunger self-interaction correction (PZ-SIC) [PZ81], which eliminates the (one-electron) self-interaction error and restores the correct asymptotic behavior of the xc potential. However, because of its special form, the PZ-SIC breaks the invariance of the energy functional under unitary transformations of the single-particle orbitals. Chapter 6 discusses the upcoming challenges due to the unitary variance and rigorously extends the PZ-SIC formalism to fractional particle numbers. This extension enables the investigation of the straight-line condition, a criterion that measures the correction of the many-electron self-interaction error, for semilocal xc approximations within the PZ-SIC framework (cf. Section 3.3) [VSP07]. Additionally, a new algorithm based on existing approaches from the literature [GU97; KKJ11; Hof+12; Bor+15] is presented for the practical application of the PZ-SIC.

Chapter 7 presents the results for the ionization potential and the straight-line condition for three different small model systems using the PZ-SIC with the LDA and the GGA functional PBE [PBE96]. Applying the PZ-SIC to the TASK [AK19] and r^{2}SCAN [Fur+20a; Fur+20b] meta-GGAs leads to additional numerical challenges, which can be addressed by introducing a new construction principle that explicitly ensures numerical stability for meta-GGAs within the PZ-SIC framework. The results for LDA, PBE, and a modified version of TASK for improved numerical stability within the PZ-SIC framework indicate that the self-interaction error is overcorrected for all considered semilocal density functional approximations using the PZ-SIC.

Therefore, Chapter 8 introduces a modification of the PZ-SIC in combination with the LDA. In this formulation, inspired by the concept of range-separated hybrid functionals [HSE03; YTH04; SKB09], the self-interaction correction of the Hartree term is applied

only in the long-range regime, with the range of this correction controlled by a parameter γ. For the exchange part, two different strategies are employed: in the first, only the self-interaction error of the LDA is corrected in the long-range regime; in the second, the entire LDA functional evaluated on the total electron density is screened to its short-range contribution. While the second approach proves to be numerically advantageous, the range-separation parameter γ in both cases can be tuned to closely fulfill the straight-line condition for the total energy as a function of the particle number and to yield accurate values for the ionization potential.

Chapter 2

Density Functional Theory and Time-Dependent Density Functional Theory

Density functional theory (DFT) and time-dependent density functional theory (TDDFT) are exact formalisms for describing many-particle quantum mechanical problems. This chapter provides a brief introduction to the basics of DFT and TDDFT, along with their numerical realization in the `BTDFT` program code [Sch17; SK18], which is based on real-space and real-time simulation techniques.

2.1 Ground-State Density Functional Theory

Predicting quantum physical properties using the original formulation of quantum mechanics involves solving the time-independent Schrödinger equation [Sch26]

$$\hat{H}|\Psi_i\rangle = E_i|\Psi_i\rangle\,, \tag{2.1}$$

where E_i is the energy eigenvalue corresponding to the quantum state $|\Psi_i\rangle$, and the N-particle Hamiltonian operator is given by

$$\hat{H} = \underbrace{\sum_{j=1}^{N} -\frac{\hbar^2}{2m}\nabla_{\mathbf{r}_j}^2}_{=:\hat{T}} + \underbrace{\sum_{j=1}^{N} v(\mathbf{r}_j)}_{=:\hat{V}} + \underbrace{\frac{1}{2}\sum_{\substack{j,k=1\\ j\neq k}}^{N} \omega(\mathbf{r}_j,\mathbf{r}_k)}_{=:\hat{W}}\,. \tag{2.2}$$

Here, $\hbar$ is the reduced Planck constant, m is the mass of the particle, and $\nabla_{\mathbf{r}_j}^2$ denotes the Laplace operator acting on the coordinate $\mathbf{r}_j$ of the jth particle. The terms $\hat{T}$, $\hat{V}$, and $\hat{W}$ represent the kinetic, potential, and interaction energies, respectively. The many-particle wave function $\Psi_i(\mathbf{x}_1,\mathbf{x}_2,\ldots,\mathbf{x}_N)$ in Eq. (2.1) depends on the coordinates $\mathbf{x}_k = (\mathbf{r}_k,\sigma_k)$, where each $\mathbf{x}_k$ is a tuple consisting of the space coordinate $\mathbf{r}_k$ and spin σ_k of the kth particle. Because this wave function depends on $3N$ spatial coordinates, solving Eq. (2.1) becomes computationally infeasible as N increases. Consequently, the numerical cost grows exponentially, a challenge that Walter Kohn famously referred to as the "exponential wall" of quantum mechanics [Koh99].

Numerous approaches have been developed to approximate the solution. These include the variational ansatz by James and Coolidge [JC33] for early studies of the H_2 molecule and Hartree-Fock theory [Har28; Foc30] for later applications. However, in most practical applications, the many-body wave function itself is not of primary

interest. Instead, the focus lies on physical properties such as the ground-state energy, dipole moment, or polarizability.

The fundamental principle of DFT is that the electron density $n(\mathbf{r})$ uniquely determines all ground-state properties, a result that was formally proven by Hohenberg and Kohn (HK) in 1964 [HK64]. Their second theorem establishes the existence of a universal functional,

$$F[n] = \langle \Psi[n] | \hat{T} + \hat{W} | \Psi[n] \rangle, \tag{2.3}$$

where $\hat{T}$ and $\hat{W}$ denote the kinetic and interaction energy operators, respectively. Together with the external potential $v_{\text{ext}}(\mathbf{r})$, this functional defines the total energy,

$$E_v[n] = F[n] + \int v_{\text{ext}}(\mathbf{r}) n(\mathbf{r}) \, \mathrm{d}^3 r \, . \tag{2.4}$$

The true ground-state density $n_0(\mathbf{r})$ can then be obtained by minimizing the energy functional with respect to the density

$$\frac{\delta}{\delta n(\mathbf{r})} \left\{ E_v[n] - \mu \left(\int n(\mathbf{r}') \, \mathrm{d}^3 r' - N \right) \right\} = 0 \, , \tag{2.5}$$

where $\mu = \partial E_v / \partial N$, the chemical potential, is a Lagrange multiplier enforcing the constraint of the correct particle number N [Cap06; Lev79; Lev82].

In the Kohn-Sham (KS) formulation [KS65] using the Born-Oppenheimer approximation [BO27] the energy functional is partitioned as

$$E_{\text{KS}}[n] = T_{\text{s}}[n] + E_{\text{ext}}[n] + E_{\text{H}}[n] + E_{\text{xc}}[n_\uparrow, n_\downarrow] \, , \tag{2.6}$$

with the spin-up and spin-down densities $n_\uparrow$ and $n_\downarrow$, respectively. The first term describes the (single-particle) kinetic energy

$$T_{\text{s}}[n] = T_{\text{s}}[\{\varphi_{i\sigma}[n]\}] = -\frac{\hbar^2}{2m} \sum_{\sigma=\uparrow,\downarrow} \sum_{j=1}^{N_\sigma} \int \varphi_{j\sigma}^*(\mathbf{r}) \nabla^2 \varphi_{j\sigma}(\mathbf{r}) \, \mathrm{d}^3 r \, , \tag{2.7}$$

which depends on the N_σ occupied non-interacting fermionic KS quasi-particles $\{\varphi_{i\sigma}\}$ with spin σ. The Hartree energy, expressed in Gaussian units (which are used throughout this work), is given by

$$E_{\text{H}}[n] = \frac{e^2}{2} \iint \frac{n(\mathbf{r}) n(\mathbf{r}')}{|\mathbf{r} - \mathbf{r}'|} \, \mathrm{d}^3 r' \, \mathrm{d}^3 r \, , \tag{2.8}$$

with the elementary charge e and describes the classical electrostatic interaction between the electrons. The external energy is expressed as

$$E_{\text{ext}}[n] = \int v_{\text{ext}}(\mathbf{r}) n(\mathbf{r}) \, \mathrm{d}^3 r \, , \tag{2.9}$$

with v_{ext} being the external potential which contains e. g. the electrostatic potential of the nuclei. The exchange-correlation (xc) energy $E_{\text{xc}}[n_\uparrow, n_\downarrow]$ contains all remaining energy contributions from the interaction of the particles in the system. The single-particle KS

equations, shown in the spin-polarized formulation [BH72], are given by

$$\underbrace{\left(-\frac{\hbar^2}{2m}\nabla^2 + v_{\mathrm{KS}\sigma}[n_\uparrow, n_\downarrow](\mathbf{r})\right)}_{\hat{H}_{\mathrm{KS}\sigma}} \varphi_{j\sigma}(\mathbf{r}) = \epsilon_{j\sigma}\varphi_{j\sigma}(\mathbf{r}), \tag{2.10}$$

where $\hat{H}_{\mathrm{KS}\sigma}$ represents the KS Hamiltonian and $\varphi_{j\sigma}$ are the KS orbitals. The eigenvalues $\{\epsilon_{j\sigma}\}$ are the associated single-particle energies (with $\epsilon_{1\sigma} < \cdots < \epsilon_{N\sigma}$). $v_{\mathrm{KS}\sigma}$ is the effective KS potential calculated via the functional derivative of the energy formulation of Eq. (2.6):

$$v_{\mathrm{KS}\sigma}[n_\uparrow, n_\downarrow](\mathbf{r}) = \frac{\delta E_{\mathrm{KS}}[n]}{\delta n_\sigma(\mathbf{r})} = v_{\mathrm{ext}}(\mathbf{r}) + v_{\mathrm{H}}[n](\mathbf{r}) + v_{\mathrm{xc}\sigma}[n_\uparrow, n_\downarrow](\mathbf{r})\,, \tag{2.11}$$

with the Hartree potential

$$v_{\mathrm{H}}[n](\mathbf{r}) = e^2 \int \frac{n(\mathbf{r}')}{|\mathbf{r} - \mathbf{r}'|}\,\mathrm{d}^3 r' \tag{2.12}$$

and $v_{\mathrm{xc}\sigma}[n_\uparrow, n_\downarrow] = \delta E_{\mathrm{xc}}[n_\uparrow, n_\downarrow]/\delta n_\sigma$. Together with the kinetic energy operator, $v_{\mathrm{KS}\sigma}$ builds the KS Hamiltonian $\hat{H}_{\mathrm{KS}\sigma}$. For the exact energy functional, the absolute squared KS orbitals sum up to the true ground-state density

$$n(\mathbf{r}) = n_\uparrow(\mathbf{r}) + n_\downarrow(\mathbf{r}) = \sum_{\sigma=\uparrow,\downarrow} \sum_{j=1}^{N_\sigma} |\varphi_{j\sigma}(\mathbf{r})|^2\,. \tag{2.13}$$

This KS formulation consisting of Eqs. (2.10), (2.11), and (2.13) is typically solved in an iterative scheme to obtain the ground-state quantities of a system.

At the core of every DFT calculation lies the xc part of the energy functional $E_{\mathrm{xc}}[n_\uparrow, n_\downarrow]$ and its derivative $v_{\mathrm{xc}\sigma}[n_\uparrow, n_\downarrow]$. This term is typically divided into its exchange $E_{\mathrm{x}}[n]$ and correlation $E_{\mathrm{c}}[n_\uparrow, n_\downarrow]$ components to simplify the development of suitable approximations. Since no exact expression for $E_{\mathrm{xc}}[n_\uparrow, n_\downarrow]$ is known yet, appropriate approximations are essential. Neglecting $E_{\mathrm{xc}}[n_\uparrow, n_\downarrow]$ entirely would reduce DFT to the Hartree approximation, which provides significantly less accurate results. As a result, the success of DFT in accurately describing physical properties depends crucially on the quality of the chosen xc approximation. Furthermore, the specific choice of the xc functional not only affects the accuracy of the results but also impacts the computational cost of solving the KS ground-state equations. Thus, the main goal of any density functional approximation (DFA) is to strike an optimal balance between accuracy and computational efficiency.

2.2 Time-Dependent Density Functional Theory

The HK theorems provide the foundation for calculating physical ground-state properties such as the ground-state energy or polarizability. However, they are insufficient for time-dependent or truly excited-state quantities, as they establish a connection only between the ground-state density and the external potential. In contrast, for excited-state problems, the time-dependent electron density becomes the central quantity. In TDDFT, the Runge-Gross theorem [RG84] finds analogously to the HK theorem a connection between the time-dependent density $n(\mathbf{r}, t)$ and the time-dependent external potential $v_{\mathrm{ext}}(\mathbf{r}, t)$: Given an initial many-body state $|\Psi_0\rangle$ with a fixed two-particle interaction,

there exists a one-to-one mapping between the time-dependent density $n(\mathbf{r},t)$ and the external potential $v_{\text{ext}}(\mathbf{r},t)$ up to a purely time-dependent constant $c(t)$, i. e.

$$n(\mathbf{r},t) \xleftrightarrow{\text{fixed } |\Psi_0\rangle} v_{\text{ext}}(\mathbf{r},t)\,. \tag{2.14}$$

As a consequence, the time-dependent Hamilton operator $\hat{H}[n,\Psi_0](t)$ is also a functional of $n(\mathbf{r},t)$ as well as the many-body wave function $\Psi[n](t)$ (up to a time-dependent phase). Accordingly, all time-dependent physical observables become functionals of $n(\mathbf{r},t)$ and Ψ_0, i. e., $O(t) = O[n,\Psi_0](t)$ [Ull16]. Starting from the special case where the many-body ground state serves as the initial state, $|\Psi_0\rangle$ itself becomes a functional of the ground-state density. This makes O a functional that depends solely on $n(\mathbf{r},t)$ [MBW02]. Runge and Gross proposed a variational principle based on the action functional for the practical calculation of the dynamic properties. However, this led to inconsistencies in symmetry properties and causality, which were resolved by van Leeuwen by introducing a new action functional within the Keldysh formalism (for details, see Refs. [Lee98; Lee01]). The resulting variational principle leads to the time-dependent KS (TDKS) equations

$$\underbrace{\left(-\frac{\hbar^2}{2m}\nabla^2 + v_{\text{KS}\sigma}(\mathbf{r},t)\right)}_{\hat{H}_{\text{KS}\sigma}(\mathbf{r},t)}\varphi_{j\sigma}(\mathbf{r},t) = \mathrm{i}\hbar\frac{\partial}{\partial t}\varphi_{j\sigma}(\mathbf{r},t) \tag{2.15}$$

for $j = 1,\ldots,N_\sigma$, with the TDKS potential

$$v_{\text{KS}\sigma}(\mathbf{r},t) = v_{\text{ext}}(\mathbf{r},t) + e^2\int\frac{n(\mathbf{r}',t)}{|\mathbf{r}-\mathbf{r}'|}\,\mathrm{d}^3r' + v_{\text{xc}\sigma}(\mathbf{r},t)\,, \tag{2.16}$$

and the imaginary unit i. Together with the kinetic energy operator (first term in Eq. (2.15)), this defines the TDKS Hamilton operator $\hat{H}_{\text{KS}\sigma}(\mathbf{r},t)$. The time-dependent electron density is then given by Eq. (2.13), with the ground-state orbitals substituted with the time-dependent orbitals $\varphi_{j\sigma}(\mathbf{r},t)$. Similar to the ground-state xc potential, the time-dependent equivalent can be calculated via a functional derivative of the xc action functional A_{xc}

$$v_{\text{xc}\sigma}(\mathbf{r},t) = \left.\frac{\delta A_{\text{xc}}}{\delta n(\mathbf{r},\tau)}\right|_{n=n_\sigma(\mathbf{r},t)}\,, \tag{2.17}$$

with τ being the Keldysh contour time (see Refs. [Lee98; Lee01]). However, since finding approximations for the xc action in practical applications is challenging, the adiabatic approximation is commonly employed. This approximation involves evaluating the ground-state xc functional with the time-dependent density $n(\mathbf{r},t)$, thus neglecting any memory effects [FNM03]. For a detailed description of the action functional and an explicit expression using a non-interacting TDKS system, see Ref. [Vig08].

2.3 Numerical Realization: The `BTDFT` Program Package

A wide range of quantum chemistry codes for calculating the physical properties of organic molecules, such as e. g. `QChem` [Sha+14] and `Turbomole` [Bal+20], use basis sets constructed from Gaussian or Slater functions, which are combined linearly to approximate the KS orbitals $\{\varphi_{j\sigma}\}$ [Sch+07]. Gaussian basis sets, in particular, offer the advantage of enabling efficient evaluation of integral expressions similar to the Fock integral [Jen12]. However, the computational cost and accuracy of such calculations

strongly depend on the specific choice of the basis set [Hil12], making careful selection crucial for reliable results.

An alternative approach is to represent the KS orbitals directly on a real-space grid instead of using predefined basis functions. This work follows this strategy by employing the BTDFT (Bayreuth density functional theory) program package [SK18], which represents the KS orbitals (along with all related quantities, such as the KS potential) on an equidistant real-space grid, also referred to as "δ-basis" [Sch17; SK18]. The real-space grid on which the orbitals are calculated and the KS potential is evaluated can be either chosen to be an ellipsoid or defined by a density threshold around the center of the atoms in the molecule (typically chosen to be $10^{-7}\, a_0^{-3}$ in this work). The derivatives on this real-space grid are calculated by finite differences of sixth order. This real-space approach is highly parallelizable due to the sparsity of the matrix representation of the KS equations. However, its accuracy depends on the chosen grid size and spacing. Representing core orbitals, which typically exhibit high-frequency oscillations, on a real-space grid would require an impractically small grid spacing. Since valence electrons primarily govern chemical binding in molecules, the effects of core electrons and atomic cores on the valence electrons are efficiently incorporated using pseudopotentials (PPs) [HSC79; KB82; Pic89; TM91; Kro+06].

The fundamental concept of PPs is to partition the all-electron density into two components: one generated by the valence orbitals $\{\varphi^{\mathrm{v}}_{j\sigma}\}$ and the other by the core orbitals $\{\varphi^{\mathrm{c}}_{j\sigma}\}$. The modified KS potential acting on the valence particles is then expressed as

$$v^{\mathrm{ps}}_{\mathrm{KS}\sigma}[n_{\mathrm{v}}](\mathbf{r}) = v_{\mathrm{ps}}(\mathbf{r}) + v_{\mathrm{H}}[n_{\mathrm{v}}](\mathbf{r}) + v_{\mathrm{xc}\sigma}[n_{\mathrm{v}\uparrow}, n_{\mathrm{v}\downarrow}](\mathbf{r})\,, \tag{2.18}$$

where v_{ps} is the PP. To create the PP for a single atom, the modified KS potential, $v^{\mathrm{ps}}_{\mathrm{KS}\sigma}[n_{\mathrm{v}}]$, is constructed such that it reproduces the same valence KS orbitals $\{\varphi^{\mathrm{v}}_{j\sigma}\}$ as the all-electron KS potential $v_{\mathrm{KS}\sigma}[n]$ outside a given cutoff radius r_{c}. Finally, the contributions of $v_{\mathrm{H}}[n_{\mathrm{v}}]$ and $v_{\mathrm{xc}\sigma}[n_{\mathrm{v}\uparrow}, n_{\mathrm{v}\downarrow}]$ are subtracted from $v^{\mathrm{ps}}_{\mathrm{KS}\sigma}$ to calculate v_{ps} [Cap06; Che+03]. The resulting v_{ps} is then used as an element-specific PP in a KS calculation of a molecule. In practice, there are different construction principles for calculating $v^{\mathrm{ps}}_{\mathrm{KS}\sigma}$. In this work, norm-conserving Troullier-Martins type PPs are used [HSC79; KB82; TM91].

At this point, it should be noted that subtracting $v_{\mathrm{xc}\sigma}[n_{\mathrm{v}\uparrow}, n_{\mathrm{v}\downarrow}]$, which depends only on the valence density n_{v}, is an approximation. Unlike the Hartree potential $v_{\mathrm{H}}[n] = v_{\mathrm{H}}[n_{\mathrm{c}}] + v_{\mathrm{H}}[n_{\mathrm{v}}]$, the xc potential can be highly nonlinear, i. e.,

$$v_{\mathrm{xc}\sigma}[n](\mathbf{r}) \neq v_{\mathrm{xc}\sigma}[n_{\mathrm{c}}](\mathbf{r}) + v_{\mathrm{xc}\sigma}[n_{\mathrm{v}}](\mathbf{r})\,, \tag{2.19}$$

with $n = n_{\mathrm{c}} + n_{\mathrm{v}}$. As a result, this approximation is valid only if there is no significant overlap between the core density n_{c} and the valence density n_{v}. This issue can be resolved by employing the nonlinear core correction (NLCC) [LFC82; Wil+13]. For the NLCC, $v_{\mathrm{xc}\sigma}[n_{\mathrm{v}\uparrow}, n_{\mathrm{v}\downarrow}]$ in the subtraction step is replaced by $v_{\mathrm{xc}\sigma}[n_{\mathrm{c}\uparrow} + n_{\mathrm{v}\uparrow}, n_{\mathrm{c}\downarrow} + n_{\mathrm{v}\downarrow}]$. Since the PP v_{ps} no longer includes the xc effects of the core and valence electrons, the core density must be added explicitly when evaluating the xc potential in Eq. (2.18). However, using the full core charge would be numerically cumbersome since it contains high-frequency components. To address this, and based on the observation that incorporating the core density has significant effects only where its magnitude is comparable to the valence density, the core density is replaced by a pseudo-core charge $n^{\mathrm{ps}}_{\mathrm{c}}$. This pseudo-core charge equals n_{c} outside a given cutoff radius r_{pc} [PPL99].

Another important aspect for real-space codes, such as BTDFT, is the numerical challenge of calculating the Hartree potential $v_{\mathrm{H}}[n]$ directly in its integral expression of

Eq. (2.12). To circumvent this problem, `BTDFT` solves the corresponding Poisson equation

$$\nabla^2 v_\mathrm{H}(\mathbf{r}) = -4\pi e^2 n(\mathbf{r}) \tag{2.20}$$

to obtain v_H. However, since the Hartree potential decays slowly as $\sim 1/r$, using a zero-boundary condition would still require a computationally challenging large grid. Therefore, `BTDFT` employs a different boundary condition, adapted from the real-space code `PARSEC` [Kro+06; Bur+03]. In this scheme, the Hartree potential is divided into an internal part within the grid and a boundary part outside the grid, i. e., $v_\mathrm{H} = v_\mathrm{H}^\mathrm{in} + v_\mathrm{H}^\mathrm{bound}$. By choosing v_H^in to be zero outside the grid, a new Poisson equation

$$\nabla^2 v_\mathrm{H}^\mathrm{in}(\mathbf{r}) = -4\pi e^2 n(\mathbf{r}) - \underbrace{\nabla^2 v_\mathrm{H}^\mathrm{bound}(\mathbf{r})}_{=-4\pi e^2 n^\mathrm{bound}(\mathbf{r})} \tag{2.21}$$

can be formulated, while $v_\mathrm{H}^\mathrm{bound}$ is computed via a multipole expansion of 9th order [Bur+03]. The Laplacian acting on the boundary potential $v_\mathrm{H}^\mathrm{bound}$ can then be evaluated, yielding a boundary density n^bound (multiplied by the constant $-4\pi e^2$). By defining the boundary condition at the grid edge through the boundary density calculated with a 9th-order multipole expansion, the grid used to solve the Poisson equation and to calculate v_H^in in Eq. (2.21) can be chosen significantly smaller than if a zero-boundary condition is used to calculate v_H, as in Eq. (2.20).

2.4 Real-Time Propagation in TDDFT

The key challenge in TDDFT lies in solving the TDKS equations numerically to calculate physical excitation properties such as excitation energies, oscillator strengths, or transition densities. Within quantum chemistry codes, like `QChem` [Sha+14] and `Turbomole` [Bal+20], employ the frequency-domain formulation of the TDKS equations within the linear-response formalism [Cas95; Cas+98]. In contrast, in the real-time propagation scheme on a real-space grid used in this work, the time-dependent density $n(\mathbf{r}, t)$ is the only observable that can be accessed directly. Consequently, although the excitation spectrum is not immediately available, a few straightforward evaluation steps are required to obtain it, as discussed in the next section. Despite this inconvenience, the real-time, real-space approach offers several advantages [SK18; Mar03]: It is highly parallelizable both in real space and over the orbitals, making it particularly suitable for calculating larger systems compared to the linear-response approach. Moreover, unlike the linear-response formalism, real-time propagation is not limited to the linear regime, enabling the study of nonlinear phenomena, such as systems in intense laser fields [Kru+20; Coc+14; Cal+00; LG11].

A typical starting point for our real-time (and real-space) approach is the propagation of the TDKS orbitals using the time-propagation operator $\hat{U}(t, t_0)$:

$$\varphi_{j\sigma}(\mathbf{r}, t) = \hat{U}(t, t_0)\varphi_{j\sigma}(\mathbf{r}, t_0) = \hat{\tau} \exp\left\{-\frac{\mathrm{i}}{\hbar}\int_{t_0}^{t} \hat{H}_{\mathrm{KS}\sigma}(t')\,\mathrm{d}t'\right\} \varphi_{j\sigma}(\mathbf{r}, t_0)\,, \tag{2.22}$$

with the time-ordering operator $\hat{\tau}$ [CMR04]. For numerical implementations, the time t is discretized into time steps $t_k = t_0 + k\Delta t$, where Δt is the step length and $k \in \mathbb{N}_0$. If Δt is chosen sufficiently small, the exponential term in Eq. (2.22) can be approximated as

$$U(t_k + \Delta t, t_k) \approx \exp\left\{-\frac{\mathrm{i}}{\hbar}\hat{H}_{\mathrm{KS}\sigma}\left(t_k + \frac{\Delta t}{2}\right)\Delta t\right\}\,. \tag{2.23}$$

Since in a step-by-step propagation scheme, the time-propagation operator is applied in a causal manner, the time-ordering operator $\hat{\tau}$ can be neglected. In practice, `BTDFT` uses a predictor-corrector scheme [Pre07] to calculate the KS Hamilton operator at $t + \Delta t/2$. Using this midpoint approximation, the Crank-Nicolson propagator [CN47] provides an efficient scheme to approximate the exponential operator as

$$\exp\left\{-\frac{\mathrm{i}}{\hbar}\hat{H}_{\mathrm{KS}\sigma}\Delta t\right\} \approx \frac{1-\frac{\mathrm{i}}{\hbar}\hat{H}_{\mathrm{KS}\sigma}\frac{\Delta t}{2}}{1+\frac{\mathrm{i}}{\hbar}\hat{H}_{\mathrm{KS}\sigma}\frac{\Delta t}{2}}\,, \tag{2.24}$$

which is used in this work. Substituting Eq. (2.23) and Eq. (2.24) into Eq. (2.22) leads to a discretized equation

$$\left[1+\frac{\mathrm{i}}{2\hbar}\hat{H}_{\mathrm{KS}\sigma}\left(t_k+\frac{\Delta t}{2}\right)\Delta t\right]\varphi_{j\sigma}(t_k+\Delta t) = \left[1-\frac{\mathrm{i}}{2\hbar}\hat{H}_{\mathrm{KS}\sigma}\left(t_k+\frac{\Delta t}{2}\right)\Delta t\right]\varphi_{j\sigma}(t_k)\,, \tag{2.25}$$

which must be solved for each KS orbital j. In this work, the orbitals are discretized on a real-space grid, which causes Eq. (2.25) to expand into a matrix equation that can be solved numerically [Ull16]. For this purpose, `BTDFT` uses an iterative conjugate gradient method [Sch17]. While the Crank-Nicolson propagator is employed here, various other propagation algorithms are also available, as detailed in Ref. [CMR04].

2.5 Calculation of Excitation Spectra in Real-Time TDDFT

Since in real-time TDDFT, the only directly accessible physical observable is the time-dependent density $n(\mathbf{r}, t)$, excitation energies are not immediately available and must be computed in several steps. The details of these steps, as presented below, can be found in Ref. [SK18].

Calculating the absorption spectrum of a system starts by exciting the ground-state orbitals, $\{\varphi_{j\sigma}^{(0)}\}$, which correspond to the ground-state density n_0, with a so-called boost excitation. This boost excitation matches an infinitesimal short laser pulse that excites the system and is done by applying a space-dependent phase to all the orbitals

$$\varphi_{j\sigma}(\mathbf{r}, t=0) = e^{\mathrm{i}\mathbf{k}\cdot\mathbf{r}}\varphi_{j\sigma}^{(0)}(\mathbf{r})\,, \tag{2.26}$$

where $\mathbf{k}$ determines the boost direction, and the boost energy is given by $E_{\mathrm{boost}} = N\hbar^2|\mathbf{k}|^2/(2m)$ [SK18; BLL16; MK07; Rep+15]. A weak δ-like excitation ensures that all frequencies of the many-particle system are excited.

The theoretical absorption spectrum is given by the dipole strength function, defined as [Rub+12]

$$S(\omega) = -\frac{2m\omega}{3\pi e\hbar^2 k}\,\mathrm{Im}\left\{\mathrm{Tr}\left[\delta\tilde{\mu}_\gamma^{(\vartheta)}(\omega)\right]\right\}\,. \tag{2.27}$$

Here, $\delta\tilde{\mu}_\gamma^{(\vartheta)}(\omega)$ is the γ-component of the Fourier transform of the induced dipole moment

$$\delta\boldsymbol{\mu}(t) = -e\int \mathbf{r}\,(n(\mathbf{r},t) - n_0(\mathbf{r}))\,\mathrm{d}^3r\,, \tag{2.28}$$

after a boost excitation in the ϑ-direction, depending on the frequency ω. Ref. [SK18] shows that $\mathrm{Tr}\left[\delta\tilde{\mu}_\gamma^{(\vartheta)}(\omega)\right]$ can be calculated analytically for a boost excitation within the

linear response regime, leading to

$$\mathrm{Tr}\left[\delta\tilde{\mu}_{\gamma}^{(\vartheta)}(\omega)\right] = -\frac{3e\hbar k}{m}\sum_{j=1}^{\infty}\frac{f_{0j}}{\omega_{0j}}\sin(\omega_{0j}t)\,, \tag{2.29}$$

where

$$f_{0j} = \frac{2m\omega_{0j}|\mathbf{d}_{0j}|^2}{3\hbar} \tag{2.30}$$

is the oscillator strength of the transition $0 \to j$ with its frequency ω_{0j} and $\mathbf{d}_{0j} = \langle 0|\hat{\mathbf{r}}|j\rangle$. Inserting this expression into the dipole strength function of Eq. (2.27) gives the analytical form of the photoabsorption spectrum

$$S(\omega) = \sum_{j=1}^{\infty} f_{0j}\frac{\omega}{\omega_{0j}}\frac{\sin((\omega-\omega_{0j})T)}{\pi\hbar(\omega-\omega_{0j})}\,, \tag{2.31}$$

where T is the propagation time [Sch17].

This analytical form is then fitted to the numerical form to extract the excitation frequencies ω_{0j} (and oscillator strengths f_{0j}). The highest excitation frequency, $\omega_{\max}$ that can be calculated, is determined by the time step during the real-time propagation, with $\omega_{\max} \sim 1/\Delta t$. Thus, the time step must be chosen small enough to calculate excitations up to a desired frequency $\omega_{\max}$ [Sch17].

Chapter 3

Exact Properties of Exchange-Correlation Functionals

The accuracy of DFT and TDDFT calculations crucially depends on the chosen xc approximation $E_{\mathrm{xc}}[n_\uparrow, n_\downarrow]$ and its functional derivative $v_{\mathrm{xc}}[n_\uparrow, n_\downarrow]$. In this work, we investigate and apply xc approximations with a particular focus on accurately describing charge-transfer (CT) processes in DFT and TDDFT. Therefore, this chapter begins with an introduction to the CT problem within DFT, which has been the subject of numerous studies [Toz03; VZ07; Fuk16; Küm17; MK22; AK19].

A paradigm example of a CT process that illustrates many of the challenges in DFT is long-range CT, where an electron moves from a donor (D) molecule to an acceptor (A) molecule (or donor and acceptor region) over a large distance R, as illustrated in Fig. 3.1. For long-range separations, where the orbital overlap between D and A is negligible, the

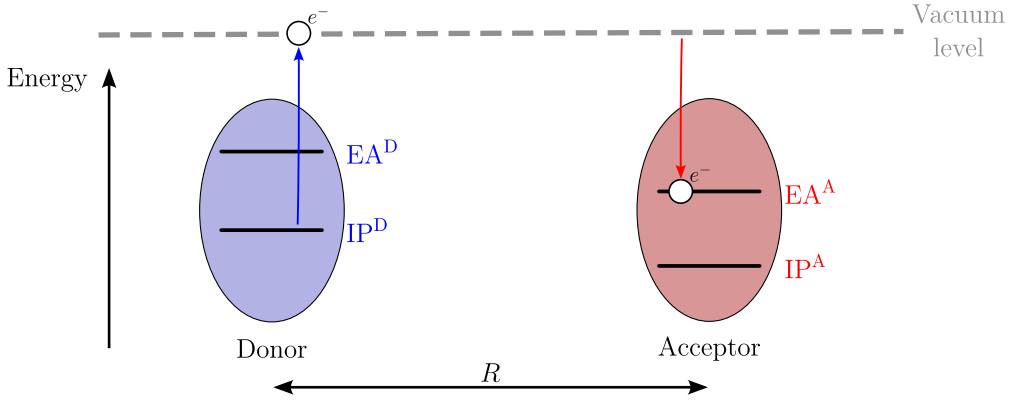

Figure 3.1: Illustration of a long-range CT process, where IP^{D} and IP^{A} denote the ionization potentials of the donor and acceptor molecules, respectively, separated by a distance R, and EA^{D} and EA^{A} represent their electron affinities.

lowest CT energy is given by

$$\Omega_{\mathrm{CT}} = \mathrm{IP}^{\mathrm{D}} - \mathrm{EA}^{\mathrm{A}} - e^2 \frac{1}{R}\,. \tag{3.1}$$

Here, IP^{D} is the ionization potential of the donor, EA^{A} is the electron affinity of the acceptor, and the last term accounts for the electrostatic interaction between the additional charge on A and the extracted charge on D [Mai17]. In the limit $R \to \infty$, this reduces to $\Omega_{\mathrm{CT}} = \mathrm{IP}^{\mathrm{D}} - \mathrm{EA}^{\mathrm{A}}$ [Toz03]. To accurately describe CT processes, such as the one given by Eq. (3.1), the xc approximation must satisfy certain exact properties, as discussed below.

3.1 Correct Asymptotic Behavior

In asymptotic regions, i. e., at large distances r from the nuclei of a neutral (and finite) system, the xc potential should decay as

$$v_{\mathrm{xc}}(\mathbf{r}) \sim -\frac{e^2}{r}\,, \tag{3.2}$$

which is governed by the exchange part of the potential, $v_{\mathrm{x}}(\mathbf{r})$ [LPS84; AB85]. Ensuring the correct asymptotic behavior of the potential is crucial to accurately reproduce the $-1/R$ dependence in Eq. (3.1). Intuitively, this behavior can be understood by considering a KS particle, specifically the highest occupied molecular orbital (HOMO), located at a large distance r from the center of the molecule. At this distance, the KS orbital should experience an attractive potential arising from two contributions: the attractive potential due to the nuclei, $\sim -e^2N/r$, and the screening effect from the remaining $N-1$ charges, $\sim e^2(N-1)/r$. This results in the asymptotic behavior of the KS potential as $-e^2/r$. Since the Hartree potential and the external potential of the nuclei cancel each other asymptotically, the correct asymptotic behavior must be determined by the xc potential v_{xc} [KK20]. HOMOs that incorporate nodal planes present additional challenges, as discussed in Refs. [GGB16; GB18].

Functionals that depend locally on the density, such as the local density approximation (LDA) [HK64], which will be introduced in Section 4.1, decay exponentially and thus underestimate the electron-nucleus interaction at large distances [VZ07].

3.2 Freedom from Self-Interaction

The one-particle self-interaction error (SIE) is evident in the KS decomposition of the ground-state energy, where the Hartree energy models the electrostatic interaction between electrons. For a one-electron ($1e$) system, where the density is determined by a single (spin-)orbital, $n_{1e} = |\varphi_1|^2$, the ground-state energy should be determined by the kinetic energy, E_{kin}, and the energy contribution of the electron in its external field, E_{ext}. Thus, the contributions of the Hartree energy and the exchange energy should cancel each other out, i. e.,

$$E_{\mathrm{H}}[n_{1e}] + E_{\mathrm{x}}[n_{1e}] \overset{!}{=} 0\,, \tag{3.3}$$

and the correlation energy should vanish [KK20; PZ81],

$$E_{\mathrm{c}}[n_{1e}, 0] \overset{!}{=} 0\,. \tag{3.4}$$

Condition (3.3) is automatically satisfied for the exact exchange energy functional, since for a one-electron system, the energy expression

$$E_{\mathrm{x}}^{\mathrm{exact}} = -\frac{e^2}{2} \sum_{\sigma=\uparrow,\downarrow} \sum_{i,j=1}^{N_\sigma} \iint \frac{\varphi_{i\sigma}^*(\mathbf{r}')\varphi_{j\sigma}^*(\mathbf{r})\varphi_{i\sigma}(\mathbf{r})\varphi_{j\sigma}(\mathbf{r}')}{|\mathbf{r}-\mathbf{r}'|}\,\mathrm{d}^3r\,\mathrm{d}^3r' \tag{3.5}$$

reduces to $-E_{\mathrm{H}}[n_{1e}]$.

Overall, this repulsion error, arising from an electron interacting with itself, results in a spurious favoring of charge delocalization, leading to an underestimation of the ionization potential (IP) values [MCY06; VS05]. While the exact exchange functional, defined in Eq. (3.5), can address the (one-particle) SIE, it is computationally expensive. Therefore, finding ways to capture the SIE using computationally less demanding

(semi-)local approximations, as introduced in Chapter 4, remains an ongoing challenge in DFT and strategies for achieving freedom from self-interaction will be discussed in later sections.

3.3 Straight-Line Condition and Derivative Discontinuity

Perdew *et al.* [Per+82] introduced an ensemble extension of DFT for systems with density $n(\mathbf{r})$ integrating to a non-integer electron number, $N_0+\eta$, where N_0 is an integer and $0<\eta<1$. Such systems are described as statistical mixtures of the ground state of two systems: one with N_0 electrons and the other with N_0+1. Consequently, the energy as a function of N follows a straight line between the integer points, given by [Per+82; YZA00]

$$E(N) = (1-\eta)E(N_0) + \eta E(N_0+1)\,. \tag{3.6}$$

This linear behavior is illustrated in Fig. 3.2. Taking Eq. (3.6) and the relation

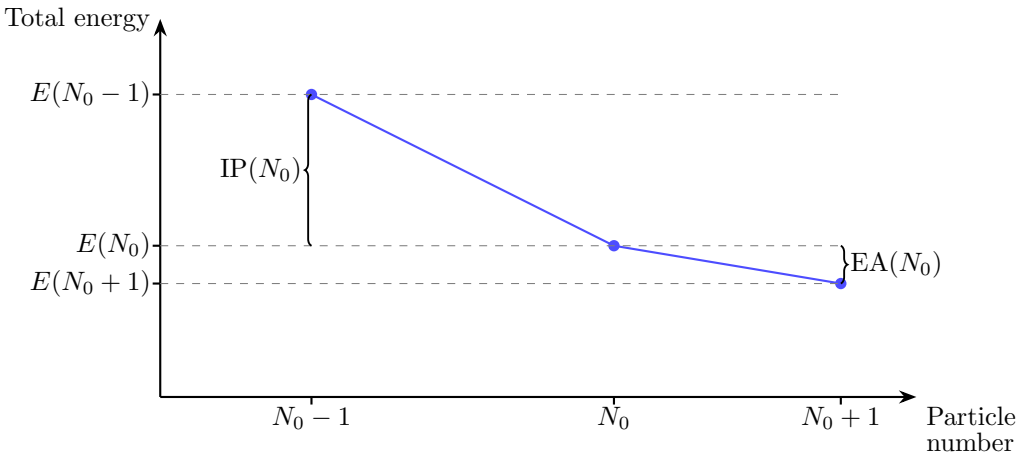

Figure 3.2: Illustration of the straight line condition: Piecewise linear ground-state energy function $E(N)$ for fractional particle numbers N.

$\partial E(N)/\partial N = \mu$, the chemical potential μ exhibits a discontinuity at integer electron numbers

$$\mu(N) = \begin{cases} -\mathrm{IP}(N_0) & N_0-1 < N \leq N_0, \\ -\mathrm{EA}(N_0) & N_0 < N \leq N_0+1\,, \end{cases} \tag{3.7}$$

where the IP and electron affinity (EA) are given by $\mathrm{IP} = E(N_0-1) - E(N_0)$ and $\mathrm{EA} = E(N_0) - E(N_0+1)$ [Per+82]. The fundamental gap Δ_g is the derivative discontinuity of the energy [YCM12]

$$\begin{aligned} \Delta_\mathrm{g} &= \mathrm{IP}(N_0) - \mathrm{EA}(N_0) \\ &= \lim_{\eta\to 0} \left\{ \left.\frac{\partial E(N)}{\partial N}\right|_{N_0+\eta} - \left.\frac{\partial E(N)}{\partial N}\right|_{N_0-\eta} \right\} \\ &= \lim_{\eta\to 0} \left\{ \left.\frac{\delta E[n]}{\delta n(\mathbf{r})}\right|_{N_0+\eta} - \left.\frac{\delta E[n]}{\delta n(\mathbf{r})}\right|_{N_0-\eta} \right\}. \end{aligned} \tag{3.8}$$

Within the KS formulation of DFT, the fundamental gap Δ_g is given by

$$\begin{aligned}\Delta_\mathrm{g} = &\underbrace{\lim_{\eta\to 0}\left(\left.\frac{\delta T_\mathrm{s}[n]}{\delta n(\mathbf{r})}\right|_{N_0+\eta} - \left.\frac{\delta T_\mathrm{s}[n]}{\delta n(\mathbf{r})}\right|_{N_0-\eta}\right)}_{=:\Delta_\mathrm{KS}} \\ &+ \underbrace{\lim_{\eta\to 0}\left(\left.\frac{\delta E_\mathrm{xc}[n]}{\delta n(\mathbf{r})}\right|_{N_0+\eta} - \left.\frac{\delta E_\mathrm{xc}[n]}{\delta n(\mathbf{r})}\right|_{N_0-\eta}\right)}_{=:\Delta_\mathrm{xc}},\end{aligned} \tag{3.9}$$

where the derivatives of the Hartree energy, $\delta E_\mathrm{H}[n]/\delta n$, and of the external energy, $\delta E_\mathrm{ext}[n]/\delta n$, are continuous at N_0 and, consequently, do not contribute to Δ_g. Here, Δ_KS is referred to as the KS gap, i. e. $\Delta_\mathrm{KS} = \epsilon_\mathrm{LUMO} - \epsilon_\mathrm{HOMO}$, and Δ_xc is the xc gap or derivative discontinuity [PL83; SS83].

The derivative discontinuity corresponds to a discontinuous jump of the xc potential when the electron number crosses an integer point. This feature is decisive for describing CT processes correctly, as can be understood as follows: Consider again a system consisting of two molecules, donor (D) and acceptor (A), separated by a large distance. When a small static external potential is applied, no CT should occur from D to A. Simple xc approximations that explicitly depend on the density, like the LDA, respond in the direction of the external field. However, the exact xc potential must counteract the static external potential to prevent the CT process. This property, fulfilled by the exact exchange functional, is also often referred to as "ultranonlocality" [Gis+99; GGB02; Faa+02; AK19; Asc+23]. When the external potential increases beyond a critical threshold – corresponding to the difference between the ionization potential (IP^D) of D and the electron affinity (EA^A) of A – exactly one electron should transfer from D to A. At this point, the xc potential must exhibit a sudden jump to stabilize the new electron configuration. This crucial discontinuous jump in the potential at integer electron numbers corresponds to the derivative discontinuity, Δ_xc [Gis+99; KKP04; KK18; Toz03].

However, (semi-)local functionals like the LDA do not exhibit a derivative discontinuity at integer particle numbers Δ_xc. As a consequence, the error in the predicted CT excitation energies by (semi-)local xc approximations is significant since it has been explicitly shown (see Ref. [Toz03]) that this error is proportional to the sum of the missing Δ_xc contributions at the donor and acceptor molecules.

3.4 Janak's Theorem and IP Theorem

The previous section introduced the IP as the energy difference between an N_0-electron system and an $(N_0 - 1)$-electron system. However, it turns out that although the KS eigenvalues are introduced merely as mathematical objects in an auxiliary system of non-interacting particles, the HOMO eigenvalue does have a rigorous physical meaning: According to Janak's theorem [Jan78],

$$\frac{\partial E}{\partial N} = \epsilon_\mathrm{HOMO}(N)\,, \tag{3.10}$$

and given the relationship $\partial E/\partial N = \mu(N)$, it can be shown that for the exact xc functional

$$\epsilon_{\mathrm{HOMO}}(N) = \begin{cases} -\mathrm{IP}(N_0) & \text{for } N_0 - 1 < N \leq N_0 \\ -\mathrm{EA}(N_0) & \text{for } N_0 < N \leq N_0 + 1 \end{cases} \tag{3.11}$$

holds [Per+82; LPS84]. Consequently, the exact xc functional must satisfy the so-called IP theorem [PL83; PL97]

$$E(N_0 - 1) - E(N_0) = -\epsilon_{\mathrm{HOMO}}(N_0)\,. \tag{3.12}$$

For the exact functional, the last equation must also hold for $\epsilon_{\mathrm{HOMO}}(N)$ with $N_0 - 1 < N \leq N_0$. However, in practice, $\epsilon_{\mathrm{HOMO}}(N_0)$ is often considered when verifying the IP theorem.

3.5 Connection Between Correct Asymptotic Behavior, Freedom from Self-Interaction and Straight-Line Condition

Although we introduced the correct asymptotic behavior, the freedom from self-interaction, and the straight-line condition as different properties of the exact xc functional, it is important to note that, while these properties are not equivalent, they all follow the principle of avoiding spurious electron-electron interactions in the system.

The connection between these three properties can be understood by considering simple hydrogen-based model systems, as outlined in Ref. [KK20]: Without eliminating the one-electron SIE, (semi-)local functionals such as the LDA typically overestimate the ground-state energy of a single hydrogen atom, predicting values higher than $-1\,\mathrm{Ry}$. Additionally, due to the incorrect asymptotic behavior of the LDA, the negatively charged hydrogen ion H^- is predicted to be unbound. Since the LDA exchange potential decays exponentially rather than as $-1/r$, it is not sufficiently binding to stabilize the H^- molecule. Moreover, the dissociation process of the H_2^+ molecule is incorrectly described by widely used (semi-)local xc approximations [BS97; ZY98; GKC04b]. Whereas the exact functional is required to yield an energetic degeneracy between a state with one electron fully localized on one nucleus and a state with $0.5\,e$ on each nucleus (semi-)local functionals such as the LDA spuriously favor a charge distribution of $-0.5\,e$ on each nucleus. This error, which is not limited to the H_2^+ molecule but has also been observed in various other systems [Per+82; Ruz+06], is a direct consequence of the violation of the straight-line condition by (semi-)local functionals. These functionals typically tend to exhibit a convex deviation from piecewise linearity, making fractional occupations energetically more favorable [KK20].

Due to the connection between these exact properties, improving one property typically enhances the description of others. This will be explicitly demonstrated for the Perdew-Zunger self-interaction correction, which removes the SIE introduced in Section 3.2 and, at the same time, improves the description of the straight-line condition. A detailed discussion of the relationship between the properties can be found in Ref. [KK20].

3.6 Further Exact Properties of Exchange-Correlation Functionals

In addition to the exact properties relevant for the accurate description of CT processes, we now turn to further exact conditions of the xc functional that are considered in this work.

3.6.1 Size Consistency

Consider a system composed of two well-separated subsystems, 1 and 2. The total energy E of the combined system should equal the sum of the ground-state energies of the individual subsystems, E_1 and E_2, i. e.,

$$E = E_1 + E_2 \,. \tag{3.13}$$

Similarly, the total electron density n should be the sum of the densities of the subsystems,

$$n(\mathbf{r}) = n_1(\mathbf{r}) + n_2(\mathbf{r}) \,, \tag{3.14}$$

where n_1 and n_2 are the densities of subsystems 1 and 2, respectively [FNM03]. Commonly used xc functionals, such as the LDA, inherently satisfy this size consistency property. However, certain approximations designed to correct the SIE in DFT, such as the average density self-interaction correction (see Section 6.1), compromise this property [LSR02; Keh+20].

3.6.2 Unitary Invariance

Another fundamental condition for any DFA is unitary invariance. This principle ensures that the total energy remains unchanged under unitary transformations of the occupied orbitals. To illustrate, consider a unitary transformation defined by a unitary matrix $\boldsymbol{U}_\sigma$, such that $\sum_{i=1}^{N_\sigma} U_{il\sigma} U^*_{ik\sigma} = \delta_{kl}$. Applying this transformation to a set of N orbitals $\{\varphi_{i\sigma}\}$ results in a new set of orbitals $\{\varphi'_{i\sigma}\}$ by

$$\varphi'_{i\sigma}(\mathbf{r}) = \sum_{j=1}^{N_\sigma} U_{ij\sigma} \varphi_{j\sigma}(\mathbf{r}) \,. \tag{3.15}$$

Both sets lead to the same density $n(\mathbf{r})$ since

$$\begin{aligned} n[\{\varphi'_{i\sigma}\}](\mathbf{r}) &= \sum_{\sigma=\uparrow,\downarrow} \sum_{i=1}^{N_\sigma} |\varphi'_{i\sigma}(\mathbf{r})|^2 = \sum_{\sigma=\uparrow,\downarrow} \sum_{k,l=1}^{N_\sigma} \underbrace{\sum_{i=1}^{N_\sigma} U^*_{ik\sigma} U_{il\sigma}}_{=\delta_{lk}} \varphi^*_{k\sigma}(\mathbf{r}) \varphi_{l\sigma}(\mathbf{r}) \\ &= \sum_{\sigma=\uparrow,\downarrow} \sum_{k=1}^{N_\sigma} |\varphi_{k\sigma}(\mathbf{r})|^2 = n[\{\varphi_{i\sigma}\}](\mathbf{r}) \,. \end{aligned} \tag{3.16}$$

The condition of unitary invariance is automatically satisfied for xc approximations that depend solely on the density. In contrast, it is not immediately evident whether this condition holds for approximations that explicitly depend on the orbitals. To ensure unitary invariance for such orbital-dependent functionals, the orbital dependence is often

reformulated in terms of the positive definite kinetic energy density

$$\tau(\mathbf{r}) = \frac{\hbar^2}{2m} \sum_{\sigma=\uparrow,\downarrow} \sum_{i=1}^{N_\sigma} |\nabla \varphi_{i\sigma}(\mathbf{r})|^2 \,, \tag{3.17}$$

which is invariant under unitary transformations of the orbitals.

Nevertheless, not all orbital-dependent functionals satisfy this condition. While the exact exchange functional defined in Eq. (3.5) is unitary invariant by construction, the self-interaction correction (SIC) introduced by Perdew and Zunger [PZ81] violates this invariance. The implications of this violation and its challenges are discussed in detail in Chapter 6.

3.6.3 Spin Scaling Relations

The spin-polarized versions of the non-interacting kinetic energy T_s as well as the exchange energy E_x can be expressed in terms of their spin-unpolarized versions by the spin-scaling relations [OP79]

$$T_\mathrm{s}[n_\uparrow, n_\downarrow] = \frac{1}{2} T_\mathrm{s}[2n_\uparrow] + \frac{1}{2} T_\mathrm{s}[2n_\downarrow] \tag{3.18}$$

and

$$E_\mathrm{x}[n_\uparrow, n_\downarrow] = \frac{1}{2} E_\mathrm{x}[2n_\uparrow] + \frac{1}{2} E_\mathrm{x}[2n_\downarrow] \,, \tag{3.19}$$

since these terms can be split into contributions depending on the spin-up and spin-down densities separately. For xc functionals depending on the previously introduced kinetic energy density $\tau(\mathbf{r})$ the spin-scaling of Eq. (3.19) becomes

$$E_\mathrm{x}[n_\uparrow, n_\downarrow] = \frac{1}{2} E_\mathrm{x}[2n_\uparrow, 2\tau_\uparrow] + \frac{1}{2} E_\mathrm{x}[2n_\downarrow, 2\tau_\downarrow] \,. \tag{3.20}$$

This scaling relation similarly applies to the corresponding exchange potential v_x, i. e.

$$v_\mathrm{x}[n_\uparrow, n_\downarrow] = v_\mathrm{x}[2n_\uparrow, 2\tau_\uparrow] + v_\mathrm{x}[2n_\downarrow, 2\tau_\downarrow] \,. \tag{3.21}$$

In contrast, the correlation energy does not obey a simple spin-scaling relation [FNM03].

Chapter 4

Exchange-Correlation Approximations

The exact exchange functional defined in Eq. (3.5) not only eliminates the SIE but also satisfies all properties of the exact exchange functional by definition. However, its practical use is limited since evaluating the double-integral expression of the exact exchange functional is computationally demanding, making it impractical for large-scale systems. In addition to the computational cost, a further challenge is finding a suitable correlation functional to pair with the exact exchange. Combining exact exchange with standard correlation functionals often leads to worse predictions of physical properties, such as atomization energies, compared to the simpler LDA, which will be introduced in the following section [KK08]. For simplicity, the spin index σ is neglected when introducing the DFAs.

4.1 Explicitly Density Dependent xc Functionals

The first and still widely used approximation is the local density approximation (LDA) [HK64], which extends to spin-dependent systems as the local spin-density approximation (LSDA) [BH72]. The exchange energy density for the LDA is derived from the homogeneous electron gas and is denoted by $e_{\mathrm{x}}^{\mathrm{hom}}(n)$, where n is the constant electron density. The exchange energy for the LDA is then expressed as an integral over $e_{\mathrm{x}}^{\mathrm{hom}}$

$$E_{\mathrm{x}}^{\mathrm{LDA}}[n] = \int e_{\mathrm{x}}^{\mathrm{hom}}(n)\Big|_{n\to n(\mathbf{r})} \,\mathrm{d}^3r = A_{\mathrm{x}} \int n^{4/3}(\mathbf{r})\,\mathrm{d}^3r\,, \tag{4.1}$$

where the constant density n is replaced by the spatially dependent density $n(\mathbf{r})$, and $A_{\mathrm{x}} = -(3/4)(3/\pi)^{1/3}$. For the correlation part, the parametrization by Perdew and Wang [PW92] based on Monte Carlo simulations [CA80] is commonly used. Since the LDA potential $v_{\mathrm{xc}}[n](\mathbf{r})$ depends solely on the density at position $\mathbf{r}$, it is classified as a local xc approximation. Although one might expect this functional to yield accurate results only for slowly varying densities, it provides reasonably good results for real molecular systems, which often exhibit highly nonuniform electron densities [Cap06; KK08]. It is argued in the literature that these beneficial properties stem from favorable error cancellation in the description of exchange and correlation within the LDA potential (for details, see Ref. [DG90]).

The next step beyond local xc functionals is the development of semilocal DFAs. These functionals depend not only on the local electron density n but also on its derivatives. Generalized Gradient Approximations (GGAs) are derived from the gradient expansion [KS65; MB68] of the xc energy $E_{\mathrm{xc}}[n]$ and the KS kinetic energy $T_{\mathrm{s}}[n]$ for slowly varying electron densities. However, using the gradient expansion directly as an approximation results in worse performance for the xc energy than the LDA, particularly

leading to spurious positive values of the correlation energy for atoms. This issue is resolved by modifying the LDA energy expression of Eq. (4.1) via an enhancement factor $F_{\mathrm{xc}}(n, \nabla n)$

$$E_{\mathrm{xc}}^{\mathrm{GGA}}[n, \nabla n] = A_{\mathrm{x}} \int n^{4/3}(\mathbf{r}) F_{\mathrm{xc}}(n(\mathbf{r}), \nabla n(\mathbf{r}))\, \mathrm{d}^3 r\,. \tag{4.2}$$

The density gradient is typically represented by the reduced density gradient [FNM03]

$$s(\mathbf{r}) = \frac{|\nabla n(\mathbf{r})|}{2(3\pi^2)^{1/3} n^{4/3}(\mathbf{r})}\,. \tag{4.3}$$

There is a great variety of empirically and nonempirically constructed GGAs [Cap06]. Later in this work, the nonempirical GGA constructed by Perdew, Burke, and Ernzerhof (PBE) [PBE96] is specifically used within the PZ-SIC framework.

Due to the explicit density dependence of the LDA and GGA functionals, they inherently lack nonlocal features and do not exhibit a derivative discontinuity and, therefore, cannot fulfill multiple of the exact properties discussed in Chapter 3.

4.2 Meta-GGA Functionals: Orbital Functionals at Semilocal Cost

Meta-generalized gradient approximations (meta-GGAs) are xc functionals that incorporate explicit orbital dependence, allowing them to exhibit nonlocal features, as demonstrated in Refs. [Yan+16; AK19; Asc+23; Leb+23; LAK24]. This explicit orbital dependence in meta-GGAs is realized through the kinetic energy density

$$\tau(\mathbf{r}) = \frac{\hbar^2}{2m} \sum_{j=1}^{N} |\nabla \varphi_j(\mathbf{r})|^2\,. \tag{4.4}$$

Since τ is still a local quantity that is straightforward to calculate, meta-GGAs retain the computational cost characteristic of semilocal functionals. Furthermore, including τ ensures that the meta-GGA energy functional remains invariant under unitary transformations of the KS orbitals. The corresponding xc energy functional of a meta-GGA can be written as

$$\begin{aligned} E_{\mathrm{xc}}^{\mathrm{mGGA}}[n, \nabla n, \tau] &= \int e_{\mathrm{xc}}^{\mathrm{mGGA}}(n(\mathbf{r}), \nabla n(\mathbf{r}), \tau(\mathbf{r}))\, \mathrm{d}^3 r \\ &= A_{\mathrm{x}} \int n^{4/3}(\mathbf{r}) F_{\mathrm{xc}}^{\mathrm{mGGA}}(n(\mathbf{r}), \nabla n(\mathbf{r}), \tau(\mathbf{r}))\, \mathrm{d}^3 r, \end{aligned} \tag{4.5}$$

where $e_{\mathrm{xc}}^{\mathrm{mGGA}}(n, \nabla n, \tau)$ is the xc energy density, and $F_{\mathrm{xc}}^{\mathrm{mGGA}}$ is the meta-GGA enhancement factor. In principle, meta-GGA functionals can additionally depend on the Laplace of the density $\nabla^2 n$. Since the meta-GGAs considered in this work only depend on the quantities defined in Eq. (4.5), this additional dependency is neglected here [AK19; SRP15; Fur+20a; Fur+20b]. In practice, the exchange part of the enhancement factor $F_{\mathrm{x}}^{\mathrm{mGGA}}$ is parametrized via the reduced density gradient, defined in Eq. (4.3), and an iso-orbital indicator, such as

$$z(\mathbf{r}) = \frac{\tau^{\mathrm{W}}(\mathbf{r})}{\tau(\mathbf{r})}\,, \tag{4.6}$$

or

$$\alpha(\mathbf{r}) = \frac{\tau(\mathbf{r}) - \tau^{\mathrm{W}}(\mathbf{r})}{\tau^{\mathrm{unif}}(\mathbf{r})}\,, \tag{4.7}$$

with the von Weizsäcker kinetic energy density

$$\tau^{\mathrm{W}}(\mathbf{r}) = \frac{\hbar^2}{8m}\frac{|\nabla n(\mathbf{r})|^2}{n(\mathbf{r})} \tag{4.8}$$

as the single-orbital limit of τ.

$$\tau^{\mathrm{unif}}(\mathbf{r}) = A_{\mathrm{s}} n^{5/3}(\mathbf{r}) \tag{4.9}$$

with

$$A_{\mathrm{s}} = \frac{3\hbar^2(3\pi^2)^{2/3}}{10m} \tag{4.10}$$

is the uniform density limit of τ. Using this parametrization, meta-GGAs can detect spatial regions within the system where the density is dominated by a single orbital, i. e., $\alpha = 0$ (or $z = 1$) or homogeneous-density regions, where $\alpha = 1$ (or $z = 0$ and $s = 0$) [KPB99].

This work focuses on two different meta-GGA functionals derived from first principles. The first is the r^{2}SCAN functional [Fur+20a; Fur+20b], a numerically improved version of the original meta-GGA SCAN [SRP15], designed to address some of the numerical intricacies present in the original formulation. The SCAN or r^{2}SCAN meta-GGAs are widely used for different applications, leading to a generally more accurate description of electronic bonding than the LDA [SRP15; Bra+16]. The second meta-GGA is the TASK functional [AK19], which fulfills the same construction principles in the exchange energy as SCAN but is explicitly designed with the focus on modeling a reasonable derivative discontinuity in the exchange part Δ_{x}. This is achieved by following the construction principle [AK19]

$$\frac{\partial e_{\mathrm{x}}^{\mathrm{mGGA}}}{\partial \tau} > 0\,. \tag{4.11}$$

Using this construction principle, the TASK meta-GGA has been shown to enhance the description of band gaps in solids [AK19; Leb+23; Bor+20].

While the explicit orbital dependence of meta-GGAs through the kinetic energy density offers the significant advantage of incorporating nonlocal features at semilocal computational cost, this orbital dependence introduces its own challenge: Unlike for the LDA or GGA expressions, the functional derivative $\delta E_{\mathrm{xc}}^{\mathrm{mGGA}}/\delta n$, and thus the corresponding xc potential, cannot be calculated straightforwardly. In principle, there are two different approaches for evaluating the potential expression for an orbital-dependent xc functional: First, within the KS framework, one can calculate the functional derivative of the orbital-dependent functional to obtain a multiplicative KS potential via the optimized effective potential method. Second, a corresponding (operator) potential can be determined within a generalized Kohn-Sham scheme by directly minimizing the energy functional with respect to the orbitals. In the following, both approaches are briefly introduced.

4.2.1 Optimized Effective Potential Method and its Approximation

Within the KS formalism, determining the KS potential requires evaluating the functional derivative $\delta E_{\mathrm{xc}}^{\mathrm{mGGA}}/\delta n_\sigma$. For explicitly orbital-dependent xc functionals, this derivative can be calculated using the optimized effective potential (OEP) scheme [SH53; TS76],

which begins by applying the chain rule:

$$v_{\mathrm{xc}\sigma}^{\mathrm{OEP}}(\mathbf{r}) = \sum_{\alpha,\beta=\uparrow,\downarrow} \sum_{i=1}^{N_\sigma} \iint \frac{\delta E_{\mathrm{xc}}[\{\varphi_{j\tau}\}]}{\delta\varphi_{i\alpha}(\mathbf{r}')} \frac{\delta\varphi_{i\alpha}(\mathbf{r}')}{\delta v_{\mathrm{KS}\beta}(\mathbf{r}'')} \frac{\delta v_{\mathrm{KS}\beta}(\mathbf{r}'')}{\delta n_\sigma(\mathbf{r})} \,\mathrm{d}^3r' \,\mathrm{d}^3r'' + \mathrm{c.c.}\,, \tag{4.12}$$

where c.c. denotes the complex conjugate. By identifying $\delta v_{\mathrm{KS}}/\delta n_\sigma$ as the inverse KS response function and evaluating $\delta\varphi_{i\alpha}/\delta v_{\mathrm{KS}\beta}$ (and the KS response function) using first-order perturbation theory, the equation can be rewritten in integral form (for details, see Ref. [KK08]). This formulation, first proposed by Krieger *et al.* [KLI92b], leads to the most commonly used form of the OEP equation:

$$v_{\mathrm{xc}\sigma}^{\mathrm{OEP}}(\mathbf{r}) = \frac{1}{2n_\sigma(\mathbf{r})} \sum_{i=1}^{N_\sigma} \Bigg\{ |\varphi_{i\sigma}(\mathbf{r})|^2 \left[u_{\mathrm{xci}\sigma}(\mathbf{r}) + \left(\bar{v}_{\mathrm{xci}\sigma}^{\mathrm{OEP}} - \bar{u}_{\mathrm{xci}\sigma} \right) \right] - \frac{\hbar^2}{m} \nabla \cdot \left[\psi_{i\sigma}^*(\mathbf{r}) \nabla \varphi_{i\sigma}(\mathbf{r}) \right] \Bigg\} + \mathrm{c.c.}\,, \tag{4.13}$$

where $\psi_{i\sigma}^*(\mathbf{r})$ is the first-order orbital shift of the ith KS orbital, and

$$u_{\mathrm{xci}\sigma}(\mathbf{r}) = \frac{1}{\varphi_{i\sigma}^*(\mathbf{r})} \frac{\delta E_{\mathrm{xc}}[\{\varphi_{j\tau}\}]}{\delta\varphi_{i\sigma}(\mathbf{r})}\,. \tag{4.14}$$

Equation (4.13) is an integral equation due to the terms

$$\bar{v}_{\mathrm{xci}\sigma}^{\mathrm{OEP}} = \int \varphi_{i\sigma}^*(\mathbf{r}) v_{\mathrm{xc}\sigma}^{\mathrm{OEP}}(\mathbf{r}) \varphi_{i\sigma}(\mathbf{r}) \,\mathrm{d}^3r \quad \text{and} \quad \bar{u}_{\mathrm{xci}\sigma} = \int \varphi_{i\sigma}^*(\mathbf{r}) u_{\mathrm{xci}\sigma}(\mathbf{r}) \varphi_{i\sigma}(\mathbf{r}) \,\mathrm{d}^3r\,, \tag{4.15}$$

and the orbital shift

$$\psi_{i\sigma}^*(\mathbf{r}) = -\sum_{\substack{j=1 \\ j\neq i}}^{\infty} \frac{\langle\varphi_{i\sigma}|u_{\mathrm{xci}\sigma} - v_{\mathrm{xc}\sigma}^{\mathrm{OEP}}|\varphi_{j\sigma}\rangle}{\epsilon_{i\sigma} - \epsilon_{j\sigma}} \varphi_{j\sigma}^*(\mathbf{r})\,. \tag{4.16}$$

Solving the integral equation (4.13) with the orbital shift term is a highly challenging computational task, as the sum in Eq. (4.16) runs over all occupied and unoccupied orbitals.

The most commonly used approach to simplify this problem is the approximation introduced by Krieger, Li, and Iafrate (KLI) [KLI92b; KLI92a]. This approximation replaces the orbital energy differences $\epsilon_{i\sigma} - \epsilon_{j\sigma}$ with a mean value $\Delta\epsilon_\sigma$. After additional steps (see Ref. [KK08]), this yields the KLI expression for the xc potential

$$v_{\mathrm{xc}\sigma}^{\mathrm{KLI}}(\mathbf{r}) = \frac{1}{2n_\sigma(\mathbf{r})} \sum_{i=1}^{N_\sigma} |\varphi_{i\sigma}(\mathbf{r})|^2 \left[u_{\mathrm{xci}\sigma}(\mathbf{r}) + \left(\bar{v}_{\mathrm{xci}\sigma}^{\mathrm{KLI}} - \bar{u}_{\mathrm{xci}\sigma} \right) \right] + \mathrm{c.c.}\,, \tag{4.17}$$

with $\bar{v}_{\mathrm{xci}\sigma}^{\mathrm{KLI}}$ and $\bar{u}_{\mathrm{xci}\sigma}$ defined analogously to Eq. (4.15). This equation can either be solved iteratively or reformulated as a set of linear equations, which can then be solved directly. This reformulation significantly reduces the computational cost compared to solving the full OEP equation.

Even though the KLI approximation provides a computationally less expensive alternative to the full OEP, it introduces its own challenges. In particular, the time-dependent formulation of the KLI approximation [UGG95] has been shown to violate

the zero-force theorem for some systems [Mun+07]. This theorem states that there must be no net force due to xc effects across the system, i. e.,

$$\int n(\mathbf{r},t)\nabla v_{\mathrm{xc}}(\mathbf{r},t)\,\mathrm{d}^3r = 0\,. \tag{4.18}$$

This violation leads to a self-excitation of the system and can cause numerical instabilities when real-time propagation schemes are applied to calculate the excitation spectra of physical systems. While it has been shown that the time-dependent OEP formulation [UGG95] satisfies the zero-force theorem, it is even more computationally demanding and often leads to numerical instabilities. As a result, it has so far only been solved for one-dimensional systems [MK06; WU08].

4.2.2 Generalized Kohn Sham Scheme

In order to avoid the difficulties that come with the time-dependent OEP, this work primarily uses a generalized Kohn-Sham (GKS) scheme to handle the explicit orbital dependence of meta-GGA functionals following Refs. [Sei+96; BF12; BK18].

Whereas the ground-state formulation of KS introduces a single Slater determinant, constructed from non-interacting single-particle orbitals, to describe the real system, the GKS formulation employs partially interacting particles that can still be represented by a single Slater determinant Φ. Consequently, the basic energy functional in GKS can be defined as $S[\Phi]$, which must be invariant under unitary transformations of the single-particle orbitals building the Slater determinant. The corresponding energy density functional $F^{\mathrm{S}}[n]$ is obtained by minimizing S with respect to the orbitals that yield the density n [Sei+96],

$$F^{\mathrm{S}}[n] = \min_{\{\varphi_{j\sigma}\}\to n(\mathbf{r})} S[\{\varphi_{j\sigma}\}]\,. \tag{4.19}$$

Similar to the energy functional of Eq. (2.4), the total energy in GKS can then be written as

$$E[n] = F^{\mathrm{S}}[n] + \int n(\mathbf{r})v_{\mathrm{ext}}(\mathbf{r})\,\mathrm{d}^3r + R^{\mathrm{S}}[n]\,, \tag{4.20}$$

where $R^{\mathrm{S}}[n]$ is the reminder energy functional. Analogous to the KS equations, the GKS equations

$$\hat{O}^{\mathrm{S}}[\{\varphi_{j\sigma}\}]\varphi_{j\sigma}(\mathbf{r}) + v_{\mathrm{R}\sigma}(\mathbf{r})\varphi_{j\sigma}(\mathbf{r}) + v_{\mathrm{ext}}(\mathbf{r})\varphi_{j\sigma}(\mathbf{r}) = \epsilon_{j\sigma}\varphi_{j\sigma}(\mathbf{r}) \tag{4.21}$$

must be solved to determine the GKS orbitals $\{\varphi_{j\sigma}\}$ and their corresponding eigenvalues $\{\epsilon_{j\sigma}\}$, where the remainder potential $v_{\mathrm{R}\sigma}(\mathbf{r})$ is obtained via the functional derivative

$$v_{\mathrm{R}\sigma}(\mathbf{r}) = \frac{\delta R^{\mathrm{S}}[n]}{\delta n_\sigma(\mathbf{r})}\,. \tag{4.22}$$

Moreover, $\hat{O}^{\mathrm{S}}[\{\varphi_{j\sigma}\}]$ represents a, in general, non-multiplicative potential operator determined by the specific choice of S [Sei+96].

Given the remainder energy functional, one could, in principle, develop approximations for $R^{\mathrm{S}}[n]$ instead of the xc energy functional $E_{\mathrm{xc}}[n]$. In practice, however, orbital-dependent functionals are typically still based on approximations to E_{xc}. Therefore, for meta-GGAs, the energy functional S takes the form

$$S[\{\varphi_{j\sigma}\}] = \langle\Phi|\hat{T}|\Phi\rangle + E_{\mathrm{xc}}^{\mathrm{mGGA}}[\{\varphi_{j\sigma}\}]\,, \tag{4.23}$$

with $\hat{T} = -\hbar^2/2m \sum_{\sigma=\uparrow,\downarrow} \sum_{j=1}^{N_\sigma} \nabla_j^2$ [BK18; Ric+23]. Calculating the functional derivative of $E_{\mathrm{xc}}^{\mathrm{mGGA}}$ with respect to the orbitals leads to

$$\hat{v}_\sigma^{\mathrm{mGGA}}(\mathbf{r}) = v_\sigma^{\mathrm{loc}}(\mathbf{r}) + \hat{v}_{\tau\sigma}^{\mathrm{GKS}}(\mathbf{r})\,. \tag{4.24}$$

The local, multiplicative part is given by

$$v_\sigma^{\mathrm{loc}}(\mathbf{r}) = \frac{\partial e_{\mathrm{xc}}^{\mathrm{mGGA}}}{\partial n_\sigma}(\mathbf{r}) - \nabla \cdot \left[\frac{\partial e_{\mathrm{xc}}^{\mathrm{mGGA}}}{\partial \nabla n_\sigma}(\mathbf{r})\right] \tag{4.25}$$

and the operator part of $\hat{v}_\sigma^{\mathrm{mGGA}}$ is

$$\hat{v}_{\tau\sigma}^{\mathrm{GKS}}(\mathbf{r}) = -\frac{\hbar^2}{2m}\nabla \cdot \frac{\partial e_{\mathrm{xc}}^{\mathrm{mGGA}}}{\partial \tau_\sigma}(\mathbf{r})\nabla\,. \tag{4.26}$$

This leads to the meta-GGA form of the GKS equations [BK18; Ric+23]

$$\left[-\frac{\hbar^2}{2m}\nabla^2 + v_{\mathrm{H}}[n](\mathbf{r}) + \hat{v}_\sigma^{\mathrm{mGGA}}[n_\uparrow, n_\downarrow](\mathbf{r}) + v_{\mathrm{ext}}(\mathbf{r})\right]\varphi_{j\sigma}(\mathbf{r}) = \epsilon_{j\sigma}\varphi_{j\sigma}(\mathbf{r})\,. \tag{4.27}$$

In summary, the GKS formulation with its Eqs. (4.21) is formally exact since the exact remainder potential $v_{\mathrm{R}\sigma}$ would lead to a set of GKS orbitals that reproduce the true ground-state density of the real interacting system [Sei+96]. In the context of using Eq. (4.23) as the meta-GGA expression for the energy functional S, solving the resulting GKS Eqs. (4.27) is significantly less computationally expensive than solving the integral equations of the OEP discussed in the previous section.

However, employing the time-dependent GKS formulation for meta-GGAs introduces additional challenges, as the kinetic energy density $\tau(\mathbf{r}, t)$ used in the meta-GGA expressions leads to as gauge variance and violates the continuity equation [Bec02; Tao05; BK18; BF12; Ric+23]. This issue is examined in detail in Chapter 5.

4.3 Limitations and First Solution Strategies for Semilocal Functionals

Due to their (semi-)local density dependence, the LDA and the PBE functional, as a GGA introduced in Section 4.1, fail to fulfill several exact properties discussed in Chapter 3 required for accurately describing CT processes:

(1) The LDA and PBE exhibit a convex behavior in the $E(N)$-curve and fail to capture the derivative discontinuity Δ_{xc} entirely. Therefore, the LDA and PBE cannot show any counteracting to an external field driving CT processes (as described at the end of Section 3.3). (2) The LDA and GGA energy functionals are unable to correct the SIE present in the Hartree energy term. This limitation arises from their local or semilocal density dependence preventing them from capturing the nonlocal character of the Hartree SIE. Moreover, they even introduce an additional SIE as the correlation energy within the LDA and PBE does not vanish for one-electron densities. (3) Although there have been attempts to design GGAs that exhibit the correct asymptotic behavior [LB94; WAY03; AK13; Car+15], common GGAs, such as the PBE potential, and local functionals like the LDA, decay exponentially rather than following the correct $-1/r$ asymptotic form.

These deficiencies of the LDA and PBE are well-known, and practical calculations have demonstrated that they result in a poor description of CT excitations in TDDFT

[Toz+99; SK18; Keh+20]. In contrast, the TASK meta-GGA, introduced in Section 4.2, is designed to exhibit a reasonable derivative discontinuity in the exchange part Δ_x enabling it to generate field-counteracting terms similar to those of the exact exchange functional [AK19]. Consequently, it is of great interest to investigate the performance of the TASK meta-GGA, as well as the r^{2}SCAN meta-GGA (which inherits a smaller Δ_x), in describing CT excitations within the time-dependent GKS framework, as discussed in the next chapter.

Additionally, the meta-GGA approach provides a step toward mitigating SIEs. Using the iso-orbital indicator α, which approaches zero in regions dominated by a single orbital, the meta-GGA correlation energy E_c^{mGGA} can be constructed to vanish when $\alpha = 0$ and full spin polarization is present [Per+99]. However, addressing the SIE in the exchange part is significantly more challenging than achieving freedom from self-correlation, as the spurious nonlocal self-interaction introduced by the Hartree energy must be compensated for by the exchange functional. A common construction principle for the exchange part in functionals such as TASK and r^{2}SCAN is to ensure that, in the one-electron limit, the exchange energy recovers the exact result for the hydrogen atom – a system with a known analytical solution. However, satisfying this condition alone does not guarantee accurate results for general many-electron systems and is therefore insufficient for a proper correction of the SIE of Hartree term [SRP15; Fur+20a; AK19].

To address the SIE in both the exchange and correlation components, Perdew and Zunger [PZ81] proposed a universal correction scheme that can, in principle, be applied to any DFA. This is achieved by defining the Perdew-Zunger SIC energy functional as

$$E_{xc}^{\mathrm{SIC}} = E_{xc}^{\mathrm{app}}[n_\uparrow, n_\downarrow] - \sum_{\sigma=\uparrow,\downarrow} \sum_{i=1}^{N_\sigma} \left\{ E_H[|\varphi_{i\sigma}|^2] + E_{xc}^{\mathrm{app}}[|\varphi_{i\sigma}|^2, 0] \right\} , \tag{4.28}$$

where $E_H[|\varphi_{i\sigma}|^2]$ and $E_{xc}^{\mathrm{app}}[|\varphi_{i\sigma}|^2, 0]$ are the single KS particle contributions to the Hartree and xc energy the PZ-SIC is applied on, respectively. A central difficulty of this SIC scheme is that the resulting energy functional is not invariant under unitary transformations of the orbitals. This introduces significant challenges in practical implementations that will be discussed in Chapter 6.

Chapter 5

Meta-Generalized Gradient Functionals in Generalized Kohn-Sham

This chapter presents the results of applying the meta-GGA approximations TASK [AK19] and r^{2}SCAN [Fur+20a; Fur+20b] within a GKS scheme. The discussion begins with the technical aspects of implementing meta-GGAs in the `BTDFT` program package using PPs. Next, the formal challenges posed by the gauge variance of the kinetic energy density and the violation of the continuity equation when using meta-GGAs in a time-dependent generalized Kohn-Sham scheme (TDGKS) are reviewed. Subsequently, the results of adopting a current-density-corrected kinetic energy density, as proposed by Becke [Bec02] and Tao [Tao05], which restores both gauge invariance and the continuity equation, are demonstrated using our real-time propagation scheme for various model systems.

Since TASK and r^{2}SCAN capture a derivative discontinuity through their explicit orbital dependence, we compare their ability to describe CT excitations to that of the LDA, which is known to fail in this context [Toz03; Mai05; Sch+19; Keh+20], as well as to more computationally expensive methods that provide an accurate description of CT excitations.

The results from this comparison and for considering the current-density correction are also published in Ref. [Ric+23]. For simplicity, the spin dependence is omitted in the expressions presented in this chapter.

5.1 Ground-State Results: Using Pseudopotentials in Meta-GGA Calculations

As discussed in Section 2.3, the real-space code `BTDFT` [SK18] employs norm-conserving Troullier-Martins type PPs [TM91] to model the interaction between atomic cores and valence electrons. However, consistent meta-GGA PPs are not yet available due to the inherent difficulty of constructing reliable PPs for orbital-dependent functionals. Although some progress has been made in developing PPs for meta-GGA functionals [YK17], the process remains complicated. In the KS framework, constructing PPs typically involves inverting pseudo-orbitals to obtain a local potential; however, for meta-GGAs, this task is further complicated by the nonlocal and non-multiplicative term $\hat{v}_\tau^{\mathrm{GKS}}$. Moreover, whereas studies on the exact exchange functional indicate that the use of inconsistent PPs does not necessarily result in large deviations [Eng09], meta-GGAs introduce additional challenges because they rely on iso-orbital indicators, such as z or α (see Eq. (4.6) and Eq. (4.7)), to identify specific spatial regions and adjust the energy

functional accordingly. This sensitivity can lead to differences between all-electron and PP-based calculations. This discrepancy can be particularly evident in systems with a single valence electron and multiple core electrons, such as the sodium atom, where only the $3s$ electron is treated as a valence electron. In such cases, the iso-orbital indicator within the meta-GGA functional may mistakenly classify the entire valence density as an iso-orbital region. In all-electron calculations, the iso-orbital indicator is evaluated on the total density, which can lead to noticeably different values for z or α. As a result, meta-GGA functionals can be more sensitive to inconsistent PPs than the LDA or GGA functionals, depending on the system in question.

This issue can, however, be mitigated in many cases through a workaround previously proposed for local hybrid functionals [SK16], which is also applicable to meta-GGA functionals. By incorporating the NLCC discussed in Section 2.3, the total core density n_c is available in addition to the PP. This core density, together with the valence density n_v, can be used to evaluate the iso-orbital indicator α, thereby avoiding a spurious detection of single-orbital regions. For this purpose, the kinetic energy density is evaluated as

$$\tau(\mathbf{r}) = \frac{\hbar^2}{2m}\left\{\left|\nabla\left(n_\mathrm{c}^{1/2}\right)\right|^2 + \left(\sum_{\substack{k \\ \text{valence} \\ \text{states}}} |\nabla\varphi_k^\mathrm{v}|^2\right)\right\}, \tag{5.1}$$

with its iso-orbital and homogeneous electron gas limits given by

$$\tau^\mathrm{W}(\mathbf{r}) = \frac{\hbar^2}{8m}\frac{|\nabla(n_\mathrm{c}(\mathbf{r}) + n_\mathrm{v}(\mathbf{r}))|^2}{n_\mathrm{c}(\mathbf{r}) + n_\mathrm{v}(\mathbf{r})}, \tag{5.2}$$

$$\tau^\mathrm{unif}(\mathbf{r}) = A_\mathrm{s}(n_\mathrm{c}(\mathbf{r}) + n_\mathrm{v}(\mathbf{r}))^{5/3}, \tag{5.3}$$

where A_s is defined in Eq. (4.10), $\{\varphi_k^\mathrm{v}\}$ are the valence orbitals, and

$$\sum_{\substack{k \\ \text{core states}}} |\nabla\varphi_k^\mathrm{c}(\mathbf{r})|^2 \approx \left|\nabla\left(n_\mathrm{c}^{1/2}(\mathbf{r})\right)\right|^2, \tag{5.4}$$

where $\{\varphi_k^\mathrm{c}\}$ are the core orbitals. The last expression is only exact for atoms with one single (doubly occupied) s core orbital. The meta-GGA equations and their derivatives, including the core correction, are shown in Appendices A.1 and A.2 for the exchange and correlation, respectively.

To evaluate the influence of incorporating the core density on the calculation of the kinetic energy density using Eq. (5.1), we compare the HOMO eigenvalues of the CO molecule and of the Li_2 molecule obtained from PP-based `BTDFT` calculations with those from all-electron calculations performed using the real-space code `DARSEC` [MKK09; MKK11]. Both approaches employ the TASK functional for exchange (with no correlation, denoted as "x"). The results are summarized in Tab. 5.1. Since the

Table 5.1: Comparison of HOMO eigenvalues for CO and Li_2 calculated using TASKx-KLI: `BTDFT` without NLCC, `BTDFT` with NLCC, and an all-electron reference calculation performed with the `DARSEC` code.

	BTDFT without n_c	**BTDFT** with n_c	**DARSEC**
CO	−8.54 eV	−8.51 eV	−8.48 eV
Li_2	−2.89 eV	−2.80 eV	−2.68 eV

operator potential for meta-GGAs within the GKS scheme, $\hat{v}^{\mathrm{mGGA}}$, is not implemented in the DARSEC program, we compare the TASKx eigenvalues obtained using the KLI approximation, as introduced in Section 4.2.1. As shown in Table 5.1, incorporating the core density n_c in the BTDFT calculation enhances agreement with the highly accurate all-electron DARSEC results. For the CO molecule, including the core correction reduces the deviation from 0.06 eV (without n_c) to 0.03 eV (with n_c). The improvement is even more pronounced for Li_2: without applying Eq. (5.1), the BTDFT results deviate by 0.21 eV from the DARSEC calculation, whereas incorporating n_c reduces the error to 0.12 eV.

The more pronounced effect of the core correction scheme in Eq. (5.1) for Li_2 compared to CO can be attributed to the different electron configurations of the atoms involved. With a single valence electron, the Li atom can mislead the iso-orbital indicator α, causing it to spuriously identify one-orbital regions near the Li cores when evaluated solely on the valence density. In contrast, for the C and O atoms, which have multiple valence electrons, the evaluation of α is less prone to such errors, resulting in more accurate predictions.

For the calculations presented in the following sections, we incorporate the core density n_c for the light atoms C, O, N, and Li to ensure that molecules containing these elements are not affected by iso-orbital detection errors. Standard PPs are used for heavier atoms with more than just $1s$ core electrons. This approach provided reliable results when compared to all-electron calculations. For future work, the development of consistent meta-GGA PPs or, as a first step, the use of a core kinetic energy density

$$\tau_\mathrm{c}(\mathbf{r}) = \frac{\hbar^2}{2m} \sum_{\substack{k \\ \text{core states}}} |\nabla \varphi_k^\mathrm{c}(\mathbf{r})|^2 \tag{5.5}$$

instead of n_c in Eq. (5.1) would be desirable.

5.2 Meta-GGAs in TDDFT

In the TDGKS scheme, meta-GGAs are typically employed in an orbital-adiabatic approximation where the meta-GGA expressions are evaluated with the time-dependent orbitals. Since meta-GGAs depend on both the electron density and the kinetic energy density, these quantities are computed as follows:

$$n(\mathbf{r}, t) = \sum_{j=1}^{N} |\varphi_j(\mathbf{r}, t)|^2 \tag{5.6}$$

and

$$\tau(\mathbf{r}, t) = \frac{\hbar^2}{2m} \sum_{j=1}^{N} |\nabla \varphi_j(\mathbf{r}, t)|^2 \,, \tag{5.7}$$

with the number of valence electrons N. The kinetic energy density τ is well defined for real-valued ground-state orbitals. However, conceptual difficulties arise when evaluating τ using complex-valued, current-carrying time-dependent orbitals, as discussed by Bates and Furche [BF12] and Bear and Kronik [BK18]. These challenges are discussed in the next section.

5.2.1 Conceptual Challenges for Kinetic Energy Density in TDDFT

The first conceptual issue with using τ in TDDFT becomes apparent when considering the gauge transformation

$$\mathbf{A}_{\text{ext}}[\Lambda](\mathbf{r},t) = \mathbf{A}_{\text{ext}}(\mathbf{r},t) + \nabla\Lambda(\mathbf{r},t) \tag{5.8}$$

$$v_{\text{ext}}[\Lambda](\mathbf{r},t) = v_{\text{ext}}(\mathbf{r},t) - \frac{\partial}{\partial t}\Lambda(\mathbf{r},t) \tag{5.9}$$

of the external vector potential $\mathbf{A}_{\text{ext}}$ and the external potential v_{ext} using the real-valued gauge function $\Lambda(\mathbf{r},t)$. This gauge transformation of the external potentials leads to a time- and position-dependent phase in the KS orbitals

$$\varphi_j[\Lambda](\mathbf{r},t) = \varphi_j(\mathbf{r},t)\exp\left(-\frac{\mathrm{i}e}{\hbar}\Lambda(\mathbf{r},t)\right) \tag{5.10}$$

(with the imaginary unit i). Calculating the kinetic energy density with $\{\varphi_k[\Lambda]\}$ leads to

$$\tau[\Lambda](\mathbf{r},t) = \tau(\mathbf{r},t) - e(\nabla\Lambda(\mathbf{r},t))\cdot\mathbf{j}_{\text{p}}(\mathbf{r},t) + \frac{e^2}{2m}|\nabla\Lambda(\mathbf{r},t)|^2 n(\mathbf{r},t)\,, \tag{5.11}$$

with the paramagnetic current density

$$\mathbf{j}_{\text{p}}(\mathbf{r},t) = \frac{\hbar}{m}\sum_{j=1}^{N}\mathrm{Im}\left[\varphi_j^*(\mathbf{r},t)\nabla\varphi_j(\mathbf{r},t)\right]\,. \tag{5.12}$$

This result demonstrates that the kinetic energy density τ in TDDFT is not gauge invariant. Since the exact xc functional is a pure functional of the density $n(\mathbf{r},t)$, which is inherently gauge invariant, the xc functional itself must also be gauge invariant. However, in meta-GGAs, this invariance is not preserved due to the explicit dependence of the GKS potential on τ.

While the gauge variance of the kinetic energy density is present in both the KS and GKS frameworks, an additional issue arises exclusively within the GKS framework. Specifically, the non-multiplicative term $\hat{v}^{\text{mGGA}}$ within the GKS Hamiltonian leads to a violation of the continuity equation, which can be seen as follows: Considering the TDGKS equations

$$\mathrm{i}\hbar\frac{\partial}{\partial t}\varphi_j(\mathbf{r},t) = \hat{H}_{\text{GKS}}(\mathbf{r},t)\varphi_j(\mathbf{r},t)\,, \tag{5.13}$$

with the TDGKS Hamiltonian (analogous to Eq. (4.27)),

$$\hat{H}_{\text{GKS}}(\mathbf{r},t) = -\frac{\hbar^2}{2m}\nabla^2 + v_{\text{H}}(\mathbf{r},t) + \hat{v}^{\text{mGGA}}(\mathbf{r},t) + v_{\text{ext}}(\mathbf{r},t)\,, \tag{5.14}$$

one can calculate the time derivative of the orbital density

$$\begin{aligned}\frac{\partial}{\partial t}|\varphi_k(\mathbf{r},t)|^2 &= \frac{1}{\mathrm{i}\hbar}\left[\varphi_k^*(\mathbf{r},t)\hat{H}_{\text{GKS}}(\mathbf{r},t)\varphi_k(\mathbf{r},t) - \varphi_k(\mathbf{r},t)\hat{H}_{\text{GKS}}(\mathbf{r},t)\varphi_k^*(\mathbf{r},t)\right]\\ &= \frac{2}{\hbar}\,\mathrm{Im}\left[\varphi_k^*(\mathbf{r},t)\hat{H}_{\text{GKS}}(\mathbf{r},t)\varphi_k(\mathbf{r},t)\right]\,.\end{aligned} \tag{5.15}$$

By substituting the GKS Hamiltonian from Eq. (5.14) and the definition of $\hat{v}^{\mathrm{mGGA}}$ from Eq. (4.24) (along with its components from Eqs. (4.25) and (4.26)), we obtain

$$\begin{aligned}\frac{\partial}{\partial t}|\varphi_k(\mathbf{r},t)|^2 &= \frac{2}{\hbar}\,\mathrm{Im}\Bigg\{\varphi_k^*(\mathbf{r},t)\Bigg[-\frac{\hbar^2}{2m}\nabla^2\varphi_k(\mathbf{r},t) + [v_{\mathrm{H}}(\mathbf{r},t) + v^{\mathrm{loc}}(\mathbf{r},t) + v_{\mathrm{ext}}(\mathbf{r},t)]\varphi_k(\mathbf{r},t) \\ &\qquad - \frac{\hbar^2}{2m}\nabla\cdot\left(\frac{\partial e_{\mathrm{xc}}^{\mathrm{mGGA}}}{\partial\tau}\nabla\varphi_k(\mathbf{r},t)\right)\Bigg]\Bigg\} \\ &= -\nabla\cdot\left\{\frac{\hbar}{m}\,\mathrm{Im}\left[\varphi_k^*(\mathbf{r},t)\nabla\varphi_k(\mathbf{r},t)\right]\left(1+\frac{\partial e_{\mathrm{xc}}^{\mathrm{mGGA}}}{\partial\tau}(\mathbf{r},t)\right)\right\}.\end{aligned} \tag{5.16}$$

Finally, summing over all orbitals k leads to

$$\frac{\partial n(\mathbf{r},t)}{\partial t} = -\nabla\cdot\left[\mathbf{j}_{\mathrm{p}}(\mathbf{r},t)\left(1+\frac{\partial e_{\mathrm{xc}}^{\mathrm{mGGA}}}{\partial\tau}(\mathbf{r},t)\right)\right]. \tag{5.17}$$

This result demonstrates that the continuity equation no longer holds due to the additional term involving $\partial e_{\mathrm{xc}}^{\mathrm{mGGA}}/\partial\tau$.

Both the gauge variance and the violation of the continuity equation can be restored by replacing the kinetic energy density of Eq. (5.7) with the modified definition

$$\hat{\tau}(\mathbf{r},t) = \tau(\mathbf{r},t) - m\frac{|\mathbf{j}_{\mathrm{p}}(\mathbf{r},t)|^2}{2n(\mathbf{r},t)}, \tag{5.18}$$

as suggested by Becke [Bec02] and Tao [Tao05]. This modified kinetic energy density can still be used to evaluate the iso-orbital indicator α. In the following, we denote the approach using $\hat{\tau}$ as "CGKS" and the one using τ as "GKS". With this modification, the operator potential $\hat{v}_\tau^{\mathrm{GKS}}$ (see Eq. (4.26)) is replaced by

$$\hat{v}_{\hat{\tau}}^{\mathrm{CGKS}} = \frac{1}{2m}\hat{\boldsymbol{\pi}}(\mathbf{r},t)\frac{\partial e_{\mathrm{xc}}^{\mathrm{mGGA}}}{\partial\hat{\tau}}(\mathbf{r},t)\hat{\boldsymbol{\pi}}(\mathbf{r},t), \tag{5.19}$$

where

$$\hat{\boldsymbol{\pi}}(\mathbf{r},t) = \hat{\mathbf{p}} - m\frac{\mathbf{j}_{\mathrm{p}}(\mathbf{r},t)}{n(\mathbf{r},t)}. \tag{5.20}$$

Here, $\hat{\mathbf{p}} = -\mathrm{i}\hbar\nabla$ is the momentum operator. In Appendix A.3, we explicitly demonstrate that the modified definition in Eq. (5.18) restores the continuity equation. Although the continuity equation is not strictly satisfied for the individual orbital densities, it holds "on average".

The violation of the continuity equation is a specific problem in the GKS approach due to the non-multiplicative nature of the GKS potential for meta-GGAs. Recently performed TDDFT calculations [HK20] within the KS scheme do not suffer from this deficiency due to the multiplicative KS potential. However, following the KS scheme with orbital-dependent functionals, as described in Section 4.2.1, is limited to the KLI approximation due to the complexity of the OEP equation. TDDFT calculations within a GKS scheme using the current-density correction have been performed by Bates and Furche [BF12] using the TPSS meta-GGA functional [Tao+03], where they found the differences between GKS and CGKS to be relatively small. While these results provide useful information for the TPSS meta-GGA, they may not be directly applicable to other meta-GGAs, such as TASK and r^{2}SCAN. In particular, the construction of TASK and r^{2}SCAN involves a stronger τ-dependence, which, as shown in Eq. (5.17) and Eq. (5.19),

is directly related to the violation of the continuity equation. Therefore, the impact of the current-density correction on these functionals within the GKS framework requires further investigation. In the following, we investigate the influence of the current-density correction on the excitation spectrum across various model systems, comparing the results with experimental values. We begin by examining small diatomic molecules and then analyzing conjugated aromatic molecules and an organic semiconductor system.

5.2.2 Time-Dependent (C)GKS Calculations Using the TASK Meta-GGA Functional

Results for Diatomic Molecules

We begin by investigating the absorption spectra of the diatomic molecules CO and Li_2 calculated with the TASKx meta-GGA (where "x" indicates that we are considering only the exchange part of the xc functional without including any correlation functional). The impact of combining the TASKx functional with the LDA correlation, referred to as TASKx+LDAc, is explored as a subsequent step for both diatomic molecules. Although for open-shell systems, the LDA-based self-interaction corrected correlation (CC) functional from Ref. [LAK22] offers an alternative that improves upon standard LDA correlation – particularly by removing SIEs and yielding accurate ground-state energies for a wide range of systems – we employ the LDA correlation directly in this work. This choice is justified for the closed-shell systems Li_2 and CO, where the SIC in the CC functional vanishes and, therefore, has no effect.

Since we have only assessed the relative accuracy of ground-state calculations using core-corrected PPs for meta-GGAs, as discussed in Section 5.1, we now extend the comparison to the absorption spectra. Specifically, we compare the results obtained with the `BTDFT` program package with all-electron reference calculations performed using the `Turbomole` code [Bal+20], which employs various Gaussian basis sets. For the CO molecule, a bond length of $2.1421\,a_0$ is used, following Ref. [Loo+18]. The computed absorption spectra are shown with a Gaussian broadening of the spectral lines, given by $\exp[-(\hbar(\omega-\omega_0)/\eta)^2]$, where $\eta = 0.025\,\text{eV}$ and $\hbar\omega_0$ denotes the excitation energy. The individual excitation energies are listed in detail in the supplementary material of Ref. [Ric+23].

Figure 5.1 shows the vertical spectra calculated with `BTDFT` and `Turbomole` within the TDGKS scheme, i. e., without using the current-density correction scheme for the kinetic energy density. The left panel displays the TASKx spectra obtained without including the LDA correlation. For the `BTDFT` calculations, we used a grid spacing of $0.2\,a_0$ and a spherical grid with a radius of $15\,a_0$. Increasing the grid radius to $22\,a_0$ led to a negligible shift in the excitation energy of less than 0.01 eV. The `Turbomole` results shown in the same panel are affected by the choice of Gaussian basis sets. As the basis set size increases, the excitation energies systematically shift toward the values obtained from the real-space real-time calculation. This trend is consistent with earlier findings that the excitation spectrum of CO is highly sensitive to the completeness of the basis set [HSK18]. The right panel of Fig. 5.1 shows a similar trend, though the basis set dependence in the `Turbomole` calculations appears less pronounced when incorporating the LDA correlation. The `BTDFT` results are shifted upward by $\sim 0.1\,\text{eV}$ from the TASKx to the TASKx+LDAc calculation. Since the results in the left and right panels of Fig. 5.1 are qualitatively the same, we conclude that the differences between `BTDFT` and `Turbomole` would disappear for calculations approaching numerical limits.

After establishing the numerical accuracy of our approach, we now turn to evaluating the impact of the current-density correction scheme applied to the TASK functional.

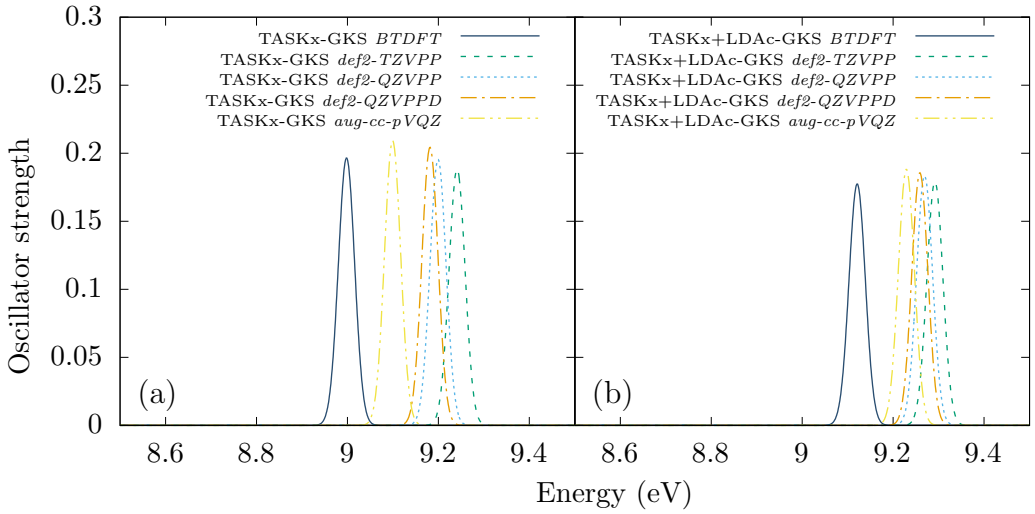

Figure 5.1: Vertical excitation spectra for CO calculated with `BTDFT` and `Turbomole` using TASKx-GKS in panel (a) and TASKx+LDAc in panel (b) using different basis sets.

The results for the CO molecule are presented in Fig. 5.2, which compares the excitation spectra calculated with (CGKS) and without (GKS) the current-density correction, using TASKx in panel (a) and TASKx+LDAc in panel (b). In both panels, the solid

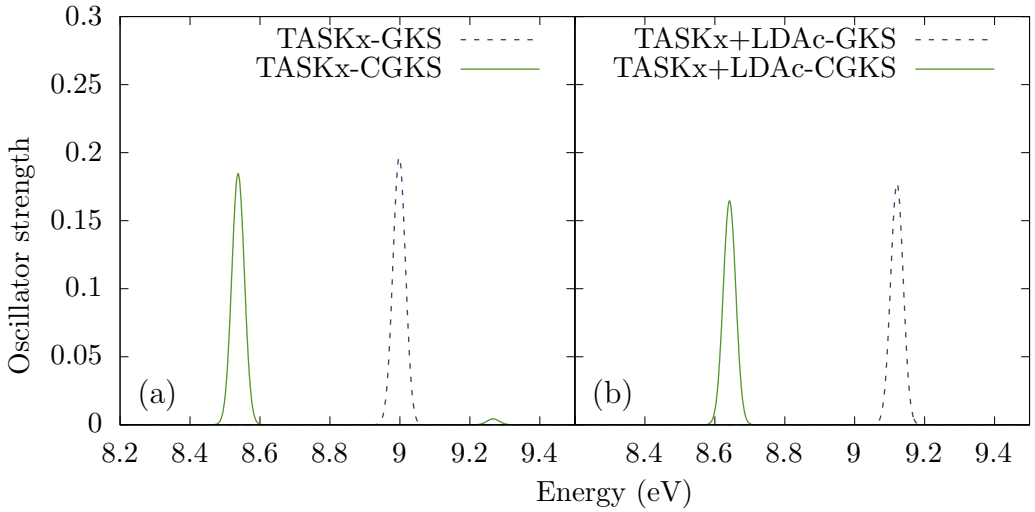

Figure 5.2: Vertical excitation spectra for CO calculated with (CGKS) and without (GKS) the current-density correction, using TASKx in panel (a) and TASKx+LDAc in panel (b).

lines correspond to calculations using the corrected kinetic energy density $\hat{\tau}$, while the dashed lines represent the uncorrected τ. The influence of the current-density correction is substantial in both cases. For TASKx, using $\hat{\tau}$ instead of τ shifts the excitation energy from 9.00 to 8.54 eV, corresponding to a redshift of 0.46 eV. A comparable redshift is observed for TASKx+LDAc, where the excitation energy decreases from 9.10 to 8.64 eV. These shifts bring the calculated excitation energies closer to our reference values. In particular, the first experimental excitation energy for CO is reported at 8.51 eV [NJO80], while a coupled-cluster calculation (CC3) calculation using Dunning's aug-cc-pVQZ

basis set [Dun89] yields a value of 8.47 eV [Loo+18].

The second diatomic molecule investigated is Li_2, for which we chose a bond length of 5.051 a_0 based on experimental data from Ref. [PJJ00]. Figure 5.3 shows the absorption spectra calculated with our real-space real-time method (`BTDFT`) and linear-response TDDFT (`Turbomole`) using TASKx-GKS without the current-density correction. For the

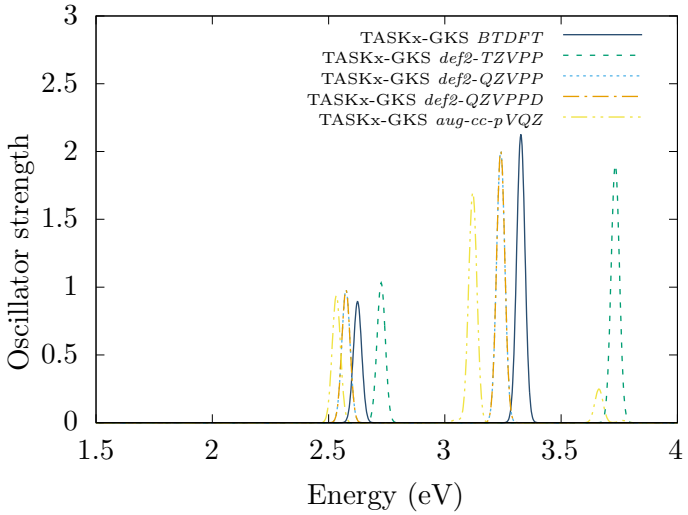

Figure 5.3: Vertical excitation spectra for Li_2 calculated with `BTDFT` and `Turbomole` using TASKx-GKS.

`BTDFT` calculations, we employed a real-space grid with a radius of 15 a_0 and a grid spacing of 0.2 a_0. TASKx-GKS calculations reveal two prominent excitation lines at 2.62 eV and 3.33 eV. Similar to the results for the CO molecule, the `Turbomole` calculations show a strong dependence on the chosen basis set, which is particularly prominent for the second excitation line. With the TZVPP basis set, the first excitation line closely matches the `BTDFT` result, whereas the second excitation line deviates significantly. Increasing the basis size to QZVPP and further to QZVPPD improves agreement and reduces the deviation in the second excitation line to approximately 0.09 eV. This level of consistency is expected, given the fundamental differences between the numerical frameworks of the two methods. Interestingly, using the aug-cc-pVQZ basis set introduces larger deviations: the second excitation line shifts to lower energies, and an additional third excitation line emerges at higher energies. Since this calculation appears sensitive to numerical details and reveals a previously unseen excitation, we consider the QZVPP/QZVPPD results to be the most reliable for our `Turbomole` calculations.

After verifying the numerical accuracy of our real-space real-time approach, we examine the influence of the current-density correction on the TASKx meta-GGA applied for the Li_2 system. The results from our `BTDFT` calculations are presented in Fig. 5.4. The dashed line represents the TASKx results obtained from calculations without the current-density correction (GKS), whereas the solid line corresponds to results from calculations that include the correction (CGKS). For the TDGKS calculations, the two prominent excitation lines are located at 2.63 eV and 3.33 eV. When incorporating the current-density correction (CGKS), these excitation energies undergo significant redshifts to 1.90 eV and 2.46 eV, corresponding to shifts of 0.73 eV and 0.87 eV for the first and second excitation lines, respectively.

In order to evaluate the effect of the current-density correction, our results are compared to experimental reference values and to CC3 calculations reported in Ref. [PJJ00].

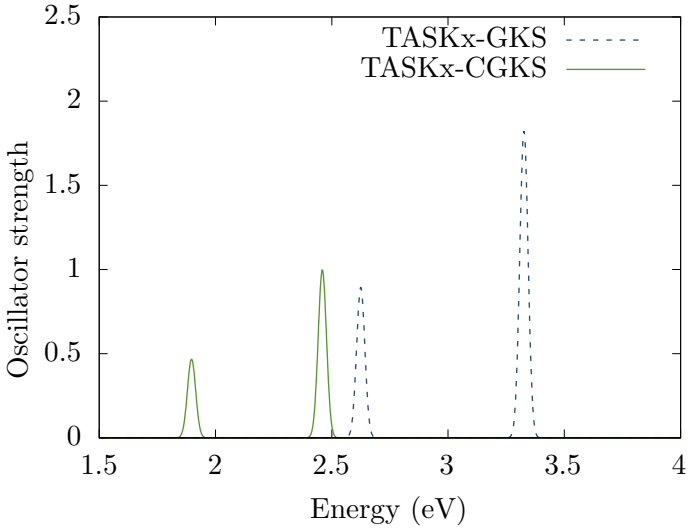

Figure 5.4: Vertical excitation spectra for Li_2 calculated with (CGKS) and without (GKS) the current-density correction using TASKx.

Using the harmonic approximation, we calculated the vertical excitation energies based on the reported data. From this, we determined the two prominent excitation lines to be at 1.86 eV and 2.57 eV for the experimental data and at 1.83 eV and 2.57 eV for the CC3 calculations. Comparing this reference data with our findings for TASKx reveals, similar to the CO calculations, that including the current-density correction leads to significantly improved agreement with the reference data. For the first excitation line, the relative error is reduced from 40.9% with TASKx-GKS to 2.2% with TASKx-CGKS, and for the second excitation line, it is reduced from 29.6% to 4.3%. Therefore, the results suggest that the current-density correction has a significant impact, with the CGKS results showing better agreement with the reference values.

Results for Organic Molecules

Having examined diatomic molecules, we now turn our attention to organic molecules. As a starting point, we investigate the impact of the current-density correction on the absorption spectrum for benzene (C_6H_6), a well-established model system characterized by its π electron configuration. Our results using the real-space real-time approach are shown for TASKx in Fig. 5.5. Looking at the energy range in which the excitation spectrum is plotted in Fig. 5.5, it becomes evident that the energy shift from GKS to CGKS for benzene is smaller compared to the previous results for CO and Li_2. The prominent excitation line for TASKx-GKS is located at 7.62 eV, while for TASKx-CGKS, it shifts to 7.48 eV, resulting in a smaller energy shift of 0.14 eV compared to our previous results. A possible explanation for the smaller shift lies in Eq. (5.17), which quantifies the extent to which the continuity equation is violated. This equation shows that the violation is directly related to the derivative $\partial e_{\mathrm{xc}}^{\mathrm{mGGA}}/\partial\tau$ of the energy density (or enhancement factor) of the employed meta-GGA functional. For the TASK meta-GGA, the magnitude of this derivative is intentionally increased to enhance its (ultra-)nonlocal features. However, this derivative's specific value depends on the system's physical properties under investigation, including the values of n, s, and α, which parameterize the meta-GGA functional. This derivative is expected to be less pronounced for systems closely resembling the homogeneous electron gas, as the meta-GGA functionals TASK

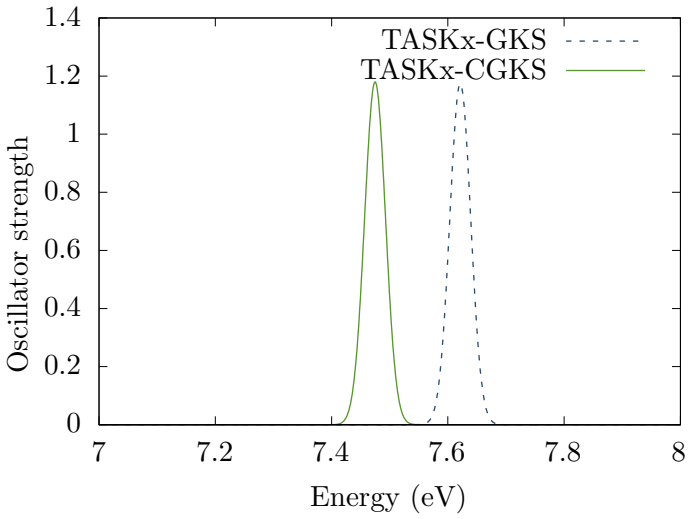

Figure 5.5: Vertical excitation spectra for benzene (C_6H_6) calculated with (CGKS) and without (GKS) the current-density correction using TASKx.

and r^{2}SCAN are designed to recover the correct homogeneous electron gas limit. In the case of benzene, its aromatic ring structure implies that the electronic distribution is more homogeneous compared to the diatomic molecules CO and Li_2. Consequently, the magnitude of $\partial e_{\mathrm{xc}}^{\mathrm{mGGA}}/\partial\tau$ is expected to be smaller, leading to a reduced violation of the continuity equation and, in turn, a smaller influence of the current-density correction.

In addition to the smaller energy shift, it is also evident that, unlike the diatomic molecules, where a notable reduction in oscillator strength was observed when transitioning from GKS to CGKS calculations, Fig. 5.5 indicates a marginal increase in oscillator strength for benzene.

Next, we focus on the organic semiconductor molecule NDI-1. This molecule exhibits a CT excitation as its first spectral line. The naphthalene diimide core of NDI-1 serves as an acceptor region, while the thiophene units attached to the molecule act as donor regions, enabling a CT process. This phenomenon has been extensively studied in previous works [Kar+11; HK20], as NDI-1 was specifically designed for applications in organic solar cells.

In contrast to the previously studied molecules, which consist solely of 1s core orbitals, the NDI-1 molecule also includes sulfur (S) atoms. For sulfur, the core correction to the kinetic energy density, as defined in Eq. (5.1), is not applicable. Therefore, we apply the core correction only to the PPs for atoms with 1s-like core electrons. For all other cases, we use standard Troullier-Martins PPs [TM91]. Detailed parameters for these PPs can be found in the supplementary material of Ref. [Ric+23]. To evaluate whether this approximation introduces deviations compared to all-electron calculations, we explicitly compare our real-space real-time results with those obtained using `Turbomole` with the QZVPP basis set, as shown in Fig. 5.6. The vertical excitation spectra calculated with `BTDFT` and `Turbomole` using the TASKx meta-GGA exhibit close agreement, with a slight deviation of 0.04 eV for the CT excitation, labeled with "CT". This agreement indicates that neglecting the core correction for the sulfur atoms in the PP does not introduce significant errors in the excitation spectra.

Figure 5.7 illustrates the vertical excitation spectra of NDI-1 calculated using TASKx without (GKS) and with (CGKS) the current-density correction, employing our real-space real-time method. Including the current-density correction results in only minor

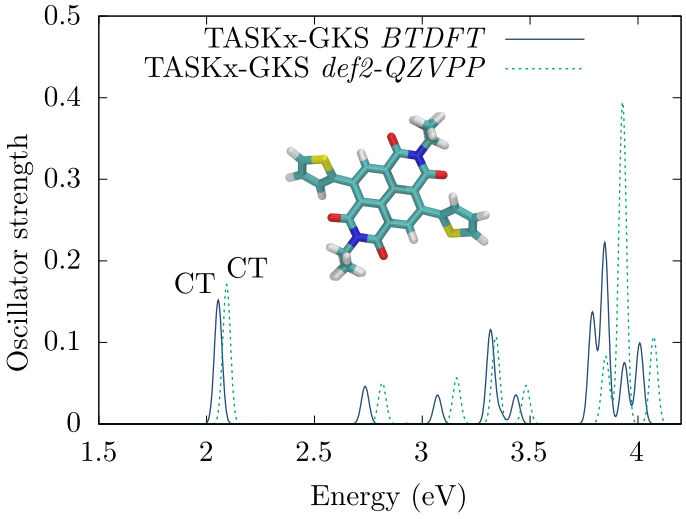

Figure 5.6: Vertical excitation spectra for NDI-1 calculated with `BTDFT` and `Turbomole` using TASKx-GKS.

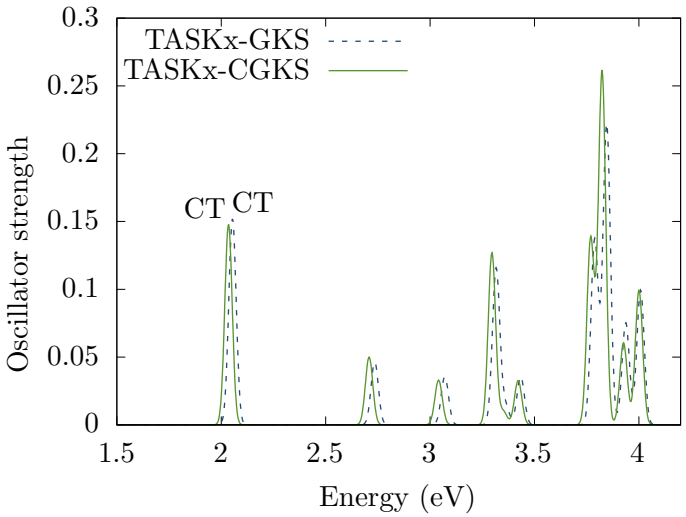

Figure 5.7: Vertical excitation spectra for NDI-1 calculated with (CGKS) and without (GKS) the current-density correction using TASKx.

differences between the two calculations. Specifically, the CT excitation energy is 2.05 eV for TASKx-GKS and 2.03 eV for TASKx-CGKS, resulting in a minimal shift of 0.02 eV. Moreover, given that the TASK meta-GGA is specifically designed to exhibit (ultra-)nonlocal features, comparing the CT excitation energy predicted by TASK to results obtained with other xc approximations is particularly interesting. For instance, the time-dependent LDA (TDLDA) functional predicts the CT excitation energy at 1.69 eV with GGA functionals yielding similar values. In contrast, an optimally tuned range-separated hybrid functional predicts a significantly higher excitation energy of 2.52 eV, which closely matches experimental observations [Kar+11]. These findings highlight the well-documented underestimation of CT excitations by (semi-)local functionals such as the LDA and GGAs. This limitation can be partly attributed to the absence of a derivative discontinuity in these functionals, as discussed in Section 4.3 [Toz+99]. The TASK meta-GGA, however, is explicitly designed to incorporate a reasonably sized

derivative discontinuity [AK19], which leads to an upward shift in the CT excitation energy by approximately 0.36 eV, improving its alignment with the experimental value. Nevertheless, while the TASK meta-GGA demonstrates significant improvement over the TDLDA, it can still not resolve the CT problem. Its prediction remains noticeably below both the experimental value and the result obtained with a range-separated hybrid functional, indicating that further improvements are necessary for accurately capturing the CT excitation.

These findings are further supported by the results from our final model system, a coupled system of two Bacteriochlorophyll (BChl) molecules. The two chromophores under consideration, BChl-302 and BChl-303, are part of the B850 ring in the light-harvesting complex 2 of the purple bacterium *Rhodoblastus acidophilus*. The absorption spectrum of a single BChl molecule is characterized by two prominent excitation lines, the Q_y and Q_x excitation. The interaction between the two molecules in the coupled system of BChl-302 and BChl-303 results in four excitations: two coupled Q_y excitations and two Q_x excitations. The Q_y excitations form a J-aggregate, consisting of one symmetric coupled excitation with a high oscillator strength and one antisymmetric coupled excitation with a low oscillator strength [SK18]. In contrast, the Q_x excitations are only weakly coupled and primarily show the characteristics of the individual BChl-302 and BChl-303 molecules. Figure 5.8 shows the absorption spectrum of the coupled system for different xc approximations. The dotted line in the left panel represents

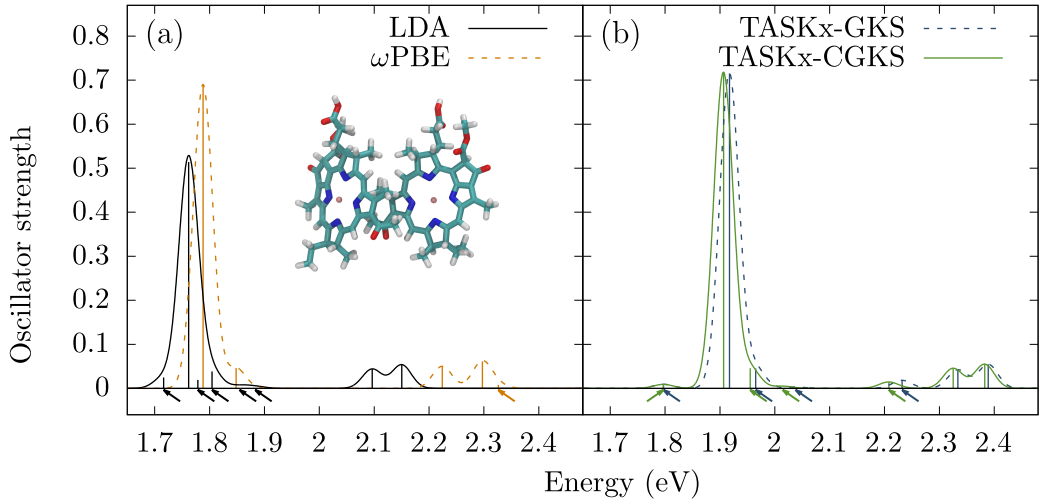

Figure 5.8: Vertical excitation spectra for the combined BChl-302-BChl-303 molecular system calculated with TDLDA and ωPBE in panel (a) and TASKx-GKS and TASKx-CGKS in panel (b). Small arrows below the energy axis highlight excitations with very low oscillator strength that lie close to stronger ones.

the excitation spectrum calculated using the optimally tuned range-separated hybrid functional ωPBE, as adapted from Ref. [Sch+19]. This spectrum exhibits the expected result of two Q_y lines around 1.8 eV: one with a high oscillator strength just below 1.8 eV and another with a low oscillator strength slightly above 1.8 eV. Additionally, two Q_x lines are observed in the energy range of 2.2 to 2.3 eV. Within the energy range shown in Fig. 5.8, an additional excitation with a small oscillator strength is present, which is marked by a small arrow below the energy axis. The left panel of Fig. 5.8 also shows the absorption spectrum calculated using the TDLDA functional. Here, the typical shortcomings of (semi-)local functionals in describing CT excitations become evident.

While the weak coupling between the two Q_x excitations is captured similarly to the ωPBE functional, with a slight shift to lower energies, the Q_y coupling is significantly affected by spurious CT excitations. Near the expected two coupled Q_y lines, four additional spurious excitations appear around 1.8 eV, as indicated by small arrows below the energy axis.

The absorption spectra calculated using the TASKx meta-GGA, both with and without the current-density correction, are presented in the right panel of Fig. 5.8. Consistent with the results for NDI-1, the influence of the current-density correction is negligible. However, evaluating the TASKx meta-GGA's ability to accurately describe the spectrum of the combined BChl-302-BChl-303 system is less straightforward. While the number of spurious CT excitations near the Q_y line is reduced compared to the TDLDA results, one spurious line appears even below the Q_y line, and another emerges near the coupled Q_x excitations. These findings confirm the results for NDI-1, indicating that the TASKx meta-GGA improves the TDLDA results but cannot fully address the CT problem.

5.2.3 Time-Dependent (C)GKS Calculations Using the r^{2}SCAN Meta-GGA Functional

Results for Diatomic Molecules

We now examine the impact of the current-density correction when using the r^{2}SCAN meta-GGA functional [Fur+20a; Fur+20b]. For a direct comparison with the exchange functional TASK, we only consider the exchange part of the r^{2}SCAN functional. An additional reason for this choice is that the derivative $\partial e_{\mathrm{xc}}^{\mathrm{mGGA}}/\partial\tau$, and consequently the derivative discontinuity, exhibits the opposite sign in the correlation part of r^{2}SCAN compared to its exchange part. As indicated by Eq. (5.17), the opposite sign of this derivative within the correlation part is expected to cause a shift in the excitation line in the opposite direction when applying the current-density correction, thereby counteracting the effect of the correction on the exchange part of the r^{2}SCAN functional.

The absorption spectra for CO (Fig. 5.9a) and Li_2 (Fig. 5.9b), calculated using our real-space real-time propagation scheme with the r^{2}SCANx meta-GGA, both with and without the current-density correction, are shown in Fig. 5.9. For CO, we observe a notable shift of the prominent excitation line from r^{2}SCAN-GKS to r^{2}SCAN-CGKS. The excitation energy decreases from 8.82 eV (r^{2}SCAN-GKS) to 8.46 eV (r^{2}SCAN-CGKS), corresponding to a shift of 0.36 eV. Although this shift is smaller than that observed for TASKx, it remains significant. Similar to TASKx, by introducing the current-density correction, the r^{2}SCAN results show closer agreement with the reference value.

The absorption spectra for the Li_2 molecule reveal an analogous trend. As shown in the right panel of Fig. 5.9, the first excitation line exhibits a redshift of 0.22 eV, from 2.15 eV (r^{2}SCAN-GKS) to 1.93 eV (r^{2}SCAN-CGKS). The second excitation line shifts by 0.28 eV, from 2.77 to 2.49 eV. Both excitation energies obtained with r^{2}SCAN-CGKS, i. e. with the current-density correction, are in closer agreement with the experimental reference values of 1.86 eV and 2.57 eV, respectively.

Results for Organic Molecules

Regarding our first organic model system, benzene, Fig. 5.10 illustrates the difference between r^{2}SCAN-GKS and r^{2}SCAN-CGKS. Similar to our observations for TASKx, the influence of the current-density correction for benzene is significantly smaller than for CO and Li_2, with a redshift of the prominent excitation line of just 0.07 eV. This can

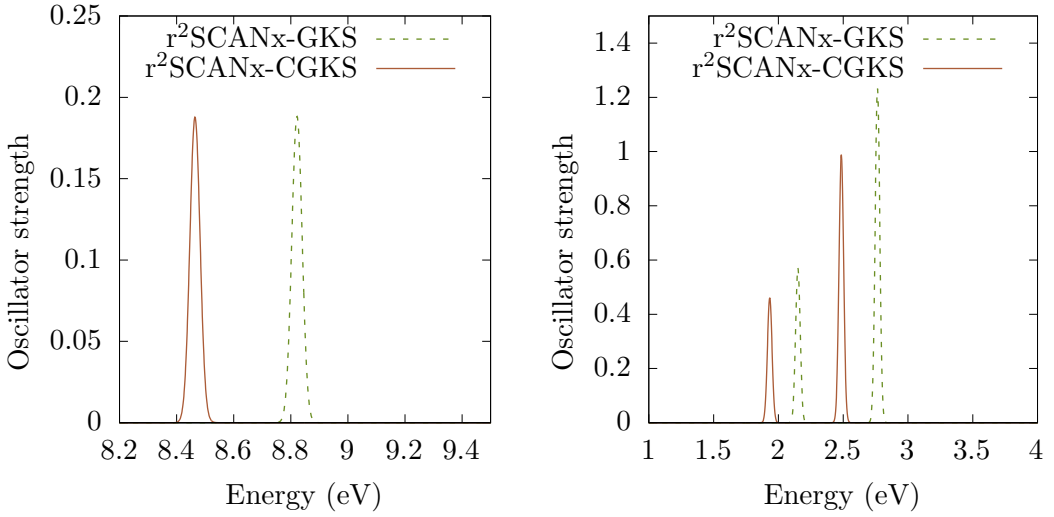

(a) Vertical excitation spectrum for CO.

(b) Vertical excitation spectrum for Li_2.

Figure 5.9: Vertical excitation spectra for CO (left panel) and Li_2 (right panel) calculated with (CGKS) and without (GKS) the current-density correction.

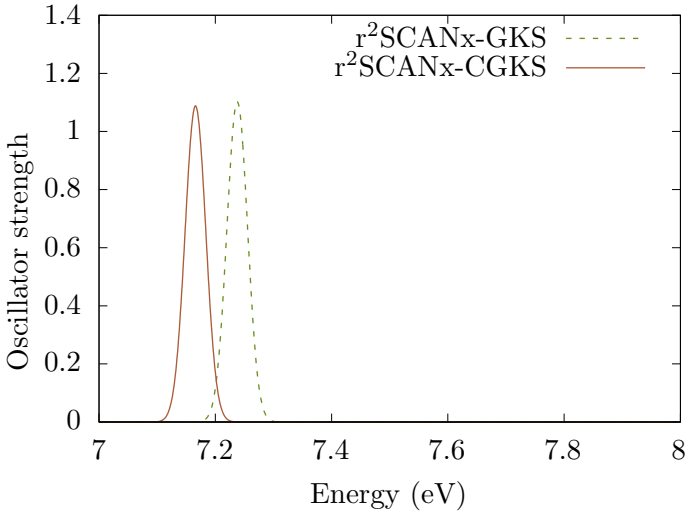

Figure 5.10: Vertical excitation spectra for benzene (C_6H_6) calculated with (CGKS) and without (GKS) the current-density correction using r^{2}SCANx.

again be attributed to the dependence of the current-density correction in Eq. (5.17) on $\partial e_{\mathrm{xc}}^{\mathrm{mGGA}}/\partial\tau$ and the electronic structure of the benzene molecule, which is closer to that of the homogeneous electron gas compared to CO or Li_2. The smaller energy shift observed for r^{2}SCANx compared to TASKx can be further explained by the weaker τ-dependence of the r^{2}SCANx meta-GGA relative to the TASKx meta-GGA.

The results using the r^{2}SCANx meta-GGA for the NDI-1 molecule are presented in Fig. 5.11. The absorption spectrum exhibits a trend comparable to that observed for TASKx: the differences between r^{2}SCAN-GKS and r^{2}SCAN-CGKS are negligible, with an energy shift of less than 0.01 eV for the CT excitation. When comparing the two meta-GGAs, the CT excitation for r^{2}SCAN-CGKS occurs at 1.92 eV, which is slightly

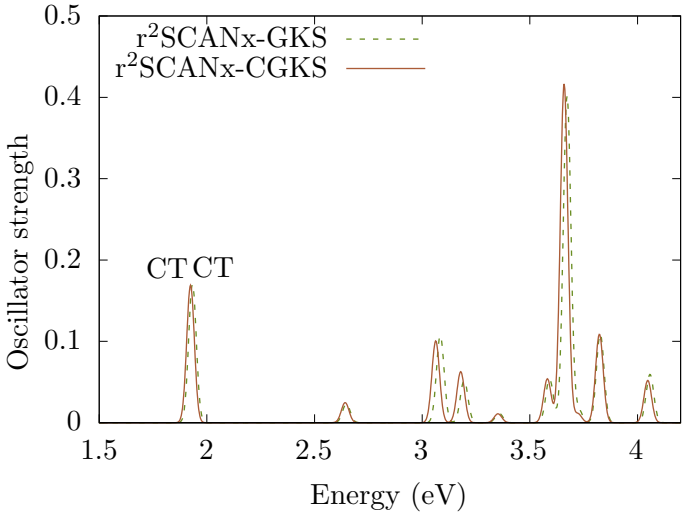

Figure 5.11: Vertical excitation spectra for NDI-1 calculated with (CGKS) and without (GKS) the current-density correction using r^{2}SCANx.

lower than the corresponding TASKx-CGKS result of 2.04 eV. As a result, r^{2}SCAN-CGKS deviates more from the reference value of 2.52 eV (computed using ωPBE) than TASKx-CGKS. This finding suggests that TASKx, with its design focusing on a stronger τ-dependence and a more pronounced derivative discontinuity, more effectively mitigates the spurious downshift of the CT excitation.

Finally, the results for our last model system, the combined BChl-302-BChl-303 system, are shown in Fig. 5.12. Again, the current-density correction has a minor effect.

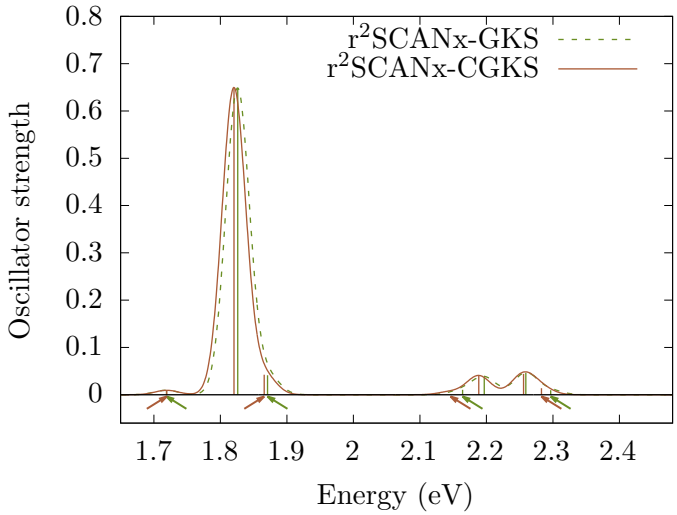

Figure 5.12: Vertical excitation spectra for the combined BChl-302-BChl-303 system calculated with (CGKS) and without (GKS) the current-density correction using r^{2}SCANx.

Both r^{2}SCANx and TASKx describe the coupling of the Q_y excitations between the individual BChl molecules with comparable accuracy. However, r^{2}SCAN introduces a spurious CT excitation just below the coupled Q_y excitations.

The situation becomes more complex in the energy range of the Q_x excitations. With r^{2}SCANx, two spurious CT excitations appear near the weakly coupled excitations. In contrast, the TASKx absorption spectrum (shown in the right panel of Fig. 5.8) reveals a single spurious CT excitation, which is separated from the coupled Q_x lines. As a result, the coupling of the Q_x lines is more distorted in r^{2}SCANx due to the presence of two closely spaced spurious CT excitations. In summary, while TASKx provides a slightly better description of the CT excitations compared to r^{2}SCANx, neither functional achieves the level of accuracy achieved by the tuned range-separated hybrid ωPBE.

5.3 Summary and Conclusion

This chapter demonstrated using the r^{2}SCAN and TASK functionals in real-space real-time TDDFT within the TDGKS scheme. We compared the results for different model systems with and without using a current-density correction that restores gauge invariance and addresses the violation of the continuity equation caused by the meta-GGA potential operator within the GKS framework. Additionally, we introduced an approach to improve the reliability of using non-consistent PPs in meta-GGA calculations by applying a core correction scheme. This approach led to enhanced accuracy, making the results comparable to those obtained from all-electron calculations.

Our results using the current-density correction for TASKx and r^{2}SCANx demonstrate that the correction can significantly influence the energetic positions of the excitation lines. The most pronounced effect is observed for the excitation spectrum of the Li_2 system, where the excitation energy shifts by more than 0.8 eV. In general, we observed a downshift in the calculated excitation energies for all model systems considered when transitioning from GKS to CGKS calculations, i. e., when including the current-density correction. Furthermore, for TASKx and r^{2}SCANx, applying the current-density correction results in better agreement with our reference values for the excitation energies of the diatomic systems. For larger conjugated organic molecules, the influence of the current-density correction (nearly) vanished. This can be explained by the following: Since the violation of the continuity equation depends on the derivative $\partial e_{\mathrm{xc}}^{\mathrm{mGGA}}/\partial\tau$ (see Eq. (5.17)), the influence of the current-density correction is a direct consequence of the differences in the electronic structure of the different systems to which $e_{\mathrm{xc}}^{\mathrm{mGGA}}$ is sensitive. Specifically, the magnitude of $\partial e_{\mathrm{xc}}^{\mathrm{mGGA}}/\partial\tau$ is a direct consequence of the system-dependent values of n, ∇n and τ upon which the meta-GGAs are parametrized. This is particularly evident for the r^{2}SCANx meta-GGA, whose τ-derivative of the enhancement factor is constructed to vanish in the homogeneous electron gas limit. As a result, the influence of the current-density correction is reduced for conjugated organic molecules with more delocalized densities, compared to the more localized densities of diatomic model systems such as CO and Li_2. Furthermore, because the TASKx meta-GGA is intentionally constructed to exhibit higher absolute values of $\partial e_{\mathrm{xc}}^{\mathrm{mGGA}}/\partial\tau$ (and thus stronger nonlocal features, see Eq. (4.11)), the absorption spectra calculated with TASKx generally exhibit a more pronounced influence from the current-density correction. However, since it is challenging to predict the influence of the current-density correction across different systems and meta-GGA functionals, applying it in all TDDFT calculations that employ meta-GGAs is recommended.

Looking at the somewhat better description of CT excitations by the TASK meta-GGA, the findings are in line with the construction strategies of the functionals, with r^{2}SCAN focusing on the ground-state energetics and TASK focusing on incorporating (ultra-)nonlocal features. However, neither functional can achieve the accuracy of optimally tuned range-separated hybrid functionals for CT excitations. This result is,

to some extent, expected: although the TASK functional is intentionally designed to exhibit a reasonably sized derivative discontinuity [Gis+99; KKP04; KK18] other factors, such as freedom from self-interaction and correct asymptotic behavior, remain important for accurately describing CT excitations. However, both TASK and r^{2}SCAN are not free from self-interaction, as they cannot entirely cancel the nonlocal SIE of the Hartree term, and their corresponding potentials exhibit exponential decay rather than the correct asymptotic behavior of $-1/r$.

Chapter 6

Self-Interaction Correction in Density Functional Theory

While meta-GGA functionals provide accurate results for many physical properties – such as the atomization energies of molecules, surface energies of metals, lattice constants of solids, and band gaps of solids [KPB99; SRP15; AK19; LAK24] – the previous chapter demonstrated that the considered meta-GGAs cannot resolve the CT problem inherent to (semi-)local xc approximations. A systematic underestimation of CT excitation energies in molecules characterizes this problem. The TASK meta-GGA functional attempts to mitigate this issue by incorporating a derivative discontinuity that introduces field-counteracting terms, thereby shifting these excitation energies closer to their accurate, higher values. However, TASK and r^{2}SCAN still fall short of the accuracy of describing CT excitations in molecules achieved by optimally tuned range-separated hybrid functionals [SKB09; Mai17; Küm17; Sch+19; Ric+23]. A known limitation of meta-GGA functionals that contributes to their deficiency in describing CT excitations is their inability to eliminate the spurious SIE (see Section 3.2) introduced by the Hartree energy term [DWH03; KK08]. Additionally, the xc potential derived from meta-GGA functionals does not exhibit the correct asymptotic behavior, further restricting their ability to describe long-range interactions accurately [Mai17; KK20].

For ground-state DFT calculations, these shortcomings lead to a delocalization error in (semi-)local xc approximations, which manifests as a failure to satisfy the straight-line condition, introduced in Section 3.3 [Per+82; YZA00; Bry+23]. This violation of the piecewise linearity can be explicitly demonstrated for the diatomic CO model system. Figure 6.1 illustrates the energy curves $E(N)$ for the CO molecule, calculated with the LSDA and the TASK functional (with LSDA correlation) within the GKS framework. The straight-line reference, which connects $E(N_0)$ and $E(N_0 - 1)$, is indicated by dotted and dashed lines, where N_0 denotes the number of electrons in the neutral system. The $E(N)$ curve (with $N = N_0 + \Delta N$) for LSDA exhibits the strongly convex behavior characteristic of (semi-)local xc approximations. While the TASK-GKS energy curve shows a slightly smaller curvature than the LSDA energy curve, it still has a pronounced convex shape, violating the piecewise linearity condition.

Both the (one-electron) SIE as well as the wrong asymptotic behavior can be addressed using a SIC scheme introduced by Perdew and Zunger [PZ81] that replaces the xc energy functional $E_{\mathrm{xc}}[n_\uparrow, n_\downarrow]$ in the ground-state energy functional by

$$E_{\mathrm{xc}}^{\mathrm{SIC}}[\{\varphi_{i\sigma}\}] = E_{\mathrm{xc}}^{\mathrm{app}}[n_\uparrow, n_\downarrow] - \sum_{\sigma=\uparrow,\downarrow} \sum_{i=1}^{N_\sigma} \left(E_{\mathrm{H}}[|\varphi_{i\sigma}|^2] + E_{\mathrm{xc}}^{\mathrm{app}}[|\varphi_{i\sigma}|^2, 0] \right), \tag{6.1}$$

where $E_{\mathrm{H}}[|\varphi_{i\sigma}|^2]$ is the Hartree energy, $E_{\mathrm{xc}}^{\mathrm{app}}[|\varphi_{i\sigma}|^2, 0]$ represents the xc approximation, both evaluated with the orbital density $|\varphi_{i\sigma}|^2$, and N_σ is the number of particles with

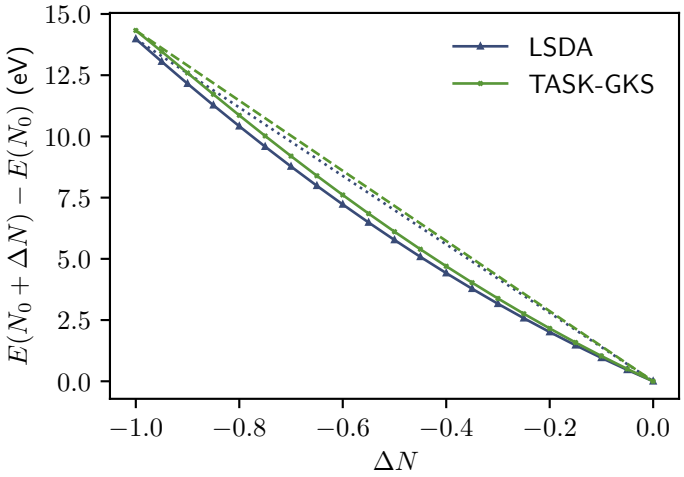

Figure 6.1: Total energy $E(N_0 + \Delta N)$ relative to the energy $E(N_0)$ of the neutral CO molecule as a function of the electron number ΔN (difference to neutral CO), calculated with LSDA and TASK-GKS. The dotted and dashed lines are the straight lines that connect $E(N_0)$ and $E(N_0 - 1)$.

spin σ. The basic idea of the Perdew-Zunger self-interaction correction (PZ-SIC) is to identify the energy contribution arising from the interaction of a single orbital with itself and to subtract this spurious self-interaction from an existing xc approximation $E_{\text{xc}}^{\text{app}}$. It is important to note that interpreting the orbital density as the contribution of a single electron to the total density is already an approximation. While the PZ-SIC can be generally applied to any xc approximation, it was initially formulated for the LDA functional. Due to the explicit dependence of Eq. (6.1) on the orbital densities $|\varphi_{i\sigma}|^2$, this energy functional introduces several challenges, which are thoroughly discussed in this chapter. First, we briefly discuss a simplified approximation of the full PZ-SIC that circumvents these challenges.

6.1 Average Density Self-Interaction Correction

The average density self-interaction correction (ADSIC) [LSR02; Mes+11; Klü+13] provides a substantially simplified alternative to the PZ-SIC expression in Eq. (6.1). Within the ADSIC approach, the orbital densities $|\varphi_{i\sigma}|^2$ are approximated by their average values, yielding the energy functional

$$E_{\text{xc}}^{\text{ADSIC}}[n_\uparrow, n_\downarrow] = E_{\text{xc}}^{\text{app}}[n_\uparrow, n_\downarrow] - \left(N E_{\text{H}}\left[\frac{n}{N}\right] + N_\uparrow E_{\text{xc}}^{\text{app}}\left[\frac{n_\uparrow}{N_\uparrow}, 0\right] + N_\downarrow E_{\text{xc}}^{\text{app}}\left[0, \frac{n_\downarrow}{N_\downarrow}\right] \right), \tag{6.2}$$

where $N_\uparrow$ and $N_\downarrow$ denote the number of spin-up and spin-down electrons, respectively, and $N = N_\uparrow + N_\downarrow$ is the total number of electrons. The computational cost of the ADSIC is significantly lower than that of the full PZ-SIC or functionals that employ the exact exchange functional. Similar to the full PZ-SIC, Eq. (6.2) can, in principle, be applied to any xc approximation but is typically used with the LSDA functional. One of the key advantages of the ADSIC is that it solely depends on the density, which avoids the technical challenges associated with orbital-dependent functionals, such as the need for the OEP method or a GKS scheme. Therefore, the xc potential can be

directly obtained by the functional derivative $\delta E_{\mathrm{xc}}^{\mathrm{ADSIC}}/\delta n_\sigma$. The resulting potential exhibits the correct asymptotic behavior of $-1/r$.

The ADSIC approach has demonstrated reliable accuracy in describing ionization processes for several model systems [Mes+11; Klü+13; Dun+17]. However, it fails to satisfy the straight-line condition, which can be demonstrated for our diatomic test system, the CO molecule: the $E(N)$ curve obtained with ADSIC, as shown in Fig. 6.2, exhibits no improvement over the LSDA results.

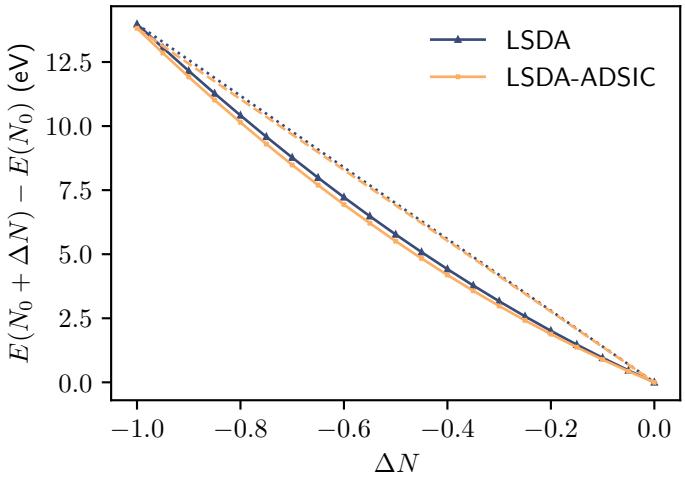

Figure 6.2: Total energy $E(N_0 + \Delta N)$ relative to the energy $E(N_0)$ of the neutral CO molecule as a function of the electron number ΔN (difference to neutral CO), calculated with LSDA and LSDA-ADSIC. The dotted and dashed lines are the straight lines that connect $E(N_0)$ and $E(N_0 - 1)$.

This finding is consistent with our previous study in Ref. [Keh+20], where we demonstrated that the application of the ADSIC in TDDFT fails to properly describe the absorption spectrum of the BChl-302 molecule, one of the two components of the combined BChl-302-BChl-303 system introduced in Section 5.2. We identified multiple spurious CT excitations in the energy range between the Q_y and Q_x excitation lines, resulting in a qualitatively similar (and in some cases even worse) description of CT excitations compared to the TDLDA results (for details, see Ref. [Keh+20]). In addition to the explicit dependence of the energy functional in Eq. (6.2) on the particle number, which breaks the size consistency of the ADSIC approach, the replacement of the orbital density $|\varphi_{i\sigma}|^2$ in the PZ-SIC expression with the averaged value n_σ/N_σ renders ADSIC a global functional. As a result, it cannot fully correct the intrinsically nonlocal SIE introduced by the Hartree term in KS theory. Moreover, since the ADSIC depends solely on the density, it lacks a derivative discontinuity and, therefore, cannot provide the necessary field-counteracting effect against an external potential driving the CT process. Consequently, this simplified SIC scheme fails to resolve the CT problem inherent to (semi-)local xc approximations.

6.2 Perdew-Zunger Self-Interaction Correction Energy Functional

Since the simplified ADSIC functional fails to accurately fulfill the straight-line condition, we revert to the original PZ-SIC formulation given by Eq. (6.1). The full ground-state

energy functional using the PZ-SIC can then be expressed as

$$E^{\mathrm{SIC}} = E_{\mathrm{kin}} + E_{\mathrm{ext}}[n] + E_{\mathrm{H}}[n] + \underbrace{E_{\mathrm{xc}}^{\mathrm{app}}[n_\uparrow, n_\downarrow] - \sum_{\sigma=\uparrow,\downarrow} \sum_{i=1}^{N_\sigma} \left(E_{\mathrm{H}}[n_{i\sigma}] + E_{\mathrm{xc}}^{\mathrm{app}}[n_{i\sigma}, 0]\right)}_{=E_{\mathrm{xc}}^{\mathrm{SIC}}}, \quad (6.3)$$

where $n_{i\sigma} = |\varphi_{i\sigma}|^2$ is the orbital density, and $n = \sum_{\sigma=\uparrow,\downarrow} \sum_{i=1}^{N_\sigma} n_{i\sigma}$ is the total electron density.

The PZ-SIC formulation of the xc energy functional offers several formal advantages: For any one-electron system with a single occupied orbital $\varphi_{1\uparrow}$, the PZ-SIC energy correction in Eq. (6.3) simplifies to $E_{\mathrm{xc}}^{\mathrm{SIC}} = -E_{\mathrm{H}}[|\varphi_{1\uparrow}|^2]$, exactly canceling the Hartree energy $E_{\mathrm{H}}[|\varphi_{1\uparrow}|^2]$. Consequently, the PZ-SIC provides an exact description for all one-electron densities. At the same time, any SIC would be redundant for the exact xc functional, as it satisfies $E_{\mathrm{H}}[n_{i\sigma}] + E_{\mathrm{xc}}[n_{i\sigma}] = 0$. This condition is correctly maintained within the PZ-SIC. Beyond eliminating SIEs, the PZ-SIC ensures that the corresponding SIC potential exhibits the correct asymptotic behavior of $-1/r$. Unlike the uncorrected LSDA or LSDA-ADSIC, using the LSDA (or a GGA) in combination with the PZ-SIC introduces a derivative discontinuity due to its explicit orbital dependence of the self-Hartree and self-xc terms in Eq. (6.3) [KK08; Per90]. Furthermore, in contrast to the simplified ADSIC approach, the full PZ-SIC energy functional preserves size consistency [Per90].

While the PZ-SIC energy functional offers several formal advantages, its special dependence on orbital densities has several challenging consequences: In principle, the PZ-SIC defined in Eq. (6.1) can be applied to any given xc approximation. However, since most xc functionals are designed for ground-state densities that do not exhibit nodal planes, it remains unclear whether their evaluation on orbital densities is fully justified. Additionally, because the xc functional directly depends on orbital densities, the PZ-SIC energy functional is not invariant under unitary transformations of the occupied orbitals, a property of the xc functional that is discussed in Section 3.6.2. Consequently, the total ground-state energy obtained from the PZ-SIC can change under a unitary transformation, described by a (unitary) matrix $\mathbf{U}_\sigma$, of the occupied orbitals, even though the ground-state density itself remains unchanged. This transformation maps an initial set of orbitals $\{\varphi_{i\sigma}\}$ to a new set $\{\varphi'_{i\sigma}\}$ as follows:

$$\varphi'_{i\sigma}(\mathbf{r}) = \sum_{j=1}^{N_\sigma} U_{ij\sigma} \varphi_{j\sigma}(\mathbf{r}) \,. \quad (6.4)$$

In practice, the unitary transformation that minimizes the PZ-SIC ground-state energy functional typically results in more localized orbitals, as these tend to increase the magnitude of the correction terms in Eq. (6.1).

In order to find the minimum of the PZ-SIC energy functional (Eq. (6.3)), its explicit orbital dependence (or implicit density dependence) can be addressed in two ways. The first approach, within the KS framework, involves treating orbital-dependent xc functionals using the OEP scheme. For the PZ-SIC, this method has been extensively discussed in previous works [Hof+12; HK12; HKK12]. However, solving the full OEP integral equation and extending this formalism to the time-dependent regime poses well-known challenges, as previously outlined. Consequently, applying the PZ-SIC through the OEP method is primarily restricted to ground-state calculations.

The second approach is based on the original formulation of the SIC by Perdew and

Zunger [PZ81] where the energy functional of Eq. (6.3) is directly minimized with respect to the orbitals. However, the resulting ground-state orbitals are no longer automatically orthonormal. While for ground-state calculations of atoms, it has been shown that the orthogonality constraint has a negligible impact on physical results [PZ81; HHL83], for molecules, it has been demonstrated that the missing orthogonality of the orbitals can have a decisive impact [PHL85]. In this work, we adopt the approach of minimizing the energy functional in Eq. (6.3) while enforcing the orthonormality of the orbitals, as detailed in the following section.

6.3 Minimization of the PZ-SIC Energy Expression

The direct variation of the ground-state energy expression using the PZ-SIC (Eq. (6.3)) leads to

$$\frac{\delta E^{\mathrm{SIC}}[\{\varphi_{i\sigma}\}]}{\delta \varphi^*_{i\sigma}(\mathbf{r})} = \hat{H}_{i\sigma}\varphi_{i\sigma}(\mathbf{r}) \tag{6.5}$$

with a set of orbital-dependent Hamilton operators

$$\hat{H}_{i\sigma} = -\frac{\hbar^2}{2m}\nabla^2 + v_{\mathrm{ext}}(\mathbf{r}) + v_{\mathrm{H}}[n](\mathbf{r}) + v_{\mathrm{xc}}[n_\uparrow, n_\downarrow](\mathbf{r}) + v^{\mathrm{SI}}[n_{i\sigma}](\mathbf{r})\,, \tag{6.6}$$

where

$$\begin{aligned} v^{\mathrm{SI}}[n_{i\sigma}](\mathbf{r}) &= -\frac{\delta}{\delta n_{i\sigma}}\left[\sum_{\sigma'=\uparrow,\downarrow}\sum_{j=1}^{N_{\sigma'}} E_{\mathrm{H}}[n_{j\sigma'}] + E_{\mathrm{xc}}[n_{j\sigma'}, 0]\right] \\ &= -\left[v_{\mathrm{H}}[n_{i\sigma}](\mathbf{r}) + v_{\mathrm{xc}}[n_{i\sigma}, 0](\mathbf{r})\right] \end{aligned} \tag{6.7}$$

is the orbital-specific SIC potential term with the orbital density $n_{i\sigma} = |\varphi_{i\sigma}|^2$. Since the Hamilton operator $\hat{H}_{i\sigma}$ in Eq. (6.6) depends on the specific orbital index $i\sigma$, the orbitals themselves are no longer eigenfunctions of the same Hamiltonian. Consequently, the resulting orbitals are not automatically orthogonal. To ensure orthogonality between the orbitals, it is necessary to explicitly incorporate the orthogonality constraint using a Lagrange multiplier $\lambda_{ji\sigma}$, thereby defining the new energy functional [HHL83]

$$S[\{\varphi_{i\sigma}\}] = E^{\mathrm{SIC}}[\{\varphi_{i\sigma}\}] - \sum_{\sigma=\uparrow,\downarrow}\sum_{i,j=1}^{N_\sigma} \lambda_{ji\sigma}\left(\langle\varphi_{i\sigma}|\varphi_{j\sigma}\rangle - \delta_{ij}\right)\,. \tag{6.8}$$

The variation of $S[\{\varphi_{i\sigma}\}]$ with respect to $\varphi^*_{i\sigma}$ leads to

$$\hat{H}_{i\sigma}\varphi_{i\sigma}(\mathbf{r}) = \sum_{j=1}^{N_\sigma} \lambda_{ji\sigma}\varphi_{j\sigma}(\mathbf{r}) \qquad \text{with} \tag{6.9a}$$

$$\boldsymbol{\lambda}_\sigma = \boldsymbol{\lambda}_\sigma^\dagger\,, \tag{6.9b}$$

where the hermiticity of $\boldsymbol{\lambda}_\sigma$ (i. e. Eq. (6.9b)) is explicitly derived in Appendix B.1. Projecting Eq. (6.9a) onto a single state yields the expression

$$\lambda_{ji\sigma} = \langle\varphi_{j\sigma}|\hat{H}_{i\sigma}|\varphi_{i\sigma}\rangle \tag{6.10}$$

for the Lagrange multiplier [KKJ11; KKJ12; Bor+15; Mes+09]. Solving the ground-state Eq. (6.9a) with Eq. (6.9b) yields the energy-minimizing orbitals. Since these orbitals are

typically more localized than the KS ground-state orbitals, they are often referred to as localized orbitals. For these localized orbitals, Fermi-Löwdin orbitals (FLOs) have been used in various studies [PRP14; Ped15]. FLOs are commonly constructed by applying a predetermined localization criterion to the KS orbitals. In contrast to this approach, we employ a variational method to determine the unitary transformation that directly minimizes the PZ-SIC energy functional with respect to the unitary transformation [PHL84; PHL85].

Unlike the (generalized) KS equations, Eq. (6.9a) is not an eigenvalue equation of a single hermitian Hamiltonian. As a result, the localized orbitals are not necessarily real-valued eigenfunctions but are generally complex-valued. This introduces an additional degree of freedom in the energy minimization during the ground-state calculation. The importance of using complex orbitals in PZ-SIC ground-state calculations has already been highlighted, for instance, in Refs. [KKJ11; Hof+12; LHJ16].

Due to the intricate form of Eqs. (6.9) compared to the well-known KS equations, the practical computation of the PZ-SIC ground state is technically challenging, and various algorithms have been developed [GU97; KKJ11; Hof+12; Bor+15]. In principle, the PZ-SIC ground state can be obtained by directly solving Eq. (6.9a) (with Eq. (6.9b)) using methods such as steepest descent or damped gradient schemes [GU97; Küm04; Mes+11; Bor+15; LHJ16]. Among the available techniques for the minimization step, we focus on the straightforward and transparent damped gradient method. In this approach, the orbitals are iteratively updated from step k to step $k+1$ according to the equation

$$\varphi_{i\sigma}^{(k+1)}(\mathbf{r}) = \varphi_{i\sigma}^{(k)}(\mathbf{r}) - \frac{d}{\hat{t}+e}\delta\varphi_{i\sigma}^{(k)}(\mathbf{r})\,, \tag{6.11}$$

where $\delta\varphi_{i\sigma}^{(k)}$ represents the search direction. Here, $\hat{t} = -\hbar^2/(2m)\nabla^2$ is the kinetic energy operator, while d and e are real-valued parameters controlling the step size and providing stabilization for components with low kinetic energy, respectively. Since the denominator of Eq. (6.11) is an operator, the equation is usually multiplied by $\hat{t}+e$ to transform it into a linear equation, which can then be solved using standard algorithms to obtain $\varphi_{i\sigma}^{(k+1)}$. After each damped-gradient iteration step, the new orbitals $\{\varphi_{i\sigma}^{(k+1)}\}$ must be normalized and the orbital-dependent Hamilton operators $\{\hat{H}_{i\sigma}\}$ with the new set of orbitals and the corresponding density $n^{(k+1)}$ must be calculated.

For the search direction $\delta\varphi_{i\sigma}^{(k)}$ at the kth iteration step, the gradient expression

$$\frac{\delta S[\{\varphi_{i\sigma}\}]}{\delta\varphi_{i\sigma}^*(\mathbf{r})} = \hat{H}_{i\sigma}\varphi_{i\sigma}(\mathbf{r}) - \sum_{j=1}^{N_\sigma}\lambda_{ji\sigma}\varphi_{j\sigma}(\mathbf{r}) \tag{6.12}$$

is typically chosen. However, Goedecker and Umrigar [GU97] proposed an alternative gradient formulation that directly incorporates the hermitian constraint of the Lagrange multiplier in Eq. (6.9b) during the minimization of the energy functional. This approach modifies Eq. (6.12) by replacing $\lambda_{ji\sigma}$ with the symmetrized expression $1/2(\lambda_{ji\sigma} + \lambda_{ij\sigma}^*)$, thereby ensuring that the hermiticity of $\boldsymbol{\lambda}_\sigma$ is automatically preserved throughout the iteration steps. Since we explicitly ensure the hermiticity of $\boldsymbol{\lambda}_\sigma$ through a unitary transformation of the orbitals, the two gradient formulations are equivalent, as detailed below.

Several studies have reported that the direct minimization scheme for calculating the PZ-SIC ground state exhibits poor convergence [Bor+15; Mes+09; Mes+11]. This poor convergence observed in the calculation of the PZ-SIC ground state compared to standard algorithms for solving the KS equations can be attributed to the fact that the PZ-SIC

energy functional of Eq. (6.1) is no longer invariant under uniform transformations. To handle the unitary variance of the energy functional and to improve the convergence of the algorithm, a two-step minimization procedure has been proposed:

The first step, or outer loop, involves the direct minimization of the energy functional with respect to the orbitals

$$\min_{\{\varphi_{i\sigma}(\mathbf{r})\}\to n(\mathbf{r})} S[\{\varphi_{i\sigma}\}]\,, \tag{6.13}$$

which can be performed using the damped gradient steps described above. The second step, or inner loop, focuses on minimizing the energy functional with respect to unitary transformations of the orbitals

$$\min_{\mathbf{U}_\sigma} S[\{\varphi_{i\sigma}\}] = \min_{\mathbf{U}_\sigma} E^{\mathrm{SIC}}[\{\varphi_{i\sigma}\}]\,. \tag{6.14}$$

For the inner loop minimization step, the derivative of the energy expression in Eq. (6.3) with respect to an infinitesimal unitary transformation is required. This derivative was first calculated for orthogonal transformations by Pederson *et al.* [PHL84] and can be straightforwardly extended to infinitesimal unitary transformations, yielding the gradient [Hof+12]

$$G_{ij\sigma} = \left.\frac{\partial E^{\mathrm{SIC}}}{\partial U^*_{ij\sigma}}\right|_{U^*_{ij\sigma}=\delta_{ij}} = \int \varphi^*_{j\sigma}(\mathbf{r})\left[v^{\mathrm{SI}}[n_{i\sigma}](\mathbf{r}) - v^{\mathrm{SI}}[n_{j\sigma}](\mathbf{r})\right]\varphi_{i\sigma}(\mathbf{r})\,\mathrm{d}^3r\,. \tag{6.15}$$

Here, $v^{\mathrm{SI}}[n_{i\sigma}]$ represents the self-interaction potential associated with the orbital density $n_{i\sigma}$ of Eq. (6.7). At the energy minimum, i. e., $G_{ij\sigma} = 0\ \forall i,j \in \{1,\dots,N_\sigma\}$, the hermitian condition of the Lagrange multiplier $\boldsymbol{\lambda}_\sigma$, Eq. (6.9b), is inherently satisfied. This relation follows from

$$\lambda_{ji\sigma} - \lambda^*_{ij\sigma} = \langle\varphi_{j\sigma}|\hat{H}_{i\sigma} - \hat{H}_{j\sigma}|\varphi_{i\sigma}\rangle = \langle\varphi_{j\sigma}|v^{\mathrm{SI}}[n_{i\sigma}] - v^{\mathrm{SI}}[n_{j\sigma}]|\varphi_{i\sigma}\rangle = 0\,, \tag{6.16}$$

where the last equality is equivalent to $G_{ij\sigma} = 0$. In our experience, ensuring the hermiticity of $\boldsymbol{\lambda}_\sigma$ during the inner loop through the variation of the orbitals with respect to the unitary transformation improves the convergence of the PZ-SIC ground-state calculation. A detailed description of our algorithm, including both the outer and inner loop, will be provided in Section 6.8.

6.4 PZ-SIC for Meta-GGAs

The PZ-SIC scheme can be straightforwardly applied to the LDA and GGA functionals, where the SIC in Eq. (6.1) effectively eliminates the spurious self-interaction contributions from both the exchange and correlation components of the LDA or GGA functional, as well as the Hartree term. For meta-GGAs, the PZ-SIC exhibits a different impact compared to other (semi-)local xc functionals. As previously discussed, meta-GGAs, such as the r^{2}SCAN [Fur+20a; Fur+20b] (or the LAK [LAK24] functional), can be constructed to be self-correlation-free, i. e., $E_{\mathrm{c}}^{\mathrm{mGGA}}[n_{i\sigma}] = 0$. Consequently, the correction term of the PZ-SIC scheme for these functionals is reduced to the exchange part of the xc functional and the Hartree term ($E_{\mathrm{H}}[n_{i\sigma}] + E_{\mathrm{x}}[n_{i\sigma}]$). The orbital-dependent Hamiltonian can be derived analogously to the GKS case in Section 4.2.2 by varying the meta-GGA energy expression with respect to the orbitals. For meta-GGAs, written in terms of the parameters $\{s^2_\sigma, \alpha_\sigma\}$ as employed in TASK and r^{2}SCAN (see Appendix A.1), the

orbital-dependent Hamiltonian within the PZ-SIC framework is expressed as

$$\hat{H}^{\tau}_{i\sigma} = -\frac{\hbar^2}{2m}\nabla^2 + v_{\text{ext}}(\mathbf{r}) + v_{\text{H}}[n](\mathbf{r}) + v^{\text{loc}}_{\sigma}[s^2_{\sigma}, \alpha_{\sigma}](\mathbf{r}) + \hat{v}^{\text{GKS}}_{\tau\sigma}[s^2_{\sigma}, \alpha_{\sigma}](\mathbf{r}) - \left(v_{\text{H}}[n_{i\sigma}](\mathbf{r}) + v^{\text{loc}}_{\sigma}[s^2_{i\sigma}, \alpha = 0](\mathbf{r}) + \hat{v}^{\text{GKS}}_{\tau\sigma}[s^2_{i\sigma}, \alpha = 0](\mathbf{r})\right), \quad (6.17)$$

where

$$s_{i\sigma}(\mathbf{r}) = \frac{|\nabla n_{i\sigma}(\mathbf{r})|}{2(3\pi^2)^{1/3} n^{4/3}_{i\sigma}(\mathbf{r})} \quad (6.18)$$

is the reduced gradient density evaluated at the orbital density $n_{i\sigma}$, and the iso-orbital indicator α is defined in Eq. (4.7). The terms v^{loc}_{σ} and $\hat{v}^{\text{GKS}}_{\tau\sigma}$ denote the multiplicative and operator components of the meta-GGA potential, as defined in Eq. (4.25) and Eq. (4.26), respectively. However, evaluating the TASK and r^{2}SCAN meta-GGA expressions at orbital densities with $\alpha = 0$ instead of ground-state densities introduces numerical challenges. These issues, which can significantly affect the stability of our PZ-SIC ground-state calculations, are discussed in detail in Section 7.2.1.

Additionally, the use of meta-GGA functionals within the ground-state PZ-SIC framework introduces an important subtlety: since Eq. (6.9a) does not correspond to an eigenvalue equation, the resulting orbitals are generally complex-valued. This property can result in a gauge variance of the kinetic energy density and a violation of the continuity equation, analogous to the challenges observed in the TDGKS framework. As in the TDGKS case, these issues can be addressed by replacing the kinetic energy density τ with the gauge-invariant formulation

$$\hat{\tau}(\mathbf{r}) = \tau(\mathbf{r}) - m\frac{|\mathbf{j}_{\text{p}}(\mathbf{r})|^2}{2n(\mathbf{r})}, \quad (6.19)$$

where $\mathbf{j}_{\text{p}}(\mathbf{r})$ is the paramagnetic current density. The full expression for the orbital-dependent Hamiltonian incorporating the current-density correction for meta-GGAs is provided in Appendix B.2.

6.5 PZ-SIC Expressions for Non-Integer Particle Numbers

So far, we have only discussed the PZ-SIC ground-state equations for systems with an integer number of electrons. To investigate the delocalization error of various xc approximations within the PZ-SIC framework, we aim to compute the $E(N)$ curve for different functionals and evaluate the extent to which the straight-line condition is satisfied, similar to Fig. 6.1. However, extending the PZ-SIC formalism to non-integer particle numbers is less straightforward than in the KS scheme due to the unitary variance inherent to the PZ-SIC.

Similar to the extension of the KS theory to systems with non-integer electron numbers [Per+82], we introduce an occupation number $f_{i\sigma}$ for each orbital. The total charge density is then expressed as

$$n(\mathbf{r}) = \sum_{\sigma=\uparrow,\downarrow}\sum_{i=1}^{N_\sigma} n_{i\sigma}(\mathbf{r}) = \sum_{\sigma=\uparrow,\downarrow}\sum_{i=1}^{N_\sigma} f_{i\sigma}|\varphi_{i\sigma}(\mathbf{r})|^2, \quad (6.20)$$

where the orbital density is given by $n_{i\sigma} = f_{i\sigma}|\varphi_{i\sigma}|^2$. Using these definitions for n and $n_{i\sigma}$ to evaluate the PZ-SIC energy functional E^{SIC}, the variation of the energy functional

$S[\{\varphi_{i\sigma}\}]$ of Eq. (6.8) with respect to $\varphi^*_{i\sigma}$ leads to

$$f_{i\sigma}\hat{H}_{i\sigma}\varphi_{i\sigma}(\mathbf{r}) = \sum_{j=1}^{N_\sigma} \lambda_{ji\sigma}\varphi_{j\sigma}(\mathbf{r}) \quad \text{with} \tag{6.21a}$$

$$\boldsymbol{\lambda}_\sigma = \boldsymbol{\lambda}_\sigma^\dagger, \tag{6.21b}$$

where $\hat{H}_{i\sigma}$ depends on the modified expressions for the density and orbital density while N_σ is the number of orbitals with $f_{i\sigma} > 0$. By projecting Eq. (6.21a) onto a single orbital, we obtain the Lagrange multiplier as

$$\lambda_{ji\sigma} = \langle \varphi_{j\sigma} | f_{i\sigma}\hat{H}_{i\sigma} | \varphi_{i\sigma} \rangle \,. \tag{6.22}$$

However, applying the unitary transformation that minimizes the PZ-SIC energy functional to a set of orbitals with a non-integer number of electrons introduces a unique challenge not encountered within the KS formalism. In KS theory, handling occupation numbers is straightforward: the occupation numbers $\{f_{i\sigma}\}$ are determined according to the Aufbau principle, resulting in fully occupied orbitals up to the HOMO-1, with only the HOMO being fractionally occupied. This procedure establishes a direct relationship between the occupation numbers and the set of KS orbitals. Within the PZ-SIC formalism, however, two key challenges arise when attempting to apply the Aufbau principle, both of which are addressed in the following sections: (1) Since the PZ-SIC ground state equation (6.21a) is not an eigenvalue equation and therefore lacks eigenvalues, no quantity can be directly interpreted as an orbital energy. This raises the question: Is there a quantity within the PZ-SIC formalism that can be interpreted as single-particle energies analogous to the KS eigenvalues? (2) How do the occupation numbers of a set of orbitals change when a unitary transformation is applied, which, simply put, generates the new orbitals by mixing (and/or rotating) the old orbitals (see Eq. (6.4))?

6.6 Orbital Energies in PZ-SIC

In KS theory, the physical interpretation of the KS eigenvalues as ionization energies is justified by Janak's theorem [Jan78]

$$\frac{\partial E}{\partial f_{i\sigma}} = \epsilon_{i\sigma} \,, \tag{6.23}$$

where the derivative of the ground-state energy with respect to the occupation number $f_{i\sigma}$ exactly yields the KS eigenvalue $\epsilon_{i\sigma}$. As discussed in Section 3.4, this relation can be used to show that the HOMO eigenvalue in KS theory is equal to the negative of the IP, i. e., $\epsilon_{\text{HOMO}} = -\text{IP}$ which is commonly referred to as the IP theorem in DFT.

In order to find an expression for the localized orbital energies within the PZ-SIC formalism that is equivalent to the KS eigenvalues, we can extend Janak's theorem by calculating the derivative of the energy expression E^{SIC} with respect to the occupation

number $f_{i\sigma}$:

$$\begin{aligned}\frac{\partial E^{\mathrm{SIC}}}{\partial f_{i\sigma}} =& \frac{\partial}{\partial f_{i\sigma}}\left[-\frac{\hbar^2}{2m}\sum_{\sigma'=\uparrow,\downarrow}\sum_{k=1}^{N_{\sigma'}} f_{k\sigma'}\int \varphi^*_{k\sigma'}(\mathbf{r})\nabla^2\varphi_{k\sigma'}(\mathbf{r})\,\mathrm{d}^3r\right] \\ &+ \int \frac{\delta}{\delta n_\sigma}\left\{E_{\mathrm{H}}[n] + E_{\mathrm{xc}}[n_\uparrow, n_\downarrow] + \int v_{\mathrm{ext}}(\mathbf{r}')n(\mathbf{r}')\,\mathrm{d}^3r'\right\}\frac{\partial n_\sigma}{\partial f_{i\sigma}}\,\mathrm{d}^3r \\ &- \sum_{\sigma'=\uparrow,\downarrow}\sum_{j=1}^{N_{\sigma'}}\int \frac{\delta}{\delta n_{j\sigma}}\left\{E_{\mathrm{H}}[n_{j\sigma'}] + E_{\mathrm{xc}}[n_{j\sigma'}, 0]\right\}\frac{\partial n_{j\sigma}}{\partial f_{i\sigma}}\,\mathrm{d}^3r \qquad (6.24) \\ =& -\frac{\hbar^2}{2m}\langle\varphi_{i\sigma}|\nabla^2|\varphi_{i\sigma}\rangle + \langle\varphi_{i\sigma}|v_{\mathrm{H}}[n] + v_{\mathrm{xc}}[n_\uparrow, n_\downarrow] + v_{\mathrm{ext}}|\varphi_{i\sigma}\rangle \\ &- \langle\varphi_{i\sigma}|v_{\mathrm{H}}[n_{i\sigma}] + v_{\mathrm{xc}}[n_{i\sigma}, 0]|\varphi_{i\sigma}\rangle \\ =& \langle\varphi_{i\sigma}|\hat{H}_{i\sigma}|\varphi_{i\sigma}\rangle = \frac{\lambda_{ii\sigma}}{f_{i\sigma}} =: \lambda'_{ii\sigma}\,.\end{aligned}$$

This implies that the diagonal elements, $\lambda'_{ii\sigma} = \langle\varphi_{i\sigma}|\hat{H}_{i\sigma}|\varphi_{i\sigma}\rangle$, can be interpreted as orbital energies, as first pointed out by Vydrov *et al.* [VSP07]. Due to this physical interpretation, and because the PZ-SIC energy expression can be rewritten in a form that explicitly includes the sum over the diagonal elements of the Lagrange multiplier $\lambda'_{ii\sigma}$, as shown in Appendix B.4, the PZ-SIC energy functional is minimized by occupying the localized orbitals in ascending order of $\lambda'_{ii\sigma}$, with only the HOMO being fractionally occupied ($0 < f_{\mathrm{HOMO}} \leq 1$). As a consequence, the IP theorem within the PZ-SIC framework takes the form

$$\lambda'_{\mathrm{HOMO\,HOMO}} = \frac{\lambda_{\mathrm{HOMO\,HOMO}}}{f_{\mathrm{HOMO}}} = -\mathrm{IP}\,. \qquad (6.25)$$

However, this result may appear contradictory if the PZ-SIC energy functional E^{SIC} in S of Eq. (6.8) is replaced by a unitary-invariant expression, such as the conventional KS energy E_{KS}. Any unitary transformation can then be applied without changing the energy, making the diagonal elements of $\boldsymbol{\lambda}_\sigma$ arbitrary. In that case, how can these diagonal elements have a physical interpretation? In Appendix B.5, we resolve this apparent contradiction by demonstrating that the Hermiticity condition ensures that the largest diagonal element of $\boldsymbol{\lambda}_\sigma$ is equivalent to the KS HOMO eigenvalue.

We close this section with an additional remark: Historically [GU97; VS05; PHL85], the eigenvalues of the Lagrange multiplier $\boldsymbol{\lambda}_\sigma$, commonly referred to as the canonical eigenvalues $\{\epsilon^{\mathrm{can}}_{i\sigma}\}$, have been frequently used as the PZ-SIC equivalent to the KS eigenvalues. These canonical eigenvalues can be computed by

$$\epsilon^{\mathrm{can}}_{i\sigma}\delta_{ij} = \left(\mathbf{W}^\dagger_\sigma\boldsymbol{\lambda}_\sigma\mathbf{W}_\sigma\right)_{ij}\,, \qquad (6.26)$$

with the unitary matrix $\mathbf{W}_\sigma$ consisting of the eigenvectors of $\boldsymbol{\lambda}_\sigma$. The interpretation of $\{\epsilon^{\mathrm{can}}_{i\sigma}\}$ as the orbital energies, analogous to the KS eigenvalues, stems from the fact that the PZ-SIC ground-state equation can be transformed using the so-called canonical orbitals,

$$\psi^{\mathrm{can}}_{i\sigma}(\mathbf{r}) = \sum_{k=1}^{N_\sigma} W^*_{ki\sigma}\varphi_{k\sigma}(\mathbf{r})\,, \qquad (6.27)$$

into an eigenvalue equation similar to the KS equation. This takes the form

$$\hat{H}_\sigma^{\text{can}}\psi_{i\sigma}^{\text{can}}(\mathbf{r}) = \epsilon_{i\sigma}^{\text{can}}\psi_{i\sigma}^{\text{can}}(\mathbf{r}) \tag{6.28}$$

with the (*not* orbital-dependent) Hamiltonian [Mes+09; KKJ11]

$$\hat{H}_\sigma^{\text{can}} = -\frac{\hbar^2}{2m}\nabla^2 + v_{\text{ext}}(\mathbf{r}) + v_{\text{H}}[n](\mathbf{r}) + v_{\text{xc}}[n_\uparrow, n_\downarrow](\mathbf{r}) \\ - \sum_{i=1}^{N_\sigma}(v_{\text{H}}[n_{i\sigma}](\mathbf{r}) + v_{\text{xc}}[n_{i\sigma}, 0](\mathbf{r}))|\varphi_{i\sigma}\rangle\langle\varphi_{i\sigma}|\,. \tag{6.29}$$

Solving the eigenvalue equation (6.28) yields the canonic orbitals $\{\psi_{i\sigma}^{\text{can}}\}$. However, since these canonic orbitals do not minimize the PZ-SIC energy functional of Eq. (6.3), the corresponding canonic eigenvalues do *not* have the physical interpretation of orbital energies.

6.7 Unitary Transformation with Fractional Occupation Number

In the KS formalism, a direct connection between the occupation numbers $\{f_{i\sigma}\}$ and the orbitals $\{\varphi_{i\sigma}\}$ is maintained by following the Aufbau principle after solving the KS equations. However, within the PZ-SIC formalism, this connection is broken by applying the energy-minimizing unitary transformation, which involves mixing (and/or rotating) all occupied orbitals $\{\varphi_{i\sigma}\}$ to obtain the new set $\{\varphi'_{i\sigma}\}$. This raises the question of how to update the occupation numbers $\{f_{i\sigma}\}$ of the original set of orbitals to $\{f'_{i\sigma}\}$ after applying the unitary transformation. To address this, we transform the normalized orbitals by using Eq. (6.4) while keeping the occupation numbers fixed, i. e., $f'_{i\sigma} \equiv f_{i\sigma}$. Varying the SIC energy expression in Eq. (6.3) with respect to the unitary transformation defined in Eq. (6.4), as part of the inner-loop minimization, results in the gradient

$$G_{ij\sigma} = \left.\frac{\partial E^{\text{SIC}}}{\partial U_{ij\sigma}^*}\right|_{U_{ij\sigma}^*=\delta_{ij}} = \int \varphi_{j\sigma}^*(\mathbf{r})\left[f_{i\sigma}\hat{H}_{i\sigma} - f_{j\sigma}\hat{H}_{j\sigma}\right]\varphi_{i\sigma}(\mathbf{r})\,\mathrm{d}^3r\,. \tag{6.30}$$

Unlike the gradient expression in Eq. (6.15), this formulation explicitly incorporates the occupation numbers $f_{i\sigma}$ and $f_{j\sigma}$. A detailed derivation of $G_{ij\sigma}$ is provided in Appendix B.3. As in the case of integer electron numbers, the condition $G_{ij\sigma} = 0$ enforces the hermiticity of the newly defined Lagrange multiplier $\boldsymbol{\lambda}_\sigma$ in Eq. (6.22). However, in contrast to the PZ-SIC formulation with an integer number of electrons, the unitary transformation of the normalized orbitals can lead to a change in the electron density. Specifically, the density before the unitary transformation, given by $\sum_{\sigma=\uparrow,\downarrow}\sum_{i=1}^{N_\sigma} f_{i\sigma}|\varphi_{i\sigma}|^2$, may differ from the density after the transformation, given by $\sum_{\sigma=\uparrow,\downarrow}\sum_{i=1}^{N_\sigma} f_{i\sigma}|\varphi'_{i\sigma}|^2$. Therefore, the electron density must be recalculated after applying the unitary transformation.

In order to ensure the energy-minimizing occupation of the orbitals during our PZ-SIC ground-state calculation, both the electron density and the Lagrange multiplier $\boldsymbol{\lambda}_\sigma$ are updated throughout the algorithm. Specifically, after each damped gradient step in the outer loop and the application of the energy-minimizing unitary transformation, the diagonal elements of $\boldsymbol{\lambda}_\sigma$, $\lambda_{ii\sigma}$, are recalculated. The occupation numbers are then

assigned in ascending order of the orbital energies, corresponding to $\lambda'_{ii\sigma} = \lambda_{ii\sigma}/f_{i\sigma}$. The details of our algorithm are described in the following section.

However, one might consider an alternative approach to address the challenge of transforming the occupation numbers from $\{f_{i\sigma}\}$ to $\{f'_{i\sigma}\}$ by directly transforming the occupation numbers along to their corresponding orbitals. This can be achieved by redefining the unitary transformation as

$$\sqrt{f'_{i\sigma}}\varphi'_{i\sigma}(\mathbf{r}) = \sum_{j=1}^{N_\sigma} U_{ij\sigma}\sqrt{f_{j\sigma}}\varphi_{j\sigma}(\mathbf{r})\,. \tag{6.31}$$

While it is straightforward to show that the density calculated via Eq. (6.20) using $\{\varphi'_{i\sigma}\}$ with $\{f'_{i\sigma}\}$ preserves the density spanned by $\{\varphi_{i\sigma}\}$ with $\{f_{i\sigma}\}$, the transformed orbitals are not necessarily orthogonal within the spin channel containing the fractionally occupied HOMO, this can be seen as follows:

$$\begin{aligned}
\langle\sqrt{f'_{i\sigma}}\varphi'_{i\sigma}|\sqrt{f'_{j\sigma}}\varphi'_{j\sigma}\rangle &= \sum_{k,l=1}^{N_\sigma} U^*_{ik\sigma}U_{jl\sigma}\sqrt{f_{k\sigma}f_{l\sigma}}\underbrace{\int \varphi^*_{k\sigma}(\mathbf{r})\varphi_{l\sigma}(\mathbf{r})\,\mathrm{d}^3r}_{=\delta_{kl}} = \sum_{k=1}^{N_\sigma} U^*_{ik\sigma}U_{jk\sigma}f_{k\sigma} \\
&= \underbrace{\sum_{k=1}^{N_\sigma} U^*_{ik\sigma}U_{jk\sigma}}_{=\delta_{ij}} + (f_{\mathrm{HOMO}}-1)U^*_{i\mathrm{HOMO}\sigma}U_{j\mathrm{HOMO}\sigma} \\
&= \delta_{ij} + (f_{\mathrm{HOMO}}-1)U^*_{i\mathrm{HOMO}\sigma}U_{j\mathrm{HOMO}\sigma} \neq \delta_{ij}\sqrt{f_{i\sigma}f_{j\sigma}}\,.
\end{aligned} \tag{6.32}$$

Moreover, the transformation of the occupation numbers in Eq. (6.31) would result in the fractional occupation of multiple orbitals, which contradicts the principle of minimizing the energy by ensuring that only the highest-energy orbital (HOMO) is fractionally occupied, as discussed in Section 6.6. Given these shortcomings concerning orthogonality and the violation of the principle that only the HOMO is fractionally occupied (discussed in detail in Appendix B.6), we discard this approach.

6.8 Algorithm for Minimizing the PZ-SIC Energy

The following section presents the algorithm steps for calculating the PZ-SIC ground state. As previously mentioned, the algorithm consists of two steps: an outer loop that minimizes the PZ-SIC energy functional S defined in Eq. (6.8) with respect to the orbitals,

$$\min_{\{\varphi_{i\sigma}(\mathbf{r})\}\to n(\mathbf{r})} S[\{\varphi_{i\sigma}\}]\,, \tag{6.33}$$

and an inner loop that optimizes the PZ-SIC energy with respect to the unitary transformation,

$$\min_{\mathbf{U}_\sigma} S[\{\varphi_{i\sigma}\}] = \min_{\mathbf{U}_\sigma} E^{\mathrm{SIC}}[\{\varphi_{i\sigma}\}]\,. \tag{6.34}$$

A quick overview of the whole algorithm as a simplified flow chart is given in Fig. 6.3.

The detailed steps of the algorithm, including both the outer and inner loop, will be described in the following. The occupation numbers $\{f_{i\sigma}\}$ are explicitly included in all equations of both loops. For a ground-state calculation with an integer particle number, the condition $f_{i\sigma} = 1$ holds for all $i \in \{1,\ldots,N_\sigma\}$.

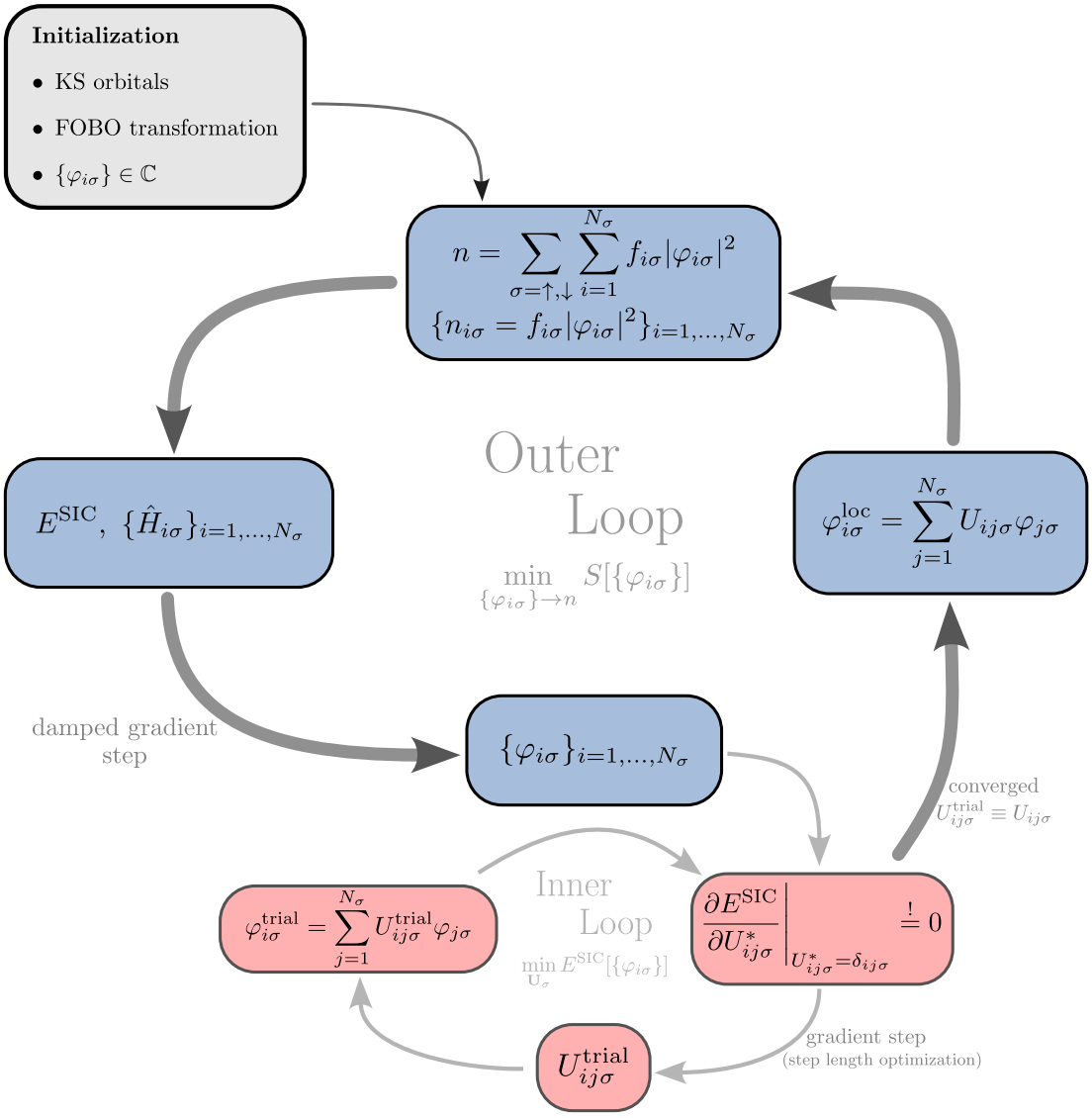

Figure 6.3: Schematic illustration of the PZ-SIC algorithm. The algorithm is initialized with a standard KS calculation. The outer loop optimizes the PZ-SIC energy with respect to the orbitals by damped gradient steps. The inner loop finds the optimal unitary transformations for the PZ-SIC energy functional. Subsequently, this optimal unitary transformation is applied to obtain the localized orbitals $\{\varphi^{\mathrm{loc}}_{i\sigma}\}$.

6.8.1 Outer Loop: Orbital Variation Algorithm

The variation of the energy functional S with respect to the orbital $\varphi^*_{i\sigma}$ leads to the ground-state equations in Eq. (6.21). In the following, we use the notation

$$\lambda'_{ji\sigma} = \langle \varphi_{j\sigma} | \hat{H}_{i\sigma} | \varphi_{i\sigma} \rangle \tag{6.35}$$

and

$$\lambda_{ji\sigma} = \langle \varphi_{j\sigma} | f_{i\sigma} \hat{H}_{i\sigma} | \varphi_{i\sigma} \rangle \,, \tag{6.36}$$

where $\lambda_{ji\sigma} = f_{i\sigma} \lambda'_{ji\sigma}$. The steps marked with * are specifically required for calculating the ground state of a system with a non-integer electron number.

Initialization

1. In order to improve the convergence of the algorithm for determining the PZ-SIC ground state, the KS ground state of the underlying xc functional (without the PZ-SIC) is first obtained self-consistently through a standard DFT calculation by solving the KS equations

$$\left(-\frac{\hbar^2}{2m} \nabla^2 + v_{\text{ext}}(\mathbf{r}) + v_{\text{H}}[n](\mathbf{r}) + v_{\text{xc}}[n_\uparrow, n_\downarrow](\mathbf{r}) \right) \tilde{\varphi}^{(0)}_{i\sigma}(\mathbf{r}) = \epsilon_{i\sigma} \tilde{\varphi}^{(0)}_{i\sigma}(\mathbf{r}) \tag{6.37}$$

   to obtain a set of initial orbitals $\{\tilde{\varphi}^{(0)}_{i\sigma}\} \in \mathbb{R}$ and the corresponding KS eigenvalues $\{\epsilon_{i\sigma}\}$. The initial occupation numbers $\{f^{(0)}_{i\sigma}\}$ are obtained by following the Aufbau principle.

2. Using the simple Foster-Boys (FOBO) localization scheme [Boy60; FB60], which will be described in more detail in the following section, the orbitals are pre-localized and broken in their symmetry to obtain $\{\varphi^{\text{FOBO}}_{i\sigma}\}$. For this purpose, the same algorithm as for finding the energy-minimizing transformation (see Section 6.8.2) is applied using the orbital-specific term [PM89; Mes+11; Hof+12]

$$v^{\text{FOBO}}_{i\sigma}(\mathbf{r}) = \mathbf{r}^2 - 2\mathbf{r} \cdot \langle \tilde{\varphi}^{(0)}_{i\sigma} | \mathbf{r} | \tilde{\varphi}^{(0)}_{i\sigma} \rangle \,. \tag{6.38}$$

3. Multiply the orbitals with a small complex phase

$$\varphi^{(0)}_{i\sigma}(\mathbf{r}) = e^{-\mathrm{i}\epsilon_{i\sigma}} \varphi^{\text{FOBO}}_{i\sigma}(\mathbf{r}) \,, \tag{6.39}$$

   with the eigenvalue $\epsilon_{i\sigma}$ of the KS calculation, to shift them into the complex plane, i. e. $\{\varphi_{i\sigma}\} \in \mathbb{C}$.

4. Calculate the orbital-dependent Hamiltonians $\{\hat{H}_{i\sigma}\}$ of Eq. (6.6) by evaluating the potentials with the density $n^{(0)} = \sum_{\sigma=\uparrow,\downarrow} \sum_{i=1}^{N_\sigma} f^{(0)}_{i\sigma} |\varphi^{(0)}_{i\sigma}|^2$ and the orbital densities $\{n^{(0)}_{i\sigma} = f^{(0)}_{i\sigma} |\varphi^{(0)}_{i\sigma}|^2\}$.

5. Calculate the energy-minimizing transformation using the algorithm described in Section 6.8.2, transform the orbitals $\{\varphi^{(0)}_{i\sigma}\}$ to obtain the corresponding localized orbitals $\{\varphi^{\text{loc}(0)}_{i\sigma}\}$, and use the localized orbitals to recalculate $\{\hat{H}_{i\sigma}\}$.

6. Calculate the matrix elements $\lambda'^{(0)}_{ji\sigma} = \langle \varphi^{\text{loc}(0)}_{j\sigma} | \hat{H}^{(0)}_{i\sigma} | \varphi^{\text{loc}(0)}_{i\sigma} \rangle$.

7.* Assign the occupation numbers in ascending order of $\lambda'^{(0)}_{ii\sigma}$ to obtain $\{f^{\text{loc}(0)}_{i\sigma}\}$.

8. Calculate the error criterion

$$\Delta^{(k)}_{\mathrm{error}\sigma} = \sqrt{\frac{1}{N_\sigma}\sum_{j=1}^{N_\sigma}\left(\frac{\sqrt{\int\left|\hat{H}^{(k)}_{j\sigma}\varphi^{\mathrm{loc}(k+1)}_{j\sigma} - \sum_{l=1}^{N_\sigma}\lambda'^{(k)}_{lj\sigma}\varphi^{\mathrm{loc}(k+1)}_{l\sigma}\right|^2 \mathrm{d}^3r}}{|\epsilon_{\max}| + \sqrt{\int\left|\sum_{l=1}^{N_\sigma}\lambda'^{(k)}_{lj\sigma}\varphi^{\mathrm{loc}(k+1)}_{l\sigma}\right|^2 \mathrm{d}^3r}}\right)^2}. \quad (6.40)$$

where $\epsilon_{\max}$ is the estimated maximum eigenvalue on the grid (described in Appendix B.7) and check if it is under a set threshold (e. g. 1.0×10^{-6}). Alternatively to the error criterion of Eq. (6.40), one could use $|\lambda_{jj\sigma}|$ instead of $\epsilon_{\max}$ as $|\lambda_{jj\sigma}|$ is independent of the grid spacing.

Algorithm Steps

1. Perform a damped gradient step as described in Section 6.3:

   - Update the orbitals:

$$\varphi^{(k+1)}_{i\sigma}(\mathbf{r}) = \varphi^{\mathrm{loc}(k)}_{i\sigma}(\mathbf{r}) - \frac{d^{(k)}}{\hat{t}+e}\left[\hat{H}^{(k)}_{i\sigma}\varphi^{\mathrm{loc}(k)}_{i\sigma}(\mathbf{r}) - \sum_{j=1}^{N_\sigma}\frac{1}{2}\frac{\lambda^{(k)}_{ji\sigma}+\lambda^{*(k)}_{ij\sigma}}{f^{\mathrm{loc}(k)}_{i\sigma}}\varphi^{\mathrm{loc}(k)}_{j\sigma}(\mathbf{r})\right]. \quad (6.41)$$

     $d^{(k)}$ is the step size for which an initial value is chosen, $\hat{t}$ is the kinetic-energy operator, and e is a value that approximately corresponds to the depth of the density-dependent part of the potential. A smaller value of e speeds up convergence but reduces the stability of the iterations.

   - Orthogonalize the orbitals using the Löwdin orthogonalization scheme [Löw50] (for details see Appendix B.8) and then normalize them.[1]
   - Calculate the error criterion $\Delta^{(k+1)}_{\mathrm{error}\sigma}$ using the new orbitals $\{\varphi^{(k+1)}_{i\sigma}\}$.
   - Depending on whether the error criterion has decreased or increased, set a new value for the step size $d^{(k+1)}$. In this work, we chose the following criterion for adjusting d:
     - If $\dfrac{\Delta^{(k+1)}_{\mathrm{error}}}{\Delta^{(k)}_{\mathrm{error}}} < 0.95$: $d^{(k+1)} = 1.05d^{(k)}$.
     - If $\dfrac{\Delta^{(k+1)}_{\mathrm{error}}}{\Delta^{(k)}_{\mathrm{error}}} \geq 1.00$: $d^{(k+1)} = 0.90d^{(k)}$.
     - Otherwise: $d^{(k+1)} = d^{(k)}$,

     with $\Delta_{\mathrm{error}} = \sum_{\sigma=\uparrow,\downarrow}\Delta_{\mathrm{error}\sigma}$. Before the start of the algorithm, a starting value for $d^{(0)}$, an upper limit $d_{\max}$, and a lower limit $d_{\min}$ must be set.

2. Calculate the new density $n^{(k+1)} = \sum_{\sigma=\uparrow,\downarrow}\sum_{i=1}^{N_\sigma} f^{(k)}_{i\sigma}|\varphi^{(k+1)}_{i\sigma}|^2$ and the orbital-dependent Hamiltonians $\{\hat{H}^{(k+1)}_{i\sigma}\}$.

3.* Determine the diagonal elements $\langle\varphi^{(k+1)}_{i\sigma}|\hat{H}^{(k+1)}_{i\sigma}|\varphi^{(k+1)}_{i\sigma}\rangle$ and set the occupation numbers to obtain $\{f^{(k+1)}_{i\sigma}\}$.

[1] Since the search direction of Eq. (6.41) already incorporates the orthogonality constraint, the orthogonalization step is only included for numerical stability.

4. Calculate the energy-minimizing unitary transformation and apply the transformation to $\{\varphi_{i\sigma}^{(k+1)}\}$ to obtain $\{\varphi_{i\sigma}^{\mathrm{loc}(k+1)}\}$ and update $\{\hat{H}_{i\sigma}^{(k+1)}\}$.
5. Calculate the Lagrange multiplier $\lambda_{ji\sigma}^{\prime(k+1)} = \langle\varphi_{j\sigma}^{\mathrm{loc}(k+1)}|\hat{H}_{i\sigma}^{(k+1)}|\varphi_{i\sigma}^{\mathrm{loc}(k+1)}\rangle$.
6.* Set $\{f_{i\sigma}^{\mathrm{loc}(k+1)}\}$ in ascending order to the diagonal elements $\lambda_{ii\sigma}^{\prime(k+1)}$.
7. Check whether the error criterion Δ_{error} is fulfilled (e. g., 1.0×10^{-6}). If not, repeat the algorithm steps until convergence.

6.8.2 Inner Loop: Energy-Minimizing Unitary Transformation

To find the energy-minimizing unitary transformation, we adapt the algorithm developed by Hofmann *et al.* [Hof+12], which employs a conjugate gradient method while directly accounting for the unitary constraint of the transformation. Additionally, this algorithm incorporates a step-length optimization scheme following an idea based on Ref. [AEK09] to enhance computational performance. A detailed description of the quantities involved in this algorithm is provided in Ref. [Hof+12]. The additional steps we introduced, specifically required for calculating the energy-minimizing unitary transformation in systems with non-integer electron numbers, are marked with *.

Initialization

1. Set the number of iterations $k = 0$, the directional derivative of the previous step $H_{ij\sigma}^{(-1)} = 0$, and $\tilde{\varphi}_{i\sigma}^{(0)}(\mathbf{r}) = \sum_{j=1}^{N_\sigma} U_{ij\sigma}^{(0)} \varphi_{j\sigma}(\mathbf{r})$ with $\mathbf{U}_\sigma^{(0)} = \mathbf{I}$ (where $\mathbf{I}$ is the identity matrix).
2. Set a trial step length l^{trial}.

Algorithm Steps

1. Compute:
   - the energy gradient[2] $G_{ij\sigma}^{(k)} = \langle\varphi_{j\sigma}^{(k)}|f_{i\sigma}\hat{H}_{i\sigma}^{(k)} - f_{j\sigma}\hat{H}_{j\sigma}^{(k)}|\varphi_{i\sigma}^{(k)}\rangle$.
   - the search direction $H_{ij\sigma}^{(k)} = G_{ij\sigma}^{(k)} + \gamma^{(k)} H_{ij\sigma}^{(k-1)}$ with $\gamma_\sigma^{(k)} = \frac{\langle \mathbf{G}_\sigma^{(k)} - \mathbf{G}_\sigma^{(k-1)}, \mathbf{G}_\sigma^{(k)} \rangle}{\langle \mathbf{G}_\sigma^{(k-1)}, \mathbf{G}_\sigma^{(k-1)} \rangle}$, where the brackets are defined as $\langle \mathbf{X}, \mathbf{Y} \rangle = \frac{1}{2} \mathrm{Re}\{\mathrm{Tr}(\mathbf{X}\mathbf{Y}^\dagger)\}$, $\mathbf{X}, \mathbf{Y} \in \mathbb{C}^{n \times n}$.
   - the derivative of the SIC energy with respect to the step size l_σ (evaluated at $l_\sigma = 0$) $m_\sigma^{(k)}(0) = -2\langle \mathbf{H}_\sigma^{(k)}, \mathbf{G}_\sigma^{(k)} \rangle$.
2. Determine $\mathbf{M}_\sigma^{(k)}$ and $D_{om\sigma}^{(k)} = \lambda_{m\sigma}^{(k)} \delta_{om}$ from the diagonalization of $-i\mathbf{H}_\sigma^{(k)} = \mathbf{M}_\sigma^{(k)\dagger} \mathbf{D}_\sigma^{(k)} \mathbf{M}_\sigma^{(k)}$. Here, $\{\lambda_{m\sigma}^{(k)}\}$ are the eigenvalues of $-i\mathbf{H}_\sigma^{(k)}$.
3. Perform a trial step (for the step length optimization) with the step length l^{trial} and compute:
   - $U_{ij\sigma}^{\mathrm{trial}} = \sum_{n,m=1}^{N_\sigma} M_{mi\sigma}^{*(k)} \exp\{-\mathrm{i} l^{\mathrm{trial}} \lambda_{m\sigma}^{(k)}\} M_{mn\sigma}^{(k)} U_{nj\sigma}^{(k)}$
   - $\tilde{\varphi}_{i\sigma}^{\mathrm{trial}}(\mathbf{r}) = \sum_{j=1}^{N_\sigma} U_{ij\sigma}^{\mathrm{trial}} \varphi_{j\sigma}(\mathbf{r})$ and $\{v^{\mathrm{SI\ trial}}[n_{i\sigma}](\mathbf{r})\}$
   - * $\tilde{n}^{\mathrm{trial}}(\mathbf{r}) = \sum_{\sigma=\uparrow,\downarrow} \sum_{i=1}^{N_\sigma} f_{i\sigma} |\tilde{\varphi}_{i\sigma}^{\mathrm{trial}}(\mathbf{r})|^2$ and thus completely $\{\hat{H}_{i\sigma}^{\mathrm{trial}}\}$
   - $G_{ij\sigma}^{\mathrm{trial}} = \langle\tilde{\varphi}_{j\sigma}^{\mathrm{trial}}|f_{i\sigma}\hat{H}_{i\sigma}^{\mathrm{trial}} - f_{j\sigma}\hat{H}_{j\sigma}^{\mathrm{trial}}|\tilde{\varphi}_{i\sigma}^{\mathrm{trial}}\rangle$

[2] For integer particle number the gradient $G_{ij\sigma}^{(k)}$ reduces to $G_{ij\sigma}^{(k)} = \langle\varphi_{j\sigma}^{(k)}|v^{\mathrm{SI}(k)}[n_{i\sigma}] - v^{\mathrm{SI}(k)}[n_{j\sigma}]|\varphi_{i\sigma}^{(k)}\rangle$.

- $m_\sigma^{(k)}(l^{\text{trial}}) = -2\langle \mathbf{H}_\sigma^{(k)}, \mathbf{G}_\sigma^{\text{trial}} \rangle$
- $l_\sigma^{\text{opt}(k)} = \frac{-m_\sigma^{(k)}(0) l^{\text{trial}}}{m^{(k)}(l^{\text{trial}}) - m_\sigma^{(k)}(0)}$

4. Set the step length according to the cutoff criterion $l_\sigma^{\text{cut}(k)} = \frac{\pi}{2 \max \lambda_{m\sigma}^{(k)}}$:
   If $0 \leq l_\sigma^{\text{opt}(k)} \leq l_\sigma^{\text{cut}(k)}$, then choose $l_\sigma^{(k)} = l_\sigma^{\text{opt}(k)}$. Otherwise, set $l_\sigma^{(k)} = 0.2 l^{\text{cut}(k)}$.
5. Perform a conjugate gradient step with the step size $l^{(k)}$ and compute:
   - $U_{ij\sigma}^{(k+1)} = \sum_{n,m=1}^{N_\sigma} M_{mi\sigma}^{(k)*} \exp\{-\mathrm{i} l_\sigma^{(k)} \lambda_{m\sigma}^{(k)}\} M_{mn\sigma}^{(k)} U_{nj\sigma}^{(k)}$
   - $\tilde{\varphi}_{i\sigma}^{(k+1)}(\mathbf{r}) = \sum_{j=1}^{N_\sigma} U_{ij\sigma}^{(k+1)} \varphi_{j\sigma}(\mathbf{r})$ and $\{v^{\text{SI}(k+1)}[n_{i\sigma}](\mathbf{r})\}$
   - * $\tilde{n}^{(k+1)}(\mathbf{r}) = \sum_{\sigma=\uparrow,\downarrow} \sum_{i=1}^{N_\sigma} f_{i\sigma} |\tilde{\varphi}_{i\sigma}^{(k+1)}(\mathbf{r})|^2$ and thus completely $\{\hat{H}_{i\sigma}^{(k+1)}\}$
6. Check the convergence criterion $\max(\mathbf{G}_\sigma)$. If it is not below a defined threshold, repeat the algorithm until convergence.

FOBO Minimization and Avoidance of Numerical Oscillations

For improved convergence in finding the energy-minimizing unitary transformation after the initial KS ground state calculation (see initialization of the outer loop algorithm), we pre-localize the KS orbitals. This is achieved by calculating the unitary transformation that minimizes the simple FOBO [Boy60; FB60] spatial localization criterion, given by

$$B_\sigma[\{\varphi_{i\sigma}\}] = \sum_{i=1}^{N_\sigma} \left[\langle \varphi_{i\sigma} | \mathbf{r}^2 | \varphi_{i\sigma} \rangle - \langle \varphi_{i\sigma} | \mathbf{r} | \varphi_{i\sigma} \rangle^2 \right] \tag{6.42}$$

for every spin channel σ. Minimizing this criterion with respect to a unitary transformation yields the gradient

$$G_{ij\sigma} = \left. \frac{\partial B_\sigma[\{\varphi_{i\sigma}\}]}{\partial U_{ij\sigma}^*} \right|_{U_{ij\sigma}^* = \delta_{ij}} = \langle \varphi_{j\sigma} | v_{i\sigma}^{\text{FOBO}} - v_{j\sigma}^{\text{FOBO}} | \varphi_{i\sigma} \rangle \,, \tag{6.43}$$

which can be used in the described algorithm, where $v_{i\sigma}^{\text{FOBO}}$ is the orbital-dependent FOBO potential defined in Eq. (6.38) [PM89; Hof+12].

In some cases, oscillations between different states are observed during the algorithm used to calculate the energy-minimizing or FOBO unitary transformation. These oscillations can be observed in the error criterion $\max(\mathbf{G}_\sigma)$. In order to reduce unnecessary iterations, a simple criterion for detecting oscillations is employed. Specifically, the absolute difference between the current error criterion at iteration step k and the error criterion values from the previous ten iterations (i. e., from $k-1$ to $k-11$) is computed, and the minimum of these differences is taken. This value is then divided by the average of the error criterion values from the last ten iterations. The criterion can be written as

$$\mathcal{E}_\sigma^{(k)} = \frac{1}{\frac{1}{10} \sum_{i=k-1}^{k-11} \max\left(\mathbf{G}_\sigma^{(i)}\right)} \min \left[\begin{pmatrix} \left| \max\left(\mathbf{G}_\sigma^{(k-1)}\right) - \max\left(\mathbf{G}_\sigma^{(k)}\right) \right| \\ \vdots \\ \left| \max\left(\mathbf{G}_\sigma^{(k-11)}\right) - \max\left(\mathbf{G}_\sigma^{(k)}\right) \right| \end{pmatrix} \right] . \tag{6.44}$$

If the value of $\mathcal{E}_\sigma^{(k)}$ falls below 10^{-8}, we abort the inner loop minimization algorithm.

Chapter 7

Results for the Perdew-Zunger Self-Interaction Correction

In this chapter, the PZ-SIC [PZ81] is applied in combination with various xc functionals to a small test set. We begin by focusing on the LSDA and the GGA in the form of the PBE functional [PBE96]. To assess the performance of these xc functionals within the PZ-SIC framework, we analyze the delocalization error by studying the total energy curve $E(N)$ as a function of fractional electron numbers.

In addition, we investigate the IP obtained via the ΔSCF approach, defined as $\Delta\text{SCF} = E(N_0 - 1) - E(N_0)$, where N_0 is the number of electrons of the neutral system. We compare these values to the HOMO energy, determined either as the KS eigenvalue in calculations using the uncorrected functional (without using the PZ-SIC) within KS theory, or as the highest occupied diagonal element $\lambda'_{ii\sigma} = \langle\varphi_{i\sigma}|\hat{H}_{i\sigma}|\varphi_{i\sigma}\rangle$ within the PZ-SIC formalism, as described in Section 6.6.

Finally, we extend the application of the PZ-SIC to meta-GGAs and address numerical challenges encountered in calculations performed using our real-space code `BTDFT` [SK18]. To resolve the numerical challenges obtained with the TASK and r^{2}SCAN metaGGAs using the PZ-SIC, we introduce a modified version of the meta-GGA TASK. Subsequently, we present the results for our model systems, calculated using this modified meta-GGA within the PZ-SIC framework.

7.1 Results for LSDA and PBE Using the PZ-SIC

We apply our algorithm described in Section 6.8 for calculating the PZ-SIC ground state for a small test set using the real-space program `BTDFT`, which employs norm-conserving LSDA PPs of the Troullier-Martins type [TM91]. The influence of employing LSDA PPs in LSDA calculations using the PZ-SIC (LSDA-SIC) is not immediately apparent. However, since Goedecker and Umrigar reported only a minor impact from employing consistent LSDA-SIC PPs, we adopt LSDA PPs with the cutoff radii specified in Appendix B.9. For our real-space grid, we used a grid spacing of $0.2\,\mathrm{a_0}$, and its size is enclosed by atomic-centered spheres with radii determined by the point at which the electron density taken from the PPs falls below the threshold of $10^{-7}\,\mathrm{a_0^{-3}}$. Further numerical parameters for the chosen grid, the PPs, and the PZ-SIC ground state algorithm are listed in Appendix B.9.

We begin by applying the PZ-SIC algorithm to the diatomic CO molecule and calculating its energy curve as a function of fractional occupation numbers. To compare our results with the experimental IP reported in Ref. [Hub79], we use the experimental bond length of $2.132\,\mathrm{a_0}$. We apply our algorithm to compute the energy curve for the LSDA and the PBE functional, with and without using the PZ-SIC. The calculations cover electron numbers ranging from the neutral molecule (N_0 electrons) to the positively

charged cation, with fractional occupation numbers varied in steps of 0.05. The resulting curves are shown in Fig. 7.1. The left panel of Fig. 7.1 shows the energy curve between

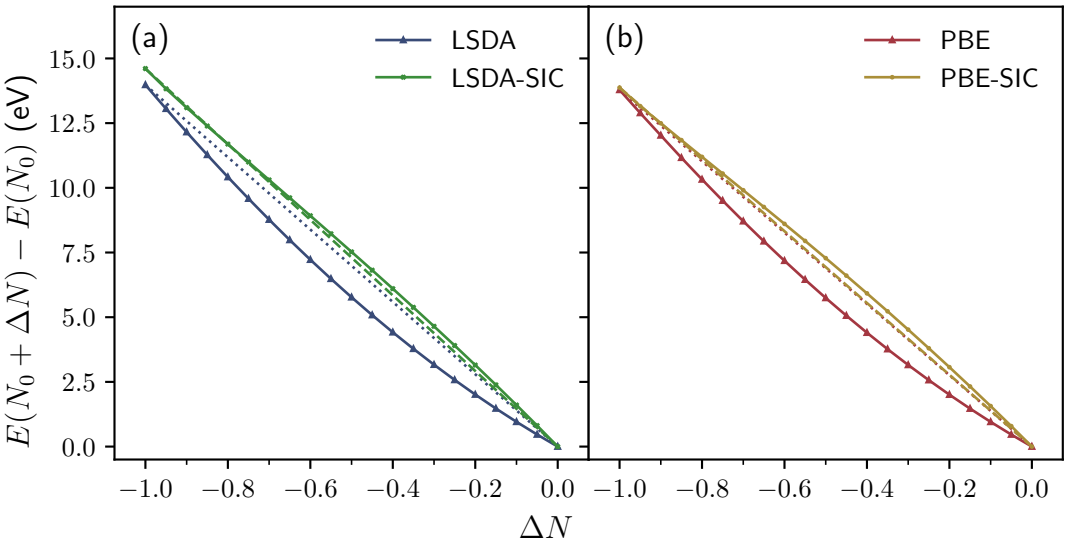

Figure 7.1: Total energy $E(N_0+\Delta N)$ relative to the energy $E(N_0)$ of the neutral CO molecule as a function of the electron number ΔN (difference to neutral CO), calculated with LSDA, LSDA-SIC (left panel), and PBE, PBE-SIC (right panel). The dotted and dashed lines are the straight lines that connect $E(N_0)$ and $E(N_0 - 1)$.

the neutral CO molecule and its cation, calculated using the LSDA with and without the PZ-SIC. The dotted and dashed lines are included to highlight deviations from the exact straight-line connection, representing the linear interpolations between the total energies of the N_0- and $(N_0 - 1)$-electron systems for the respective functionals. The LSDA leads to a strongly convex energy curve with a pronounced deviation from the exact straight-line connection between $E(N_0)$ and $E(N_0 - 1)$ with a nearly quadratic shape. Applying the PZ-SIC reduces this deviation significantly, resulting in a closer approximation to the straight line. However, upon closer inspection, the energy curve shows a slightly concave behavior, indicating an overcorrection. Closer to the positively charged CO^+ molecule, the energy curve shows a change in curvature to a slightly convex curvature. This change in curvature of the energy curves can also be observed in the HOMO energy as a function of the fractional particle number since $\partial E/\partial N = \epsilon_{\text{HOMO}}$ in KS DFT and $\partial E/\partial N = \lambda_{\text{HOMO HOMO}}/f_{\text{HOMO}}$ within the PZ-SIC formalism, as illustrated for all our calculations in Appendix B.14.

The overcorrection observed in the energy curves when employing the PZ-SIC is consistent with our results for the IP, presented in Table 7.1. For the CO molecule,

Table 7.1: IP values for CO calculated as the total energy difference $\Delta\text{SCF} = E(N_0 - 1) - E(N_0)$ and the HOMO eigenvalue of the neutral molecule (in eV). The experimental IP is taken from Ref. [Hub79].

CO	**LSDA**	**LSDA-SIC**	**PBE**	**PBE-SIC**	**Exp. IP**
ΔSCF	13.98	14.61	13.78	13.87	14.01
ϵ_{HOMO}	−9.07	−16.39	−9.06	−16.01	

the IP obtained via the ΔSCF approach, defined as $\Delta\text{SCF} = E(N_0 - 1) - E(N_0)$, is remarkably accurate when calculated with the LSDA, deviating from the experimental value by only 0.03 eV. However, applying the PZ-SIC worsens the agreement, increasing the deviation to 0.60 eV. Despite the accurate ΔSCF result within LSDA, the HOMO eigenvalue, which should match the negative IP value according to the IP theorem, deviates significantly from the experimental value by 4.94 eV. This discrepancy arises from the incorrect asymptotic behavior of the LSDA potential and the spurious SIE, both of which contribute to a pronounced underestimation of the absolute value of ϵ_{HOMO}. With the application of the PZ-SIC, the HOMO energy, given by the diagonal element $\langle\varphi_{\text{HOMO}}|\hat{H}_{\text{HOMO}}|\varphi_{\text{HOMO}}\rangle$ (see Section 6.6), is shifted to lower values. Although this correction reduces the deviation from the experimental value to 2.38 eV, the predicted ϵ_{HOMO} is now overcorrected and becomes too negative. Overall, the description of the IP using the HOMO eigenvalue is significantly less accurate compared to the ΔSCF method.

The energy curve for the CO molecule obtained with the PBE functional, shown in the right panel of Fig. 7.1, exhibits a behavior similar to that of the LSDA result, with a strongly convex shape. While applying the PZ-SIC improves the agreement with the exact piecewise linear behavior of the total energy, the PBE-SIC curve shows a more pronounced concave curvature than the LSDA-SIC result. This suggests that the PBE-SIC approach leads to a stronger overcorrection of the SIE.

Similar to the LSDA, the PBE potential also exhibits deficiencies in describing the IP, leading to a significant underestimation of the experimental IP by the absolute value of the HOMO energy, as shown in Tab. 7.1. Although applying the PZ-SIC improves the HOMO eigenvalue, it overcorrects, overestimating the absolute value of the HOMO eigenvalue by 2.00 eV relative to the experimental reference value. The ΔSCF value for PBE-SIC is closer to the experimental result than that of the uncorrected PBE functional, with a deviation of only 0.14 eV.

The next system under investigation is the single-bonded H_2O molecule, for which we use the structural coordinates provided by the NIST Computational Chemistry Comparison and Benchmark Database [Joh22]. The results for the energy curves $E(N)$ are shown in Fig. 7.2. The results for both the LSDA and PBE functionals exhibit a pronounced convex curvature, which is more pronounced for the H_2O molecule than for the CO molecule. This enhanced delocalization error in H_2O is plausible, as its molecular structure – characterized by hydrogen atoms and single bonds – likely results in a higher fraction of iso-orbital regions. As illustrated in the left panel of Fig. 7.2, the LSDA-SIC curve is considerably closer to the exact straight-line connection between $E(N_0)$ and $E(N_0-1)$ compared to the uncorrected LSDA functional. However, similar to the results for the CO molecule, the LSDA-SIC energy curve is slightly overcorrected, resulting in a concave curvature. Notably, near the positively charged H_2O^+ molecule (around $\Delta N = -0.75$), a change in curvature is observed, resulting in an overall S-shaped energy curve. The PBE-SIC result presented in the right panel of Fig. 7.2 exhibits a slightly stronger deviation from its straight-line connection than LSDA-SIC. Like the LSDA-SIC results, the PBE-SIC energy curve also changes curvature close to the H_2O^+ cation, resulting in an S-shaped energy curve.

The ΔSCF values and the HOMO energies for the H_2O molecule calculated with the different functionals are shown in Tab. 7.2. The ΔSCF value of the uncorrected LSDA functional overestimates the experimental IP by 0.49 eV. Unlike the case of the CO molecule, where the application of the PZ-SIC increased the ΔSCF value for both the LSDA and PBE, the correction for the H_2O molecule reduces the ΔSCF value. This adjustment decreases the error relative to the experimental IP for LSDA-SIC, bringing

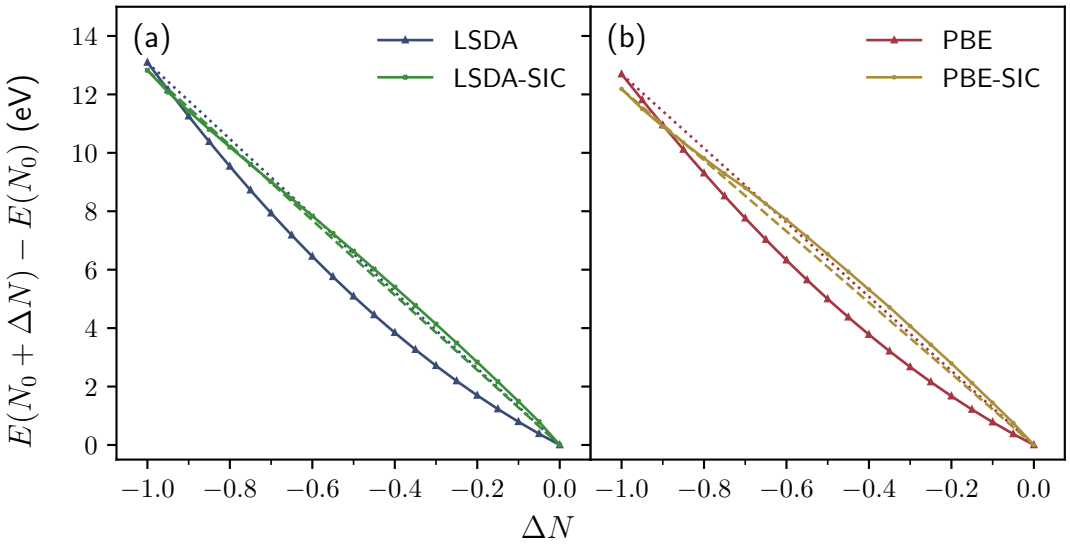

Figure 7.2: Total energy $E(N_0 + \Delta N)$ relative to the energy $E(N_0)$ of the neutral H_2O molecule as a function of the electron number ΔN (difference to neutral H_2O), calculated with LSDA, LSDA-SIC (left panel), and PBE, PBE-SIC (right panel). The dotted and dashed lines are the straight lines that connect $E(N_0)$ and $E(N_0 - 1)$.

Table 7.2: IP values for H_2O calculated as the total energy difference $\Delta\text{SCF} = E(N_0 - 1) - E(N_0)$ and the HOMO eigenvalue of the neutral molecule (in eV). The experimental IP is taken from Ref. [Joh22].

H_2O	LSDA	LSDA-SIC	PBE	PBE-SIC	Exp. IP
ΔSCF	13.09	12.82	12.69	12.19	12.60
ϵ_{HOMO}	−7.39	−17.63	−7.29	−17.05	

it down to 0.22 eV. Similarly, for PBE, the ΔSCF value decreases when the PZ-SIC is applied; however, this reduction leads to a slight increase in the deviation from the experimental IP, from 0.09 to 0.41 eV. For the HOMO eigenvalues, the behavior is consistent with the results observed for the CO molecule. Both the LSDA and PBE significantly underestimate the experimental IP, and applying the PZ-SIC to either functional results in a pronounced overcorrection. This overcorrection only marginally reduces the error relative to the experimental IP.

Finally, we turn to our last model system, the nitrogen molecule N_2, a symmetric system characterized by triple bonds. Because of its molecular symmetry, the binding region is closer to the uniform density limit than that of CO. We adopt a bond length of 2.074 a_0 from Ref. [Hub79] for the following calculations. The energy curves $E(N)$ for the considered functionals are shown in Fig. 7.3. Consistent with our observations for the other model systems, the LSDA and PBE energy curves exhibit a strongly convex behavior. In contrast, the LSDA-SIC curve, shown in the left panel of Fig. 7.3, has almost no curvature. I. e., the straight-line condition between $E(N_0)$ and $E(N_0 - 1)$ is well reproduced, with only minor deviations visible for ΔN values smaller than −0.8. However, a slight overcorrection, leading to a concave shape, is visible for the PBE-SIC curve in the right panel of Fig. 7.3.

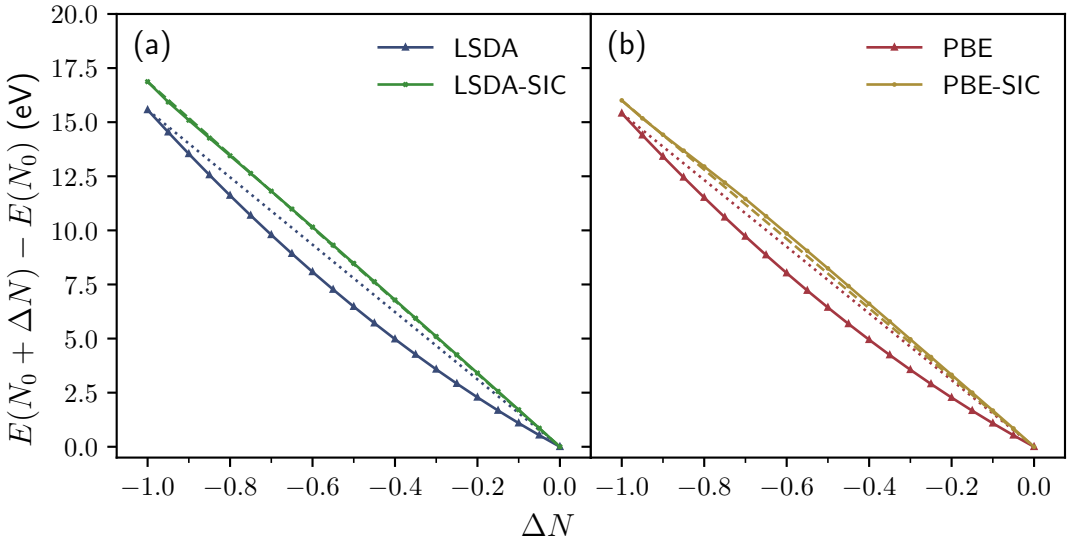

Figure 7.3: Total energy $E(N_0+\Delta N)$ relative to the energy $E(N_0)$ of the neutral N_2 molecule as a function of the electron number ΔN (difference to neutral N_2), calculated with LSDA, LSDA-SIC (left panel), and PBE, PBE-SIC (right panel). The dotted and dashed lines are the straight lines that connect $E(N_0)$ and $E(N_0 - 1)$.

The results for the IP are summarized in Tab. 7.3. Although applying the PZ-SIC

Table 7.3: IP of N_2 calculated as the total energy difference $\Delta\text{SCF} = E(N_0 - 1) - E(N_0)$ and the HOMO eigenvalue of the neutral molecule (in eV). The experimental IP is taken from Ref. [Hub79].

N_2	LSDA	LSDA-SIC	PBE	PBE-SIC	Exp. IP
ΔSCF	15.57	16.87	15.41	16.01	15.58
ϵ_{HOMO}	−10.41	−17.90	−10.37	−18.21	

improves the description of the straight-line condition, the ΔSCF value for LSDA-SIC is less accurate than for the uncorrected LSDA. The uncorrected LSDA ΔSCF value deviates from the experimental IP by only 0.01 eV, while the LSDA-SIC value deviates by 1.29 eV. A similar trend is observed for PBE, where the ΔSCF value for PBE is in closer agreement with the experimental value than that for PBE-SIC. The behavior of the absolute value of the HOMO energy follows the trends observed for the other model systems. The uncorrected LSDA and PBE functionals significantly underestimate the IP, while applying the PZ-SIC leads to severe overcorrections for both LSDA-SIC and PBE-SIC. However, for N_2, the overestimation is somewhat smaller, with deviations of 2.32 eV for LSDA-SIC and 2.63 eV for PBE-SIC, compared to the other systems.

Finally, comparing the results across all test systems, applying the PZ-SIC generally improves the fulfillment of the straight-line condition compared to the uncorrected functionals. However, for CO and H_2O, LSDA-SIC introduces an overcorrection, leading to concave energy curves, whereas, for N_2, it results in only minor deviations from the straight-line condition. Across all systems, PBE-SIC performs worse than LSDA-SIC, exhibiting stronger overcorrections and a more pronounced concave behavior in $E(N)$.

The accuracy of the ΔSCF values compared to the experimental IPs varies: for LSDA, applying the PZ-SIC improves the ΔSCF value for H_2O but worsens it for CO and N_2. For PBE, only the ΔSCF value for CO improves with the PZ-SIC. In all cases, the PZ-SIC significantly overcorrects ϵ_{HOMO}, with the largest deviations observed for H_2O: 5.03 eV for LSDA-SIC and 4.45 eV for PBE-SIC.

7.2 Application of the PZ-SIC to Meta-GGA Functionals

In contrast to the LSDA and GGA functionals, meta-GGAs explicitly depend on the orbitals via the kinetic energy density τ. This orbital dependence enables meta-GGAs to identify iso-orbital regions and enhances their sensitivity to electron localization, thereby reducing SIEs. However, these same properties can introduce numerical challenges when applying the PZ-SIC to the meta-GGA functionals TASK [AK19] and r^{2}SCAN [Fur+20a; Fur+20b]. In the following, we discuss these challenges and a construction principle for meta-GGAs to address them.

7.2.1 Numerical Challenges of Using the PZ-SIC with Meta-GGA Functionals

As an initial numerical test, we apply our PZ-SIC ground-state algorithm using meta-GGAs to our first model system, carbon monoxide (CO). The calculations are performed using the algorithm described in Section 6.8 in combination with the TASK and r^{2}SCAN meta-GGAs (without using the current-density correction). For simplicity, we restrict the calculations to the exchange-only versions of the functionals (denoted by an "x" at the end of the functional name) and to real-valued orbitals. Figure 7.4 presents the error criterion $\Delta^{(k)}_{\mathrm{error}}$ (see Eq. (6.40)) as a function of the iteration step k in the outer-loop minimization. As shown in the figure, the error criterion for the TASKx-SIC

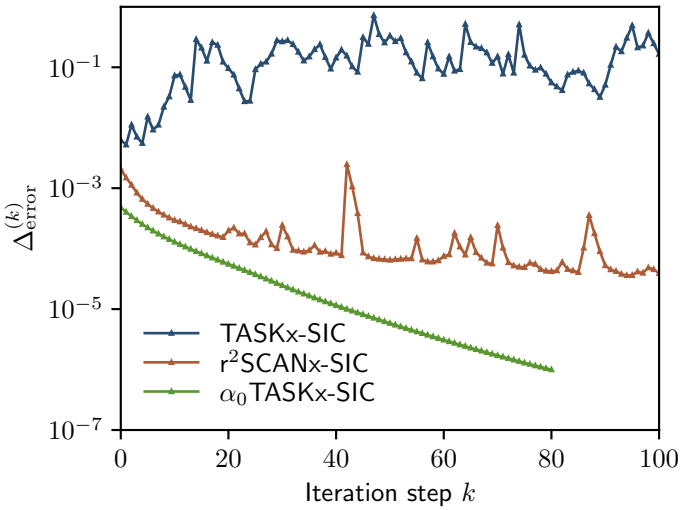

Figure 7.4: Error criterion $\Delta^{(k)}_{\mathrm{error}}$ as a function of damped gradient iteration steps k for TASKx-SIC, r^{2}SCANx-SIC, and α_0TASKx-SIC calculations for CO. The α_0TASKx functional is described at the end of Section 7.2.1.

and r^{2}SCANx-SIC calculations decreases exponentially over several iterations but then experiences an abrupt increase. This oscillatory behavior reoccurs multiple times during

the calculations, hindering the convergence of the PZ-SIC ground-state algorithm. In contrast, for the modified meta-GGA functional, α_0TASK, which will be introduced later, the error criterion decreases exponentially throughout the calculation.

To identify the source of the numerical instability, we examine the individual components of the PZ-SIC potential within the Hamiltonian operator, as defined in Eq. (6.17), during the damped gradient iteration steps on the real-space grid in `BTDFT`. The analysis reveals that oscillatory features appear in the local potential $v^{\mathrm{loc}}[s_{i\sigma}, \alpha = 0]$ of the self-xc potential of the PZ-SIC. These spurious features emerge when the meta-GGA potential is evaluated on the orbital densities. In particular, the spatial regions in which the oscillations occur correspond to those of the nodal planes of the orbital density, as illustrated in Appendix B.10 for the TASKx-SIC calculation of CO. These oscillatory features are particularly noticeable because the local potentials for TASK and r^{2}SCAN, when evaluated on the total electron density, typically exhibit smooth behavior on our real-space grid.

The observed oscillatory features in the local part of the meta-GGA potential, evaluated on orbital densities, are not restricted to the CO molecule; they occur across various systems, leading to instabilities in the PZ-SIC ground-state calculations. To identify the specific characteristics of the local part of the meta-GGA potential that contribute to these numerical challenges, we analyze the behavior of v^{loc} using a simple and transparent model orbital density. Specifically, we utilize the p_z-orbital density adapted from Ref. [AAK17] of the Na_4 cluster, defined as

$$n_p = 2n_p^0 z^2 \exp\left(-\alpha_p \sqrt{x^2 + y^2 + z^2}\right) , \tag{7.1}$$

where $\alpha_p \approx 1.0587$ and $n_p^0 = \alpha_p^5/(32\pi)$. This model orbital density exhibits a dumbbell shape, characterized by a nodal plane at $z = 0$. The local potentials v^{loc}, evaluated with n_p for the TASKx and r^{2}SCANx meta-GGA functionals, are displayed in Fig. 7.5 in the yz-plane at $x = 0$, perpendicular to the nodal plane. For the local potentials of TASKx in panel (a) and r^{2}SCANx in panel (b) of Fig. 7.5, spurious oscillatory features are visible in the region of $z = 0$ which corresponds to the nodal plane of the p-orbital density. These features distort the local potential for both functionals, with more pronounced oscillations visible for the TASKx functional compared to the r^{2}SCAN results. The panel (c) of Fig. 7.5 shows the local potential for the α_0TASKx functional, which will be introduced later in this section.

So far, we have identified that the numerical difficulties in the PZ-SIC calculations arise from the local potential of the TASK or r^{2}SCAN functionals when evaluated on orbital densities with nodal planes. To gain a more precise understanding of which terms in the local potential contribute to the oscillatory features, we will examine the expressions in detail: As shown in Eq. (4.25), the local part of the meta-GGA exchange potential is defined as

$$v^{\mathrm{loc}}(\mathbf{r}) = \frac{\partial e_{\mathrm{x}}^{\mathrm{mGGA}}}{\partial n}(\mathbf{r}) - \nabla \cdot \left[\frac{\partial e_{\mathrm{x}}^{\mathrm{mGGA}}}{\partial \nabla n}(\mathbf{r})\right] . \tag{7.2}$$

With the parametrization of the meta-GGA exchange energy density in terms of s, defined in Eq. (4.3), and $t = \tau/\tau^{\mathrm{unif}}$, we have

$$e_{\mathrm{x}}^{\mathrm{mGGA}}(s(\mathbf{r}), t(\mathbf{r})) = A_{\mathrm{x}} n^{4/3}(\mathbf{r}) F_{\mathrm{x}}(s(\mathbf{r}), t(\mathbf{r})) , \tag{7.3}$$

where $A_{\mathrm{x}} = -(3/4)(3/\pi)^{1/3}$ and F_{x} is the enhancement factor. Using this parametrization, the derivative of the exchange energy density can be expressed in terms of $F_{\mathrm{x}}(s, t)$

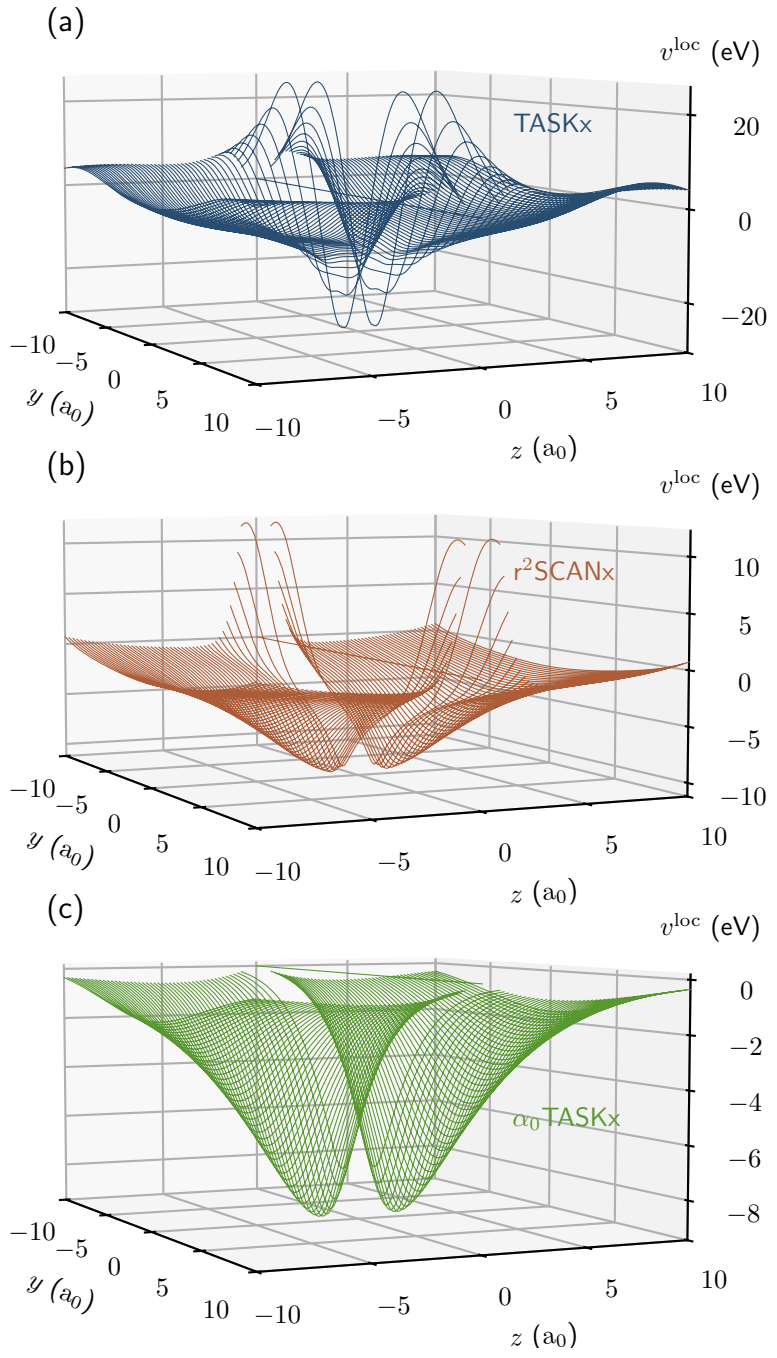

Figure 7.5: Local part of the meta-GGA potential $v^{\mathrm{loc}}[s_p^2, \alpha = 0]$ displayed in the yz-plane at $x = 0$ for TASKx (a), r^{2}SCANx (b), and α_0TASKx (c), evaluated with the orbital density n_p.

as [Asc19]

$$\frac{\partial e_{\mathrm{x}}(s,t)}{\partial n} = A_{\mathrm{x}} n^{1/3} \left[\frac{4}{3} F_{\mathrm{x}}(s,t) - \frac{4}{3} s \left.\frac{\partial F_{\mathrm{x}}}{\partial s}\right|_t - \frac{5}{3} t \left.\frac{\partial F_{\mathrm{x}}}{\partial t}\right|_s \right] . \tag{7.4}$$

Additionally, we can write

$$\begin{aligned} -\nabla \cdot \left[\frac{\partial e_{\mathrm{x}}}{\partial \nabla n}(\mathbf{r}) \right] = -A_{\mathrm{x}} \Bigg[\frac{\nabla\sqrt{n}}{\sqrt{n}} \cdot \nabla \Bigg(\underbrace{\frac{1}{2\gamma^2 n^{1/3}} \frac{1}{s} \left.\frac{\partial F_{\mathrm{x}}}{\partial s}\right|_t}_{=:h_{\mathrm{s}}} \Bigg) \\ + \underbrace{\frac{1}{2\gamma^2 n^{1/3}} \frac{1}{s} \left.\frac{\partial F_{\mathrm{x}}}{\partial s}\right|_t}_{=:h_{\mathrm{s}}} \frac{\nabla^2\sqrt{n}}{\sqrt{n}} - \frac{1}{2} n^{1/3} s \left.\frac{\partial F_{\mathrm{x}}}{\partial s}\right|_t \Bigg] , \end{aligned} \tag{7.5}$$

with $\gamma = (3\pi^2)^{1/3}$. Finally, using the auxiliary functions h_{s} defined in Eq. (7.5), the local potential can be expressed as

$$v^{\mathrm{loc}}(\mathbf{r}) = A_{\mathrm{x}} n^{1/3} \left[\frac{4}{3} F_{\mathrm{x}} - \frac{5}{6} s \left.\frac{\partial F_{\mathrm{x}}}{\partial s}\right|_t - \frac{5}{3} t \left.\frac{\partial F_{\mathrm{x}}}{\partial t}\right|_s \right] - A_{\mathrm{x}} \left[\frac{\nabla^2\sqrt{n}}{\sqrt{n}} h_{\mathrm{s}} + \frac{\nabla\sqrt{n}}{\sqrt{n}} \cdot \nabla h_{\mathrm{s}} \right] . \tag{7.6}$$

For numerical reasons, the density is treated at the same numerical level as the orbitals. This means that n is expressed in terms of $\sqrt{n}$, since in the single-orbital limit (with real-valued orbitals), the relation $\varphi = \pm\sqrt{n}$ holds [Sch+14b; Asc19].

Using the p-orbital density defined in Eq. (7.1), we systematically analyze the individual terms of Eq. (7.6) through the following steps:

1. First, we analyze each term of Eq. (7.6) individually on our real-space grid in the yz-plane at $x = 0$ to identify the origin of the oscillatory features. This analysis reveals that the oscillatory behavior arises from the term

$$\nabla h_{\mathrm{s}} \cdot \frac{\nabla\sqrt{n}}{\sqrt{n}} . \tag{7.7}$$

2. Since the term $\nabla^2\sqrt{n}/\sqrt{n}$, which also appears in Eq. (7.6), does not exhibit any oscillations and has a similar form to $\nabla\sqrt{n}/\sqrt{n}$, we conclude that the latter is not the source of the numerical instability.

3. Having excluded the second term of Eq. (7.7), we turn to the first term, ∇h_{s}. To simplify the analysis and avoid examining the individual components of this vector quantity on the grid, we focus on $|\nabla h_{\mathrm{s}}|^2$. This term is shown in Fig. 7.6 in the yz-plane (with $x = 0$) for the TASKx functional. In this figure, the oscillatory characteristics that appeared in the local potential, shown in panel (a) of Fig. 7.5, are recognizable once again.

4. To further investigate the auxiliary function h_{s}, it must be rewritten as $h_{\mathrm{s}}(s^2, \alpha)$, since the TASK and r^{2}SCAN meta-GGAs are parameterized in terms of $\{s^2, \alpha\}$ rather than $\{s, t\}$. This transformation can be achieved using the relation

$$\frac{1}{2s} \left.\frac{\partial F_{\mathrm{x}}}{\partial s}\right|_t = \left.\frac{\partial F_{\mathrm{x}}}{\partial s^2}\right|_\alpha - \frac{5}{3} \left.\frac{\partial F_{\mathrm{x}}}{\partial \alpha}\right|_{s^2} . \tag{7.8}$$

   Up to this point, the vertical bar next to the derivative indicates the variable that is held constant. In the following, this notation is omitted, and the vertical bar is used only to denote the evaluation of the derivative at a specific point.

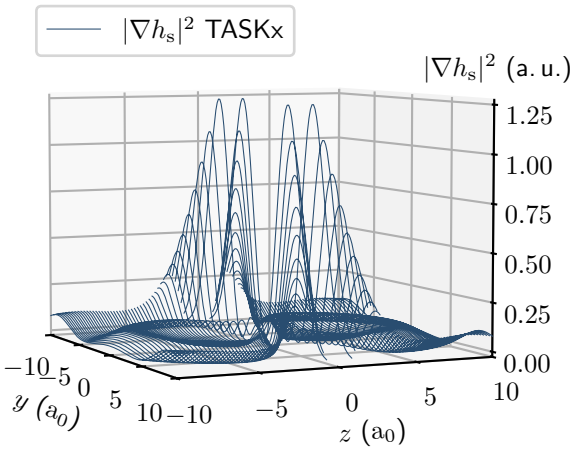

Figure 7.6: $|h_s|^2$ displayed in the yz-plane at $x = 0$ for TASKx evaluated on the orbital density n_p.

When the gradient of the auxiliary function h_s within Eq. (7.6) is evaluated with the orbital density n_p (i. e., $\alpha = 0$), it takes the form

$$\nabla h_s\left(s^2, \alpha = 0\right) = \nabla\left[\frac{1}{2\gamma^2 n^{1/3}}\left(\left.\frac{\partial F_x}{\partial s^2}\right|_{\alpha=0} - \frac{5}{3}\left.\frac{\partial F_x}{\partial \alpha}\right|_{\alpha=0}\right)\right]. \tag{7.9}$$

5. Finally, Eq. (7.9) contains two possible sources for the oscillatory features observed in the local potential depicted in Fig. 7.5: the derivative of the enhancement factor F_x with respect to s^2 and the derivative with respect to α. Notably, the terms $\partial F_x/\partial s^2|_{\alpha=0}$ are identical for the TASKx and r^{2}SCANx meta-GGAs because they share the same limit for $\alpha = 0$, as shown in detail in Appendix B.11. However, Fig. 7.5 reveals a difference in the amplitude of the oscillatory features in the local potential between the TASK functional in panel (a) and the r^{2}SCAN functional in panel (b). This discrepancy suggests that the derivative

$$\left.\frac{\partial F_x}{\partial \alpha}\right|_{\alpha=0} \tag{7.10}$$

is likely responsible for the numerical instabilities.

Based on this observation, we introduce a modified version of the TASK meta-GGA functional, α_0TASK, where the specific form is proposed by Timo Lebeda (Theoretical Physics IV, University of Bayreuth). This modification incorporates the construction principle

$$\left.\frac{\partial F_x}{\partial \alpha}\right|_{\alpha=0} \stackrel{!}{=} 0\,, \tag{7.11}$$

which ensures that the derivative of the enhancement factor with respect to α vanishes at $\alpha = 0$ (see Appendix B.12 for the definition of the enhancement factor). The resulting functional successfully removes the oscillatory features in the local potential, as evident in panel (c) of Fig. 7.5. Additionally, the PZ-SIC ground state for the CO molecule, using complex-valued orbitals, can now be computed straightforwardly (see Fig. 7.4 for the error criterion as a function of iteration steps). These results confirm our assumption

that the derivative in Eq. (7.10) is responsible for the numerical instabilities observed in the PZ-SIC calculations for TASKx and r^{2}SCANx.

The origin of the numerical instability due to the derivative $\partial F_\mathrm{x}/\partial\alpha|_{\alpha=0}$, as well as the differences between the amplitudes of the oscillatory features in the local potential between TASKx and r^{2}SCANx, can be further understood by examining this derivative of the enhancement factor for TASKx and r^{2}SCANx as a function of s, evaluated at $\alpha = 0$. The corresponding plots for both meta-GGAs are shown in Fig. 7.7. This figure

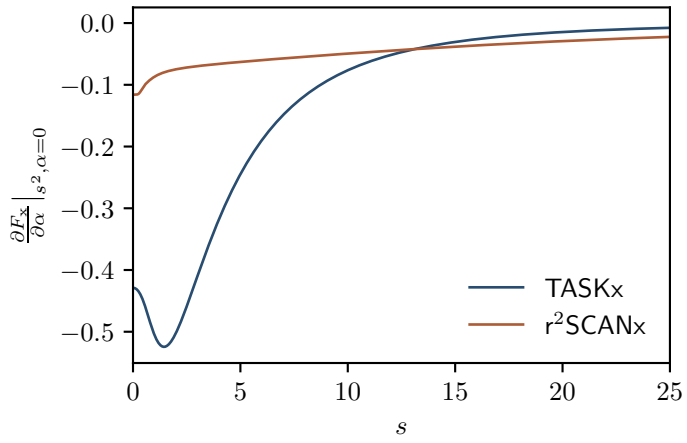

Figure 7.7: Derivative $\partial F_\mathrm{x}/\partial\alpha|_{\alpha=0}$ as a function of s for TASKx and r^{2}SCANx.

illustrates that both functionals exhibit a pronounced slope in $\partial F_\mathrm{x}/\partial\alpha|_{\alpha=0}$. This steep gradient leads to significant changes in the derivative of the enhancement factor, even for minor variations in s. As a result, the local potential v^loc experiences even more pronounced variations because the spatial gradient of $\partial F_\mathrm{x}/\partial\alpha|_{\alpha=0}$, which contributes to v^loc (see Eq. (7.9)), directly amplifies these changes in $\partial F_\mathrm{x}/\partial\alpha|_{\alpha=0}$. The differences in the slopes between TASKx and r^{2}SCANx explain the differing amplitudes of the oscillations observed in their respective local potentials (see Fig. 7.5). Specifically, the steeper slope of TASKx in Fig. 7.7 results in stronger oscillatory features for TASKx compared to r^{2}SCANx.

7.2.2 Results for α_0TASK-SIC

The α_0TASK meta-GGA successfully resolves the numerical instabilities described in the previous section. Details on the impact of modifying the TASK functional to α_0TASK, which shows only minor effects on ground-state observables calculated in GKS, are provided in Appendix B.12. The energy curves $E(N)$, obtained by applying α_0TASK exchange with LSDA correlation to the respective system, both with and without using the PZ-SIC (using $\hat{H}^\tau_{i\sigma}$, see Eq. (6.17)), are shown in Fig. 7.8. For all considered systems, the α_0TASK meta-GGA without the PZ-SIC leads to a convex behavior of the energy curve. Applying the PZ-SIC improves the behavior of $E(N)$ across all model systems, bringing the energy curve closer to the exact linear connection between $E(N_0)$ and $E(N_0 - 1)$. However, as observed in PBE-SIC calculations (see Section 7.1), an overcorrection occurs, leading to predominantly concave energy curves with α_0TASK-SIC. This concave behavior is most pronounced for H_2O, as shown in panel (b) of Fig. 7.8. Like the PBE-SIC energy curve, the α_0TASK curve exhibits a change in curvature around $\Delta N = -0.8$, resulting in an overall S-shaped curve.

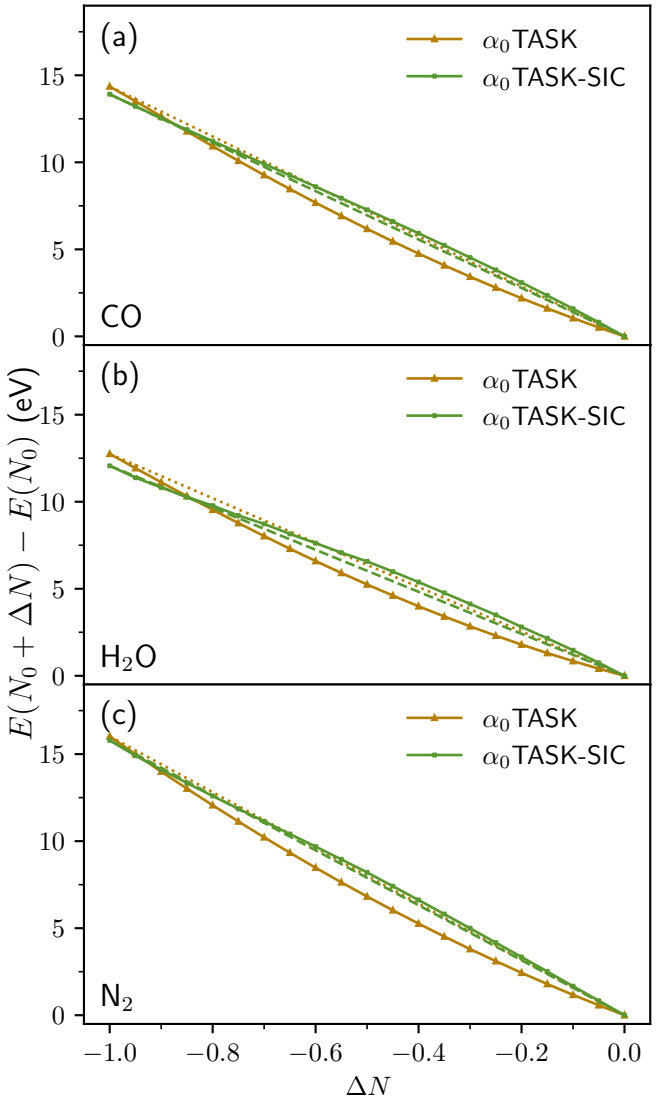

Figure 7.8: Total energy $E(N_0 + \Delta N)$ relative to the energy $E(N_0)$ of the neutral CO (panel (a)), the H_2O (panel (b)), and the N_2 (panel (c)) molecule as a function of the electron number ΔN (difference to neutral CO), calculated with α_0TASK and α_0TASK-SIC. The dotted and dashed lines are the straight lines that connect $E(N_0)$ and $E(N_0 - 1)$.

The results for the IP are presented in Tab. 7.4. The ΔSCF value for CO using α_0TASK-SIC is slightly closer to the experimental value of 14.01 eV than for α_0TASK without the PZ-SIC. The absolute value of the HOMO energy of α_0TASK, which severely

Table 7.4: Calculated IP values for CO, H_2O, and N_2 as the total energy difference $\Delta\text{SCF} = E(N_0 - 1) - E(N_0)$ and the HOMO eigenvalue of the neutral molecule (in eV). The values for the experimental IP are adapted from Section 7.1.

	α_0TASK		**α_0TASK-SIC**		**Exp. IP**
	ΔSCF	ϵ_{HOMO}	ΔSCF	ϵ_{HOMO}	
CO	14.36	−10.01	13.91	−16.51	14.01
H_2O	12.75	−7.93	12.06	−18.13	12.60
N_2	16.02	−11.22	15.79	−18.01	15.58

underestimates the experimental IP by 4.00 eV, becomes overcorrected upon applying the PZ-SIC, resulting in an overestimation of 2.50 eV. This overcorrection is even more pronounced for H_2O: with α_0TASK, the HOMO eigenvalue is underestimated by 4.67 eV, whereas applying the PZ-SIC leads to an overestimation of 5.52 eV compared to the experimental IP. For N_2, the deviation in the HOMO eigenvalue is 4.36 eV for α_0TASK and 2.43 eV for α_0TASK-SIC. While applying the PZ-SIC reduces the deviation, the resulting HOMO energy still differs strongly from the experimental value.

In comparison to the uncorrected LSDA and PBE functionals, the uncorrected α_0TASK meta-GGA systematically shifts the HOMO eigenvalue to lower energies for all three molecular systems considered. This shift reduces the underestimation of the IP as given by the absolute value of the HOMO energy. However, the impact of α_0TASK on the ΔSCF value is less consistent. For CO and N_2, the application of α_0TASK results in a larger deviation from the experimental IP compared to the LSDA and PBE, whereas for H_2O, it provides a slight improvement over the LSDA but remains marginally less accurate than PBE. Upon applying the PZ-SIC, the overcorrection of the HOMO energy is even more pronounced for CO and H_2O with α_0TASK-SIC than with LSDA-SIC or PBE-SIC, while for N_2, the HOMO energy obtained with α_0TASK-SIC lies between the values predicted by LSDA-SIC and PBE-SIC. The impact on the ΔSCF value is similarly system-dependent: α_0TASK-SIC improves the agreement with experiment for CO compared to LSDA-SIC and PBE-SIC but worsens the accuracy for H_2O, while for N_2, it yields an intermediate result between LSDA-SIC and PBE-SIC. Overall, the application of α_0TASK-SIC does not systematically improve the accuracy of the HOMO energy and the ΔSCF value compared to LSDA-SIC and PBE-SIC. Instead, the performance varies across different molecular systems.

As discussed above, the localized orbitals within the PZ-SIC framework are, in general, complex-valued. Consequently, they can carry a current density, which may necessitate the inclusion of the current-density correction of Eq. (6.19) for the kinetic energy density in meta-GGAs. Within the TDGKS framework, this correction can significantly influence physical properties, as shown in Chapter 5. However, no significant impact of the current-density correction is observed in the ground-state PZ-SIC calculations presented in this section. Detailed energy curves for our model systems, including the correction from Eq. (6.19), are provided in Appendix B.13.

7.3 Summary and Conclusion

To summarize, we calculated energy curves for fractional electron numbers using the algorithm described in Section 6.8 with the LSDA and PBE. These functionals were applied to a test set including the CO, H_2O, and N_2 molecules to assess their performance with and without using the PZ-SIC. The uncorrected functionals produced strongly convex energy curves for all model systems. In contrast, applying the PZ-SIC led to an overcorrection, resulting in concave energy curves or, in some cases, an S-shaped behavior. A similar trend was observed for the HOMO eigenvalues: while the LSDA and PBE significantly underestimated the IP, applying the PZ-SIC introduced an overcorrection, yielding overestimated IPs.

A direct application of the PZ-SIC to the meta-GGA functionals TASK and r^{2}SCAN resulted in numerical challenges within our real-space code `BTDFT`. These challenges arise from a stronger sensitivity of meta-GGAs to density variations caused by nodal planes due to their explicit dependence on the density gradient ∇n and the kinetic energy density τ, in contrast to the LSDA. Our results demonstrate that by following a construction principle outlined in Eq. (7.11), one can resolve the numerical issues and can develop meta-GGA functionals, like the introduced meta-GGA α_0TASK, compatible with the PZ-SIC. However, the results obtained with the newly introduced α_0TASK functional using the PZ-SIC exhibit similar trends to those of LSDA-SIC and PBE-SIC, namely, an overcorrection in both the energy curves and the HOMO eigenvalues.

This observation raises new considerations for the use of meta-GGA functionals in combination with the PZ-SIC since one of the design principles of the TASK and r^{2}SCAN meta-GGAs is to reproduce the exact exchange energy of the hydrogen atom in the single-orbital limit. However, applying the PZ-SIC to any xc approximation already ensures the correct description of the hydrogen atom. Consequently, combining the PZ-SIC with meta-GGAs designed to enforce this hydrogen atom norm effectively duplicates efforts to achieve the same physical result. This observation suggests a shift in perspective: instead of applying the PZ-SIC to existing meta-GGA functionals, it may be more beneficial for future work to design meta-GGAs specifically tailored to use the strengths of the PZ-SIC. For such meta-GGAs, the hydrogen atom norm can be relaxed, introducing a new degree of freedom in their development.

Instead of modifying the underlying xc approximation to address the overcorrection observed when applying the PZ-SIC, the following chapter starts with exploring an approach that modifies the PZ-SIC itself to improve the description of the straight-line condition and achieve better agreement with experimental IPs through the HOMO energy.

Chapter 8

Modifications of the Perdew-Zunger Self-Interaction Correction

The influence of the PZ-SIC has been examined in several studies. When applied to the LSDA, it improves the description of transition states in chemical reactions, leading to more accurate reaction barrier heights [PZ02; KKJ12]. It also yields better dissociation curves for odd-electron systems [GKC04b; GKC04a], improves binding energy curves for diatomic molecules, and corrects the erroneous description of the dissociation process in heteronuclear molecules by (semi-)local functionals [Ruz+06].

Despite its success, the PZ-SIC does not consistently improve results and often worsens near-equilibrium properties, a conflicting behavior known as the "Paradox of PZ-SIC" [Per+15]. For instance, LSDA-SIC has been shown to systematically predict bond lengths that are too short [GU97; CJ98; VS04; VS05; Hof+12]. While it yields a moderate improvement in atomization energies compared to the uncorrected LSDA, its accuracy remains inferior to that of GGA and meta-GGA functionals [CP82; PHL84; PHL85]. Additionally, when applied to GGA and meta-GGA functionals, the PZ-SIC frequently leads to less accurate atomization energy predictions than those obtained with the uncorrected functionals [VS04].

In the previous chapter, we investigated the effect of the PZ-SIC on the total energy curve as a function of fractional electron number. While (semi-)local functionals typically exhibit a convex behavior of the energy curve between integer electron numbers, applying the PZ-SIC yields a more linear behavior but tends to overcorrect. For the LSDA and more pronounced for PBE [PBE96] and the introduced meta-GGA functional α_0TASK (a modification of TASK [AK19]), applying the PZ-SIC results in a concave or S-shaped behavior of the total energy curve. A similar trend is observed for the HOMO energy: standard (semi-)local functionals such as the LSDA, PBE, and meta-GGAs (e. g., TASK [AK19] and r^{2}SCAN [Fur+20a; Fur+20b]) systematically underestimate the IP. Although PZ-SIC shifts the HOMO energy downward, it overcorrects, leading to deviations from the experimental IP of comparable magnitude but opposite sign relative to the uncorrected functional.

Given these limitations, this chapter explores various strategies to mitigate some of the shortcomings of the PZ-SIC discussed above. First, we review existing approaches that scale down its effect to improve energetic performance. Subsequently, we introduce alternative methods that prioritize an accurate description of experimental IPs via the HOMO energy while also aiming to enforce the straight-line condition discussed in the previous chapter.

8.1 Review of PZ-SIC Modification Strategies

The simplest approach to modify the PZ-SIC involves scaling the self-Hartree and self-xc terms by multiplying them with a global factor between 0 and 1. This method has been employed in applications such as band gap calculations, as well as in studying electronic states and binding energies, using PBE-SIC with the SIC terms often scaled by a factor of 0.5 [Jón11; KKJ12; Val+12]. However, while this approach has led to improved results for specific observables [KKJ12], it lacks a universal choice of the scaling factor and does not preserve the correct asymptotic $-1/r$ behavior of the xc potential.

Vydrov and Scuseria proposed a more systematic approach to apply a global scaling factor [Vyd+06]. This method introduces an orbital-dependent scaling factor defined as

$$X_{i\sigma}^{k} = \int \left(\frac{\tau_\sigma^{\mathrm{W}}(\mathbf{r})}{\tau_\sigma(\mathbf{r})} \right)^{k} n_{i\sigma}(\mathbf{r})\, \mathrm{d}^3 r = \int z_\sigma^k(\mathbf{r}) n_{i\sigma}(\mathbf{r})\, \mathrm{d}^3 r\,. \tag{8.1}$$

Here, τ^{W} is the single-orbital limit of the kinetic energy density, and the ratio $z_\sigma = \tau_\sigma^{\mathrm{W}}/\tau_\sigma$ therefore serves as an iso-orbital indicator that approaches 1 in single-orbital regions. The parameter $k \geq 0$ is a real-valued scaling factor, and $X_{i\sigma}^k$ takes values between 0 and 1. Using this definition, the modified SIC functional is (with $k = 1$) given by [Yam+23]

$$E_{\mathrm{xc}}^{\mathrm{SIC}} = E_{\mathrm{xc}}^{\mathrm{app}}[n_\uparrow, n_\downarrow] - \sum_{\sigma=\uparrow,\downarrow} \sum_{i=1}^{N_\sigma} X_{i\sigma}^k \left(E_{\mathrm{H}}[n_{i\sigma}] + E_{\mathrm{xc}}^{\mathrm{app}}[n_{i\sigma}, 0] \right)\,. \tag{8.2}$$

While this scaling procedure improves the description of equilibrium properties and barrier heights compared to the full PZ-SIC, it deteriorates the accuracy of dissociation processes [Ruz+07]. Moreover, the optimal scaling factor k depends on both the chosen xc approximation and the specific physical property under consideration, such as atomization energies, IPs, or reaction barrier heights [Vyd+06] and the correct asymptotic behavior is only restored for $k = 0$, i. e., the full PZ-SIC. For any nonzero scaling factor, the resulting scaled PZ-SIC potential instead decays as $-X_{\mathrm{HOMO}}^k/r$ [Ruz+07]. Beyond this specific scaling approach, alternative definitions for the global scaling factor have been proposed; see, e. g., Refs. [TKH03; VS06; Yam+20].

To further improve the approach of using a global scaling of the PZ-SIC, Zope *et al.* [Zop+19] introduced the local-scaling SIC (LSIC). In LSIC, the SIC is applied only in those spatial regions where the SIE is expected to be dominant, while the limit of the uncorrected (semi-)local xc approximation is preserved in uniform-density regions. This approach employs the iso-orbital indicator $z_\sigma = \tau_\sigma^{\mathrm{W}}/\tau_\sigma$ locally, following an idea originally proposed in Ref. [TKH03]. Since the choice of the scaling function is not unique, alternative definitions have also been explored [Bha+21; Rom+21]. Following the LSIC framework, the SIC energy functional is modified as

$$E_{\mathrm{xc}}^{\mathrm{LSIC}} = E_{\mathrm{xc}}^{\mathrm{app}}[n_\uparrow, n_\downarrow] - \sum_{\sigma=\uparrow,\downarrow} \sum_{i=1}^{N_\sigma} \Big(E_{\mathrm{H}}^{\mathrm{LSIC}}[n_{i\sigma}] + E_{\mathrm{xc}}^{\text{app-LSIC}}[n_{i\sigma}, 0] \Big), \tag{8.3}$$

where

$$E_{\mathrm{H}}^{\mathrm{LSIC}}[n_{i\sigma}] = \frac{e^2}{2} \iint [z_\sigma(\mathbf{r})]^k \frac{n_{i\sigma}(\mathbf{r})\, n_{i\sigma}(\mathbf{r}')}{|\mathbf{r} - \mathbf{r}'|}\, \mathrm{d}^3 r\, \mathrm{d}^3 r' \tag{8.4}$$

is the locally scaled self-Hartree term, and

$$E_{\mathrm{xc}}^{\text{app-LSIC}}[n_{i\sigma}, 0] = \int [z_\sigma(\mathbf{r})]^k\, n_{i\sigma}(\mathbf{r})\, \epsilon_{\mathrm{xc}}^{\mathrm{app}}[n_{i\sigma}, 0](\mathbf{r})\, \mathrm{d}^3 r \tag{8.5}$$

is the locally scaled self-xc term, where $\epsilon_{\mathrm{xc}}^{\mathrm{app}}$ donates the approximate xc energy density per particle. The scaling parameter k is a real number, typically set to 1. By applying the SIC in a spatially selective manner, LSIC significantly improves the description of physical properties such as barrier heights and dissociation curves of heteronuclear molecules. At the same time, it mitigates the deficiencies of the full PZ-SIC in describing near-equilibrium properties, including total ground-state and atomization energies. LSDA-LSIC provides more accurate atomization energies than the PBE functional and achieves a level of accuracy comparable to that of the meta-GGA SCAN (see Ref. [Zop+19] for these results).

Nevertheless, the LSIC approach has drawbacks: The orbital-dependent potential expression in LSIC, obtained from the functional derivative of Eq. (8.3) with respect to $\varphi_{i\sigma}^*$ leads to an expression that contains additional terms that depend explicitly on the iso-orbital indicator z_σ and its derivative $\delta z_\sigma / \delta \varphi_{i\sigma}^*$ [Yam+23]. Due to these additional terms, calculating the LSIC ground state fully self-consistently is numerically more demanding. Similar to previous applications of the PZ-SIC [YPP17; Yam+19; Sch+20; Yam+20; WJP22], recent studies of the LSIC have used the FLO-SIC method for finding the localized orbitals [PRP14; PB15]. Within this method, Fermi orbitals serve as localized orbitals, circumventing the need for the fully energy-minimizing orbitals obtained via the energy-minimizing unitary transformation. To further reduce the computational cost, several applications of the LSIC approach have been restricted to evaluating the energy expression in Eq. (8.3) using ground-state densities obtained from full PZ-SIC calculations [Zop+19] or employing a quasi-self-consistent approach that neglects terms involving the derivative $\delta z_\sigma / \delta \varphi_{i\sigma}^*$ (for details, see Ref. [Yam+23]). In addition to the increased numerical cost of the LSIC, its original formulation cannot be easily extended to GGAs and meta-GGAs, as these xc approximations introduce gauge inconsistencies in the self-Hartree and self-xc energy densities within the correction terms [Bha+20; Bha+21].

Moreover, in the literature, the LSIC approach has been motivated by addressing the shortcomings of the global scaling SIC functional defined in Eq. (8.2) such as its false asymptotic behavior [Zop+19; Rom+21]. However, similar to local hybrid functionals, the LSIC potential calculated via the functional derivative of the LSIC energy functional with respect to $\varphi_{i\sigma}^*$ includes an integral term of the form

$$-\frac{e^2}{2} \int \frac{z_\sigma(\mathbf{r}') n_{i\sigma}(\mathbf{r}')}{|\mathbf{r} - \mathbf{r}'|} \, \mathrm{d}^3 r' \, \varphi_{i\sigma}(\mathbf{r}) \,, \tag{8.6}$$

in which the iso-orbital indicator z_σ appears inside the integral. As explicitly shown in Ref. [Sch+14a] for local hybrid functionals, this expression leads to a false asymptotic behavior of the xc potential. Therefore, one can put into question whether the LSIC energy functional generally leads to the correct asymptotic of the corresponding potential. In any case, the LSIC approach exhibits deficiencies in describing CT-related properties. Fully self-consistent LSIC calculations using the FLO-SIC approach indicate that the resulting total energy curve for the C atom [ZYB24] fulfills the straight-line condition less accurately than the results for the full PZ-SIC. Furthermore, HOMO energies from LSDA-LSIC calculations deviate significantly from experimental IPs [Yam+23].

8.2 Long-Range Self-Interaction Correction for Hartree and (Semi-)Local Exchange

Since this work focuses on accurately describing CT-related properties, we aim to modify the PZ-SIC using an approach that ensures the correct asymptotic $-1/r$ decay of the xc potential while ensuring a more accurate fulfillment of the straight-line condition and improving the alignment of the HOMO energy with experimental IPs. Our approach can be motivated as follows: In analogy to global hybrid functionals, where a (semi-)local functional is mixed with exact exchange, the global scaling of the self-Hartree and self-xc energy terms, described in the previous section, can be viewed as a hybrid between a (semi-)local DFA and the PZ-SIC. The LSIC formulation can, in turn, be interpreted as an approach analogous to local hybrid functionals [Zop+19]. Our method, which will be presented below, follows the range-separated hybrid approach [HSE03; YTH04; TCS04; Sav20], which has been shown to successfully describe CT processes by employing (semi-)local exchange for short-range interactions and exact exchange for long-range interactions [LB07; KK08; SKB09; Ste+10; Kur+11; Kro+12; AS14; Küm17]. To adapt this concept to the PZ-SIC framework, we apply the full PZ-SIC only in the long-range regime and reduce the SIC in the short-range regime. This ensures the correct asymptotic behavior of the xc potential. At the same time, it effectively mitigates the SIE of the Hartree term associated with the HOMO, which typically dominates the density at large distances.

To implement this approach, we introduce the long-range scaling function

$$\mu^{\mathrm{lr}(\gamma)}(|\mathbf{r}-\mathbf{r}'|) = 1 - \exp(-\gamma|\mathbf{r}-\mathbf{r}'|)\,, \tag{8.7}$$

where γ is the range-separation parameter. This leads to a modified SIC, the long-range self-interaction correction (lrSIC). The expression for the xc energy is then given by

$$E_{\mathrm{xc}}^{\mathrm{lrSIC}} = E_{\mathrm{xc}}^{\mathrm{app}}[n_\uparrow, n_\downarrow] - \sum_{\sigma=\uparrow,\downarrow}\sum_{i=1}^{N_\sigma}\left(E_{\mathrm{H}}^{\mathrm{lr}(\gamma)}[n_{i\sigma}] + E_{\mathrm{x}}^{\text{lr-app}(\gamma)}[n_{i\sigma}] + E_{\mathrm{c}}^{\mathrm{app}}[n_{i\sigma}, 0]\right)\,. \tag{8.8}$$

For the long-range self-Hartree energy, we obtain

$$\begin{aligned} E_{\mathrm{H}}^{\mathrm{lr}(\gamma)}[n_{i\sigma}] &= \frac{e^2}{2}\iint \frac{\mu^{\mathrm{lr}(\gamma)}(|\mathbf{r}-\mathbf{r}'|)n_{i\sigma}(\mathbf{r})n_{i\sigma}(\mathbf{r}')}{|\mathbf{r}-\mathbf{r}'|}\,\mathrm{d}^3r\,\mathrm{d}^3r' \\ &= E_{\mathrm{H}}[n_{i\sigma}] - \underbrace{\frac{e^2}{2}\iint \frac{e^{-\gamma|\mathbf{r}-\mathbf{r}'|}n_{i\sigma}(\mathbf{r})n_{i\sigma}(\mathbf{r}')}{|\mathbf{r}-\mathbf{r}'|}\,\mathrm{d}^3r\,\mathrm{d}^3r'}_{=E_{\mathrm{Yukawa}}^{(\gamma)}}\,. \end{aligned} \tag{8.9}$$

The term $E_{\mathrm{Yukawa}}^{(\gamma)}$ represents the Yukawa potential, a well-known concept in electrostatics that introduces exponential screening. In our context, this screening is employed to modify the SIC. Next, the long-range (semi-)local exchange energy is calculated based on the representation via its (semi-)local exchange hole $h_{\mathrm{x}}^{\mathrm{app}}(\mathbf{r},\mathbf{r}')$ [LP75; GL76] given by

$$E_{\mathrm{x}}^{\text{lr-app}(\gamma)}[n_{i\sigma}] = \frac{e^2}{2}\iint \mu^{\mathrm{lr}(\gamma)}(|\mathbf{r}-\mathbf{r}'|)\frac{n_{i\sigma}(\mathbf{r})h_{\mathrm{x}}^{\mathrm{app}}(\mathbf{r},\mathbf{r}')}{|\mathbf{r}-\mathbf{r}'|}\,\mathrm{d}^3r'\,\mathrm{d}^3r\,. \tag{8.10}$$

The usual exchange energy expression can be defined analogously to Eq. (8.10) without the long-range scaling function $\mu^{\mathrm{lr}(\gamma)}$. The expression for the LDA functional will be introduced in the following section. Using the lrSIC approach, the corresponding energy

functional in Eq. (8.8) smoothly interpolates between two limits: for $\gamma \to \infty$, it recovers the full PZ-SIC, while for $\gamma \to 0$, the Hartree and exchange correction terms vanish entirely. In this limit, only the correlation term is self-interaction corrected.

Finally, the corresponding Hamiltonian operator can be obtained by minimizing the ground-state energy functional using $E_{\mathrm{xc}}^{\mathrm{lrSIC}}$ defined in Eq. (8.8) with respect to $\varphi_{i\sigma}^*$. This results in the following Hamiltonian

$$\begin{aligned}\hat{H}_{i\sigma} = &-\frac{\hbar^2}{2m}\nabla^2 + v_{\mathrm{ext}}(\mathbf{r}) + v_{\mathrm{H}}[n](\mathbf{r}) + v_{\mathrm{xc}}[n_\uparrow, n_\downarrow](\mathbf{r}) \\ &- \left(v_{\mathrm{H}}[n_{i\sigma}](\mathbf{r}) - v_{\mathrm{Yukawa}}^{(\gamma)}[n_{i\sigma}](\mathbf{r}) + v_{\mathrm{x}}^{\mathrm{lr}(\gamma)}[n_{i\sigma}](\mathbf{r}) + v_{\mathrm{c}}[n_{i\sigma}, 0](\mathbf{r})\right) ,\end{aligned} \tag{8.11}$$

where the SIC terms emerge from the functional derivative $\delta E_{\mathrm{xc}}^{\mathrm{lrSIC}}/\delta\varphi_{i\sigma}^*$. In this expression, $v_{\mathrm{x}}^{\mathrm{lr}(\gamma)}$ is the screened (semi-)local exchange potential computed using the scaling function in Eq. (8.7), and $v_{\mathrm{Yukawa}}^{(\gamma)}$ is the Yukawa potential given by

$$v_{\mathrm{Yukawa}}^{(\gamma)}[n_{i\sigma}](\mathbf{r}) = e^2 \int \frac{e^{-\gamma|\mathbf{r}-\mathbf{r}'|}\, n_{i\sigma}(\mathbf{r}')}{|\mathbf{r}-\mathbf{r}'|}\, \mathrm{d}^3 r' . \tag{8.12}$$

Calculating the integral form of the Yukawa potential from Eq. (8.12) using the real-space code `BTDFT` is computationally demanding. However, similar to the Hartree potential, the Yukawa potential can be calculated by solving the screened Poisson equation

$$\left[\nabla^2 - \gamma^2\right] v_{\mathrm{Yukawa}}^{(\gamma)}[n_{i\sigma}](\mathbf{r}) = -4\pi e^2 n_{i\sigma}(\mathbf{r}) . \tag{8.13}$$

Since the Yukawa potential decays slowly as $\gamma \to 0$, enforcing a zero-boundary condition for the whole Yukawa potential would require a computationally expensive large grid. Therefore, we partition the Yukawa potential into an internal part defined within the real-space grid and, to satisfy the boundary condition, a part defined outside the grid, i. e., $v_{\mathrm{Yukawa}}^{(\gamma)\mathrm{in}} + v_{\mathrm{Yukawa}}^{(\gamma)\mathrm{bound}}$ for solving the screened Poisson equation. By choosing $v_{\mathrm{Yukawa}}^{(\gamma)\mathrm{in}}$ to vanish outside the grid, the screened Poisson equation is modified to

$$\left[\nabla^2 - \gamma^2\right] v_{\mathrm{Yukawa}}^{(\gamma)\mathrm{in}}(\mathbf{r}) = -4\pi e^2 n_{i\sigma}(\mathbf{r}) - \left[\nabla^2 - \gamma^2\right] v_{\mathrm{Yukawa}}^{(\gamma)\mathrm{bound}}(\mathbf{r}) . \tag{8.14}$$

We approximate the boundary potential by the monopole moment of the Yukawa potential

$$v_{\mathrm{Yukawa}}^{(\gamma)\mathrm{mono}}[n_{i\sigma}](\mathbf{r}) = e^2 \frac{\exp(-\gamma r)}{r} , \tag{8.15}$$

where r denotes the distance from the center of the orbital density $n_{i\sigma}$ to the point $\mathbf{r}$. The influence of using the monopole moment of the Yukawa potential as the boundary condition for solving the screened Poisson equation instead of a zero-boundary condition is discussed in Appendix B.15.

8.3 Long-Range LSDA Expression

So far, we have introduced the exponentially screened expressions for the Hartree energy. For the exchange functional within our lrSIC formulation, we employ the LSDA functional with the corresponding exponentially screened LSDA expression, which can be derived using the exact exchange functional with the screening function $\mu^{\mathrm{lr}(\gamma)}(|\mathbf{r}-\mathbf{r}'|)$ defined

in Eq. (8.7) as a starting point:

$$E_{\mathrm{x}}^{\text{lr-exact}(\gamma)} = -\frac{e^2}{2} \sum_{\sigma=\uparrow,\downarrow} \sum_{i,j=1}^{N_\sigma} \iint \mu^{\mathrm{lr}(\gamma)}(|\mathbf{r}-\mathbf{r}'|) \frac{\varphi_{i\sigma}^*(\mathbf{r})\varphi_{j\sigma}^*(\mathbf{r}')\varphi_{i\sigma}(\mathbf{r}')\varphi_{j\sigma}(\mathbf{r})}{|\mathbf{r}-\mathbf{r}'|} \,\mathrm{d}^3r\,\mathrm{d}^3r' \,. \tag{8.16}$$

Subsequently, the orbitals $\{\varphi_{i\sigma}\}$ are replaced by the particle-in-a-box orbital expressions, as described in Chapter 6 of Ref. [Par20], which presents the derivation of the LDA exchange energy, and in Ref. [Rob+62]. By solving the integrals in Eq. (8.16), one obtains the expression for the long-range LDA exchange energy

$$E_{\mathrm{x}}^{\text{lr-LDA}(\gamma)}[n] = A_{\mathrm{x}} \int n^{4/3}(\mathbf{r}) F_{\mathrm{x}}^{\text{lr-LDA}(\gamma)}(r_{\mathrm{s}}(\mathbf{r}))\,\mathrm{d}^3r \tag{8.17}$$

with the constant $A_{\mathrm{x}} = -(3/4)(3/\pi)^{1/3}$, the Wigner-Seitz radius

$$r_{\mathrm{s}}(\mathbf{r}) = \left(\frac{3}{4\pi n(\mathbf{r})}\right)^{1/3}, \tag{8.18}$$

and the enhancement factor [Rob+62]

$$F_{\mathrm{x}}^{\text{lr-LDA}(\gamma)}(r_{\mathrm{s}}) = \frac{\gamma\left\{4\frac{c_{\mathrm{x}}^2}{r_{\mathrm{s}}^2}\left[\gamma + 8\frac{c_{\mathrm{x}}}{r_{\mathrm{s}}}\arctan\left(\frac{2c_{\mathrm{x}}}{\gamma r_{\mathrm{s}}}\right)\right] - \gamma\left(12\frac{c_{\mathrm{x}}^2}{r_{\mathrm{s}}^2} + \gamma^2\right)\ln\left(1+\frac{4c_{\mathrm{x}}^2}{r_{\mathrm{s}}^2\gamma^2}\right)\right\}}{24\frac{c_{\mathrm{x}}^4}{r_{\mathrm{s}}^4}} \tag{8.19}$$

where $c_{\mathrm{x}} = (9\pi/4)^{1/3}$. The detailed derivation steps are provided in Appendix B.16. The spin-dependent exponentially screened LSDA expressions can be obtained by applying the spin-scaling relations described in Section 3.6.3, i. e., by substituting $r_{\mathrm{s}} \to 2^{-1/3} r_{\mathrm{s}\sigma}$ with $r_{\mathrm{s}\sigma} = (3/(4\pi n_\sigma))^{1/3}$.

The corresponding potential is obtained by taking the functional derivative of the long-range LDA exchange energy with respect to the density,

$$\begin{aligned} v_{\mathrm{x}}^{\text{lr-LDA}(\gamma)}(\mathbf{r}) =& \frac{\delta E_{\mathrm{x}}^{\text{lr-LDA}(\gamma)}[n(\mathbf{r}')]}{\delta n(\mathbf{r})} \\ =& A_{\mathrm{x}}\left(\frac{4}{3}n^{1/3}(\mathbf{r})F_{\mathrm{x}}^{\text{lr-LDA}(\gamma)}(r_{\mathrm{s}}(\mathbf{r})) + n^{4/3}(\mathbf{r})\frac{\partial F_{\mathrm{x}}^{\text{lr-LDA}(\gamma)}(r_{\mathrm{s}})}{\partial r_{\mathrm{s}}}(\mathbf{r})\frac{\partial r_{\mathrm{s}}}{\partial n}(\mathbf{r})\right) \\ =& \frac{1}{3}A_{\mathrm{x}}\left[4n^{1/3}(\mathbf{r})F_{\mathrm{x}}^{\text{lr-LDA}(\gamma)}(r_{\mathrm{s}}(\mathbf{r})) - \left(\frac{3}{4\pi}\right)^{1/3}\frac{\partial F_{\mathrm{x}}^{\text{lr-LDA}(\gamma)}(r_{\mathrm{s}})}{\partial r_{\mathrm{s}}}(\mathbf{r})\right] \end{aligned} \tag{8.20}$$

where

$$\frac{\partial r_{\mathrm{s}}}{\partial n} = -\frac{1}{3}\frac{r_{\mathrm{s}}}{n} \tag{8.21}$$

and

$$\frac{\partial F_{\mathrm{x}}^{\text{lr-LDA}(\gamma)}(r_{\mathrm{s}})}{\partial r_{\mathrm{s}}} = \frac{\gamma\left\{8c_{\mathrm{x}}^3\arctan\left(\frac{2c_{\mathrm{x}}}{\gamma r_{\mathrm{s}}}\right) + r_{\mathrm{s}}\gamma\left(4c_{\mathrm{x}}^2 - \left[6c_{\mathrm{x}}^2 + r_{\mathrm{s}}^2\gamma^2\right]\ln\left[1+\frac{4c_{\mathrm{x}}^2}{\gamma^2 r_{\mathrm{s}}^2}\right]\right)\right\}}{6c_{\mathrm{x}}^4}\,. \tag{8.22}$$

The spin-dependent potential is obtained by

$$v_{\mathrm{x}\sigma}^{\text{lr-LDA}(\gamma)}(\mathbf{r}) = v_{\mathrm{x}}^{\text{lr-LDA}(\gamma)}(\mathbf{r})\Big|_{n\to 2n_\sigma}\,. \tag{8.23}$$

8.4 Results for Long-Range Self-Interaction Correction for Hartree and (Semi-)Local Exchange

Following our previous tests for the full PZ-SIC, we apply the lrSIC approach with the long-range LSDA (LSDA-lrSIC) to our test set consisting of CO, H_2O, and N_2. The numerical details are reported in Appendix B.17; in the following, we present and discuss our results. We begin by analyzing the influence of the range-separation parameter γ on the behavior of the total energy as a function of the fractional electron number to assess the fulfillment of the straight-line condition. Next, we analyze the validity of the IP theorem depending on the value of γ employed. As numerical difficulties become evident in the HOMO energies, particularly for small γ values, we discuss these issues in detail in a subsequent section.

8.4.1 Straight-Line Condition for LSDA-lrSIC

We start by analyzing the fulfillment of the straight-line condition using the LSDA-lrSIC functional for different values of the range-separation parameter γ for the CO molecule. To quantify the degree of fulfillment for the considered γ values, we introduce an error value, $\Delta_{\text{lin}}(\gamma)$, which measures the deviation of the energy curve $E(N)$ from the linear connection between $E(N_0-1)$ and $E(N_0)$, where N_0 denotes the number of electrons of the neutral system:

$$\Delta_{\text{lin}}(\gamma) = \frac{\int_{N_0-1}^{N_0} |E^{(\gamma)}(N) - E^{(\gamma)}_{\text{lin}}(N)|\,\mathrm{d}N}{\int_{N_0-1}^{N_0} E^{(\gamma)}_{\text{lin}}(N)\,\mathrm{d}N} = \frac{\int_{N_0-1}^{N_0} |E^{(\gamma)}(N) - E^{(\gamma)}_{\text{lin}}(N)|\,\mathrm{d}N}{E(N_0) + \frac{1}{2}\Delta\text{SCF}}\,, \tag{8.24}$$

where $\Delta\text{SCF} = E(N_0-1) - E(N_0)$. The exact result for the linear energy function, which connects $E(N_0-1)$ and $E(N_0)$ is defined as

$$E^{(\gamma)}_{\text{lin}}(N) = E^{(\gamma)}(N_0) + (N-N_0)\left[E^{(\gamma)}(N_0) - E^{(\gamma)}(N_0-1)\right]\,. \tag{8.25}$$

The error criterion is schematically illustrated in Fig. 8.1. In this figure, the red

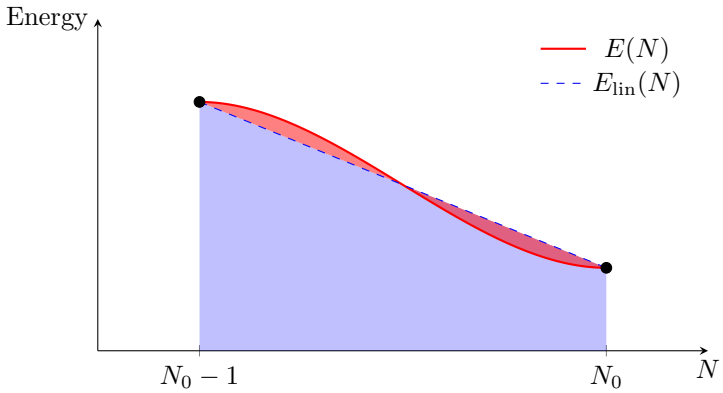

Figure 8.1: Schematic illustration of the error criterion Δ_{lin}. The red area indicates the absolute deviation between $E(N)$ and the linear function $E_{\text{lin}}(N)$ that connects $E(N_0)$ and $E(N_0-1)$. The blue area corresponds to the region below $E_{\text{lin}}(N)$.

area represents the numerator, while the blue area corresponds to the denominator of

Eq. (8.24). By normalizing our error criterion with the denominator (i. e., the blue area under the straight line connecting $E(N_0 - 1)$ and $E(N_0)$), we ensure that $\Delta_{\text{lin}}(\gamma)$ remains comparable across different model systems.

Figure 8.2 shows the results of the LSDA-lrSIC approach for the energy curves between the neutral CO molecule and its cation for γ values of 0.3, 0.6, 0.9, and $1.2\,\mathrm{a_0^{-1}}$ shown in panel (a) to (d). As evident from the energy curve in panel (a), the correction

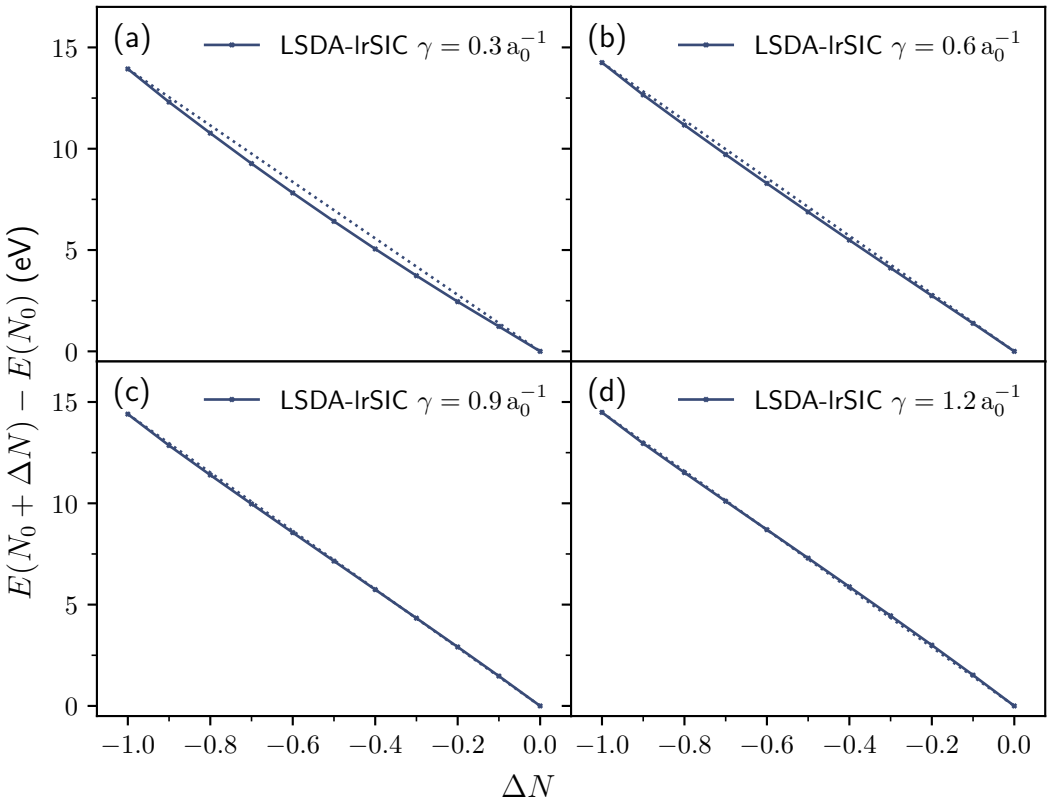

Figure 8.2: Energy curves for CO using LSDA-lrSIC with different range-separation parameters: $\gamma = 0.3$ (a), 0.6 (b), 0.9 (c), and $1.2\,\mathrm{a_0^{-1}}$ (d). The dotted lines indicate the straight-line reference, highlighting deviations from the straight-line condition.

terms with $\gamma = 0.3\,\mathrm{a_0^{-1}}$ remain too weak to eliminate the convex curvature of the uncorrected LSDA functional. Increasing the range-separation parameter also increases the SIC, which is reflected in the energy curves: The convex behavior of the energy curve decreases as γ increases from 0.3 to $0.6\,\mathrm{a_0}^{-1}$, and a nearly linear behavior is observed for $\gamma = 0.9\,\mathrm{a_0}^{-1}$ in panel (c). For $\gamma = 1.2\,\mathrm{a_0}^{-1}$ in panel (d), however, a slight overcorrection occurs, resulting in a mildly S-shaped energy curve.

In order to evaluate the deviation of the energy curves more rigorously, we additionally use the error criterion Δ_{lin}. The results for different values of γ are presented in Fig. 8.3. The gray dashed horizontal lines represent the error of the uncorrected LSDA functional and the LSDA functional using the full PZ-SIC (LSDA-SIC). Comparing these two references highlights the improvement already achieved by the full PZ-SIC, as observed in Chapter 7, where the deviation from the straight-line condition decreases significantly from the LSDA to LSDA-SIC. To systematically analyze the effect of the range-separation parameter γ within our lrSIC framework, we computed the deviation from the straight-line condition for LSDA-lrSIC in steps of $0.1\,\mathrm{a_0^{-1}}$. As the deviation approaches values

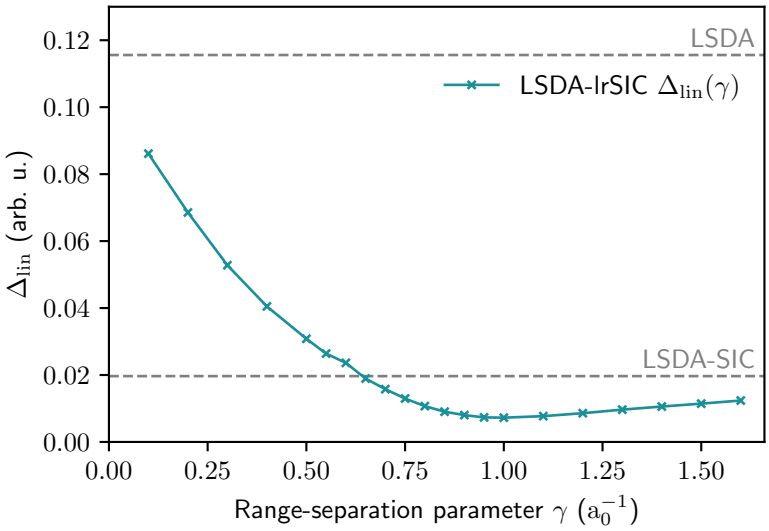

Figure 8.3: Error value Δ_{lin} quantifying the deviation of energy curves from the straight-line condition for CO, computed with LSDA-lrSIC for different γ. The gray dotted lines indicate the LSDA and LSDA-SIC values.

comparable to the full PZ-SIC, we refined the step size to $0.05\,\mathrm{a}_0^{-1}$ to capture the trend more accurately. The results reveal a strong decrease of Δ_{lin} with increasing γ, eventually falling below the value for LSDA-SIC at approximately $\gamma = 0.6\,\mathrm{a}_0^{-1}$. The minimal deviation from the straight-line condition is observed at $\gamma = 1.0\,\mathrm{a}_0^{-1}$, reducing the error by approximately 63% compared to the LSDA-SIC error (from $\Delta_{\mathrm{lin}} = 1.97 \times 10^{-2}$ to 0.73×10^{-2}). For $\gamma > 1.0\,\mathrm{a}_0^{-1}$, the deviation increases slightly, indicating a growing overcorrection at higher γ values. This trend is consistent with the fact that, in the limit of large γ, the lrSIC formulation approaches the full PZ-SIC, which shows an overcorrection for the CO molecule.

We now turn to the H_2O molecule as our second model system. Figure 8.4 illustrates the energy curves computed with LSDA-lrSIC for the different values of the range-separation parameter γ. The LSDA-lrSIC results for $\gamma = 0.3\,\mathrm{a}_0^{-1}$ and $0.6\,\mathrm{a}_0^{-1}$, shown in panels (a) and (b), respectively, exhibit a convex deviation from the linear connection between $E(N_0 - 1)$ and $E(N_0)$. This deviation appears more pronounced than in the case of the CO molecule. In contrast, for $\gamma = 0.9\,\mathrm{a}_0^{-1}$ and $1.2\,\mathrm{a}_0^{-1}$, the deviation becomes slightly S-shaped, with the energy curve for $\gamma = 1.2\,\mathrm{a}_0^{-1}$ exhibiting the smallest deviation from the straight-line condition among the considered γ values in Fig. 8.4. This effect, where a stronger SIC is needed for the H_2O molecule compared to CO, can be attributed to the presence of two hydrogen atoms in the H_2O molecule. These hydrogen atoms create additional iso-orbital regions where SIEs are particularly pronounced. In these regions, the cancellation between the Hartree term and the LSDA exchange is insufficient, necessitating a larger γ to enforce the straight-line condition.

The trend observed in the energy curves for H_2O is further reflected in the error values Δ_{lin} for the LSDA-lrSIC calculations with different range-separation parameters, as shown in Fig. 8.5. Notably, the horizontal gray line of the uncorrected LSDA yields a larger Δ_{lin} value for H_2O than for CO, reflecting a more pronounced convex deviation from the straight-line condition, which aligns with the expectation that SIEs are more pronounced in H_2O than in CO when using the LSDA functional. Applying the lrSIC approach leads again to a rapid decrease in Δ_{lin}. For $\gamma \geq 0.65\,\mathrm{a}_0^{-1}$, Δ_{lin} falls below the

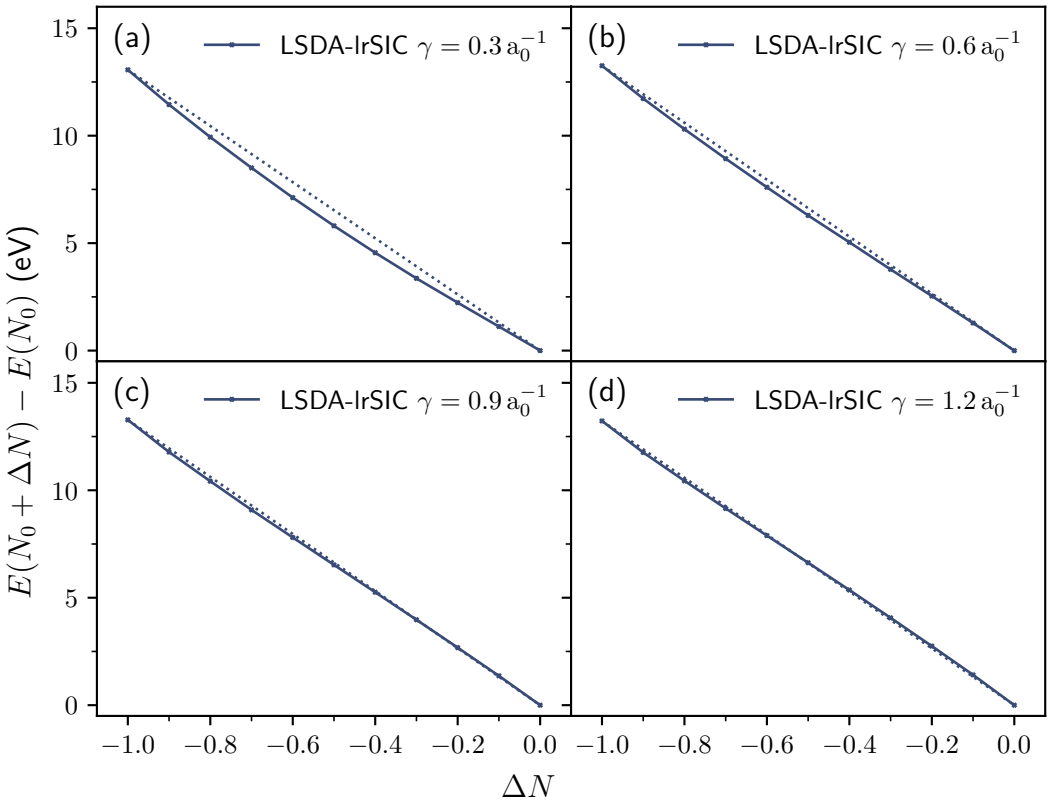

Figure 8.4: Energy curves for H_2O using LSDA-lrSIC with different range-separation parameters: $\gamma = 0.3$ (a), 0.6 (b), 0.9 (c), and $1.2\,\mathrm{a}_0^{-1}$ (d). The dotted lines indicate the straight-line reference, highlighting deviations from the straight-line condition.

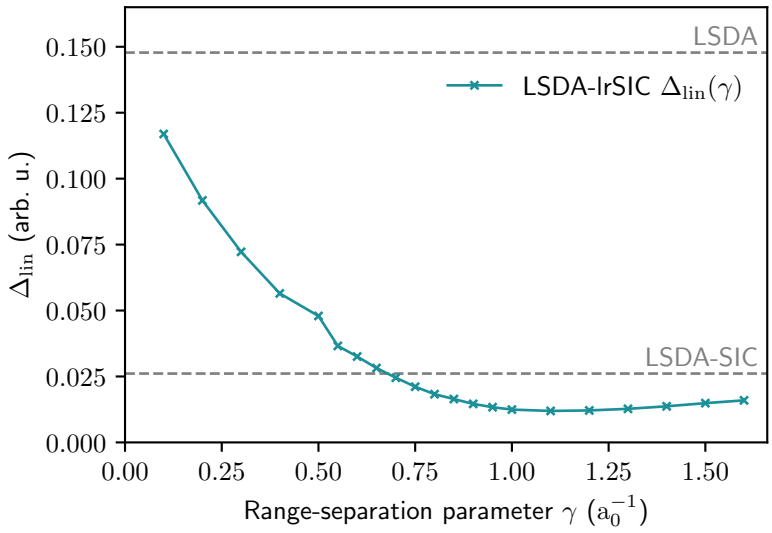

Figure 8.5: Error value Δ_{lin} quantifying the deviation of energy curves from the straight-line condition for H_2O, computed with LSDA-lrSIC for different γ. The gray dotted lines indicate the LSDA and LSDA-SIC values.

LSDA-SIC value, reaching a minimum at $\gamma = 1.1\,\mathrm{a}_0^{-1}$. For $\gamma > 1.1\,\mathrm{a}_0^{-1}$, Δ_{lin} increases again. These results are consistent with the trends observed in the energy curves and confirm that a slightly larger range-separation parameter is required to minimize the deviation from the exact straight-line condition in H_2O compared to CO.

Finally, we turn to the last model system, the N_2 molecule. The energy curves for different values of the range-separation parameter γ are shown in Fig. 8.6. In panel (a),

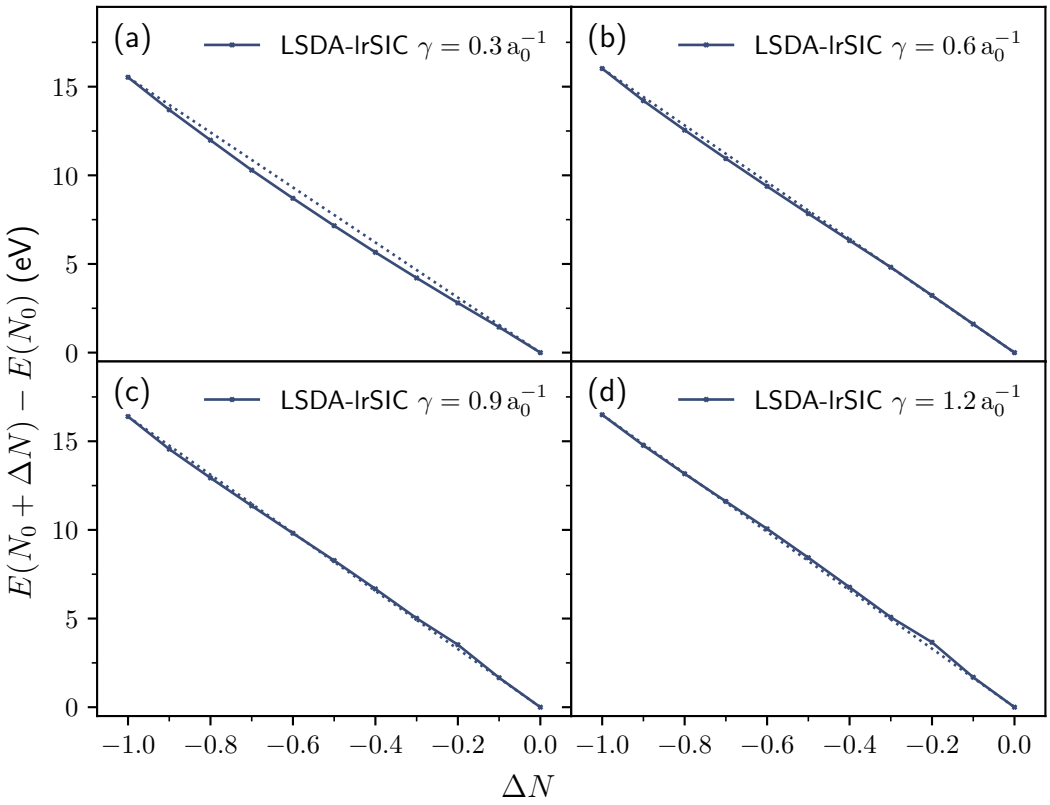

Figure 8.6: Energy curves for N_2 using LSDA-lrSIC with different range-separation parameters: $\gamma = 0.3$ (a), 0.6 (b), 0.9 (c), and $1.2\,\mathrm{a}_0^{-1}$ (d). The dotted lines indicate the straight-line reference, highlighting deviations from the straight-line condition.

the energy curve for $\gamma = 0.3\,\mathrm{a}_0^{-1}$ exhibits a convex shape. However, a slight change in curvature is noticeable near the neutral N_2 molecule, i. e., close to $\Delta N = 0$. Increasing the range-separation parameter to $\gamma = 0.6\,\mathrm{a}_0^{-1}$ (panel (b)) leads to a smaller deviation from the straight line connecting $E(N_0)$ and $E(N_0 - 1)$. For $\gamma = 0.9\,\mathrm{a}_0^{-1}$, signs of overcorrection become apparent as the energy curve forms an S-shaped behavior. For $\gamma = 1.2\,\mathrm{a}_0^{-1}$, this behavior appears to get slightly more pronounced, with a change in curvature at approximately $\Delta N = -0.75$.

These trends are consistent with the behavior of the error value Δ_{lin} as a function of γ, illustrated in Fig. 8.7. Similar to the results for CO and H_2O, Δ_{lin} decreases rapidly for small γ values, below the error value of the uncorrected LSDA, as indicated by the upper gray dashed line in Fig. 8.7. However, in contrast to CO and H_2O, the error for N_2 reaches its minimum at $\gamma = 0.8\,\mathrm{a}_0^{-1}$, and for larger values of γ, the error increases again, though it slightly decreases for $\gamma > 1.3\,\mathrm{a}_0^{-1}$. Despite these minor fluctuations, the $\Delta_{\mathrm{lin}}(\gamma)$ curve remains above the error value of the full PZ-SIC (LSDA-SIC). However, the error value for LSDA-SIC for N_2 ($\Delta_{\mathrm{lin}} = 0.42 \times 10^{-2}$) is considerably smaller than

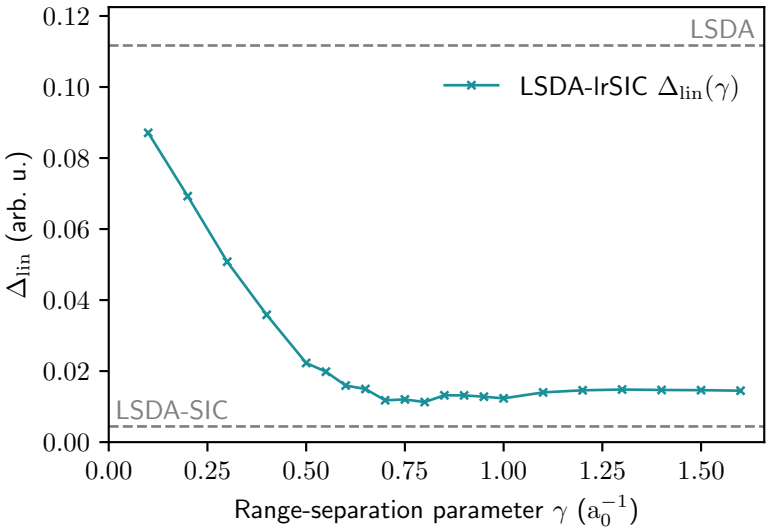

Figure 8.7: Error value Δ_{lin} quantifying the deviation of energy curves from the straight-line condition for N_2, computed with LSDA-lrSIC for different γ. The gray dotted lines indicate the LSDA and LSDA-SIC values.

the corresponding values for CO (1.97×10^{-2}) and H_2O (2.61×10^{-2}), suggesting that the full PZ-SIC applied to the LSDA functional yields the most promising results for fulfilling the straight-line condition for N_2.

8.4.2 IP Theorem for LSDA-lrSIC

After analyzing the energy curves concerning the straight-line condition, we now focus on the IP theorem for different values of the range-separation parameter γ. To explore this, we compute the HOMO energy of the neutral molecule, as well as the total ground-state energies of the neutral system and its cation, for γ values ranging from 0.1 to $1.0\,\mathrm{a}_0^{-1}$ in steps of $0.05\,\mathrm{a}_0^{-1}$. The results for the CO molecule are presented in Fig. 8.8. The HOMO energy, defined within our SIC calculations as $\epsilon_{\mathrm{HOMO}} \equiv \lambda'_{\mathrm{HOMO\,HOMO}}$ (see Section 6.6), exhibits a strong dependence on the range-separation parameter γ, varying by 2.33 eV from $-12.88\,\mathrm{eV}$ for $\gamma = 0.1$ to $-15.21\,\mathrm{eV}$ for $\gamma = 1.0\,\mathrm{a}_0^{-1}$. For small γ values, the HOMO energy underestimates the experimental IP from Ref. [Hub79], with the negative experimental IP value indicated by a gray dashed horizontal line. As γ increases and the LSDA-lrSIC functional approaches the full PZ-SIC (LSDA-SIC), the absolute value of the HOMO energy overestimates the experimental IP.

However, looking at the HOMO energy curve in Fig. 8.8, we observe significant variations for $\gamma < 0.4\,\mathrm{a}_0^{-1}$. For these values, the HOMO energies initially become more negative and then increase abruptly. This behavior can be attributed to numerical difficulties in finding the true energy-minimizing unitary transformation for small values of the range-separation parameter γ, as well as to additional issues related to the enhancement factor of the screened LSDA energy functional (see Eq. (8.19)) evaluated on orbital densities. These aspects will be discussed in detail in the subsequent section.

Due to the numerical artifacts for $\gamma < 0.4\,\mathrm{a}_0^{-1}$, our analysis focuses on larger values of γ. At approximately $\gamma = 0.5\,\mathrm{a}_0^{-1}$, the HOMO energy for the CO molecule most closely matches the experimental IP. In contrast to the HOMO energy, the negative ΔSCF value exhibits a weaker dependence on γ, varying by only 0.73 eV across the considered range

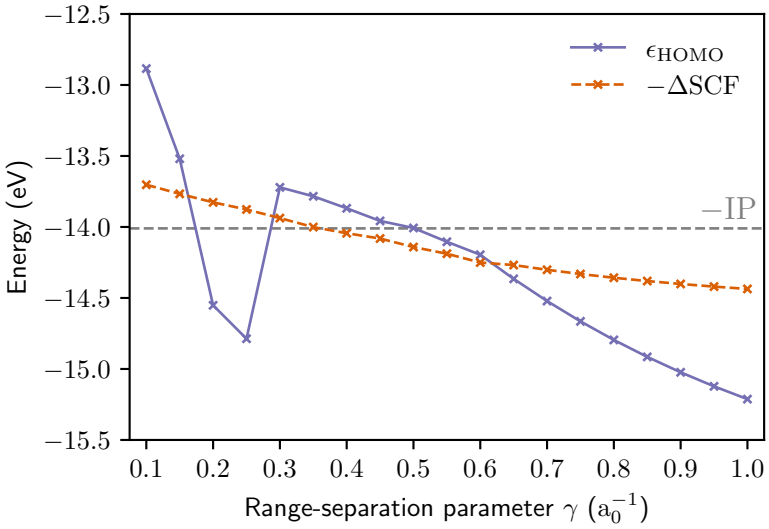

Figure 8.8: HOMO energies, ϵ_{HOMO}, and $-\Delta\mathrm{SCF} = -(E(N_0 - 1) - E(N_0))$ values for CO, calculated using LSDA-lrSIC, as a function of the range-separation parameter γ. The gray horizontal line indicates the negative experimental IP value.

of γ. The IP theorem, $\Delta\mathrm{SCF} = -\lambda'_{\mathrm{HOMO\,HOMO}}$, is satisfied for a γ value between 0.6 and $0.65\,\mathrm{a}_0^{-1}$, where the calculated IP reaches approximately $-14.26\,\mathrm{eV}$. This corresponds to a deviation of $0.25\,\mathrm{eV}$ from the experimental value.

The results for the HOMO energy and ΔSCF curves as a function of the range-separation parameter for the H_2O molecule, shown in Fig. 8.9, closely follow the trends previously discussed for CO. As in the case of CO, the ΔSCF values in Fig. 8.9 show

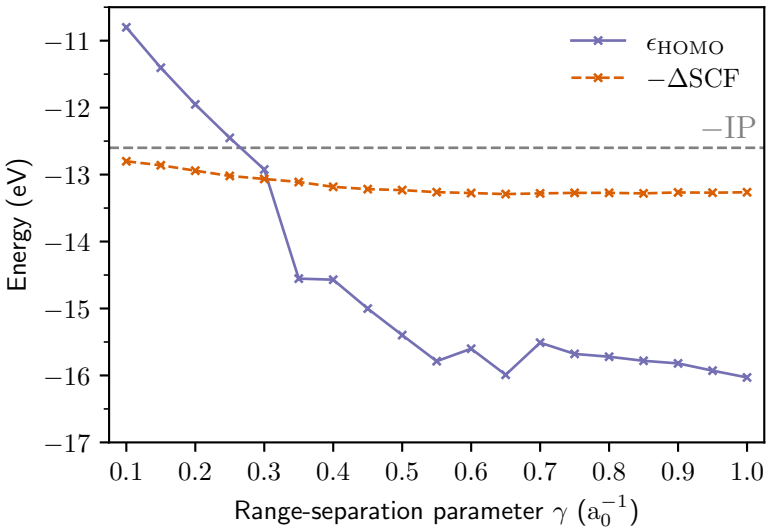

Figure 8.9: HOMO energies, ϵ_{HOMO}, and $-\Delta\mathrm{SCF} = -(E(N_0 - 1) - E(N_0))$ values for H_2O, calculated using LSDA-lrSIC, as a function of the range-separation parameter γ. The gray horizontal line indicates the negative experimental IP value.

only a weak dependence on γ, with a maximum variation of $0.46\,\mathrm{eV}$. However, unlike CO, the ΔSCF values consistently overestimate the experimental IP [Joh22] for all

considered range-separation parameters. This observation is consistent with our previous findings for the uncorrected LSDA functional and LSDA-SIC, which both overestimate the experimental IP by 0.49 eV and 0.22 eV, respectively.

An analysis of the HOMO energy as a function of γ again reveals numerical difficulties, particularly for values near $\gamma = 0.3\,\mathrm{a}_0^{-1}$, where the HOMO energy curves exhibit a large jump from $\gamma = 0.3$ to $0.35\,\mathrm{a}_0^{-1}$ (see the next section for a detailed discussion). Due to these numerical issues, it is difficult to specify the exact γ value at which the HOMO energy aligns with the negative experimental IP or the ΔSCF value. This value can only be estimated to be $\gamma = 0.27\,\mathrm{a}_0^{-1}$ for agreement with the experimental IP, and $\gamma = 0.3\,\mathrm{a}_0^{-1}$ for fulfillment of the IP theorem.

Finally, the results for our last model system N_2 are illustrated in Fig. 8.10. Similar

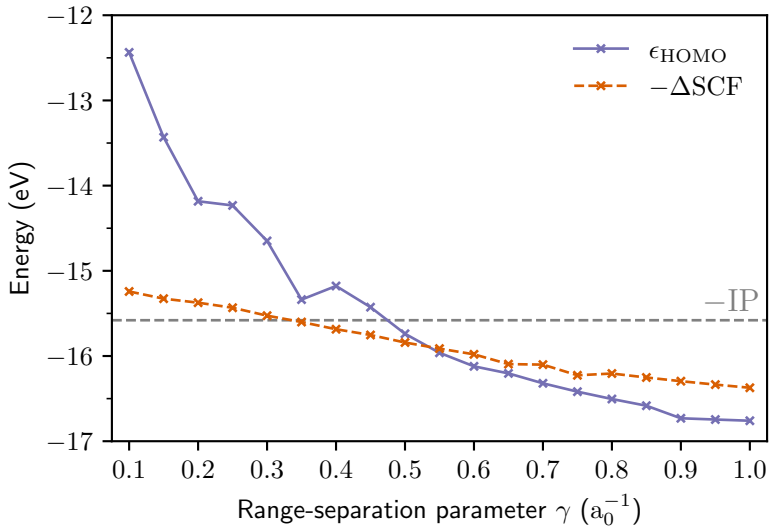

Figure 8.10: HOMO energies, ϵ_{HOMO}, and $-\Delta\mathrm{SCF} = -(E(N_0 - 1) - E(N_0))$ values for N_2, calculated using LSDA-lrSIC, as a function of the range-separation parameter γ. The gray horizontal line indicates the negative experimental IP value.

to the previously discussed systems, the HOMO energy for the N_2 molecule exhibits a stronger dependence on the range-separation parameter γ than the ΔSCF value. However, unlike the case of H_2O, the ΔSCF values do not consistently overestimate the experimental IP. The IP theorem, $\epsilon_{\mathrm{HOMO}} = -\Delta\mathrm{SCF}$, is fulfilled at approximately $\gamma = 0.53\,\mathrm{a}_0^{-1}$, where the computed IP deviates from the experimental IP value from Ref. [Hub79] by 0.31 eV – a larger deviation than observed for CO. Overall, the HOMO energy curve seems to be numerically more stable for the considered values of the range-separation parameter with only small oscillations for $\gamma < 0.4\,\mathrm{a}_0^{-1}$.

In summary, the range-separation parameter can be optimized depending on the system, similar to the known optimal tuning of range-separated hybrid functionals to satisfy the IP theorem. The value of the range-separation parameter at which $\epsilon_{\mathrm{HOMO}} = -\Delta\mathrm{SCF}$ is system-dependent. This system dependency is especially apparent for our test set for the H_2O molecule, where the optimal value deviates strongly from CO and N_2.

Comparing the optimal values of γ for the fulfillment of the IP theorem with those for the straight-line condition reveals that the IP-optimal γ values are consistently smaller across all considered systems. This difference arises from a change in the curvature of the total energy as a function of fractional particle number near the neutral molecule.

While these changes only slightly affect the total energy, they cause strong variations – particularly a drop – in the HOMO energies close to the neutral molecule. This behavior of the HOMO energy curves, which is especially pronounced for the H_2O molecule, is shown in Appendix B.19.

8.4.3 Numerical Difficulties for LSDA-lrSIC Calculations

The HOMO energy curves for the CO and H_2O molecules, presented in Section 8.4.2, reveal oscillations for some values of the range-separation parameter within our LSDA-lrSIC approach. This behavior is particularly evident for $\gamma < 0.6\,\mathrm{a}_0^{-1}$ and can be attributed to several numerical challenges associated with our lrSIC method, where the self-Hartree and self-exchange terms within the SIC are screened to their long-range regime.

The first aspect is the numerical challenge of finding the energy-minimizing unitary transformation for small values of the range-separation parameter γ. This can be understood by considering the gradient matrix of the derivative of the lrSIC energy expression in Eq. (8.8) with respect to the unitary transformation for integer particle numbers

$$G_{ij\sigma} = \langle \varphi_{j\sigma} | v^{\mathrm{SI}(\gamma)}[n_{i\sigma}] - v^{\mathrm{SI}(\gamma)}[n_{j\sigma}] | \varphi_{i\sigma} \rangle \,, \tag{8.26}$$

with the self-interaction term

$$v^{\mathrm{SI}(\gamma)}[n_{i\sigma}](\mathbf{r}) = -\left[v_{\mathrm{H}}[n_{i\sigma}](\mathbf{r}) - v^{(\gamma)}_{\mathrm{Yukawa}}[n_{i\sigma}](\mathbf{r}) + v_{\mathrm{x}}^{\mathrm{lr}(\gamma)}[n_{i\sigma}](\mathbf{r}) + v_{\mathrm{c}}[n_{i\sigma}, 0](\mathbf{r}) \right] . \tag{8.27}$$

The self-interaction potential defined in Eq. (8.27) reduces within our lrSIC approach to the negative correlation potential $-v_{\mathrm{c}}[n_{i\sigma}]$ as $\gamma \to 0$. Since the correlation potential is generally much smaller in magnitude than the exchange and Hartree terms that dominate $v^{\mathrm{SI}(\gamma)}[n_{i\sigma}]$ for larger γ, the overall self-interaction potential becomes significantly reduced in this limit. Consequently, the difference $v^{\mathrm{SI}(\gamma)}[n_{i\sigma}] - v^{\mathrm{SI}(\gamma)}[n_{j\sigma}]$ in Eq. (8.26) also tends to be small, leading to small values of all elements in the matrix $\mathbf{G}_\sigma$. Since the energy minimum with respect to the unitary transformation is reached when $\mathbf{G}_\sigma = 0$, we must define a convergence criterion that requires $\max(\mathbf{G}_\sigma)$ to fall below a predefined threshold in our algorithm for finding the energy-minimizing unitary transformation. However, as $\mathbf{G}_\sigma$ naturally decreases in magnitude for small γ, it becomes increasingly difficult to distinguish between a genuinely converged global energy minimum and numerical artifacts due to this automatic suppression. Therefore, we tightened the convergence criterion for our lrSIC calculations from our previously used value of 1.0×10^{-7} to $5.0 \times 10^{-8}\,\mathrm{Ry}$.

As illustrated in Appendix B.19, this issue is less pronounced for fractional particle numbers, which can be understood from the differing structure of the gradient matrix. For the spin channel containing the fractionally occupied HOMO, the matrix elements are given by

$$G_{ij\sigma} = \langle \varphi_{j\sigma} | f_{i\sigma} \hat{H}_{i\sigma} - f_{j\sigma} \hat{H}_{j\sigma} | \varphi_{i\sigma} \rangle \,, \tag{8.28}$$

where it explicitly depends on the occupation numbers $\{f_{i\sigma}\}$, and $\hat{H}_{i\sigma}$ is defined in Eq. (8.11). As only the HOMO is fractional occupied, i. e. $f_{\mathrm{HOMO}} \neq 1$, the difference of $f_{\mathrm{HOMO}}\hat{H}_{\mathrm{HOMO}} - f_{j\sigma}\hat{H}_{j\sigma}$ (with $j = 1, \ldots, \mathrm{HOMO} - 1$) becomes inherently larger which reduces the numerical problem of finding the true energy minimum with respect to the unitary transformation.

This numerical challenge of finding the true HOMO energy, along with the energy-minimizing ground state for small γ values, can also be understood from a more conceptual point of view: As the range-separation parameter γ approaches 0, the magnitude of

the SIC energy terms within the lrSIC energy functional that explicitly depend on the orbital densities decreases. Consequently, the energy functional becomes less sensitive to unitary transformations of the orbitals. However, such transformations can still significantly change the entries of the Lagrange multiplier matrix and specifically its diagonal elements $\lambda'_{ii\sigma}$ and, therefore, the HOMO energy $\lambda'_{\mathrm{HOMO\,HOMO}}$. This can be seen, for example, in an LSDA-lrSIC calculation for CO with $\gamma = 0.3\,\mathrm{a}_0^{-1}$, where starting the calculation from two different initial states (an uncorrected LSDA calculation or an LSDA-lrSIC calculation with $\gamma = 0.35\,\mathrm{a}_0^{-1}$) results in two different ground states, but with almost the same energy differing by only 0.005 eV. However, the corresponding HOMO energies differ strongly: the energetically lower state exhibits a HOMO energy of -13.72 eV while for the energetically higher state, the HOMO energy is -14.61 eV. As briefly discussed in the numerical details of our lrSIC calculations in Appendix B.17, a similar behavior of almost degenerate ground states could be seen for the H_2O molecule for the LSDA-lrSIC calculations with $\gamma = 0.45\,\mathrm{a}_0^{-1}$ and $0.5\,\mathrm{a}_0^{-1}$.

The numerical difficulties due to the unitary transformation with small γ values and the near-degeneracy of ground-state energies, despite significant variations in the HOMO energy, are further enhanced by intrinsic numerical challenges introduced by the long-range LSDA expression. This becomes evident when considering the enhancement factor in Eq. (B.102), which can be rewritten as a sum of four terms

$$\begin{aligned} F_{\mathrm{x}}^{\text{lr-LDA}(\gamma)}(r_{\mathrm{s}}) =& \frac{1}{6}\frac{\gamma^2 r_{\mathrm{s}}^2}{c_{\mathrm{x}}^2} + \frac{4}{3}\frac{\gamma r_{\mathrm{s}}}{c_{\mathrm{x}}}\arctan\left(\frac{2c_{\mathrm{x}}}{\gamma r_{\mathrm{s}}}\right) - \frac{1}{2}\frac{\gamma^2 r_{\mathrm{s}}^2}{c_{\mathrm{x}}^2}\ln\left[1+\frac{4c_{\mathrm{x}}^2}{r_{\mathrm{s}}^2\gamma^2}\right] \\ & - \frac{1}{24}\frac{\gamma^4 r_{\mathrm{s}}^4}{c_{\mathrm{x}}^4}\ln\left[1+\frac{4c_{\mathrm{x}}^2}{r_{\mathrm{s}}^2\gamma^2}\right] \\ =:& F_1(r_{\mathrm{s}}) + F_2(r_{\mathrm{s}}) + F_3(r_{\mathrm{s}}) + F_4(r_{\mathrm{s}})\,. \end{aligned} \tag{8.29}$$

For small densities, i. e., $n \to 0$, which is equivalent to $r_{\mathrm{s}} \to \infty$, the enhancement factor satisfies

$$\lim_{r_{\mathrm{s}}\to\infty} F_{\mathrm{x}}^{\text{lr-LDA}(\gamma)}(r_{\mathrm{s}}) = 1\,. \tag{8.30}$$

However, the individual terms in Eq. (8.29) exhibit the following asymptotic behavior

$$\lim_{r_{\mathrm{s}}\to\infty} F_1 = \infty, \quad \lim_{r_{\mathrm{s}}\to\infty} F_2 = \frac{8}{3}, \quad \lim_{r_{\mathrm{s}}\to\infty} F_3 = -2, \quad \lim_{r_{\mathrm{s}}\to\infty} F_4 = -\infty\,. \tag{8.31}$$

This implies that only the sum of F_1 and F_4 converges, resulting in a partial cancellation in the low-density limit, yielding

$$\lim_{r_{\mathrm{s}}\to\infty}(F_1 + F_4) = \frac{1}{3}\,, \tag{8.32}$$

while the individual terms of F_1 and F_4 diverge as $r_{\mathrm{s}} \to \infty$. A similar behavior can be observed for the derivative of the enhancement factor

$$\begin{aligned} \frac{\partial F_{\mathrm{x}}^{\text{lr-LDA}(\gamma)}}{\partial r_{\mathrm{s}}} =& \frac{2}{3}\frac{\gamma^2 r_{\mathrm{s}}}{c_{\mathrm{x}}^2} + \frac{4}{3}\frac{\gamma}{c_{\mathrm{x}}}\arctan\left(\frac{2c_{\mathrm{x}}}{\gamma r_{\mathrm{s}}}\right) - \frac{\gamma^2 r_{\mathrm{s}}}{c_{\mathrm{x}}^2}\ln\left[1+\frac{4c_{\mathrm{x}}^2}{r_{\mathrm{s}}^2\gamma^2}\right] \\ & - \frac{1}{6}\frac{\gamma^4 r_{\mathrm{s}}^3}{c_{\mathrm{x}}^4}\ln\left[1+\frac{4c_{\mathrm{x}}^2}{r_{\mathrm{s}}^2\gamma^2}\right] \\ =:& \partial_{r_{\mathrm{s}}}F_1(r_{\mathrm{s}}) + \partial_{r_{\mathrm{s}}}F_2(r_{\mathrm{s}}) + \partial_{r_{\mathrm{s}}}F_3(r_{\mathrm{s}}) + \partial_{r_{\mathrm{s}}}F_4(r_{\mathrm{s}})\,, \end{aligned} \tag{8.33}$$

where $\partial_{r_{\mathrm{s}}}F_2$ and $\partial_{r_{\mathrm{s}}}F_3$ vanish individually as $r_{\mathrm{s}} \to \infty$, while $\partial_{r_{\mathrm{s}}}F_1$ and $\partial_{r_{\mathrm{s}}}F_4$ diverge to ∞ and $-\infty$, respectively. However, their sum vanishes in this limit.

The behavior of the enhancement factor and its derivative, where only the sum of the individual terms converges to a constant as $n \to 0$ (or $r_\mathrm{s} \to \infty$), but the individual terms diverge, can lead to numerical challenges. These difficulties become particularly relevant when evaluating the screened LDA potential (see Eq. (8.20)) with orbital densities incorporating nodal planes. In the spatial region corresponding to the nodal plane of the orbital density, oscillatory features emerge in the screened LDA potential evaluated with the orbital density. Unlike in the asymptotic outer region of the system, where all orbitals decay to zero, the other orbitals in the region of the nodal plane of a specific orbital do not necessarily vanish. This issue is crucial when computing the gradient of the energy with respect to the unitary transformation (see Eq. (8.26)), as the product of $v^{\mathrm{SI}(\gamma)}[n_{i\sigma}]$ with the orbital $\varphi_{j\sigma}$ (with $i \neq j$) can amplify the spurious oscillatory features of the potential in the spatial region of the nodal plane of orbital i, leading to numerical difficulties in the ground-state calculation within our lrSIC approach. Various attempts to mitigate these numerical difficulties in the screened LDA potential are discussed in Appendix B.18.

In summary, although the application of the lrSIC approach revealed some numerical challenges, they did not occur for values of the range-separation parameter γ that are relevant within our test set for achieving an energy curve that closely follows the straight-line connection between the energy values of the neutral molecule and its cation. Therefore, these challenges are not expected to pose general limitations when applying the lrSIC approach in physically relevant cases.

8.5 Short-Range (Semi-)Local Exchange with Long-Range Hartree Self-Interaction Correction

Our previously introduced lrSIC approach reduced the overcorrection of the full PZ-SIC while still ensuring the correct asymptotic behavior of the xc potential by screening the orbital-dependent self-Hartree and self-exchange terms to its long-range regime. However, typical range-separated hybrid functionals designed to describe CT excitations achieve the correct asymptotic behavior of the xc potential in a slightly different way: they screen the (semi-)local exchange functional entirely to its short-range contribution and treat the long-range contribution by exact exchange [KK08; SKB09; Ste+10; Kur+11]. Transferring this concept even more directly to the SIC framework than in the previous lrSIC approach, one might also consider an alternative SIC functional, defined as

$$E_\mathrm{xc}^\mathrm{lrHcSIC} = E_\mathrm{x}^{\text{sr-app}(\gamma)}[n_\uparrow, n_\downarrow] + E_\mathrm{c}^\mathrm{app}[n_\uparrow, n_\downarrow] - \sum_{\sigma=\uparrow,\downarrow} \sum_{i=1}^{N_\sigma} \left(E_\mathrm{H}^{\mathrm{lr}(\gamma)}[n_{i\sigma}] + E_\mathrm{c}^\mathrm{app}[n_{i\sigma}, 0] \right) , \tag{8.34}$$

where the (semi-)local exchange energy functional $E_\mathrm{x}^{\text{sr-app}(\gamma)}$ evaluated on the total density is screened to its short-range contribution using the function

$$\mu^{\mathrm{sr}(\gamma)}(|\mathbf{r} - \mathbf{r}'|) = \exp(-\gamma|\mathbf{r} - \mathbf{r}'|) \, . \tag{8.35}$$

The correction term in Eq. (8.34) is reduced to the long-range self-Hartree term $E_\mathrm{H}^{\mathrm{lr}(\gamma)}$ (using the function $\mu^{\mathrm{lr}(\gamma)}$ defined in Eq. (8.7)) and the self-interaction term of the

(semi-)local correlation functional $E_\mathrm{c}^\mathrm{app}[n_{i\sigma}, 0]$. This leads to the corresponding orbital-dependent Hamiltonian

$$\begin{aligned}\hat{H}_{i\sigma} = &-\frac{\hbar^2}{2m}\nabla^2 + v_\mathrm{ext}(\mathbf{r}) + v_\mathrm{H}[n](\mathbf{r}) + v_\mathrm{x}^{\mathrm{sr}(\gamma)}[n_\uparrow, n_\downarrow](\mathbf{r}) + v_\mathrm{c}^\mathrm{app}[n_\uparrow, n_\downarrow](\mathbf{r}) \\ &- \Big(v_\mathrm{H}[n_{i\sigma}](\mathbf{r}) - v_\mathrm{Yukawa}^{(\gamma)}[n_{i\sigma}](\mathbf{r}) + v_\mathrm{c}[n_{i\sigma}, 0](\mathbf{r})\Big)\,,\end{aligned} \tag{8.36}$$

with the short-range (semi-)local exchange potential $v_\mathrm{x}^{\mathrm{sr}(\gamma)}$.

This approach, referred to as lrHcSIC, still ensures the correct asymptotic behavior of the xc potential and corrects the SIE of the Hartree term in the long-range density region, where the HOMO typically dominates the density. For $\gamma \to 0$, the energy functional in Eq. (8.34) reduces to the uncorrected (semi-)local exchange functional, with only the SIC of the correlation functional remaining. In the limit $\gamma \to \infty$ and in the long-range regime, the energy functional reduces to the SIC of the Hartree term and a full self-correlation correction, while the short-range (semi-)local exchange vanishes.

At first glance, it may seem counterintuitive that the exchange part of the energy functional in Eq. (8.34) in the long-range limit reduces to a pure SIC of the Hartree term. However, this can be explained by the observation that the three approaches – range-separated hybrids, the lrSIC approach, and the lrHcSIC approach – do not differ in the long-range regime, where the HOMO dominates the density and, therefore, the total density effectively reduces to an orbital density: For a range-separated hybrid functional, the exchange energy functional in the long-range limit corresponds to the exact exchange functional modified by the Gaussian error function $\mathrm{erf}(\gamma|\mathbf{r}-\mathbf{r}'|)$ which leads to [Lei+97]

$$E_\mathrm{x}^\text{lr-exact} = -\frac{e^2}{2}\sum_{\sigma=\uparrow,\downarrow}\sum_{i,j=1}^{N_\sigma}\iint \mathrm{erf}(\gamma|\mathbf{r}-\mathbf{r}'|)\frac{\varphi_{i\sigma}^*(\mathbf{r})\varphi_{j\sigma}^*(\mathbf{r}')\varphi_{i\sigma}(\mathbf{r}')\varphi_{j\sigma}(\mathbf{r})}{|\mathbf{r}-\mathbf{r}'|}\,\mathrm{d}^3r\,\mathrm{d}^3r'\,. \tag{8.37}$$

However, in the long-range regime, once the HOMO dominates, this expression simplifies to

$$E_\mathrm{x}^\text{lr-exact} = -E_\mathrm{H}[|\varphi_\mathrm{HOMO}|^2]\,. \tag{8.38}$$

The same behavior is straightforward to see for both the exchange part of the lrSIC and lrHcSIC energy expressions in Eq. (8.8) and Eq. (8.34), respectively.

For practical applications of the lrHcSIC approach, we again employ the LSDA functional as our (semi-)local xc approximation. The short-range LSDA (sr-LSDA) energy functional $E_\mathrm{x}^{\text{sr-LDA}(\gamma)}$ can be derived analogously to the long-range expression by replacing $\mu^{\mathrm{lr}(\gamma)}$ with $\mu^{\mathrm{sr}(\gamma)}$ from Eq. (8.35). Specifically, it is obtained by replacing the enhancement factor with

$$F_\mathrm{x}^{\text{sr-LDA}(\gamma)} = 1 - F_\mathrm{x}^{\text{lr-LDA}(\gamma)} \tag{8.39}$$

as given in Ref. [Rob+62], where $F_\mathrm{x}^{\text{lr-LDA}(\gamma)}$ is defined in Eq. (8.19). The corresponding potential expression $v_\mathrm{x}^{\text{sr-LDA}(\gamma)}$ follows from Eq. (8.20), with the additional substitution

$$\frac{\partial F_\mathrm{x}^{\text{sr-LDA}(\gamma)}}{\partial r_\mathrm{s}} = -\frac{\partial F_\mathrm{x}^{\text{lr-LDA}(\gamma)}}{\partial r_\mathrm{s}}\,. \tag{8.40}$$

By evaluating the potential expression of the sr-LDA functional with the total density within the lrHcSIC approach, the numerical difficulties observed for the lr-LDA expression evaluated on orbital densities with nodal planes (see Section 8.4.3) can be circumvented.

8.6 Results for Short-Range Exchange with Long-Range Hartree Self-Interaction Correction

For the application of the lrHcSIC approach together with the short-range LSDA functional (sr-LSDA-lrHcSIC) to our test set consisting of CO, H_2O, and N_2, we use the same numerical parameters as in previous applications of the lrSIC approach. The convergence criteria are the only parameters we adjust: we set $\max(\mathbf{G}_\sigma) = 1.0 \times 10^{-7}$ Ry for the inner loop algorithm and $\Delta_{\text{error},\sigma} = 3.0 \times 10^{-6}$ for the outer loop algorithm (for definitions of these criteria, see Section 6.8). Tests using a tighter convergence criterion of 1.0×10^{-6} did not result in any changes to the results of our sr-LSDA-lrHcSIC calculations.

As in previous sections, we begin by analyzing the straight-line condition and then examine the predicted IP values, considering various values of the range-separation parameter γ in both cases.

8.6.1 Straight-Line Condition for sr-LSDA-lrHcSIC

We start by applying the sr-LSDA-lrHcSIC functional to the CO molecule. The results for different values of the range-separation parameter are shown in Fig. 8.11. Similar

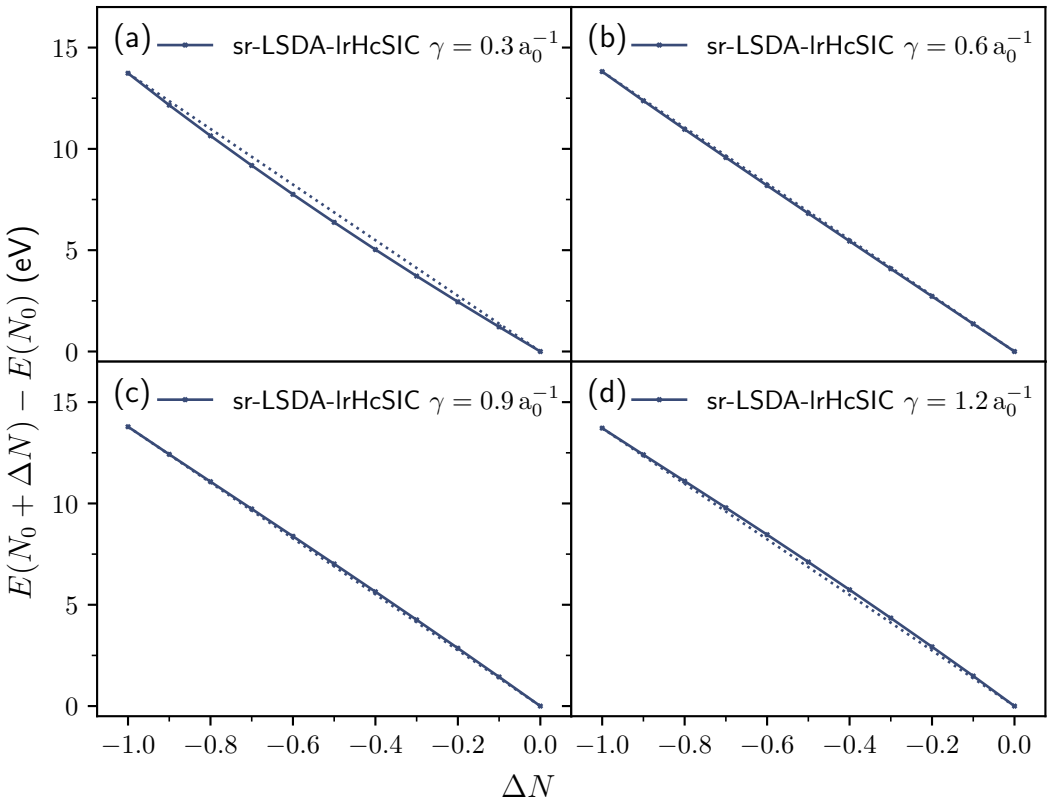

Figure 8.11: Energy curves for CO using sr-LSDA-lrHcSIC with different range-separation parameters: $\gamma = 0.3$ (a), 0.6 (b), 0.9 (c), and $1.2\,a_0^{-1}$ (d). The dotted lines indicate the straight-line reference, highlighting deviations from the straight-line condition.

to the previous results for LSDA-lrSIC, panel (a) of Fig. 8.11 reveals that for a range-separation parameter of $\gamma = 0.3\,a_0^{-1}$, the SIC of the Hartree term remains too weak to

significantly mitigate the spurious convex curvature of the energy curve calculated with the LSDA functional. However, for $\gamma = 0.6\,\mathrm{a}_0^{-1}$ in panel (b), the deviation from the dotted straight-line connection between $E(N_0 - 1)$ and $E(N_0)$ (where N_0 is the number of electrons in the neutral molecule) is significantly reduced, leaving only a very weak convex curvature in the energy curve. For $\gamma = 0.9\,\mathrm{a}_0^{-1}$ in panel (c) and $\gamma = 1.2\,\mathrm{a}_0^{-1}$ in panel (d), the SIC of the Hartree term becomes too short-ranged, leading to an overcorrection and causing the energy curve to become increasingly concave.

This trend is also reflected in the error criterion shown in Fig. 8.12, which quantifies the deviation of the energy curve from the exact straight-line connection for different γ values. For this purpose, the error criterion Δ_{lin} (for the definition, see Eq. (8.24)) is

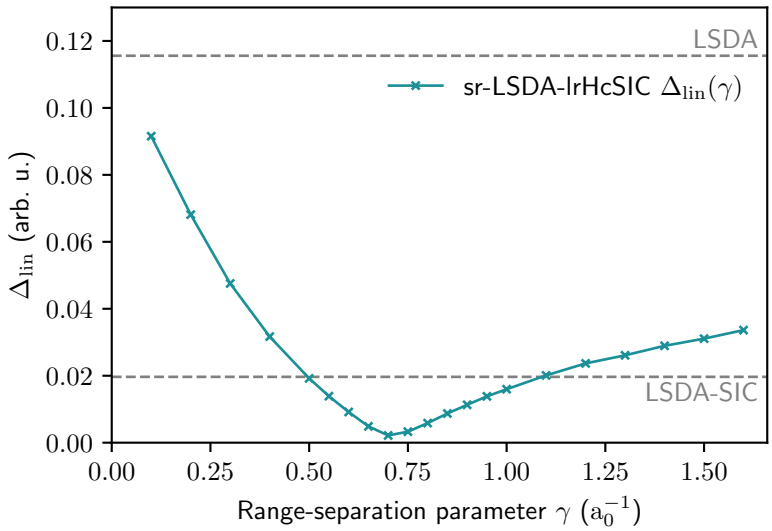

Figure 8.12: Error value Δ_{lin} quantifying the deviation of energy curves from the straight-line condition for CO, computed with sr-LSDA-lrHcSIC for different γ. The gray dotted lines indicate the LSDA and LSDA-SIC values.

evaluated for γ values ranging from 0.1 to $1.6\,\mathrm{a}_0^{-1}$ in steps of $0.1\,\mathrm{a}_0^{-1}$. In the range where the error falls below that of the full PZ-SIC, the step size is further refined to $0.05\,\mathrm{a}_0^{-1}$. The results show that Δ_{lin} decreases rapidly for small values of γ and reaches the value of the full PZ-SIC at approximately $\gamma = 0.5\,\mathrm{a}_0^{-1}$. Our sr-LSDA-lrHcSIC calculation exhibits the smallest deviation from the straight-line condition at $\gamma = 0.7\,\mathrm{a}_0^{-1}$, where the error criterion is reduced by 89% compared to the LSDA-SIC calculation (from $\Delta_{\mathrm{lin}} = 1.97 \times 10^{-2}$ to 0.22×10^{-2}). Additionally, with the lrHcSIC approach, the minimum value obtained in our LSDA-lrSIC calculation ($\Delta_{\mathrm{lin}} = 0.73 \times 10^{-2}$) is further reduced by 71%. For γ values greater than $0.7\,\mathrm{a}_0^{-1}$ in Fig. 8.12, the deviation from the exact straight-line condition increases again, indicating an increasing concave curvature of the energy curve, as already observed in Fig. 8.11.

After analyzing the results for the CO molecule, we now turn to the H_2O molecule. The energy curves using sr-LSDA-lrHcSIC for different values of γ are again plotted in Fig. 8.13. The results exhibit a trend similar to that of the CO molecule. For $\gamma = 0.3\,\mathrm{a}_0^{-1}$ in panel (a), the energy curve exhibits a convex behavior. As the range-separation parameter increases, the convexity gradually decreases, and for $\gamma = 0.9\,\mathrm{a}_0^{-1}$ in panel (c), the curve shows a slight concave deviation from the straight-line connection between $E(N_0)$ and $E(N_0 - 1)$, indicated by a dotted line. At $\gamma = 1.2\,\mathrm{a}_0^{-1}$ in panel (d), the energy curve becomes concave. However, in contrast to CO, all energy curves for H_2O exhibit a

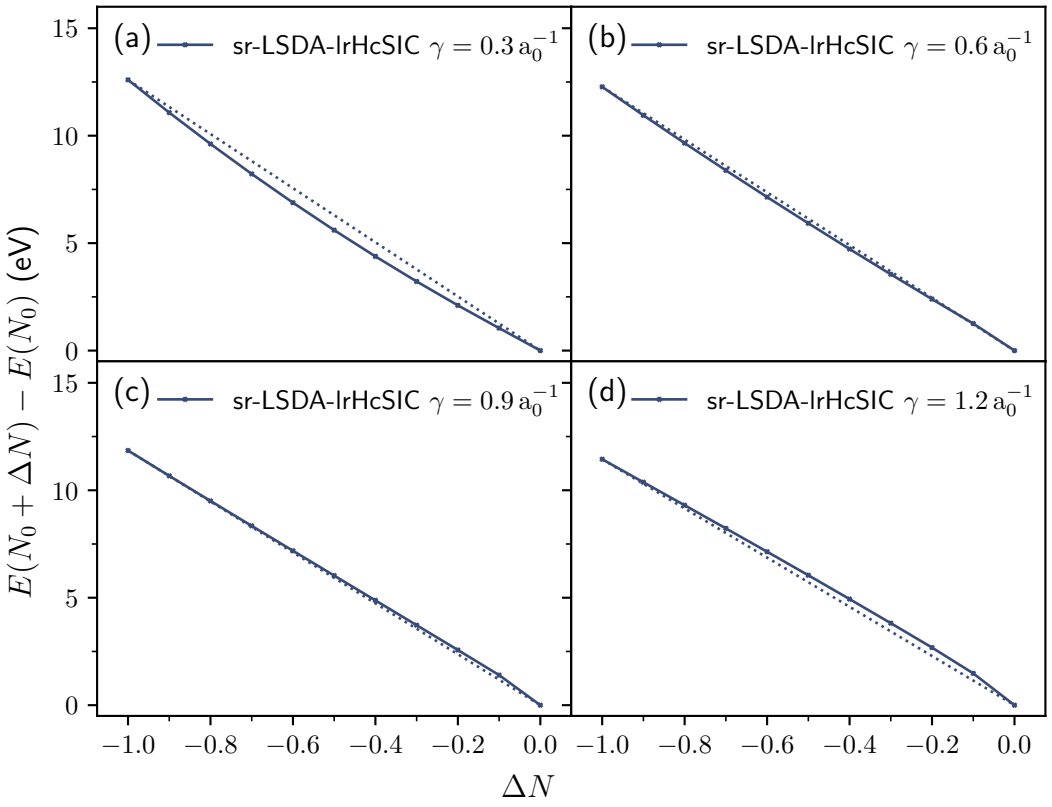

Figure 8.13: Energy curves for H_2O using sr-LSDA-lrHcSIC with different range-separation parameters: $\gamma = 0.3$ (a), 0.6 (b), 0.9 (c), and $1.2\,\mathrm{a_0^{-1}}$ (d). The dotted lines indicate the straight-line reference, highlighting deviations from the straight-line condition.

noticeable change in curvature near the neutral molecule at $\Delta N = -0.1$. This results in a rapid decrease in the HOMO energy in this region, as shown in the corresponding figures in Appendix B.20. The observed transition from convex to concave curvature suggests that the optimal range-separation parameter for fulfilling the straight-line condition lies between $\gamma = 0.6$ and $0.9\,\mathrm{a_0^{-1}}$.

Figure 8.14, which illustrates our error criterion Δ_{lin} for different values of the range-separation parameter, confirms that the error decreases with increasing γ, reaching its minimum at $\gamma = 0.8\,\mathrm{a_0^{-1}}$ in the range where the change in curvature occurs before increasing again as the energy curve becomes concave. At this value, the deviation from the exact straight-line condition is reduced by 67% compared to LSDA-SIC. Notably, the minimum error obtained with the LSDA-lrHcSIC approach lies even below the smallest value found in our previous LSDA-lrSIC calculations, achieving an additional reduction of 30%.

Finally, we turn to the energy curves of the N_2 molecule illustrated in Fig. 8.15. Again, the results for using sr-LSDA-lrHcSIC with a range-separation parameter of $0.3\,\mathrm{a_0^{-1}}$ in panel (a) exhibit a convex behavior of the energy curve. However, in contrast to the transition from convex to concave observed for CO and H_2O for increasing γ values, the energy curves for larger γ values in N_2 develop an S-shaped deviation from the linear connection of the energy values of the neutral molecule and its cation. This behavior, which is already visible for $\gamma = 0.6\,\mathrm{a_0^{-1}}$ in panel (b), becomes more pronounced

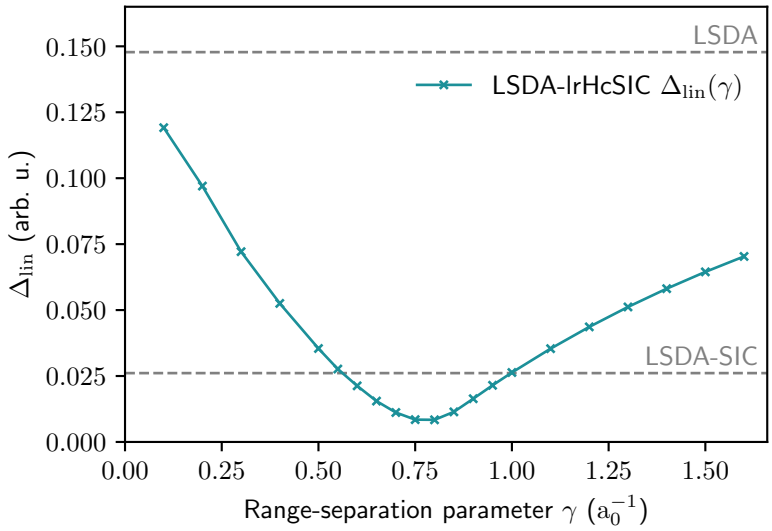

Figure 8.14: Error value Δ_{lin} quantifying the deviation of energy curves from the straight-line condition for H_2O, computed with sr-LSDA-lrHcSIC for different γ. The gray dotted lines indicate the LSDA and LSDA-SIC values.

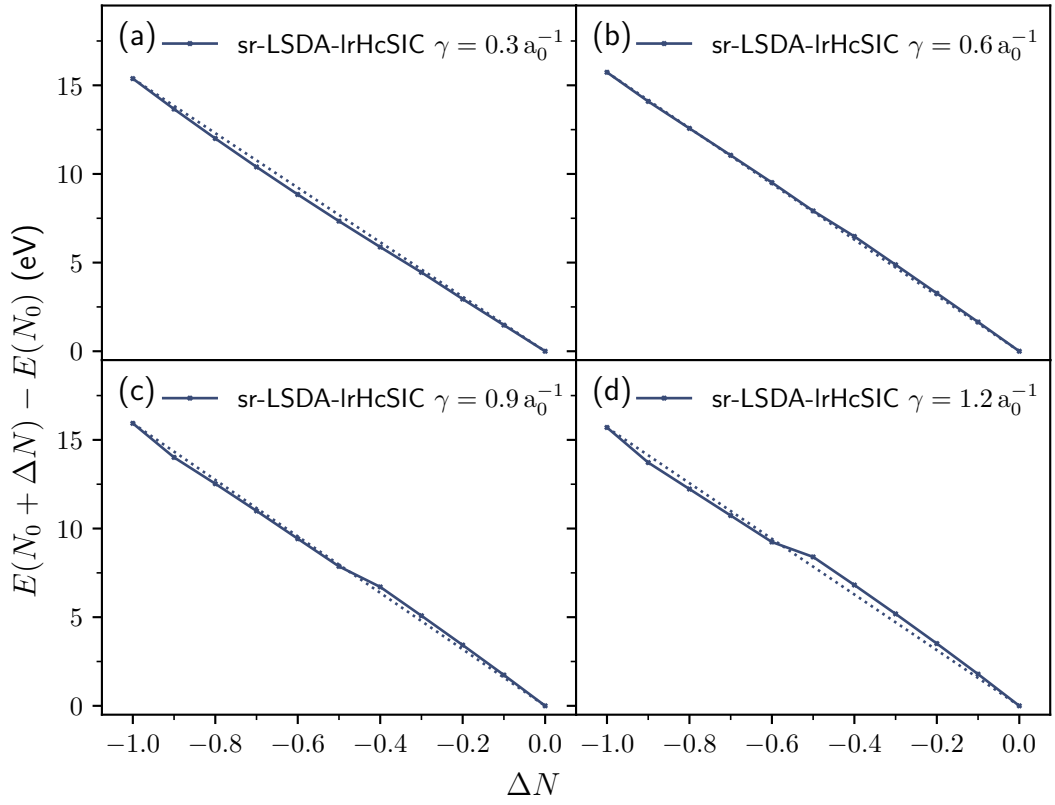

Figure 8.15: Energy curves for N_2 using sr-LSDA-lrHcSIC with different range-separation parameters: $\gamma = 0.3$ (a), 0.6 (b), 0.9 (c), and $1.2\,\mathrm{a_0^{-1}}$ (d). The dotted lines indicate the straight-line reference, highlighting deviations from the straight-line condition.

as γ increases to $0.9\,\mathrm{a}_0^{-1}$ in panel (c) and $1.2\,\mathrm{a}_0^{-1}$ in panel (d) of Fig. 8.15.

This growing deviation from the exact straight-line behavior is also reflected in our error criterion, shown in Fig. 8.16, where the error value increases for γ values greater than $0.5\,\mathrm{a}_0^{-1}$. The minimum error using our LSDA-lrHcSIC approach is found

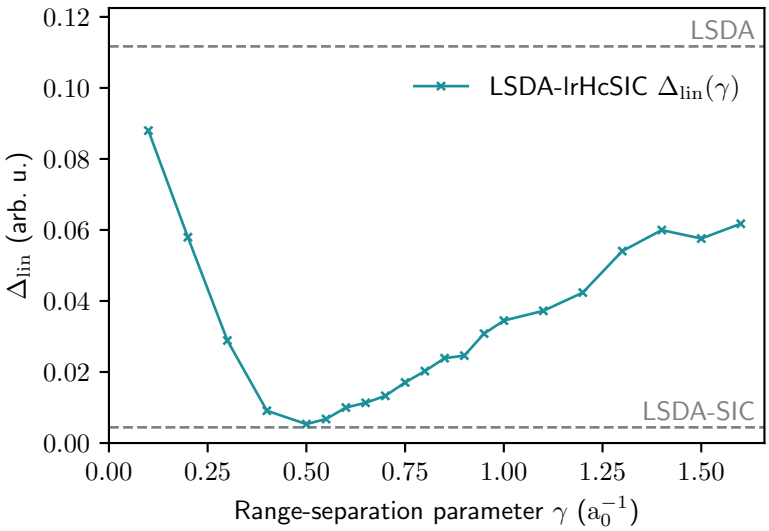

Figure 8.16: Error value Δ_{lin} quantifying the deviation of energy curves from the straight-line condition for N_2, computed with sr-LSDA-lrHcSIC for different γ. The gray dotted lines indicate the LSDA and LSDA-SIC values.

at $\gamma = 0.5\,\mathrm{a}_0^{-1}$. Although the corresponding Δ_{lin} value remains slightly above that of LSDA with full PZ-SIC, it is strongly reduced compared to our previous LSDA-lrSIC approach, decreasing from 1.18×10^{-2} to 0.52×10^{-2}.

Overall, the lrHcSIC approach provides a slightly better fulfillment of the straight-line condition for our test set than the previously tested lrSIC approach. The optimal γ values for the three systems all fall within a range of 0.5 to $0.8\,\mathrm{a}_0^{-1}$, raising the hope that this range could be suitable for a broader class of systems.

8.6.2 IP Theorem for sr-LSDA-lrHcSIC

After investigating the performance of the sr-LSDA-lrHcSIC functional with respect to the straight-line condition, we now turn to the $\Delta\mathrm{SCF} = E(N_0 - 1) - E(N_0)$ values and the HOMO energies of the respective neutral molecule. In our SIC calculations, the latter corresponds to the highest occupied element of the Lagrange multiplier matrix ($\lambda'_{\mathrm{HOMO\,HOMO}} \equiv \epsilon_{\mathrm{HOMO}}$).

The results for the CO molecule, evaluated in steps of $0.05\,\mathrm{a}_0^{-1}$ for the range-separation parameter γ, are shown in Fig. 8.17. The negative ΔSCF value remains nearly independent of γ, exhibiting only minor variations within a range of 0.22 eV from $\gamma = 0.1$ to $1.0\,\mathrm{a}_0^{-1}$ and slightly underestimating the negative value of the experimental IP, which is indicated by the horizontal gray dashed line in Fig. 8.17. In contrast, the HOMO energies are highly sensitive to the choice of γ, varying from -11.13 to -14.69 eV. Compared to the results for our previous lrSIC approach in Section 8.4.2, both the ΔSCF and HOMO energy curves remain numerically stable for $\gamma > 0.1\,\mathrm{a}_0^{-1}$, as the numerical challenges associated with evaluating the screened LSDA expressions on orbital densities are avoided within the lrHcSIC framework.

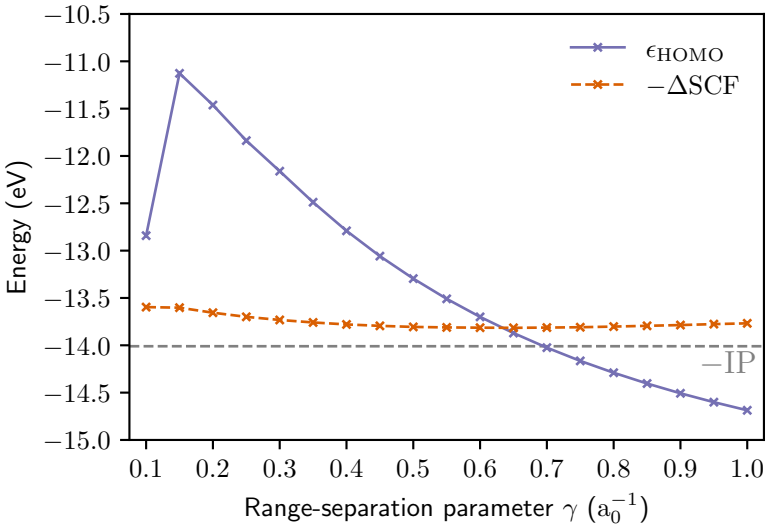

Figure 8.17: HOMO energies, ϵ_{HOMO}, and $-\Delta\mathrm{SCF} = -(E(N_0 - 1) - E(N_0))$ values for CO, calculated using sr-LSDA-lrHcSIC, as a function of the range-separation parameter γ. The gray horizontal line indicates the negative experimental IP value.

Only for $\gamma = 0.1\,\mathrm{a}_0^{-1}$ the HOMO energy curve exhibits a pronounced drop. As in the lrSIC approach, this strong variation for small values of the range-separation parameter can be attributed to numerical challenges in finding the true energy-minimizing unitary transformation when the correction terms in the SIC potential become very small (see the discussion at the beginning of Section 8.4.3).

However, since the IP theorem is satisfied at higher values of the range-separation parameter, this numerical artifact at small γ lies outside the physically relevant region. The IP theorem, i. e., the point where the HOMO energy curve and the ΔSCF curve meet, is fulfilled at approximately $\gamma = 0.65\,\mathrm{a}_0^{-1}$, yielding an IP value of 13.81 eV, which underestimates the experimental IP of 14.01 eV by only 0.20 eV. When comparing the optimal values for fulfilling the IP theorem and the straight-line condition, it becomes clear that the two values are very close to each other, with the optimal γ for the IP theorem being just slightly lower ($\gamma = 0.65\,\mathrm{a}_0^{-1}$) than that for the straight-line condition ($\gamma = 0.7\,\mathrm{a}_0^{-1}$).

Turning to the H_2O molecule, the results for the HOMO energy and the negative ΔSCF value as a function of the range-separation parameter γ are illustrated in Fig. 8.18. The ΔSCF value is again less sensitive to variations in the range-separation parameter (range: 1.02 eV) than the HOMO energy (range: 5.20 eV). In the case of H_2O, the numerical artifacts previously encountered with the lrSIC approach are no longer present, indicating the improved numerical performance of the lrHcSIC method. The IP theorem for the sr-LSDA-lrHcSIC calculation is fulfilled for a range-separation parameter of approximately $\gamma = 0.24\,\mathrm{a}_0^{-1}$, where both the HOMO energy and the ΔSCF value closely match the experimental IP, deviating by only 0.03 eV.

Comparing the optimal range-separation values for satisfying the IP theorem ($\gamma = 0.24\,\mathrm{a}_0^{-1}$) and the straight-line condition ($\gamma = 0.8\,\mathrm{a}_0^{-1}$) reveals a larger deviation between the optimal values for H_2O compared to the CO molecule. This more significant discrepancy can be attributed to the change in curvature of the energy values as a function of fractional particle numbers near the neutral molecule with N_0 electrons for the different range-separation parameters. While these lead to only minor changes in

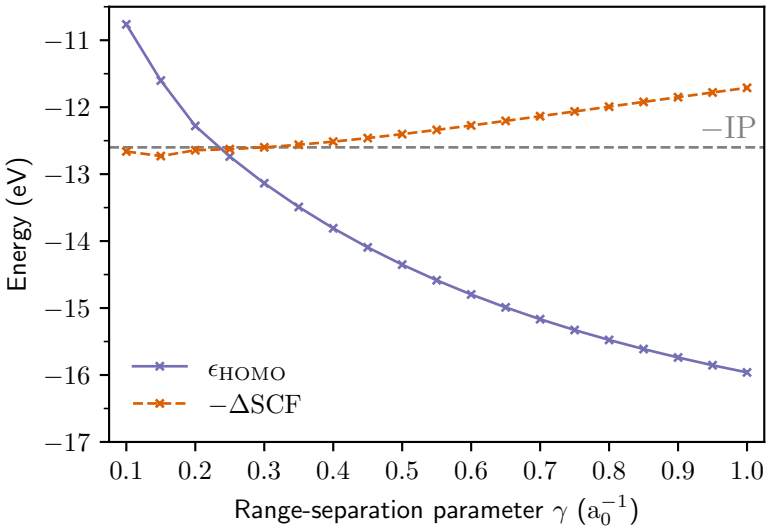

Figure 8.18: HOMO energies, ϵ_{HOMO}, and $-\Delta\mathrm{SCF} = -(E(N_0 - 1) - E(N_0))$ values for H_2O, calculated using sr-LSDA-lrHcSIC, as a function of the range-separation parameter γ. The gray horizontal line indicates the negative experimental IP value.

the total energy, the more pronounced variations in curvature result in a rapid change of the HOMO energy near the neutral molecule, as illustrated in Appendix B.20. As a consequence, although the HOMO energy may remain approximately constant over a wide range of fractional occupation numbers – thereby yielding a good average fulfillment of the straight-line condition – the IP theorem may still be poorly satisfied since the value of ϵ_{HOMO} at the neutral molecule can differ substantially from its values at fractional occupations.

We now turn to the results of our last model system in Fig. 8.19, the N_2 molecule. Similar to the previous model systems, the ΔSCF value is less sensitive to changes in the range-separation parameter (range: 0.87 eV) than the HOMO energy (range: 5.17 eV). However, as observed for the CO molecule, numerical artifacts arise for small values of γ, which are limited to the region $\gamma \leq 0.2\,a_0^{-1}$ and can be attributed to difficulties in finding the true energy-minimizing unitary transformation in this regime of the range-separation parameter.

The IP theorem is fulfilled for higher values of γ, at approximately $0.35\,a_0^{-1}$, with only a slight deviation of 0.12 eV from the experimental IP value. For the N_2 molecule, the optimal range-separation parameter for satisfying the IP theorem lies closer to that for fulfilling the straight-line condition ($\gamma = 0.5\,a_0^{-1}$) than in the case of H_2O. This small deviation between the two optimal values can again be attributed to more prominent variations in the HOMO energy near the neutral N_2 molecule (see Appendix B.20).

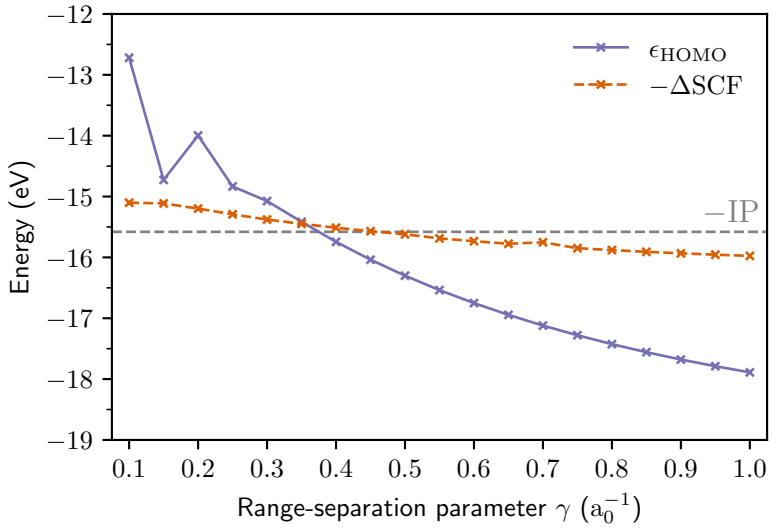

Figure 8.19: HOMO energies, ϵ_{HOMO}, and $-\Delta\mathrm{SCF} = -(E(N_0 - 1) - E(N_0))$ values for N_2, calculated using sr-LSDA-lrHcSIC, as a function of the range-separation parameter γ. The gray horizontal line indicates the negative experimental IP value.

8.7 Summary and Conclusion

In this chapter, we introduced new SIC approaches based on a range-separation scheme, which divides the exchange part of the SIC energy functional into a long and short-range part. This strategy aims to mitigate the overcorrection observed in the full PZ-SIC (see Chapter 7) while preserving the correct asymptotic behavior of the xc potential.

In the first approach, referred to as lrSIC, the SIE of the (semi-)local exchange functional and the Hartree term is corrected only in the long-range regime. Although this approach violates certain formal constraints of the exact xc functional – such as freedom from one-electron self-interaction and size consistency (for a system-dependent tuning) – its application together with the LSDA to the test set of CO, H_2O, and N_2 has demonstrated that the IP theorem can be satisfied and the straight-line condition can be closely resembled for specific values of the range-separation parameter γ. However, the optimal value of γ varies across systems and thus requires a system-dependent tuning procedure.

While the overall performance of the lrSIC approach is promising, numerical difficulties arise in the results for HOMO energies at specific values of the range-separation parameter γ. In particular, for small values of γ, the lrSIC approach exhibits numerical instabilities. Although this range of low γ values is not relevant for fulfilling the straight-line condition, it can become relevant in the case of the H_2O molecule, where the IP theorem is satisfied within this numerically unstable region.

These numerical challenges can be almost completely resolved through a new approach, referred to as lrHcSIC, in which the range-separated exchange function is no longer evaluated on orbital densities that exhibit nodal planes, which can lead to numerical instabilities. Instead, the (semi-)local exchange functional, which is evaluated on the total electron density (free of nodal planes), is screened to its short-range regime. Within this framework, only the long-range Hartree SIE and the SIE of the correlation functional are corrected.

Applying this new approach with the short-range LSDA functional to our test

systems eliminates numerical instabilities within the physically relevant range of the range-separation parameter γ where both the IP theorem and the straight-line condition hold. Moreover, when the IP theorem is satisfied, the predicted IP value obtained with the sr-LSDA-lrHcSIC functional is even closer to the experimental reference than that of the previously discussed LSDA-lrSIC approach. Additionally, for specific values of the range-separation parameter, the straight-line condition can be satisfied more accurately for the considered model systems than with the earlier lrSIC method.

Due to its ability to satisfy the IP theorem and the straight-line condition, the sr-LSDA-lrHcSIC functional offers a promising route for describing CT excitations in TDDFT within a self-interaction corrected framework. In contrast to range-separated hybrid functionals, it does not rely on exact exchange and thus avoids the computational cost of evaluating Fock integrals. Therefore, it remains a worthwhile direction of future work to assess how well the lrHcSIC approach can describe CT excitations in TDDFT applications.

Appendix A

Complementary Work Meta-GGAs in GKS

A.1 Functional Derivatives of Meta-GGA Exchange Including the Nonlinear Core Correction

The exchange part of a meta-GGA can generally be written as

$$E_{\mathrm{x}}^{\mathrm{mGGA}}[n] = \int e_{\mathrm{x}}^{\mathrm{mGGA}}(s(\mathbf{r}), t(\mathbf{r}))\,\mathrm{d}^3 r = A_{\mathrm{x}} \int n^{4/3}(\mathbf{r}) F_{\mathrm{x}}(s(\mathbf{r}), t(\mathbf{r}))\,\mathrm{d}^3 r\,, \tag{A.1}$$

where $A_{\mathrm{x}} = -(3\pi^2)^{1/3}(3e^2)/(4\pi)$, e_{x} is the exchange energy density, and F_{x} is the meta-GGA enhancement factor. In the following, spin-independent expressions are given; the spin-polarized expressions can be derived using the spin-scaling relations, as introduced at the end of this section.

The enhancement factor is parametrized by the dimensionless variables

$$s(\mathbf{r}) = \frac{|\nabla n(\mathbf{r}) + \nabla n_c(\mathbf{r})|}{2\gamma(n(\mathbf{r}) + n_c(\mathbf{r}))^{4/3}}\,, \tag{A.2}$$

with $\gamma = (3\pi^2)^{1/3}$, and

$$t(\mathbf{r}) = \frac{\tau(\mathbf{r})}{\tau^{\mathrm{unif}}(\mathbf{r})} = \frac{5}{3}\frac{\sum_{i=1}^{N} |\nabla\varphi_i(\mathbf{r})|^2 + |\nabla\sqrt{n_c(\mathbf{r})}|^2}{\gamma^2(n(\mathbf{r}) + n_c(\mathbf{r}))^{5/3}}\,, \tag{A.3}$$

where

$$\tau(\mathbf{r}) = \frac{\hbar^2}{2m}\left(\sum_{i=1}^{N} |\nabla\varphi_i(\mathbf{r})|^2 + |\nabla\sqrt{n_c(\mathbf{r})}|^2\right) \tag{A.4}$$

is the kinetic energy density and

$$\tau^{\mathrm{unif}}(\mathbf{r}) = A_{\mathrm{s}}(n(\mathbf{r}) + n_c(\mathbf{r}))^{5/3} \tag{A.5}$$

is its uniform-density limit with $A_{\mathrm{s}} = 3\hbar^2\gamma^2/(10m)$. For Eq. (A.4), the approximation from Section 5.1 in the main text is used, where n is the valence density and n_{c} the core density. Since the core density n_{c} is kept fixed, the functional derivative

$$\frac{\delta E_{\mathrm{x}}^{\mathrm{mGGA}}}{\delta\varphi_i^*(\mathbf{r})} = \int \frac{\delta E_{\mathrm{x}}^{\mathrm{mGGA}}}{\delta n(\mathbf{r}')}\frac{\delta n(\mathbf{r}')}{\delta\varphi_i^*(\mathbf{r})}\,\mathrm{d}^3 r' + \int \frac{\delta E_{\mathrm{x}}^{\mathrm{mGGA}}}{\delta\tau(\mathbf{r}')}\frac{\delta\tau(\mathbf{r}')}{\delta\varphi_i^*(\mathbf{r})}\,\mathrm{d}^3 r' \tag{A.6}$$

is calculated only with respect to the valence orbital φ_i^* [Asc19]. In this expression, the dependencies on the density and the kinetic energy density are treated as independent.

While the functional derivative is given by $\delta E_{\mathrm{x}}^{\mathrm{mGGA}}/\delta\tau(\mathbf{r}') = (\partial e_{\mathrm{x}}^{\mathrm{mGGA}}/\partial\tau)(\mathbf{r}')$, the derivative with respect to the density leads to

$$\begin{aligned}\frac{\delta E_{\mathrm{x}}^{\mathrm{mGGA}}}{\delta n(\mathbf{r})} &= \frac{\partial e_{\mathrm{x}}^{\mathrm{mGGA}}}{\partial n}(\mathbf{r}) + \int \frac{\delta E_{\mathrm{x}}^{\mathrm{mGGA}}}{\delta \nabla' n(\mathbf{r}')} \cdot \frac{\delta \nabla' n(\mathbf{r}')}{\delta n(\mathbf{r})}\,\mathrm{d}^3 r \\ &= \frac{\partial e_{\mathrm{x}}^{\mathrm{mGGA}}}{\partial n}(\mathbf{r}) + \int \frac{\delta E_{\mathrm{x}}^{\mathrm{mGGA}}}{\delta \nabla' n(\mathbf{r}')} \cdot \nabla' \delta(\mathbf{r}-\mathbf{r}')\,\mathrm{d}^3 r' = \frac{\partial e_{\mathrm{x}}^{\mathrm{mGGA}}}{\partial n}(\mathbf{r}) - \nabla \cdot \left(\frac{\partial e_{\mathrm{x}}^{\mathrm{mGGA}}}{\partial \nabla n}(\mathbf{r})\right).\end{aligned} \tag{A.7}$$

Together with

$$\frac{\delta n(\mathbf{r}')}{\delta \varphi_i^*(\mathbf{r})} = \varphi_i(\mathbf{r})\delta(\mathbf{r}-\mathbf{r}') \tag{A.8}$$

and

$$\frac{\delta \tau(\mathbf{r}')}{\delta \varphi_i^*(\mathbf{r})} = \frac{\hbar^2}{2m}\nabla'\varphi_i(\mathbf{r}') \cdot \nabla' \delta(\mathbf{r}-\mathbf{r}') \tag{A.9}$$

the functional derivative of the meta-GGA exchange energy can be written as

$$\begin{aligned}\frac{\delta E_{\mathrm{x}}^{\mathrm{mGGA}}}{\delta \varphi_i^*(\mathbf{r})} = &\left\{\frac{\partial e_{\mathrm{x}}^{\mathrm{mGGA}}}{\partial n}(\mathbf{r}) - \nabla \cdot \left(\frac{\partial e_{\mathrm{x}}^{\mathrm{mGGA}}}{\partial \nabla n}(\mathbf{r})\right)\right\}\varphi_i(\mathbf{r}) \\ &- \frac{\hbar^2}{2m}\left\{\frac{\partial e_{\mathrm{x}}^{\mathrm{mGGA}}}{\partial \tau}(\mathbf{r})\nabla^2\varphi_i(\mathbf{r}) + \nabla\left(\frac{\partial e_{\mathrm{x}}^{\mathrm{mGGA}}}{\partial \tau}(\mathbf{r})\right)\cdot\nabla\varphi_i(\mathbf{r})\right\}.\end{aligned} \tag{A.10}$$

In terms of the enhancement factor $F_{\mathrm{x}}^{\mathrm{mGGA}}$ parametrized in $\{s,t\}$, the derivatives of the exchange energy are expressed as

$$\begin{aligned}\frac{\partial e_{\mathrm{x}}^{\mathrm{mGGA}}}{\partial n} &= \frac{4}{3}A_{\mathrm{x}}n^{1/3}F_{\mathrm{x}}(s,t) + A_{\mathrm{x}}n^{4/3}\left.\frac{\partial F_{\mathrm{x}}}{\partial s}\right|_t\frac{\partial s}{\partial n} + A_{\mathrm{x}}n^{4/3}\left.\frac{\partial F_{\mathrm{x}}}{\partial t}\right|_s\frac{\partial t}{\partial n} \\ &= A_{\mathrm{x}}n^{1/3}\left[\frac{4}{3}F_{\mathrm{x}}(s,t) - \frac{4}{3}\frac{n}{n+n_{\mathrm{c}}}s\left.\frac{F_{\mathrm{x}}}{\partial s}\right|_t - \frac{5}{3}\frac{n}{n+n_{\mathrm{c}}}t\left.\frac{\partial F_{\mathrm{x}}}{\partial t}\right|_s\right]\end{aligned} \tag{A.11}$$

and

$$\begin{aligned}\frac{\partial e_{\mathrm{x}}^{\mathrm{mGGA}}}{\partial \nabla n} = A_{\mathrm{x}}n^{4/3}\left.\frac{\partial F}{\partial s}\right|_t\frac{\partial s}{\partial \nabla n} &= A_{\mathrm{x}}\frac{n^{4/3}}{(n+n_{\mathrm{c}})^{4/3}}\left.\frac{\partial F_{\mathrm{x}}}{\partial s}\right|_t\frac{\nabla n + \nabla n_{\mathrm{c}}}{2\gamma|\nabla n + \nabla n_{\mathrm{c}}|} \\ &= A_{\mathrm{x}}\frac{n^{4/3}}{(n+n_{\mathrm{c}})^{4/3}}\frac{1}{s}\left.\frac{\partial F_{\mathrm{x}}}{\partial s}\right|_t\frac{\nabla n + \nabla n_{\mathrm{c}}}{4\gamma^2(n+n_{\mathrm{c}})^{4/3}},\end{aligned} \tag{A.12}$$

which leads to

$$\begin{aligned}-\nabla\cdot\left(\frac{\partial e_{\mathrm{x}}^{\mathrm{mGGA}}}{\partial \nabla n}\right) = -\frac{1}{2}A_{\mathrm{x}}\Bigg[&\frac{\nabla n + \nabla n_{\mathrm{c}}}{n+n_{\mathrm{c}}}\cdot\nabla\left(\frac{n^{4/3}}{(n+n_{\mathrm{c}})^{4/3}}\frac{1}{2\gamma^2(n+n_{\mathrm{c}})^{1/3}}\frac{1}{s}\left.\frac{\partial F_{\mathrm{x}}}{\partial s}\right|_t\right) \\ &+ \frac{n^{4/3}}{(n+n_{\mathrm{c}})^{4/3}}\frac{1}{2\gamma^2(n+n_{\mathrm{c}})^{1/3}}\frac{1}{s}\left.\frac{\partial F_{\mathrm{x}}}{\partial s}\right|_t\frac{\nabla^2(n+n_{\mathrm{c}})}{n+n_{\mathrm{c}}} \\ &- \frac{n^{4/3}}{(n+n_{\mathrm{c}})^{4/3}}\frac{1}{2\gamma^2(n+n_{\mathrm{c}})^{1/3}}\frac{1}{s}\left.\frac{\partial F_{\mathrm{x}}}{\partial s}\right|_t\frac{|\nabla n + \nabla n_{\mathrm{c}}|^2}{(n+n_{\mathrm{c}})^2}\Bigg].\end{aligned} \tag{A.13}$$

For numerical reasons (see Ref. [Sch+14b]), the density is typically written in terms of its square root. Therefore Eq. (A.13) is rewritten to

$$-\nabla\cdot\left(\frac{\partial e_{\mathrm{x}}^{\mathrm{mGGA}}}{\partial\nabla n}\right)=-A_{\mathrm{x}}\left[\frac{\nabla\sqrt{n+n_{\mathrm{c}}}}{\sqrt{n+n_{\mathrm{c}}}}\cdot\nabla\left(\frac{n^{4/3}}{(n+n_{\mathrm{c}})^{4/3}}\frac{1}{2\gamma^2(n+n_{\mathrm{c}})^{1/3}}\frac{1}{s}\left.\frac{\partial F_{\mathrm{x}}}{\partial s}\right|_t\right)\right.$$
$$\left.+\frac{n^{4/3}}{(n+n_{\mathrm{c}})^{4/3}}\frac{1}{2\gamma^2(n+n_{\mathrm{c}})^{1/3}}\frac{1}{s}\left.\frac{\partial F_{\mathrm{x}}}{\partial s}\right|_t\frac{\nabla^2\sqrt{n+n_{\mathrm{c}}}}{\sqrt{n+n_{\mathrm{c}}}}-\frac{1}{2}n^{1/3}\frac{n}{n+n_{\mathrm{c}}}s\left.\frac{\partial F_{\mathrm{x}}}{\partial s}\right|_t\right]. \quad \text{(A.14)}$$

The last derivative of the energy density is

$$\frac{\partial e_{\mathrm{x}}^{\mathrm{mGGA}}}{\partial\tau}=A_{\mathrm{x}}n^{4/3}\left.\frac{\partial F_{\mathrm{x}}}{\partial t}\right|_s\frac{\partial t}{\partial\tau}=\frac{10m}{3\hbar^2}A_{\mathrm{x}}\frac{n^{4/3}}{(n+n_{\mathrm{c}})^{4/3}}\frac{1}{\gamma^2(n+n_{\mathrm{c}})^{1/3}}\left.\frac{\partial F_{\mathrm{x}}}{\partial t}\right|_s \quad \text{(A.15)}$$

which leads to

$$-\frac{\hbar^2}{2m}\left[\frac{\partial e_{\mathrm{x}}^{\mathrm{mGGA}}}{\partial\tau}\nabla^2\varphi_i+\nabla\varphi_i\cdot\nabla\left(\frac{\partial e_{\mathrm{x}}^{\mathrm{mGGA}}}{\partial\tau}\right)\right]$$
$$=-\frac{5}{3}A_{\mathrm{x}}\left[\frac{n^{4/3}}{(n+n_{\mathrm{c}})^{4/3}}\frac{1}{\gamma^2(n+n_{\mathrm{c}})^{1/3}}\left.\frac{\partial F_{\mathrm{x}}}{\partial t}\right|_s\nabla^2\varphi_i\right.$$
$$\left.+\nabla\varphi_i\cdot\nabla\left(\frac{n^{4/3}}{(n+n_{\mathrm{c}})^{4/3}}\frac{1}{\gamma^2(n+n_{\mathrm{c}})^{1/3}}\left.\frac{\partial F_{\mathrm{x}}}{\partial t}\right|_s\right)\right]. \quad \text{(A.16)}$$

With the definition of the auxiliary functions

$$g(n,n_{\mathrm{c}})=\frac{n}{n+n_{\mathrm{c}}}=\frac{1}{1+\frac{n_{\mathrm{c}}}{n}}, \quad \text{(A.17)}$$

$$h_s=\frac{1}{2}\frac{g(n,n_{\mathrm{c}})^{4/3}}{\gamma^2(n+n_{\mathrm{c}})^{1/3}}\frac{1}{s}\left.\frac{\partial F_{\mathrm{x}}}{\partial s}\right|_t, \quad \text{(A.18)}$$

and

$$h_t=\frac{5}{3}\frac{g(n,n_{\mathrm{c}})^{4/3}}{\gamma^2(n+n_{\mathrm{c}})^{1/3}}\left.\frac{\partial F_{\mathrm{x}}}{\partial t}\right|_s \quad \text{(A.19)}$$

one obtains the final result

$$\frac{\delta E_{\mathrm{x}}^{\mathrm{mGGA}}}{\delta\varphi_i^*}=\varphi_iA_{\mathrm{x}}n^{1/3}\left[\frac{4}{3}F_{\mathrm{x}}-g(n,n_{\mathrm{c}})\frac{5}{6}s\left.\frac{\partial F_{\mathrm{x}}}{\partial s}\right|_t-g(n,n_{\mathrm{c}})\frac{5}{3}t\left.\frac{\partial F_{\mathrm{x}}}{\partial t}\right|_s\right]$$
$$-\varphi_iA_{\mathrm{x}}\left[h_s\frac{\nabla^2\sqrt{n+n_{\mathrm{c}}}}{\sqrt{n+n_{\mathrm{c}}}}+\nabla h_s\cdot\frac{\nabla\sqrt{n+n_{\mathrm{c}}}}{\sqrt{n+n_{\mathrm{c}}}}\right]-A_{\mathrm{x}}\left[h_t\nabla^2\varphi_i+\nabla h_t\cdot\nabla\varphi_i\right]. \quad \text{(A.20)}$$

The meta-GGAs used in this work are typically parametrized in $\{s,\alpha\}$ or more specifically in $\{s^2,\alpha\}$ with

$$\alpha(\mathbf{r})=\frac{\tau(\mathbf{r})-\tau^{\mathrm{W}}(\mathbf{r})}{\tau^{\mathrm{unif}}(\mathbf{r})} \quad \text{(A.21)}$$

with the von Weizsäcker kinetic energy density

$$\tau^{\mathrm{W}}(\mathbf{r})=\frac{\hbar^2}{8m}\frac{|\nabla n(\mathbf{r})+\nabla n_{\mathrm{c}}(\mathbf{r})|^2}{n(\mathbf{r})+n_{\mathrm{c}}(\mathbf{r})}. \quad \text{(A.22)}$$

For a change in variables $\alpha = t - 5s^2/3$ is used along with the derivatives of the enhancement factor in $\{s^2, \alpha\}$:

$$\frac{1}{2s}\left.\frac{\partial F_\mathrm{x}}{\partial s}\right|_t = \left.\frac{\partial F_\mathrm{x}}{\partial s^2}\right|_t = \left.\frac{\partial F_\mathrm{x}}{\partial s^2}\right|_\alpha - \frac{5}{3}\left.\frac{\partial F_\mathrm{x}}{\partial \alpha}\right|_{s^2} \qquad \text{and} \qquad \left.\frac{\partial F_\mathrm{x}}{\partial t}\right|_s = \left.\frac{\partial F_\mathrm{x}}{\partial \alpha}\right|_{s^2} \tag{A.23}$$

Then, Eq. (A.20) can be expressed in terms of the parameters s^2, α as

$$\begin{aligned}\frac{\delta E_\mathrm{x}^\mathrm{mGGA}}{\delta \varphi_i^*} = \varphi_i A_\mathrm{x} n^{1/3}\left[\frac{4}{3}F_\mathrm{x} - g(n,n_\mathrm{c})\frac{5}{3}s^2\left.\frac{\partial F_\mathrm{x}}{\partial s^2}\right|_\alpha - g(n,n_\mathrm{c})\frac{5}{3}\alpha\left.\frac{\partial F_\mathrm{x}}{\partial \alpha}\right|_{s^2}\right] \\ - \varphi_i A_\mathrm{x}\left[h_s\frac{\nabla^2\sqrt{n+n_\mathrm{c}}}{\sqrt{n+n_\mathrm{c}}} + \nabla h_s \cdot \frac{\nabla\sqrt{n+n_\mathrm{c}}}{\sqrt{n+n_\mathrm{c}}}\right] - A_\mathrm{x}\left[h_t\nabla^2\varphi_i + \nabla h_t\cdot\nabla\varphi_i\right]\end{aligned} \tag{A.24}$$

with

$$h_s = \frac{g(n,n_\mathrm{c})^{4/3}}{\gamma^2(n+n_\mathrm{c})^{1/3}}\left(\left.\frac{\partial F_\mathrm{x}}{\partial s^2}\right|_\alpha - \frac{5}{3}\left.\frac{\partial F_\mathrm{x}}{\partial \alpha}\right|_{s^2}\right) \tag{A.25}$$

and

$$h_t = \frac{5}{3}\frac{g(n,n_\mathrm{c})^{4/3}}{\gamma^2(n+n_\mathrm{c})^{1/3}}\left.\frac{\partial F_\mathrm{x}}{\partial \alpha}\right|_{s^2}. \tag{A.26}$$

Current Correction in TDGKS

The current correction in the TDGKS scheme, discussed in Section 5.2 and proposed by Becke [Bec02] and Tao [Tao05], involves modifying the kinetic energy density by replacing τ with

$$\hat{\tau}(\mathbf{r},t) = \tau(\mathbf{r},t) - m\frac{|\mathbf{j}_\mathrm{p}(\mathbf{r},t)|^2}{2(n(\mathbf{r},t)+n_\mathrm{c}(\mathbf{r},t))}, \tag{A.27}$$

where the paramagnetic current density is defined in Eq. (5.12). Here, the core density n_c is explicitly included to maintain consistency with the previous notation.

This modification introduces the additional term

$$\begin{aligned}\frac{\delta}{\delta\varphi_i^*(\mathbf{r},t)}\left[-m\frac{|\mathbf{j}_\mathrm{p}(\mathbf{r}',t)|^2}{2(n(\mathbf{r}',t)+n_\mathrm{c}(\mathbf{r}'))}\right] = \\ - \frac{\mathbf{j}_\mathrm{p}(\mathbf{r}',t)}{n(\mathbf{r}',t)+n_\mathrm{c}(\mathbf{r}')}\frac{\hbar}{2\mathrm{i}}[\varphi_i(\mathbf{r}',t)\nabla'\delta(\mathbf{r}-\mathbf{r}') - \delta(\mathbf{r}-\mathbf{r}')\nabla'\varphi_i(\mathbf{r}',t)] \\ + \frac{m}{2}\frac{|\mathbf{j}_\mathrm{p}(\mathbf{r}',t)|^2}{(n(\mathbf{r}',t)+n_\mathrm{c}(\mathbf{r}'))^2}\varphi_i(\mathbf{r}',t)\delta(\mathbf{r}-\mathbf{r}').\end{aligned} \tag{A.28}$$

Therefore, Eq. (A.10) modifies to

$$\begin{aligned}\frac{\delta E_\mathrm{x}^\mathrm{mGGA}}{\delta\varphi_i^*} = \varphi_i\left\{\frac{\partial e_\mathrm{x}^\mathrm{mGGA}}{\partial n} - \nabla\cdot\left(\frac{\partial e_\mathrm{x}^\mathrm{mGGA}}{\partial\nabla n}\right)\right\} \\ - \frac{\hbar^2}{2m}\left\{\frac{\partial e_\mathrm{x}^\mathrm{mGGA}}{\partial\hat{\tau}}\nabla^2\varphi_i + \nabla\varphi_i\cdot\nabla\left(\frac{\partial e_\mathrm{x}^\mathrm{mGGA}}{\partial\hat{\tau}}\right)\right\} \\ + \frac{\hbar}{2\mathrm{i}}\left[\nabla\cdot\left(\frac{\partial e_\mathrm{xc}^\mathrm{mGGA}}{\partial\hat{\tau}}\frac{\mathbf{j}_\mathrm{p}}{n+n_\mathrm{c}}\varphi_i\right) + \frac{\mathbf{j}_\mathrm{p}}{n+n_\mathrm{c}}\frac{\partial e_\mathrm{xc}^\mathrm{mGGA}}{\partial\hat{\tau}}\cdot\nabla\varphi_i\right] + \frac{m}{2}\frac{|\mathbf{j}_\mathrm{p}|^2}{(n+n_\mathrm{c})^2}\frac{\partial e_\mathrm{xc}^\mathrm{mGGA}}{\partial\hat{\tau}}\varphi_i \\ = \varphi_i\left\{\frac{\partial e_\mathrm{x}^\mathrm{mGGA}}{\partial n} - \nabla\cdot\left(\frac{\partial e_\mathrm{x}^\mathrm{mGGA}}{\partial\nabla n}\right)\right\} + \frac{1}{2m}\hat{\boldsymbol{\pi}}\cdot\left[\frac{\partial e_\mathrm{xc}^\mathrm{mGGA}}{\partial\hat{\tau}}\hat{\boldsymbol{\pi}}\varphi_i\right]\end{aligned} \tag{A.29}$$

where $\hat{\boldsymbol{\pi}} = (\hbar/\mathrm{i})\nabla - m\mathbf{j}_\mathrm{p}/(n+n_\mathrm{c})$.

The spin-polarized equations can be obtained using the spin-scaling relationships introduced in Section 3.6.3, i. e. evaluating the equations at $n = 2n_\sigma = 2\sum_{j=1}^{N_\sigma} |\varphi_{j\sigma}|^2$ and $\tau = 2\tau_\sigma = 2\sum_{j=1}^{N_\sigma} \hbar^2/(2m)|\nabla\varphi_{j\sigma}|^2$ with N_σ as the number of occupied orbitals with spin σ.

A.2 Functional Derivatives of Meta-GGA Correlation Including the Nonlinear Core Correction

The meta-GGA correlation is typically written as

$$E_\mathrm{c}^\mathrm{mGGA}[n_\uparrow, n_\downarrow] = \int n(\mathbf{r})\epsilon_\mathrm{c}(r_\mathrm{s}(\mathbf{r}), \zeta(\mathbf{r}), s(\mathbf{r}), \alpha(\mathbf{r}))\,\mathrm{d}^3r \tag{A.30}$$

with the correlation energy density per particle ϵ_c depending on the core-corrected Wigner-Seitz radius and the spin spin-polarization factor

$$r_\mathrm{s}(\mathbf{r}) = \left(\frac{3}{4\pi(n(\mathbf{r}) + n_\mathrm{c}(\mathbf{r}))}\right)^{1/3} \qquad \text{and} \qquad \zeta(\mathbf{r}) = \frac{n_\uparrow(\mathbf{r}) - n_\downarrow(\mathbf{r})}{n(\mathbf{r}) + n_\mathrm{c}(\mathbf{r})}\,, \tag{A.31}$$

respectively. s is defined as in Eq. (A.2) and α is defined as

$$\begin{aligned}\alpha(\mathbf{r}) &= \frac{\tau(\mathbf{r}) - \tau^\mathrm{W}(\mathbf{r})}{\tau^\mathrm{unif}(\mathbf{r})} \\ &= \frac{\frac{\hbar^2}{2m}\left(\sum_{\sigma=\uparrow,\downarrow}\sum_{i=1}^{N_\sigma} |\nabla\varphi_{i\sigma}(\mathbf{r})|^2 + |\nabla\sqrt{n_\mathrm{c}(\mathbf{r})}|^2\right) - \frac{\hbar^2}{8m}\frac{|\nabla n(\mathbf{r}) + \nabla n_c(\mathbf{r})|^2}{(n(\mathbf{r}) + n_c(\mathbf{r}))}}{A_\mathrm{s}(n(\mathbf{r}) + n_\mathrm{c}(\mathbf{r}))^{5/3} d_\mathrm{s}(\zeta(\mathbf{r}))}\end{aligned} \tag{A.32}$$

with

$$d_\mathrm{s}(\zeta) = \frac{1}{2}\left[(1+\zeta)^{5/3} + (1-\zeta)^{5/3}\right]. \tag{A.33}$$

For the correlation expressions $n = n_\uparrow + n_\downarrow$ as well as $\tau = \tau_\uparrow + \tau_\downarrow$ is used.

Analogous to the exchange part, the derivative with respect to the valence orbital $\varphi_{i\sigma}^*$ leads to

$$\begin{aligned}\frac{\delta E_\mathrm{c}^\mathrm{mGGA}}{\delta\varphi_{i\sigma}^*(\mathbf{r})} = \varphi_{i\sigma}(\mathbf{r})&\left\{\frac{\partial(n\epsilon_\mathrm{c})}{\partial n_\sigma}(\mathbf{r}) - \nabla\cdot\left(\frac{\partial(n\epsilon_\mathrm{c})}{\partial\nabla n_\sigma}(\mathbf{r})\right)\right\} \\ &- \frac{\hbar^2}{2m}\left[\frac{\partial(n\epsilon_\mathrm{c})}{\partial\tau_\sigma}(\mathbf{r})\nabla^2\varphi_{i\sigma}(\mathbf{r}) + \nabla\varphi_{i\sigma}(\mathbf{r})\cdot\nabla\left(\frac{\partial(n\epsilon_\mathrm{c})}{\partial\tau_\sigma}(\mathbf{r})\right)\right].\end{aligned} \tag{A.34}$$

(The time-dependent application with the current-density correction, i. e., replacing τ with $\hat{\tau}$ as discussed in Section 5.2, can be carried out analogously to the treatment of the exchange part.)

The derivatives of r_s, ζ, s and α with respect to n_σ, ∇n_σ and τ_σ are:

$$\frac{\partial r_\mathrm{s}}{\partial n_\sigma} = -\frac{1}{3}\frac{r_\mathrm{s}}{n + n_\mathrm{c}}\,, \tag{A.35}$$

$$\frac{\partial\zeta}{\partial n_\sigma} = \frac{\pm 1 - \zeta}{n + n_\mathrm{c}}\,, \tag{A.36}$$

$$\frac{\partial s}{\partial n_\sigma} = -\frac{4}{3}\frac{s}{n + n_\mathrm{c}}\,, \qquad \frac{\partial s}{\partial\nabla n_\sigma} = \frac{\nabla n + \nabla n_\mathrm{c}}{4\gamma^2(n + n_\mathrm{c})^{8/3}}\frac{1}{s}\,, \tag{A.37}$$

$$\frac{\partial\alpha}{\partial n_\sigma} = -\frac{5}{3}\frac{\alpha}{n+n_\mathrm{c}} + \frac{1}{n+n_\mathrm{c}}\frac{\tau^\mathrm{W}}{\tau^\mathrm{unif}} + \frac{\alpha}{n+n_\mathrm{c}}(\zeta\mp 1)\frac{d_\mathrm{s}'(\zeta)}{d_\mathrm{s}(\zeta)}\,,$$
$$\frac{\partial\alpha}{\partial\nabla n_\sigma} = -\frac{10}{3d_\mathrm{s}(\zeta)}\frac{\nabla n+\nabla n_\mathrm{c}}{4\gamma^2(n+n_\mathrm{c})^{8/3}}\,, \tag{A.38}$$

and

$$\frac{\partial\alpha}{\partial\tau_\sigma} = \frac{1}{\tau^\mathrm{unif}} \tag{A.39}$$

with

$$d_\mathrm{s}'(\zeta) = \frac{\partial d_\mathrm{s}}{\partial\zeta} = \frac{5}{6}\left[(1+\zeta)^{2/3} - (1-\zeta)^{2/3}\right]. \tag{A.40}$$

Using these expressions the derivatives of Eq. (A.34) can be written as

$$\begin{aligned}\frac{\partial(n\epsilon_\mathrm{c})}{\partial n_\sigma} =&\epsilon_\mathrm{c} + n\frac{\partial\epsilon_\mathrm{c}}{\partial n_\sigma} = \epsilon_\mathrm{c} + n\left(\frac{\partial\epsilon_\mathrm{c}}{\partial r_\mathrm{s}}\frac{\partial r_\mathrm{s}}{\partial n_\sigma} + \frac{\partial\epsilon_\mathrm{c}}{\partial\zeta}\frac{\partial\zeta}{\partial n_\sigma} + \frac{\partial\epsilon_\mathrm{c}}{\partial s}\frac{\partial s}{\partial n_\sigma} + \frac{\partial\epsilon_\mathrm{c}}{\partial\alpha}\frac{\partial\alpha}{\partial n_\sigma}\right)\\ =&\epsilon_\mathrm{c} - \frac{1}{3}\frac{n}{n+n_\mathrm{c}}r_\mathrm{s}\frac{\partial\epsilon_\mathrm{c}}{\partial r_\mathrm{s}} + (\pm 1-\zeta)\frac{n}{n+n_\mathrm{c}}\frac{\partial\epsilon_\mathrm{c}}{\partial\zeta} - \frac{4}{3}\frac{n}{n+n_\mathrm{c}}s\frac{\partial\epsilon_\mathrm{c}}{\partial s}\\ &+\left[-\frac{5}{3}\alpha\frac{n}{n+n_\mathrm{c}} + \frac{n}{n+n_\mathrm{c}}\frac{\tau^\mathrm{W}}{\tau^\mathrm{unif}} + \alpha\frac{n}{n+n_\mathrm{c}}(\zeta\mp 1)\frac{d_\mathrm{s}'(\zeta)}{d_\mathrm{s}(\zeta)}\right]\frac{\partial\epsilon_\mathrm{c}}{\partial\alpha}\,,\end{aligned} \tag{A.41}$$

$$\begin{aligned}\frac{\partial(n\epsilon_\mathrm{c})}{\partial\nabla n_\sigma} =&n\frac{\partial\epsilon_\mathrm{c}}{\partial\nabla n_\sigma} = n\left(\frac{\partial\epsilon_\mathrm{c}}{\partial s}\frac{\partial s}{\partial\nabla n_\sigma} + \frac{\partial\epsilon_\mathrm{c}}{\partial\alpha}\frac{\partial\alpha}{\partial\nabla n_\sigma}\right)\\ =&\frac{n}{(n+n_\mathrm{c})^{8/3}}\frac{\nabla n+\nabla n_\mathrm{c}}{4\gamma^2}\frac{1}{s}\frac{\partial\epsilon_\mathrm{c}}{\partial s} - \frac{10}{3d_\mathrm{s}(\zeta)}\frac{n}{(n+n_\mathrm{c})^{8/3}}\frac{\nabla n+\nabla n_\mathrm{c}}{4\gamma^2}\frac{\partial\epsilon_\mathrm{c}}{\partial\alpha}\,,\end{aligned} \tag{A.42}$$

and

$$\frac{\partial(n\epsilon_\mathrm{c})}{\partial\tau_\sigma} = n\frac{\partial\epsilon_\mathrm{c}}{\partial\tau_\sigma} = n\frac{\partial\epsilon_\mathrm{c}}{\partial\alpha}\frac{\partial\alpha}{\partial\tau_\sigma} = \frac{1}{A_\mathrm{s}d_\mathrm{s}(\zeta)}\frac{n}{(n+n_\mathrm{c})^{5/3}}\frac{\partial\epsilon_\mathrm{c}}{\partial\alpha}\,. \tag{A.43}$$

By defining the auxiliary functions

$$h_\mathrm{s} = \frac{1}{2\gamma^2}\frac{1}{(n+n_\mathrm{c})^{2/3}}g(n,n_\mathrm{c})\frac{1}{s}\frac{\partial\epsilon_\mathrm{c}}{\partial s}\,, \tag{A.44}$$

$$h_\alpha = \frac{1}{2A_\mathrm{s}d_\mathrm{s}(\zeta)}\frac{1}{(n+n_\mathrm{c})^{2/3}}g(n,n_\mathrm{c})\frac{\partial\epsilon_\mathrm{c}}{\partial\alpha}\,, \tag{A.45}$$

with $g(n,n_\mathrm{c}) = 1/(1+n_\mathrm{c}/n)$ the derivatives can be rewritten to

$$\frac{\partial(n\epsilon_\mathrm{c})}{\partial n_\sigma} =\epsilon_\mathrm{c} - \frac{1}{3}g(n,n_\mathrm{c})r_\mathrm{s}\frac{\partial\epsilon_\mathrm{c}}{\partial r_\mathrm{s}} + (\pm 1-\zeta)g(n,n_\mathrm{c})\frac{\partial\epsilon_\mathrm{c}}{\partial\zeta} - \frac{4}{3}g(n,n_\mathrm{c})s\frac{\partial\epsilon_\mathrm{c}}{\partial s} \tag{A.46}$$

$$+\left[-\frac{5}{3}\alpha g(n,n_\mathrm{c}) + \alpha g(n,n_\mathrm{c})(\zeta\mp 1)\frac{d_\mathrm{s}'(\zeta)}{d_\mathrm{s}(\zeta)}\right]\frac{\partial\epsilon_\mathrm{c}}{\partial\alpha} + h_\alpha\frac{|\nabla\sqrt{n+n_\mathrm{c}}|^2}{\sqrt{n+n_\mathrm{c}}}\,, \tag{A.47}$$

$$\frac{\partial(n\epsilon_\mathrm{c})}{\partial\nabla n_\sigma} = [h_\mathrm{s}-h_\alpha]\frac{\nabla\sqrt{n+n_\mathrm{c}}}{\sqrt{n+n_\mathrm{c}}}\,, \tag{A.48}$$

and

$$\frac{\partial(n\epsilon_\mathrm{c})}{\partial\tau_\sigma} = 2h_\alpha\,. \tag{A.49}$$

With the $h_0 = h_\mathrm{s} - h_\alpha$ the divergence of Eq. (A.46) is

$$\begin{aligned}\nabla \cdot \left(\frac{\partial(n\epsilon_\mathrm{c})}{\partial \nabla n_\sigma} \right) &= \nabla \cdot \left(h_0 \frac{\nabla\sqrt{n+n_\mathrm{c}}}{\sqrt{n+n_\mathrm{c}}} \right) \\ &= \nabla h_0 \cdot \frac{\nabla\sqrt{n+n_\mathrm{c}}}{\sqrt{n+n_\mathrm{c}}} + h_0 \frac{\nabla^2\sqrt{n+n_\mathrm{c}}}{\sqrt{n+n_\mathrm{c}}} - h_0 \frac{|\nabla\sqrt{n+n_\mathrm{c}}|^2}{n+n_\mathrm{c}} \,. \end{aligned} \tag{A.50}$$

With

$$h_\mathrm{s} \frac{|\nabla\sqrt{n+n_\mathrm{c}}|^2}{n+n_\mathrm{c}} = \frac{1}{2\gamma^2} \frac{1}{(n+n_\mathrm{c})^{2/3}} g(n,n_\mathrm{c}) \frac{1}{s} \frac{\partial \epsilon_\mathrm{c}}{\partial s} \frac{|\nabla(n+n_\mathrm{c})|^2}{4(n+n_\mathrm{c})^2} = g(n,n_\mathrm{c}) \frac{1}{2} s \frac{\partial \epsilon_\mathrm{c}}{\partial s} \tag{A.51}$$

it can be expressed as

$$\nabla \cdot \left(\frac{\partial(n\epsilon_\mathrm{c})}{\partial \nabla n_\sigma} \right) = \nabla h_0 \cdot \frac{\nabla\sqrt{n+n_\mathrm{c}}}{\sqrt{n+n_\mathrm{c}}} + h_0 \frac{\nabla^2\sqrt{n+n_\mathrm{c}}}{\sqrt{n+n_\mathrm{c}}} - g(n,n_\mathrm{c}) \frac{1}{2} s \frac{\partial \epsilon_\mathrm{c}}{\partial s} + h_\alpha \frac{|\nabla\sqrt{n+n_\mathrm{c}}|^2}{n+n_\mathrm{c}} \,. \tag{A.52}$$

This leads to the final expression for the derivative of the meta-GGA correlation energy

$$\begin{aligned}\frac{\delta E_\mathrm{c}^\mathrm{mGGA}}{\delta \varphi_{i\sigma}^*} &= \varphi_{i\sigma} \left[\frac{\partial(n\epsilon_\mathrm{c})}{\partial n_\sigma} - \nabla \cdot \left(\frac{\partial(n\epsilon_\mathrm{c})}{\partial \nabla n_\sigma} \right) \right] - \frac{\hbar^2}{2m} \left[\frac{\partial(n\epsilon_\mathrm{c})}{\partial \tau_\sigma} \nabla^2 \varphi_{i\sigma} + \nabla \varphi_{i\sigma} \cdot \nabla \left(\frac{\partial(n\epsilon_\mathrm{c})}{\partial \tau_\sigma} \right) \right] \\ &= \varphi_{i\sigma} \Bigg[\epsilon_\mathrm{c} - \frac{1}{3} g(n,n_\mathrm{c}) r_\mathrm{s} \frac{\partial \epsilon_\mathrm{c}}{\partial r_\mathrm{s}} + (\pm 1 - \zeta) g(n,n_\mathrm{c}) \frac{\partial \epsilon_\mathrm{c}}{\partial \zeta} - \frac{5}{6} g(n,n_\mathrm{c}) s \frac{\partial \epsilon_\mathrm{c}}{\partial s} \\ &\quad + \alpha g(n,n_\mathrm{c}) \left(-\frac{5}{3} + (\zeta \mp 1) \frac{d_\mathrm{s}'(\zeta)}{d_\mathrm{s}(\zeta)} \right) \frac{\partial \epsilon_\mathrm{c}}{\partial \alpha} - \nabla h_0 \cdot \frac{\nabla\sqrt{n+n_\mathrm{c}}}{\sqrt{n+n_\mathrm{c}}} - h_0 \frac{\nabla^2\sqrt{n+n_\mathrm{c}}}{\sqrt{n+n_\mathrm{c}}} \Bigg] \\ &\quad - \frac{\hbar^2}{m} \left[h_\alpha \nabla^2 \varphi_{i\sigma} - \nabla \varphi_{i\sigma} \cdot \nabla h_\alpha \right] \,. \end{aligned} \tag{A.53}$$

A.3 Continuity Equation for Meta-GGAs in Time-Dependent GKS

For meta-GGAs in TDGKS, the continuity equation can be restored by applying the current-density correction given in Eq. (5.19). This can be explicitly demonstrated by

evaluating the contribution of Eq. (5.19) to Eq. (5.16) in Section 5.2:

$$
\begin{aligned}
&\frac{2}{\hbar}\operatorname{Im}\left[\varphi_k^*\left(\frac{1}{2m}\hat{\boldsymbol{\pi}}\frac{\partial e_{\mathrm{xc}}^{\mathrm{mGGA}}}{\partial\hat{\tau}}\hat{\boldsymbol{\pi}}\right)\varphi_k\right]\\
=&\frac{1}{m\hbar}\operatorname{Im}\left[\varphi_k^*\left(\frac{\hbar}{\mathrm{i}}\nabla-m\frac{\mathbf{j}_{\mathrm{p}}}{n}\right)\frac{\partial e_{\mathrm{xc}}^{\mathrm{mGGA}}}{\partial\hat{\tau}}\left(\frac{\hbar}{\mathrm{i}}\nabla-m\frac{\mathbf{j}_{\mathrm{p}}}{n}\right)\varphi_k\right]\\
=&-\frac{\hbar}{m}\operatorname{Im}\left[\varphi_k^*\nabla\cdot\left(\frac{\partial e_{\mathrm{xc}}^{\mathrm{mGGA}}}{\partial\hat{\tau}}\nabla\varphi_k\right)\right]-\operatorname{Im}\left[\frac{1}{\mathrm{i}}\varphi_k^*\nabla\cdot\left(\frac{\partial e_{\mathrm{xc}}^{\mathrm{mGGA}}}{\partial\hat{\tau}}\frac{\mathbf{j}_{\mathrm{p}}}{n}\varphi_k\right)\right]\\
&-\operatorname{Im}\left[\frac{1}{\mathrm{i}}\varphi_k^*\frac{\mathbf{j}_{\mathrm{p}}}{n}\frac{\partial e_{\mathrm{xc}}^{\mathrm{mGGA}}}{\partial\hat{\tau}}\cdot\nabla\varphi_k\right]+\frac{m}{\hbar}\operatorname{Im}\left[\varphi_k^*\frac{|\mathbf{j}_{\mathrm{p}}|^2}{n^2}\frac{\partial e_{\mathrm{xc}}^{\mathrm{mGGA}}}{\partial\hat{\tau}}\varphi_k\right]\\
=&-\frac{\hbar}{m}\nabla\cdot\left[\operatorname{Im}\left(\varphi_k^*\nabla\varphi_k\right)\frac{\partial e_{\mathrm{xc}}^{\mathrm{mGGA}}}{\partial\hat{\tau}}\right]\\
&+\operatorname{Re}\left[\varphi_k^*\left(\nabla\cdot\left(\frac{\partial e_{\mathrm{xc}}^{\mathrm{mGGA}}}{\partial\hat{\tau}}\frac{\mathbf{j}_{\mathrm{p}}}{n}\varphi_k\right)+\frac{\mathbf{j}_{\mathrm{p}}}{n}\frac{\partial e_{\mathrm{xc}}^{\mathrm{mGGA}}}{\partial\hat{\tau}}\cdot\nabla\varphi_k\right)\right]\\
=&-\frac{\hbar}{m}\nabla\cdot\left[\operatorname{Im}\left(\varphi_k^*\nabla\varphi_k\right)\frac{\partial e_{\mathrm{xc}}^{\mathrm{mGGA}}}{\partial\hat{\tau}}\right]+|\varphi_k|^2\nabla\cdot\left(\frac{\partial e_{\mathrm{xc}}^{\mathrm{mGGA}}}{\partial\hat{\tau}}\frac{\mathbf{j}_{\mathrm{p}}}{n}\right)\\
&+2\frac{\partial e_{\mathrm{xc}}^{\mathrm{mGGA}}}{\partial\hat{\tau}}\frac{\mathbf{j}_{\mathrm{p}}}{n}\cdot\operatorname{Re}\left[\varphi_k^*\nabla\varphi_k\right]\\
=&-\frac{\hbar}{m}\nabla\cdot\left[\operatorname{Im}\left(\varphi_k^*\nabla\varphi_k\right)\frac{\partial e_{\mathrm{xc}}^{\mathrm{mGGA}}}{\partial\hat{\tau}}\right]+|\varphi_k|^2\nabla\cdot\left(\frac{\partial e_{\mathrm{xc}}^{\mathrm{mGGA}}}{\partial\hat{\tau}}\frac{\mathbf{j}_{\mathrm{p}}}{n}\right)+\frac{\partial e_{\mathrm{xc}}^{\mathrm{mGGA}}}{\partial\hat{\tau}}\frac{\mathbf{j}_{\mathrm{p}}}{n}\cdot\nabla|\varphi_k|^2\\
=&-\frac{\hbar}{m}\nabla\cdot\left[\operatorname{Im}\left(\varphi_k^*\nabla\varphi_k\right)\frac{\partial e_{\mathrm{xc}}^{\mathrm{mGGA}}}{\partial\hat{\tau}}\right]+\nabla\cdot\left[\frac{\partial e_{\mathrm{xc}}^{\mathrm{mGGA}}}{\partial\hat{\tau}}\frac{\mathbf{j}_{\mathrm{p}}}{n}|\varphi_k|^2\right]\\
=&-\nabla\cdot\left[\frac{\partial e_{\mathrm{xc}}^{\mathrm{mGGA}}}{\partial\hat{\tau}}\left(\mathbf{j}_k-\mathbf{j}_{\mathrm{p}}\frac{|\varphi_k|^2}{n}\right)\right]
\end{aligned}
\tag{A.54}
$$

where $\mathbf{j}_k(\mathbf{r},t)$ is the current density of orbital $\varphi_k(\mathbf{r},t)$.

Summing over the occupied orbitals k gives

$$
\sum_{k=1}^{N}\frac{2}{\hbar}\operatorname{Im}\left[\varphi_k^*\left(\frac{1}{2m}\hat{\boldsymbol{\pi}}\frac{\partial e_{\mathrm{xc}}^{\mathrm{mGGA}}}{\partial\hat{\tau}}\hat{\boldsymbol{\pi}}\right)\varphi_k\right]=-\nabla\cdot\left[\frac{\partial e_{\mathrm{xc}}^{\mathrm{mGGA}}}{\partial\hat{\tau}}\left(\mathbf{j}_{\mathrm{p}}-\mathbf{j}_{\mathrm{p}}\frac{n}{n}\right)\right]=0 \tag{A.55}
$$

which restores the continuity equation

$$
\frac{\partial}{\partial t}n(\mathbf{r},t)=-\nabla\mathbf{j}_{\mathrm{p}}(\mathbf{r},t)\,. \tag{A.56}
$$

Excluding the sum over k and explicitly including the contribution of the kinetic energy operator in Eq. (5.16), one obtains

$$
\frac{\partial}{\partial t}|\varphi_k|^2=-\nabla\cdot\left[\mathbf{j}_k+\frac{\partial e_{\mathrm{xc}}^{\mathrm{mGGA}}}{\partial\hat{\tau}}\left(\mathbf{j}_k-\mathbf{j}_{\mathrm{p}}\frac{|\varphi_k|^2}{n}\right)\right]\,. \tag{A.57}
$$

This result shows that the continuity equation does not hold for each orbital density. Consequently, one may interpret that the continuity equation (A.56) only holds "on average".

Based on an idea from Thilo Aschebrock, an alternative current-density correction to the kinetic energy density can be defined as:

$$\hat{\tau}(\mathbf{r},t) = \tau(\mathbf{r},t) - \frac{m}{2}\sum_{k=1}^{N}\frac{|\mathbf{j}_\mathrm{k}(\mathbf{r},t)|^2}{|\varphi_k(\mathbf{r},t)|^2} \tag{A.58}$$

It can be shown that this definition of the current-density correction restores the continuity equation for each orbital density (see supplementary material of Ref. [Ric+23]).

Appendix B

Complementary Work Self-Interaction Correction

B.1 Hermiticity of the Lagrange Multiplier in PZ-SIC

The hermiticity of the Lagrange multiplier $\boldsymbol{\lambda}_\sigma$ in Eq. (6.9a) can be explicitly demonstrated, as previously shown for time-dependent SIC in Ref. [Mes+09]. By decomposing $\boldsymbol{\lambda}_\sigma$ into its Hermitian part $\boldsymbol{\mu}_\sigma$ and anti-Hermitian part $\boldsymbol{\kappa}_\sigma$, the energy functional in Eq. (6.8) can be reformulated as

$$S[\{\varphi_{i\sigma}\}] = E^{\mathrm{SIC}} - \sum_{\sigma=\uparrow,\downarrow} \sum_{i,j=1}^{N_\sigma} (\mu_{ji\sigma} + \kappa_{ji\sigma}) \left(\langle \varphi_{i\sigma} | \varphi_{j\sigma} \rangle - \delta_{ij}\right) . \tag{B.1}$$

The functional S can be further decomposed into real and imaginary parts, where the imaginary part is given by

$$\mathrm{Im}(S[\{\varphi_{i\sigma}\}]) = - \sum_{\sigma=\uparrow,\downarrow} \sum_{i,j=1}^{N_\sigma} \kappa_{ji\sigma} \langle \varphi_{i\sigma} | \varphi_{j\sigma} \rangle \, . \tag{B.2}$$

Since $\boldsymbol{\mu}_\sigma$ is Hermitian, it follows that

$$\mathrm{Im} \left[- \sum_{\sigma=\uparrow,\downarrow} \sum_{i,j=1}^{N_\sigma} \mu_{ji\sigma} \langle \varphi_{i\sigma} | \varphi_{j\sigma} \rangle \right] = 0 \, . \tag{B.3}$$

Because the real and imaginary parts of S can be varied independently, the variation of the imaginary part with respect to $\varphi^*_{k\sigma}$ gives

$$\frac{\delta \, \mathrm{Im}(S[\{\varphi_{i\sigma}\}])}{\delta \varphi^*_{k\sigma}(\mathbf{r})} = 0 \quad \Leftrightarrow \quad \sum_{i=j}^{N_\sigma} \kappa_{jk\sigma} \varphi_{j\sigma}(\mathbf{r}) = 0 \, . \tag{B.4}$$

This equation must hold for all orbitals k and all spatial points $\mathbf{r}$. As a result, we conclude that

$$\boldsymbol{\kappa}_\sigma = 0 \, , \tag{B.5}$$

ensuring that $\boldsymbol{\lambda}_\sigma$ is Hermitian.

B.2 Hamiltonian for Meta-GGAs Using the PZ-SIC with Current-Density Correction

When using $\hat{\tau}$ from Eq. (6.19) with the paramagnetic current density

$$\mathbf{j}_\mathrm{p}(\mathbf{r}) = \sum_{\sigma=\uparrow,\downarrow} \mathbf{j}_{\mathrm{p}\sigma} = \frac{\hbar}{m} \sum_{\sigma=\uparrow,\downarrow} \sum_{i=1}^{N_\sigma} \mathrm{Im}[\varphi_{i\sigma}^*(\mathbf{r}) \nabla \varphi_{i\sigma}(\mathbf{r})], \tag{B.6}$$

instead of τ, and recalculating the variation of the meta-GGA energy with respect to the orbitals, the local part of the potential v_σ^loc (see Eq. (4.25)) remains unchanged. However, for the operator part, we obtain

$$\hat{v}_{\hat{\tau}}^\mathrm{CGKS}[s_\sigma^2, \alpha](\mathbf{r}) = \frac{1}{2m} \hat{\boldsymbol{\pi}}_\sigma(\mathbf{r}) \frac{\partial e_\mathrm{xc}^\mathrm{mGGA}}{\partial \hat{\tau}}(\mathbf{r}) \hat{\boldsymbol{\pi}}_\sigma(\mathbf{r}), \tag{B.7}$$

where

$$\hat{\boldsymbol{\pi}}_\sigma(\mathbf{r}) = \hat{\mathbf{p}} - m \frac{\mathbf{j}_{\mathrm{p}\sigma}(\mathbf{r})}{n_\sigma(\mathbf{r})}, \tag{B.8}$$

and $\hat{\mathbf{p}} = -\mathrm{i}\hbar\nabla$. The Hamiltonian operator using $\hat{\tau}$, $\hat{H}_{i\sigma}^{\hat{\tau}}$, is derived analogously to that in Eq. (6.17), with the corresponding operator

$$\hat{\boldsymbol{\pi}}_{i\sigma}(\mathbf{r}) = \hat{\mathbf{p}} - m \frac{\mathbf{j}_{i\sigma}(\mathbf{r})}{n_{i\sigma}(\mathbf{r})} \tag{B.9}$$

where $\mathbf{j}_{i\sigma} = \hbar/m \ \mathrm{Im}[\varphi_{i\sigma}^* \nabla \varphi_{i\sigma}]$ depends on a single orbital. In detail, the Hamiltonian for a meta-GGA parametrized in $\{s^2, \alpha\}$ using the PZ-SIC can be written as

$$\begin{aligned}
\hat{H}_{i\sigma}^{\hat{\tau}} = &-\frac{\hbar^2}{2m}\nabla^2 + v_\mathrm{ext} + v_\mathrm{H}[n] + \left(v_\mathrm{xc}^\mathrm{local}[s_\sigma, \alpha_\sigma] - v_\mathrm{H}[n_{i\sigma}] - v_\mathrm{xc}^\mathrm{local}[s_{i\sigma}, \alpha = 0]\right) \\
&+ \frac{1}{2m}\Bigg[\hat{\mathbf{p}} \left(\left.\frac{\partial e_\mathrm{xc}}{\partial \hat{\tau}}\right|_{s_\sigma,\alpha_\sigma} - \left.\frac{\partial e_\mathrm{xc}}{\partial \hat{\tau}}\right|_{s_{i\sigma},\alpha=0} \right) \hat{\mathbf{p}} + m^2 \left(\left.\frac{\partial e_\mathrm{xc}}{\partial \hat{\tau}}\right|_{s_\sigma,\alpha_\sigma} \frac{\mathbf{j}_{p\sigma}^2}{n_\sigma^2} - \left.\frac{\partial e_\mathrm{xc}}{\partial \hat{\tau}}\right|_{s_{i\sigma},\alpha=0} \frac{\mathbf{j}_{i\sigma}^2}{n_{i\sigma}^2} \right) \\
&\qquad - \Bigg\{ m \left(\left.\frac{\partial e_\mathrm{xc}}{\partial \hat{\tau}}\right|_{s_\sigma,\alpha_\sigma} \frac{\mathbf{j}_{p\sigma}}{n_\sigma} - \left.\frac{\partial e_\mathrm{xc}}{\partial \hat{\tau}}\right|_{s_{i\sigma},\alpha=0} \frac{\mathbf{j}_{i\sigma}}{n_{i\sigma}} \right) \hat{\mathbf{p}}_\sigma \\
&\qquad\qquad + m \hat{\mathbf{p}}_\sigma \left(\left.\frac{\partial e_\mathrm{xc}}{\partial \hat{\tau}}\right|_{s_\sigma,\alpha_\sigma} \frac{\mathbf{j}_{p\sigma}}{n_\sigma} - \left.\frac{\partial e_\mathrm{xc}}{\partial \hat{\tau}}\right|_{s_{i\sigma},\alpha=0} \frac{\mathbf{j}_{i\sigma}}{n_{i\sigma}} \right) \Bigg\} \Bigg].
\end{aligned} \tag{B.10}$$

The spin-dependent components of the potential are obtained by applying the spin-independent expressions together with the spin-scaling relations $n \to 2n_\sigma$ and $\tau \to 2\tau_\sigma$ (and analogous for the single-orbital-dependent expressions).

B.3 Derivation of the PZ-SIC Energy Variation with Respect to the Unitary Transformation

The unitary transformation of a set of orbitals $\{\varphi_{i\sigma}\}$ to another set $\{\varphi'_{i\sigma}\}$ is defined as

$$\varphi'_{i\sigma}(\mathbf{r}) = \sum_{j=1}^{N_\sigma} U_{ij\sigma} \varphi_{j\sigma}(\mathbf{r}), \tag{B.11}$$

where $U_{ij\sigma}$ is a unitary matrix, i. e. satisfying $\sum_k U^*_{ki\sigma}U_{kj\sigma} = \delta_{ij}$. Here, N_σ denotes the number of orbitals with occupation numbers $f_{i\sigma} > 0$, and σ is the spin index.

For an infinitesimal unitary transformation $U_{ij\sigma} = \delta_{ij} + \omega_{ij\sigma}$, the unitarity condition simplifies, neglecting terms of order $\omega^2_{ij\sigma}$ or higher, to

$$\sum_{k=1}^{N_\sigma} U^*_{ki\sigma}U_{kj\sigma} = \sum_{k=1}^{N_\sigma}(\delta_{ki} + \omega^*_{ki\sigma})(\delta_{kj} + \omega_{kj\sigma}) \tag{B.12}$$

$$= \sum_{k=1}^{N_\sigma}(\delta_{ki}\delta_{kj} + \delta_{ki}\omega_{kj\sigma} + \delta_{kj}\omega^*_{ki\sigma}) \tag{B.13}$$

$$= \delta_{ij} + \omega_{ij\sigma} + \omega^*_{ji\sigma} \overset{!}{=} \delta_{ij}, \tag{B.14}$$

which leads to the condition

$$\omega_{ij\sigma} = -\omega^*_{ji\sigma}. \tag{B.15}$$

The variation of the PZ-SIC energy with respect to an infinitesimal unitary transformation can be written, using the chain rule, as

$$\begin{aligned}&\left.\frac{\partial E^{\mathrm{SIC}}[\{\varphi'_{i\sigma}\}]}{\partial U^*_{\alpha\beta\sigma}}\right|_{U^*_{\alpha\beta\sigma}=\delta_{\alpha\beta}}\\ &\quad= \int \sum_{k=1}^{N_\sigma}\left[\frac{\delta E^{\mathrm{SIC}}[\{\varphi'_{i\sigma}\}]}{\delta\varphi'_{k\sigma}(\mathbf{r})}\frac{\partial\varphi'_{k\sigma}(\mathbf{r})}{\partial U^*_{\alpha\beta\sigma}} + \frac{\delta E^{\mathrm{SIC}}[\{\varphi'_{i\sigma}\}]}{\delta\varphi'^*_{k\sigma}(\mathbf{r})}\frac{\partial\varphi'^*_{k\sigma}(\mathbf{r})}{\partial U^*_{\alpha\beta\sigma}}\right]\Bigg|_{U^*_{\alpha\beta\sigma}=\delta_{\alpha\beta}} \mathrm{d}^3r\end{aligned} \tag{B.16}$$

with the PZ-SIC energy expression E^{SIC} defined in Eq. (6.3).

The functional derivative of the PZ-SIC energy with respect to the orbital k is

$$\left.\frac{\delta E^{\mathrm{SIC}}[\{\varphi'_{i\sigma}\}]}{\delta\varphi'_{k\sigma}(\mathbf{r})}\right|_{U^*_{\alpha\beta\sigma}=\delta_{\alpha\beta}} = f_{k\sigma}\hat{H}_{k\sigma}\varphi^*_{k\sigma}(\mathbf{r}) \quad \text{and} \tag{B.17}$$

$$\left.\frac{\delta E^{\mathrm{SIC}}[\{\varphi'_{i\sigma}\}]}{\delta\varphi'^*_{k\sigma}(\mathbf{r})}\right|_{U^*_{\alpha\beta\sigma}=\delta_{\alpha\beta}} = f_{k\sigma}\hat{H}_{k\sigma}\varphi_{k\sigma}(\mathbf{r}) \tag{B.18}$$

with the occupation number $f_{k\sigma}$ of the kth orbital with spin σ. The derivative of the orbital with respect to the unitary transformation reduces to

$$\begin{aligned}\left.\frac{\partial\varphi'_{k\sigma}(\mathbf{r})}{\partial U^*_{\alpha\beta\sigma}}\right|_{U^*_{\alpha\beta\sigma}=\delta_{\alpha\beta}} &= \sum_l \varphi_{l\sigma}(\mathbf{r})\frac{\partial U_{kl\sigma}}{\partial U^*_{\alpha\beta\sigma}} = \sum_l \varphi_{l\sigma}(\mathbf{r})\frac{\partial\omega_{kl\sigma}}{\partial\omega^*_{\alpha\beta\sigma}} = -\sum_l \varphi_{l\sigma}(\mathbf{r})\frac{\partial\omega^*_{lk\sigma}}{\partial\omega^*_{\alpha\beta\sigma}}\\ &= -\sum_l \varphi_{l\sigma}(\mathbf{r})\delta_{l\alpha}\delta_{k\beta} = -\varphi_{\alpha\sigma}(\mathbf{r})\delta_{k\beta}\end{aligned} \tag{B.19}$$

and analogously

$$\left.\frac{\partial\varphi'^*_{k\sigma}(\mathbf{r})}{\partial U^*_{\alpha\beta\sigma}}\right|_{U^*_{\alpha\beta\sigma}=\delta_{\alpha\beta}} = \sum_l \varphi^*_{l\sigma}(\mathbf{r})\frac{\partial U^*_{kl\sigma}}{\partial U^*_{\alpha\beta\sigma}} = \varphi^*_{\beta\sigma}(\mathbf{r})\delta_{k\alpha}\,. \tag{B.20}$$

Inserting the results in Eq. (B.16) leads to the gradient

$$\begin{aligned} G_{\alpha\beta\sigma} &= \left.\frac{\partial E^{\mathrm{SIC}}}{\partial U^{*}_{\alpha\beta\sigma}}\right|_{U^{*}_{\alpha\beta\sigma}=\delta_{\alpha\beta}} \\ &= \int \sum_{k=1}^{N_\sigma} \left[f_{k\sigma} \hat{H}_{k\sigma} \varphi_{k\sigma}(\mathbf{r})^{*} (-\delta_{k\beta} \varphi_{\alpha\sigma}(\mathbf{r})) + f_{k\sigma} \hat{H}_{k\sigma} \varphi_{k\sigma}(\mathbf{r}) \delta_{k\alpha} \varphi^{*}_{\beta\sigma}(\mathbf{r}) \right] \mathrm{d}^3 r \\ &= \int \varphi^{*}_{\beta\sigma}(\mathbf{r}) (f_{\alpha\sigma} \hat{H}_{\alpha\sigma} - f_{\beta\sigma} \hat{H}_{\beta\sigma}) \varphi_{\alpha\sigma}(\mathbf{r}) \, \mathrm{d}^3 r = -\langle \varphi_{\beta\sigma} | f_{\beta\sigma} \hat{H}_{\beta\sigma} - f_{\alpha\sigma} \hat{H}_{\alpha\sigma} | \varphi_{\alpha\sigma} \rangle \,. \end{aligned} \tag{B.21}$$

For a system with an integer number of electrons (i. e. $f_{i\sigma} = 1$ for all i), the gradient reduces to

$$G_{\alpha\beta\sigma} = -\langle \varphi_{\beta\sigma} | v^{\mathrm{SI}}[n_{\beta\sigma}] - v^{\mathrm{SI}}[n_{\alpha\sigma}] | \varphi_{\alpha\sigma} \rangle \,, \tag{B.22}$$

with $v^{\mathrm{SI}}[n_{\beta\sigma}] = -(v_{\mathrm{H}}[n_{\beta\sigma}] + v_{\mathrm{xc}}[n_{\beta\sigma}, 0])$.

B.4 Alternative Formulation of the PZ-SIC Ground-State Energy through Orbital Energies

Within the KS theory, the ground-state energy expression can be written in terms of the KS eigenvalues as [KS65; Cap06]

$$E_{\mathrm{KS}}[n] = \sum_{\sigma=\uparrow,\downarrow} \sum_{i=1}^{N_\sigma} \epsilon_{i\sigma} - E_{\mathrm{H}}[n] - \sum_{\sigma=\uparrow,\downarrow} \int v_{\mathrm{xc}\sigma}[n_\uparrow, n_\downarrow](\mathbf{r}) n_\sigma(\mathbf{r}) \, \mathrm{d}^3 r + E_{\mathrm{xc}}[n_\uparrow, n_\downarrow] \,. \tag{B.23}$$

Typically, the sum over the KS eigenvalues $\{\epsilon_{i\sigma}\}$ is the main contribution to the ground-state energy expression in Eq. (B.23). This also motivates the Aufbau principle, which states that orbitals must be occupied in ascending order to minimize the energy functional E_{KS}.

A similar reformulation of the PZ-SIC energy expression can be derived by starting from the ground-state equation (6.9a)

$$\begin{aligned} f_{i\sigma} \hat{H}_{i\sigma} \varphi_{i\sigma}(\mathbf{r}) &= \sum_{j=1}^{N_\sigma} \lambda_{ji\sigma} \varphi_{j\sigma}(\mathbf{r}) \\ \Leftrightarrow \sum_{\sigma=\uparrow,\downarrow} \sum_{i=1}^{N_\sigma} \int \varphi^{*}_{i\sigma}(\mathbf{r}) f_{i\sigma} \hat{H}_{i\sigma} \varphi_{i\sigma}(\mathbf{r}) \, \mathrm{d}^3 r &= \sum_{\sigma=\uparrow,\downarrow} \sum_{i,j=1}^{N_\sigma} \int \varphi^{*}_{i\sigma}(\mathbf{r}) \lambda_{ji\sigma} \varphi_{j\sigma} \, \mathrm{d}^3 r \\ \Leftrightarrow \sum_{\sigma=\uparrow,\downarrow} \sum_{i=1}^{N_\sigma} \frac{\lambda_{ii\sigma}}{f_{i\sigma}} &= \sum_{\sigma=\uparrow,\downarrow} \sum_{i=1}^{N_\sigma} \int \varphi^{*}_{i\sigma}(\mathbf{r}) \hat{H}_{i\sigma} \varphi_{i\sigma}(\mathbf{r}) \, \mathrm{d}^3 r \,, \end{aligned} \tag{B.24}$$

where the right-hand side of the equation is

$$\begin{aligned}\sum_{\sigma=\uparrow,\downarrow}\sum_{i=1}^{N_\sigma}\int \varphi_{i\sigma}^*(\mathbf{r})\hat{H}_{i\sigma}\varphi_{i\sigma}(\mathbf{r})\,\mathrm{d}^3r = \\ E_{\mathrm{kin}} + E_{\mathrm{ext}} + \underbrace{\int v_{\mathrm{H}}[n](\mathbf{r})n(\mathbf{r})\,\mathrm{d}^3r}_{=2E_{\mathrm{H}}[n]} + \sum_{\sigma=\uparrow,\downarrow}\int v_{\mathrm{xc}\sigma}[n_\uparrow,n_\downarrow](\mathbf{r})n_\sigma(\mathbf{r})\,\mathrm{d}^3r \\ - \sum_{\sigma=\uparrow,\downarrow}\sum_{i=1}^{N_\sigma}\int \varphi_{i\sigma}^*(\mathbf{r})\left[v_{\mathrm{H}}[n_{i\sigma}](\mathbf{r}) + v_{\mathrm{xc}}[n_{i\sigma},0](\mathbf{r})\right]\varphi_{i\sigma}(\mathbf{r})\,\mathrm{d}^3r\,. \end{aligned} \tag{B.25}$$

With $\lambda_{ii\sigma}/f_{i\sigma} = \lambda'_{ii\sigma}$, the energy functional in Eq. (6.3) can be written as

$$\begin{aligned}E^{\mathrm{SIC}} = \sum_{\sigma=\uparrow,\downarrow}\sum_{i=1}^{N_\sigma}\lambda'_{ii\sigma} - E_{\mathrm{H}}[n] - \int v_{\mathrm{xc}\sigma}[n_\uparrow,n_\downarrow](\mathbf{r})n_\sigma(\mathbf{r})\,\mathrm{d}^3r + E_{\mathrm{xc}}^{\mathrm{app}}[n_\uparrow,n_\downarrow] \\ + \sum_{\sigma=\uparrow,\downarrow}\sum_{i=1}^{N_\sigma}E_{\mathrm{H}}[n_{i\sigma}] + \sum_{\sigma=\uparrow,\downarrow}\sum_{i=1}^{N_\sigma}\int n_{i\sigma}(\mathbf{r})v_{\mathrm{xc}}[n_{i\sigma},0]\,\mathrm{d}^3r - \sum_{\sigma=\uparrow,\downarrow}\sum_{i=1}^{N_\sigma}E_{\mathrm{xc}}^{\mathrm{app}}[n_{i\sigma},0]\,.\end{aligned} \tag{B.26}$$

Finally, reformulating Eq. (6.1) to

$$\begin{aligned}E_{\mathrm{xc}}^{\mathrm{SIC}}[\{\varphi_{i\sigma}\}] =& E_{\mathrm{xc}}^{\mathrm{app}}[n_\uparrow,n_\downarrow] - \sum_{\sigma=\uparrow,\downarrow}\sum_{i=1}^{N_\sigma}\left(E_{\mathrm{H}}[n_{i\sigma}] + E_{\mathrm{xc}}^{\mathrm{app}}[n_{i\sigma},0]\right) \\ \Leftrightarrow -\sum_{\sigma=\uparrow,\downarrow}\sum_{i=1}^{N_\sigma}E_{\mathrm{xc}}^{\mathrm{app}}[n_{i\sigma},0] =& E_{\mathrm{xc}}^{\mathrm{SIC}}[\{\varphi_{i\sigma}\}] - E_{\mathrm{xc}}^{\mathrm{app}}[n_\uparrow,n_\downarrow] + \sum_{\sigma=\uparrow,\downarrow}\sum_{i=1}^{N_\sigma}E_{\mathrm{H}}[n_{i\sigma}]\end{aligned} \tag{B.27}$$

and substituting the result into Eq. (B.26) leads to

$$\begin{aligned}E^{\mathrm{SIC}} = \sum_{\sigma=\uparrow,\downarrow}\sum_{i=1}^{N_\sigma}\lambda'_{ii\sigma} - E_{\mathrm{H}}[n] - \sum_{\sigma=\uparrow,\downarrow}\int v_{\mathrm{xc}}[n_\uparrow,n_\downarrow](\mathbf{r})n_\sigma(\mathbf{r})\,\mathrm{d}^3r + E_{\mathrm{xc}}^{\mathrm{SIC}}[\{\varphi_{i\sigma}\}] \\ + 2\sum_{\sigma=\uparrow,\downarrow}\sum_{i=1}^{N_\sigma}E_{\mathrm{H}}[n_{i\sigma}] + \sum_{\sigma=\uparrow,\downarrow}\sum_{i=1}^{N_\sigma}\int v_{\mathrm{xc}}[n_{i\sigma},0](\mathbf{r})n_{i\sigma}(\mathbf{r})\,\mathrm{d}^3r\,.\end{aligned} \tag{B.28}$$

Similar to the case of the KS eigenvalues, the diagonal elements $\lambda'_{ii\sigma}$ here are typically the main contributions to the energy function. Consequently, this observation further suggests that, in the PZ-SIC framework, the local orbitals should be occupied in ascending order of the $\lambda'_{ii\sigma}$ values, analogous to the Aufbau principle in the KS formalism.

B.5 Consistency of Single-Orbital Energies in PZ-SIC and Kohn-Sham Theory

Within the PZ-SIC formalism the energy functional S of Eq. (6.8) consists of the energy functional E^{SIC} and the orthonormality constraint of the orbitals using a Lagrange multiplier. However, as briefly discussed at the end of Section 6.6, one could also consider defining a similar energy functional which consists of the unitary-invariant KS

energy functional E_{KS} instead of the SIC energy functional E^{SIC}. This leads to the functional

$$S_{\mathrm{KS}}[\{\varphi_{i\sigma}\}] = E_{\mathrm{KS}}[n] - \sum_{\sigma=\uparrow,\downarrow} \sum_{i,j=1}^{N_\sigma} \lambda_{ji\sigma} \left(\langle \varphi_{i\sigma} | \varphi_{j\sigma} \rangle - \delta_{ij} \right) . \tag{B.29}$$

For a non-integer electron number, minimizing the energy functional S_{KS} with respect to the orbital $\varphi^*_{i\sigma}$ leads

$$f_{i\sigma} \hat{H}_{\mathrm{KS}\sigma} \varphi_{i\sigma}(\mathbf{r}) = \sum_{j=1}^{N_\sigma} \lambda_{ji\sigma} \varphi_{j\sigma}(\mathbf{r}) \quad \text{and} \tag{B.30a}$$

$$\boldsymbol{\lambda}_\sigma = \boldsymbol{\lambda}_\sigma^\dagger \, , \tag{B.30b}$$

with the KS Hamiltonian $H_{\mathrm{KS}\sigma}$ (defined in Eq. (2.10)), and the Lagrange multiplier $\lambda_{ji\sigma} = \langle \varphi_{j\sigma} | f_{i\sigma} \hat{H}_{\mathrm{KS}\sigma} | \varphi_{i\sigma} \rangle$. The orbitals $\{\varphi_{i\sigma}\}$ form an orthonormal set but are *not* eigenfunctions of the KS Hamiltonian.

It can be shown that the eigenvalues of the matrix $\boldsymbol{\lambda}_\sigma$ correspond exactly to the KS eigenvalues $\{\epsilon^{\mathrm{KS}}_{i\sigma}\}$ (explicitly denoted with "KS"). This can be demonstrated as follows: the diagonalization of $\boldsymbol{\lambda}_\sigma$ can be expressed as

$$\epsilon^{\mathrm{KS}}_{i\sigma} \delta_{ij} = \left(\mathbf{W}^\dagger_\sigma \boldsymbol{\lambda}_\sigma \mathbf{W}_\sigma \right)_{ij} \tag{B.31}$$

with the unitary matrix $\mathbf{W}_\sigma$. The corresponding eigenfunctions, i. e. the KS orbitals, are obtained via the transformation

$$\varphi^{\mathrm{KS}}_{i\sigma}(\mathbf{r}) = \sum_{k=1}^{N_\sigma} W^*_{ki\sigma} \varphi_{k\sigma}(\mathbf{r}) \tag{B.32}$$

and the inverse transformation is

$$\varphi_{i\sigma}(\mathbf{r}) = \sum_{k=1}^{N_\sigma} W_{ik\sigma} \varphi^{\mathrm{KS}}_{k\sigma}(\mathbf{r}) \, . \tag{B.33}$$

Substituting the inverse transformation from Eq. (B.33) into Eq. (B.30a) leads to

$$\hat{H}_{\mathrm{KS}\sigma} \varphi^{\mathrm{KS}}_{l\sigma}(\mathbf{r}) = \epsilon^{\mathrm{KS}}_{l\sigma} \varphi^{\mathrm{KS}}_{l\sigma}(\mathbf{r}) \, , \tag{B.34}$$

thereby recovering the KS equations.

Considering the findings of Section 6.6, this result may seem counterintuitive: How can the diagonal elements of the Lagrange multiplier $\lambda_{ii\sigma}/f_{i\sigma}$ have the physical interpretation of orbital energies (see Section 6.6) if the eigenvalues of $\boldsymbol{\lambda}_\sigma$ correspond to the KS eigenvalues $\epsilon^{\mathrm{KS}}_{i\sigma}$? This apparent contradiction can be resolved by considering the hermiticity condition of the Lagrange multiplier, which imposes specific constraints on its structure:

In the KS framework, where the Hamiltonian is orbital-independent, the hermiticity condition can be explicitly written as

$$\lambda_{ji\sigma} - \lambda^*_{ij\sigma} = 0 \quad \Leftrightarrow \quad (f_{i\sigma} - f_{j\sigma}) \langle \varphi_{j\sigma} | \hat{H}_{\mathrm{KS}\sigma} | \varphi_{i\sigma} \rangle = 0 \, . \tag{B.35}$$

For $i, j \in \{1, \ldots, \mathrm{HOMO} - 1\}$, this equation is automatically satisfied, as the orbitals below the HOMO are fully occupied. That is, for $i = \mathrm{HOMO}$ and $j \neq \mathrm{HOMO}$, the

equation simplifies to

$$(f_{\mathrm{HOMO}} - f_{j\sigma})\langle\varphi_{j\sigma}|\hat{H}_{\mathrm{KS}\sigma}|\varphi_{\mathrm{HOMO}}\rangle = 0\,. \tag{B.36}$$

Since the HOMO is the only fractionally occupied state, the hermiticity condition ensures that all off-diagonal elements involving the HOMO vanish. As a result, $\boldsymbol{\lambda}_\sigma$ takes the form

$$\begin{pmatrix} \lambda_{11} & \lambda_{12} & \cdots & \lambda_{1(\mathrm{HOMO}-1)} & 0 \\ \lambda_{21} & \lambda_{22} & \cdots & \lambda_{2(\mathrm{HOMO}-1)} & 0 \\ \vdots & \vdots & \ddots & \vdots & \vdots \\ \lambda_{(\mathrm{HOMO}-1)1} & \lambda_{(\mathrm{HOMO}-1)2} & \cdots & \lambda_{(\mathrm{HOMO}-1)(\mathrm{HOMO}-1)} & 0 \\ 0 & 0 & \cdots & 0 & \lambda_{\mathrm{HOMO\,HOMO}} \end{pmatrix}. \tag{B.37}$$

Thus, the highest occupied diagonal element of $\boldsymbol{\lambda}_\sigma$ is equal to its highest eigenvalue, which corresponds to the KS eigenvalue ϵ_{HOMO}, resolving the apparent contradiction.

B.6 Alternative Definition of the Unitary Transformation with Fractional Occupation Numbers

To transform the occupation numbers together with the orbitals under a unitary transformation, one might consider the alternative definition

$$\sqrt{f'_{i\sigma}}\varphi'_{i\sigma}(\mathbf{r}) = \sum_{j=1}^{N_\sigma} U_{ij\sigma}\sqrt{f_{j\sigma}}\varphi_{j\sigma}(\mathbf{r}) \Leftrightarrow \tilde{\varphi}'_{i\sigma} = \sum_{j=1}^{N_\sigma} U_{ij\sigma}\tilde{\varphi}_{j\sigma}, \tag{B.38}$$

where $\tilde{\varphi}_{i\sigma} \coloneqq \sqrt{f_{i\sigma}}\varphi_{i\sigma}$. Using this definition, it is easy to show that the density is preserved since

$$\begin{aligned} n'(\mathbf{r}) &= \sum_{\sigma=\uparrow,\downarrow}\sum_{i=1}^{N_\sigma} f'_{i\sigma}|\varphi'_{i\sigma}(\mathbf{r})|^2 \\ &= \sum_{\sigma=\uparrow,\downarrow}\sum_{i=1}^{N_\sigma}\left(\sum_{k=1}^{N_\sigma} U^*_{ik\sigma}\sqrt{f_{k\sigma}}\varphi^*_{k\sigma}(\mathbf{r})\right)\left(\sum_{l=1}^{N_\sigma} U_{il\sigma}\sqrt{f_{l\sigma}}\varphi_{l\sigma}(\mathbf{r})\right) \\ &= \sum_{\sigma=\uparrow,\downarrow}\sum_{k,l=1}^{N_\sigma}\underbrace{\sum_{i=1}^{N_\sigma} U^*_{ik\sigma}U_{il\sigma}}_{=\delta_{lk}}\sqrt{f_{k\sigma}}\sqrt{f_{l\sigma}}\varphi^*_{k\sigma}(\mathbf{r})\varphi_{l\sigma}(\mathbf{r}) \\ &= \sum_{\sigma=\uparrow,\downarrow}\sum_{k=1}^{N_\sigma} f_{k\sigma}|\varphi_{k\sigma}(\mathbf{r})|^2 = n(\mathbf{r})\,. \end{aligned} \tag{B.39}$$

However, the orthonormality constraint of the SIC energy functional, which depends on $\{\tilde{\varphi}_{i\sigma}\}$, must be rewritten as

$$S[\{\tilde{\varphi}_{i\sigma}\}] = E^{\mathrm{SIC}}[\{\tilde{\varphi}_{i\sigma}\}] - \sum_{\sigma=\uparrow,\downarrow}\sum_{i,j=1}^{N_\sigma}\lambda_{ji\sigma}\left(\langle\tilde{\varphi}_{i\sigma}|\tilde{\varphi}_{j\sigma}\rangle - f_{i\sigma}\delta_{ij}\right), \tag{B.40}$$

where E^{SIC} is evaluated with the density $n = \sum_{\sigma=\uparrow,\downarrow} \sum_{i=1}^{N_\sigma} |\tilde{\varphi}_{i\sigma}|^2$ and the orbital density $n_{i\sigma} = |\tilde{\varphi}_{i\sigma}|^2$.

This approach, however, presents significant conceptual downsides: (1) The orbitals after the unitary transformation are no longer necessarily orthogonal in the spin channel with the fractionally occupied HOMO as shown in Eq. (6.32) in Section 6.7. (2) Using the definition in Eq. (B.38) to transform the occupation numbers would result in the fractional occupation of multiple orbitals. However, this contradicts the principle that only the HOMO should be fractionally occupied in order to minimize the total energy, as discussed in Section 6.6. (3) Minimizing the energy functional defined in Eq. (B.40) with respect to $\tilde{\varphi}^*_{i\sigma}$ is inherently challenging, as the functional derivative of the orthonormality constraint involves the term $\delta f_{i\sigma}/\delta\tilde{\varphi}_{i\sigma}$, which cannot be computed straightforwardly.

B.7 Maximum Estimated Eigenvalue on the Real-Space Grid

We estimate the maximum eigenvalue $\epsilon_{\max}$ that can be represented on our real-space grid for the error criterion within our PZ-SIC ground-state algorithm. The wave function φ_{max}, which generates the maximum kinetic energy and hence the maximum eigenvalue, is given by

$$\varphi_{\max} = \pm f\,, \tag{B.41}$$

where the sign alternates between consecutive grid points, and $f \in \mathbb{R}$. The value of f can be determined using the normalization condition of the wave function $\varphi_{\max}$:

$$\int |\varphi_{\max}|^2 \,\mathrm{d}^3r = \int f^2 \,\mathrm{d}^3r = \sum_{i=1}^{N_\mathrm{g}} f^2\Delta x = N_\mathrm{g} f^2 \Delta x \stackrel{!}{=} 1 \quad \Leftrightarrow \quad f = \frac{1}{\sqrt{N_\mathrm{g}\Delta x}}\,, \tag{B.42}$$

where N_g is the number of grid points and Δx is the grid spacing. We use 6th-order finite differences, denoted as ∇_6, to calculate derivatives on our real-space grid within the `BTDFT` program code. Thus, applying the kinetic energy operator to the orbital $\varphi_{\max}$ yields

$$\begin{aligned} -\frac{\hbar^2}{2m}\nabla_6^2\varphi_{\max} = \\ -\frac{\hbar^2}{2m}\Bigg(&\frac{2\varphi_{\max}(x-3\Delta x) - 27\varphi_{\max}(x-2\Delta x) + 270\varphi_{\max}(x-\Delta x)}{180(\Delta x)^2} - \frac{490\varphi_{\max}(x)}{180(\Delta x)^2} \\ &+ \frac{270\varphi_{\max}(x+\Delta x) - 27\varphi_{\max}(x+2\Delta x) + 2\varphi_{\max}(x+3\Delta x)}{180(\Delta x)^2}\Bigg)\,. \end{aligned} \tag{B.43}$$

Using $\varphi_{\max}(x) = f$, $\varphi_{\max}(x\pm\Delta x) = -f$, $\varphi_{\max}(x\pm 2\Delta x) = f$, and $\varphi_{\max}(x+3\Delta x) = -f$, we find

$$-\frac{\hbar^2}{2m}\varphi_{\max}(x)\nabla_6^2\varphi_{\max}(x) = \frac{\hbar^2}{2m}\frac{272 f^2}{45(\Delta x)^2}\,. \tag{B.44}$$

When integrating this result over the grid, the estimated value for $\epsilon_{\max}$ is given by

$$\begin{aligned}\epsilon_{\max} =& \frac{\hbar^2}{2m}\int \frac{272f^2}{45(\Delta x)^2}\,\mathrm{d}^3r = \frac{\hbar^2}{2m}\sum_{i=1}^{N_\mathrm{g}}\frac{272f^2}{45(\Delta x)^2}\Delta x = \frac{\hbar^2}{2m}N_\mathrm{g}\frac{272f^2}{45(\Delta x)^2}\Delta x \\ =& \frac{\hbar^2}{2m}\frac{272}{45(\Delta x)^2}\,,\end{aligned} \tag{B.45}$$

where the expression for f in Eq. (B.42) has been used in the final step.

B.8 Löwdin Orthogonalization

The Löwdin orthogonalization [Löw50] is a symmetric orthogonalization method for a set of N orbitals $\{\varphi_i\}$ (the spin index σ is omitted here to simplify notation). The orthogonalization scheme starts by calculating the overlap matrix

$$S_{ij} = \langle\varphi_i|\varphi_j\rangle\,. \tag{B.46}$$

Next, the matrix $\mathbf{S}$ is diagonalized as follows:

$$\mathbf{S}_\mathrm{diag} = \mathbf{U}^\dagger\mathbf{S}\mathbf{U}\,, \tag{B.47}$$

where $\mathbf{U}$ is a unitary matrix. The inverse square root of $\mathbf{S}_\mathrm{diag}$ is then calculated by inverting its diagonal elements and taking their square roots, yielding the matrix $\mathbf{S}_\mathrm{diag}^{-1/2}$. Transforming this matrix back to the original basis yields

$$\mathbf{S}^{-1/2} = \mathbf{U}\mathbf{S}_\mathrm{diag}^{-1/2}\mathbf{U}^\dagger\,. \tag{B.48}$$

Finally, the orthogonalized set of orbitals $\{\varphi_i'\}$ is obtained by applying the transformation:

$$\varphi_i'(\mathbf{r}) = \sum_{j=1}^{N} S_{ij}^{-1/2}\varphi_j(\mathbf{r}) \tag{B.49}$$

Using this orthogonalization scheme can be beneficial since it can be shown that the resulting orthogonalized orbitals are the closest to the original non-orthogonal functions in the least-squares sense [CK57; May02].

B.9 Numerical Details of the PZ-SIC Calculations

For the PZ-SIC calculations in Chapter 7, we employed our grid-based real-time code `BTDFT` [SK18] with a grid spacing of $0.2\,\mathrm{a_0}$. The grid was enclosed within atom-centered spheres with radii of $(9.45, 7.82, 8.67, 8.52)\,\mathrm{a_0}$ for the elements C, O, H, and N, respectively. These radii were determined based on the point where the atomic electron density, taken from the PPs, dropped below a threshold of $10^{-7}\,\mathrm{a_0}^{-3}$.

The Hartree potential was computed by solving the Poisson equation on an extended ellipsoidal grid with half-axes of $(25, 25, 25)\,\mathrm{a_0}$, using a 9th-order multipole expansion to establish the boundary conditions.

To model the atomic cores and core electrons, we utilized norm-conserving Troullier-Martins PPs [TM91] with the following cutoff radii: C $1.09\,\mathrm{a_0}$ (s and p), O $1.10\,\mathrm{a_0}$ (s and p), H $1.39\,\mathrm{a_0}$ (s), and N $0.99\,\mathrm{a_0}$ (s and p). In the Kleinman-Bylander transformation [KB82], the local component was p for oxygen and s for all other elements.

The convergence criterion for all calculations was set to $\Delta_{\text{error}\sigma} = 10^{-6}$. For the outer loop algorithm, the initial value of d was 0.5, with bounds set between 0.5 and 2.0. The parameter e was taken as the lowest value of the local part of the potential (i. e., the KS potential). For our inner loop algorithm, the trial step length was $l^{\text{trial}} = 0.1$, and the convergence criterion for $\max(\boldsymbol{G}_\sigma)$ was set to 10^{-6} Ry.

B.10 Oscillatory Features in v^{loc} for the TASKx-SIC Calculation of CO

As described in Section 7.2.1, we encountered numerical difficulties when calculating the PZ-SIC ground state for the CO molecule using the TASKx and r^{2}SCANx meta-GGA functionals. These difficulties manifest as oscillations in the error criterion during the damped gradient iterations of our PZ-SIC ground-state algorithm, as shown in Fig. 7.4.

To identify the origin of these oscillations, we analyzed the components of the PZ-SIC potentials within the orbital-dependent Hamiltonian $\hat{H}^{\tau}_{i\sigma}$ (defined in Eq. (6.17)) during the outer loop iteration steps where the orbitals where restricted to the real space. This analysis revealed spurious oscillatory features in the local potential $v^{\text{loc}}[s_{i\sigma}, \alpha = 0]$ of the PZ-SIC term. For illustration, Fig. B.1 shows the local potential of the TASKx meta-GGA, evaluated with the orbital density of the lowest-energy local orbital φ_1 of CO at iteration step $k = 100$. In Fig. B.1, the local potential is plotted in the yz-plane (with

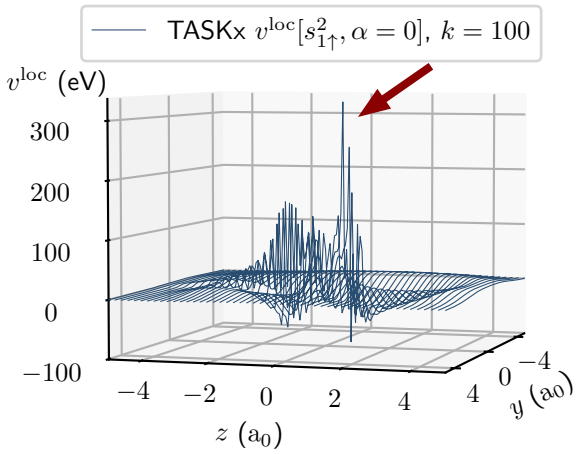

Figure B.1: Local part of the TASKx meta-GGA potential $v^{\text{loc}}[s^2_1, \alpha = 0]$ displayed in the yz-plane at $x = 0$ after 100 damped gradient iteration steps for a TASKx-SIC calculation for CO. The red arrow indicates the oscillatory features in the local potential.

$x = 0$), where the bond axis of the CO molecule aligns with the z-direction. Notably, oscillatory features in the potential are visible in the spatial region indicated by the red arrow.

As evident in Fig. B.2, the spatial region where the oscillatory features in the potential appear corresponds to the nodal plane of the orbital density used to evaluate the TASKx meta-GGA. This spatial region is analogously indicated by a red arrow in Fig. B.2.

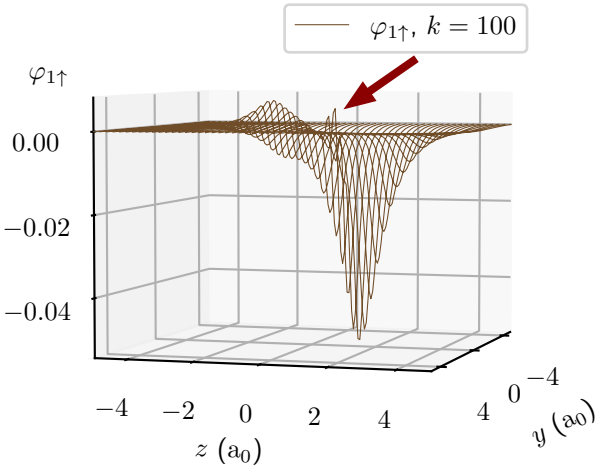

Figure B.2: Local orbital φ_1 displayed in the yz-plane at $x = 0$ after 100 damped gradient iterations for a TASKx-SIC calculation for CO. The red arrow indicates the position of the nodal plane.

B.11 Functional Derivatives of the TASK and r^{2}SCAN Meta-GGAs

The following sections provide the enhancement factors and their derivatives with respect to s^2 and α for the TASK [AK19; Asc19] and r^{2}SCAN [Fur+20a; Fur+20b] exchange meta-GGAs. It is also explicitly shown that $\partial F_\mathrm{x}/\partial s^2|_{\alpha=0}$ yields the same expression for both TASK and r^{2}SCAN.

Enhancement Factor for TASK Exchange

The enhancement factor for TASK is [AK19; Asc19]

$$F_\mathrm{x}^\mathrm{TASK}(s,\alpha) = h_\mathrm{x}^0 g_\mathrm{x}(s) + [1 - f_\mathrm{x}(\alpha)]\left[h_\mathrm{x}^1(s) - h_\mathrm{x}^0\right][g_\mathrm{x}(s)]^d \tag{B.50}$$

with the constants $h_\mathrm{x}^0 = 1.174$ and $d = 10$ and the functions

$$g_\mathrm{x}(s) = 1 - \exp\left(-cs^{-1/2}\right), \tag{B.51}$$

$$h_\mathrm{x}^1(s) = \sum_{\nu=0}^{2} a_\nu R_\nu(s^2), \tag{B.52}$$

$$f_\mathrm{x}(\alpha) = \sum_{\nu=0}^{4} b_\nu R_\nu(\alpha), \tag{B.53}$$

where $c = 4.9479$ and $R_\nu(x)$ are the rational Chebyshev functions of degree ν. The Chebyshev functions are

$$R_0(x) = 1, \tag{B.54}$$

$$R_1(x) = \frac{x-1}{x+1}, \tag{B.55}$$

$$R_2(x) = \frac{x^2 - 6x + 1}{(x+1)^2}, \tag{B.56}$$

$$R_3(x) = \frac{x^3 - 15x^2 + 15x - 1}{(x+1)^3}\,, \tag{B.57}$$

$$R_4(x) = \frac{x^4 - 28x^3 + 70x^2 - 28x + 1}{(x+1)^4}\,. \tag{B.58}$$

The coefficients are

$$\begin{aligned} a_0 &= 0.938719\,, & a_1 &= -0.076371\,, & a_2 &= -0.0150899\,, \\ b_0 &= -0.628591\,, & b_1 &= -2.10315\,, & b_2 &= -0.5\,, \\ b_3 &= 0.103153\,, & b_4 &= 0.128591\,. \end{aligned} \tag{B.59}$$

The derivative with respect to s^2 is

$$\begin{aligned} \left.\frac{\partial F_{\mathrm{x}}^{\mathrm{TASK}}}{\partial s^2}\right|_{\alpha} = &\left\{h_{\mathrm{x}}^0 + d\left[1 - f_{\mathrm{x}}(\alpha)\right]\left[h_{\mathrm{x}}^1(s) - h_{\mathrm{x}}^0\right]\left[g_{\mathrm{x}}(s)\right]^{d-1}\right\}\frac{\partial g_{\mathrm{x}}(s)}{\partial s^2} \\ &+ \left[1 - f_{\mathrm{x}}(\alpha)\right]\left[g_{\mathrm{x}}(s)\right]^d \frac{\partial h_{\mathrm{x}}^1(s)}{\partial s^2} \end{aligned} \tag{B.60}$$

with

$$\frac{\partial g_{\mathrm{x}}(s)}{\partial s^2} = -\frac{c}{4s^{5/2}}\exp\left(-cs^{-1/2}\right) \quad \text{and} \tag{B.61}$$

$$\frac{\partial h_{\mathrm{x}}^1(s)}{\partial s^2} = \sum_{\nu=1}^{2} a_\nu \frac{\partial R_\nu(s^2)}{\partial s^2}\,. \tag{B.62}$$

And the derivative with respect to α is

$$\left.\frac{\partial F_{\mathrm{x}}^{\mathrm{TASK}}}{\partial \alpha}\right|_{s^2} = -\left[h_{\mathrm{x}}^1(s) - h_{\mathrm{x}}^0\right]\left[g_{\mathrm{x}}(s)\right]^d \frac{\partial f_{\mathrm{x}}(\alpha)}{\partial \alpha} \tag{B.63}$$

with

$$\frac{\partial f_{\mathrm{x}}(\alpha)}{\partial \alpha} = \sum_{\nu=1}^{4} b_\nu \frac{\partial R_\nu(\alpha)}{\partial \alpha}\,. \tag{B.64}$$

The derivatives evaluated at $\alpha = 0$ for the iso-orbital case (for the correction term within the PZ-SIC) are

$$\left.\frac{\partial F_{\mathrm{x}}^{\mathrm{TASK}}}{\partial s^2}\right|_{\alpha=0} = h_{\mathrm{x}}^0 \frac{\partial g_{\mathrm{x}}(s)}{\partial s^2} \tag{B.65}$$

and

$$\left.\frac{\partial F_{\mathrm{x}}^{\mathrm{TASK}}}{\partial \alpha}\right|_{\alpha=0} = -\left[h_{\mathrm{x}}^1(s) - h_{\mathrm{x}}^0\right]\left[g_{\mathrm{x}}(s)\right]^d \left.\frac{\partial f_{\mathrm{x}}(\alpha)}{\partial \alpha}\right|_{\alpha=0} \tag{B.66}$$

with $\partial f_{\mathrm{x}}(\alpha)/\partial\alpha|_{\alpha=0} = 2b_1 - 8b_2 + 18b_3 - 32b_4$.

Enhancement Factor for r^{2}SCAN Exchange

The enhancement factor for the r^{2}SCAN meta-GGA is

$$F_{\mathrm{x}}^{\mathrm{r^2SCAN}}(s, \bar{\alpha}) = \left\{h_{\mathrm{x}}^1(s) + f_{\mathrm{x}}(\bar{\alpha})\left[h_{\mathrm{x}}^0 - h_{\mathrm{x}}^1(s)\right]\right\} g_{\mathrm{x}}(s) \tag{B.67}$$

with $h_{\mathrm{x}}^0 = 1.174$,

$$\bar{\alpha}(s, \alpha) = \frac{\alpha}{1 + \eta\frac{5}{3}s^2}\,, \tag{B.68}$$

with $\eta = 0.001$ and the functions

$$h_{\mathrm{x}}^1(s) = 1 + k_1 - \frac{k_1}{1 + \frac{x(s)}{k_1}}\,, \tag{B.69}$$

$$g_{\mathrm{x}}(s) = 1 - \exp\left(-\frac{a_1^{\mathrm{SCAN}}}{s^{1/2}}\right)\,, \tag{B.70}$$

$$f_{\mathrm{x}}(\bar{\alpha}) = \begin{cases} \exp\left[-\frac{c_{1\mathrm{x}}^{\mathrm{SCAN}}\bar{\alpha}}{1-\bar{\alpha}}\right] & \text{for } \bar{\alpha} < 0 \\ \sum_{i=0}^{7} c_{\mathrm{x}_i}\bar{\alpha}^i & \text{for } 0 \leq \bar{\alpha} \leq 2.5 \\ -d_{\mathrm{x}}^{\mathrm{SCAN}} \exp\left[\frac{c_{2\mathrm{x}}^{\mathrm{SCAN}}}{1-\bar{\alpha}}\right] & \text{for } \bar{\alpha} \geq 2.5 \end{cases} \tag{B.71}$$

with

$$x(s) = \left[c_\eta c_2 \exp\left(-\frac{s^4}{d_{p2}^4}\right) + \mu\right] s^2\,. \tag{B.72}$$

The constants are

$$\begin{aligned} k_1 = 0.065\,, \qquad c_\eta = \left[\frac{20}{27} + \eta\frac{5}{3}\right]\,, \qquad c_2 = -\sum_{i=7}^{7} i c_{\mathrm{x}i}[1 - h_{\mathrm{x}}^0] \approx -0.162742\,, \\ d_{p2} = 0.361\,, \quad a_1^{\mathrm{SCAN}} = 4.9479\,, \qquad c_{1\mathrm{x}}^{\mathrm{SCAN}} = 0.667\,, \\ c_{2\mathrm{x}}^{\mathrm{SCAN}} = 0.8\,, \qquad d_{\mathrm{x}}^{\mathrm{SCAN}} = 1.24\,, \end{aligned} \tag{B.73}$$

and

$$\begin{aligned} c_{x_{0\ldots7}} = (&1, -0.667, -0.4445555, -0.663086601049, \\ &1.451297044490, -0.887998041597, \\ &0.234528941479, -0.023185843322)\,. \end{aligned} \tag{B.74}$$

The derivative with respect to s^2 is

$$\begin{aligned} \left.\frac{\partial F_{\mathrm{x}}^{\mathrm{r^2SCAN}}}{\partial s^2}\right|_\alpha = &\left\{h_{\mathrm{x}}^1(s) + f_{\mathrm{x}}(\bar{\alpha})\left[h_{\mathrm{x}}^0 - h_{\mathrm{x}}^1(s)\right]\right\}\frac{\partial g_{\mathrm{x}}(s)}{\partial s^2} + (1 - f_{\mathrm{x}}(\bar{\alpha}))\frac{\partial h_{\mathrm{x}}^1(s)}{\partial s^2} g_{\mathrm{x}}(s^2) \\ &+ \frac{\partial f_{\mathrm{x}}(\bar{\alpha})}{\partial \bar{\alpha}}\left.\frac{\partial \bar{\alpha}}{\partial s^2}\right|_\alpha \left[h_{\mathrm{x}}^0 - h_{\mathrm{x}}^1(s)\right] g_{\mathrm{x}}(s) \end{aligned} \tag{B.75}$$

with

$$\frac{\partial g_{\mathrm{x}}(s)}{\partial s^2} = -\frac{a_1^{\mathrm{SCAN}}}{4s^{5/2}} \exp\left(-a_1^{\mathrm{SCAN}} s^{-1/2}\right)\,, \tag{B.76}$$

$$\frac{\partial h_{\mathrm{x}}^1(s)}{\partial s^2} = \frac{1}{\left(1 + \frac{x(s)}{k_1}\right)^2}\frac{\partial x(s)}{\partial s^2}\,, \tag{B.77}$$

$$\frac{\partial x(s)}{\partial s^2} = \left(1 - \frac{2s^4}{d_{p2}^4}\right) c_\eta c_2 \exp\left(-\frac{s^4}{d_{p2}^4}\right) + \mu\,. \tag{B.78}$$

and

$$\left.\frac{\partial \bar{\alpha}}{\partial s^2}\right|_\alpha = -\frac{\frac{5}{3}\eta\alpha}{\left(1 + \eta\frac{5}{3}s^2\right)^2}\,. \tag{B.79}$$

And the derivative with respect to α is

$$\left.\frac{\partial F_{\mathrm{x}}^{\mathrm{r^2SCAN}}}{\partial \alpha}\right|_{s^2} = \frac{\partial f_{\mathrm{x}}(\bar{\alpha})}{\partial \bar{\alpha}} \left.\frac{\partial \bar{\alpha}}{\partial \alpha}\right|_{s^2} \left[h_{\mathrm{x}}^0 - h_{\mathrm{x}}^1(s)\right] g_{\mathrm{x}}(s) \tag{B.80}$$

with

$$\frac{\partial f_{\mathrm{x}}(\bar{\alpha})}{\partial \bar{\alpha}} = \begin{cases} -\frac{c_{1x}^{\mathrm{SCAN}}}{(1-\bar{\alpha})^2} \exp\left(-\frac{c_{1x}^{\mathrm{SCAN}}\bar{\alpha}}{1-\bar{\alpha}}\right) & \text{for } \bar{\alpha} < 0 \\ \sum_{i=1}^{7} c_{x_i} \bar{\alpha}^{i-1} & \text{for } 0 \leq \bar{\alpha} \leq 2.5 \\ -d_{\mathrm{x}}^{\mathrm{SCAN}} \exp\left(\frac{c_{2x}^{\mathrm{SCAN}}}{1-\bar{\alpha}}\right) \frac{c_{2x}^{\mathrm{SCAN}}}{(1-\bar{\alpha})^2} & \text{for } \bar{\alpha} \geq 2.5 \end{cases} \tag{B.81}$$

and

$$\left.\frac{\partial \bar{\alpha}}{\partial \alpha}\right|_{s^2} = \frac{1}{1 + \eta \frac{5}{3} s^2}\,. \tag{B.82}$$

The derivatives evaluated at $\alpha = 0$ for the iso-orbital case are

$$\left.\frac{\partial F_{\mathrm{x}}^{\mathrm{r^2SCAN}}}{\partial s^2}\right|_{\alpha=0} = h_{\mathrm{x}}^0 \frac{\partial g_{\mathrm{x}}(s)}{\partial s^2} \tag{B.83}$$

and

$$\left.\frac{\partial F_{\mathrm{x}}^{\mathrm{r^2SCAN}}}{\partial \alpha}\right|_{\alpha=0} = -\frac{c_{1x}^{\mathrm{SCAN}}}{1 + \eta \frac{5}{3} s^2} \left[h_{\mathrm{x}}^0 - h_{\mathrm{x}}^1(s)\right] g_{\mathrm{x}}(s)\,. \tag{B.84}$$

Since $a_1^{\mathrm{SCAN}} \equiv c$ in the definitions of $g_{\mathrm{x}}(s)$ for TASK and r^{2}SCAN, as shown in Eq. (B.51) and Eq. (B.70), it is clear that the derivatives of the enhancement factors of TASK and r^{2}SCAN with respect to s^2, evaluated at $\alpha = 0$, are identical. This identity has been used to locate the origin of the numerical challenges encountered during the PZ-SIC ground-state calculations with TASK and r^{2}SCAN exchange (see Section 7.2.1).

B.12 Enhancement Factor for α_0TASK

The α_0TASK meta-GGA modifies the TASK meta-GGA such that the construction principle defined in Eq. (7.11) is fulfilled. This new meta-GGA functional has the same form as the TASK meta-GGA:

$$F_{\mathrm{x}}^{\alpha_0\mathrm{TASK}}(s,\alpha) = h_{\mathrm{x}}^0 g_{\mathrm{x}}(s) + \left[1 - f_{\mathrm{x}}^{\alpha_0\mathrm{TASK}}\right] \left[h_{\mathrm{x}}^1(s) - h_{\mathrm{x}}^0\right] \left[g_{\mathrm{x}}(s)\right]^d \tag{B.85}$$

The construction principle of Eq. (7.11) is fulfilled by satisfying

$$\left.\frac{\partial f_{\mathrm{x}}^{\alpha_0\mathrm{TASK}}}{\partial \alpha}\right|_{\alpha=0} = 0\,. \tag{B.86}$$

This is achieved by modifying the function $f_{\mathrm{x}}(\alpha)$ from TASK to

$$f_{\mathrm{x}}^{\alpha_0\mathrm{TASK}}(\alpha) = \sum_{\nu=0}^{5} b_\nu^{\alpha_0\mathrm{TASK}} R_\nu(\alpha) \tag{B.87}$$

with the additional Chebyshev function

$$R_5(x) = 16\left(\frac{x-1}{x+1}\right)^5 - 20\left(\frac{x-1}{x+1}\right)^3 + 5\frac{x-1}{x+1} \tag{B.88}$$

and

$$b_{0\ldots5}^{\alpha_0\mathrm{TASK}} = (-0.628591, -2.18017, -0.5, 0.141661, 0.128591, 0.0385072)\,. \tag{B.89}$$

The modified function $f_\mathrm{x}^{\alpha_0\mathrm{TASK}}$, along with the original function f_x from TASK, is shown in panel (a) of Fig. B.3. Panel (b) of Fig. B.3 displays the corresponding

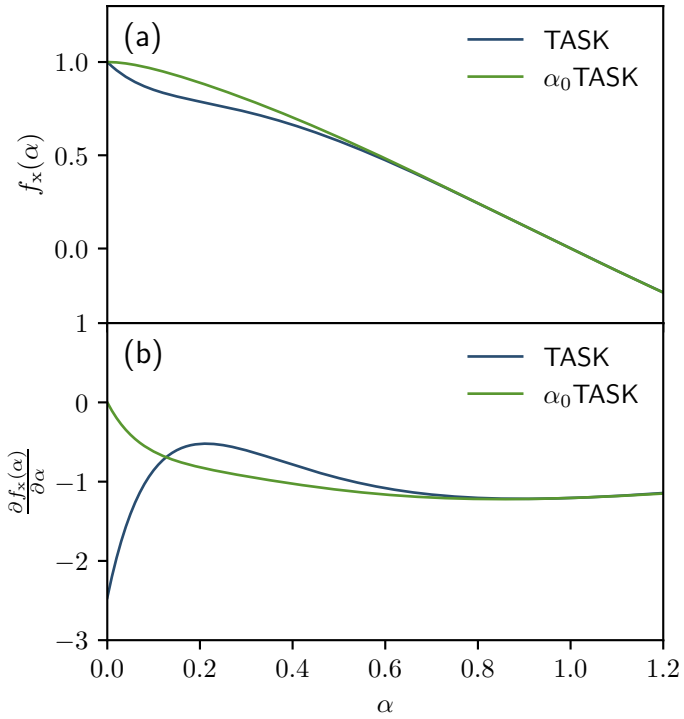

Figure B.3: $f_\mathrm{x}(\alpha)$ and $\partial f_\mathrm{x}(\alpha)/\partial\alpha$ for TASK and α_0TASK.

derivatives of $f_\mathrm{x}^{\alpha_0\mathrm{TASK}}$ and f_x with respect to α. In this figure, the designed properties of $f_\mathrm{x}^{\alpha_0\mathrm{TASK}}(\alpha)$ become evident: While $f_\mathrm{x}(\alpha)$ for the TASK functional exhibits a strong derivative at $\alpha = 0$, $f_\mathrm{x}^{\alpha_0\mathrm{TASK}}(\alpha)$ flattens out at 1 as α approaches 0, resulting in $\partial f_\mathrm{x}^{\alpha_0\mathrm{TASK}}/\partial\alpha|_{\alpha=0} = 0$.

Table B.1 illustrates the HOMO and LUMO eigenvalues for TASK-GKS and α_0TASK-GKS calculations. For all model systems, the HOMO eigenvalue shifts slightly to lower

Table B.1: HOMO and LUMO eigenvalues for the CO, H_2O, and N_2 molecules using TASK-GKS and α_0TASK-GKS (with LSDA correlation).

	TASK-GKS		**α_0TASK-GKS**	
	ϵ_HOMO	ϵ_LUMO	ϵ_HOMO	ϵ_LUMO
CO	−9.86	−1.42	−10.01	−1.31
H_2O	−7.88	−0.89	−7.93	−1.00
N_2	−11.05	−1.51	−11.22	−1.36

energies from TASK to α_0TASK by approximately 0.1 to 0.2 eV. No general trend is observed for the LUMO eigenvalue, with a shift of 0.1 to 0.15 eV from TASK to α_0TASK.

Looking at the energy curves in Fig. B.4 for our test set consisting of CO, H_2O, and N_2 for TASK and α_0TASK (with LSDA correlation), only minimal differences between

the two meta-GGAs are visible. The curvature of the $E(N)$ curves and the energy values

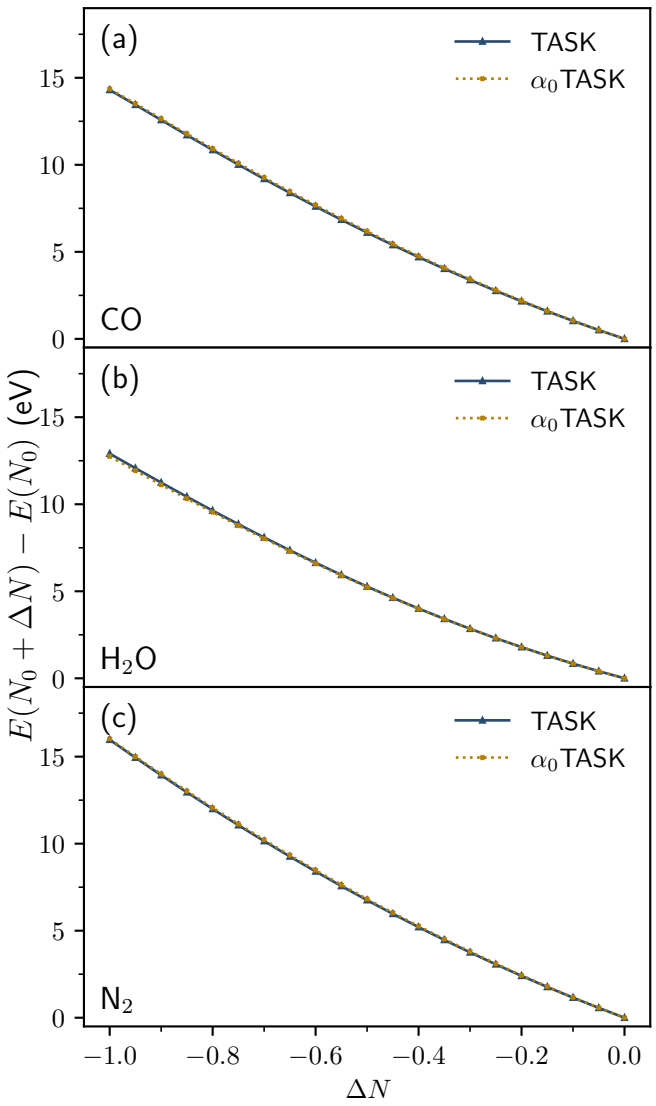

Figure B.4: Total energy difference to the neutral CO (panel (a)), H_2O (panel (b)), and N_2 (panel (c)) molecule as a function of the electron number change ΔN calculated with TASK and α_0TASK τ.

are only slightly affected by the transition from TASK to α_0TASK. This suggests that the changes introduced in α_0TASK have a minimal impact on the physical properties predicted for our test set.

B.13 Results for α_0TASK-SIC with Current-Density Correction

As outlined in the main text, PZ-SIC calculations require using complex orbitals for energy minimization. However, since complex orbitals can carry a current density, it may be necessary to incorporate the current-density correction to the kinetic energy density, as defined in Eq. (6.19). Figure B.5 shows the energy curves calculated using

α_0TASK (with LSDA correlation) applying the PZ-SIC, both with and without the current-density correction, labeled as α_0TASK-SIC $\hat{\tau}$ and α_0TASK-SIC τ, respectively. This figure illustrates that the differences between calculations with and without the

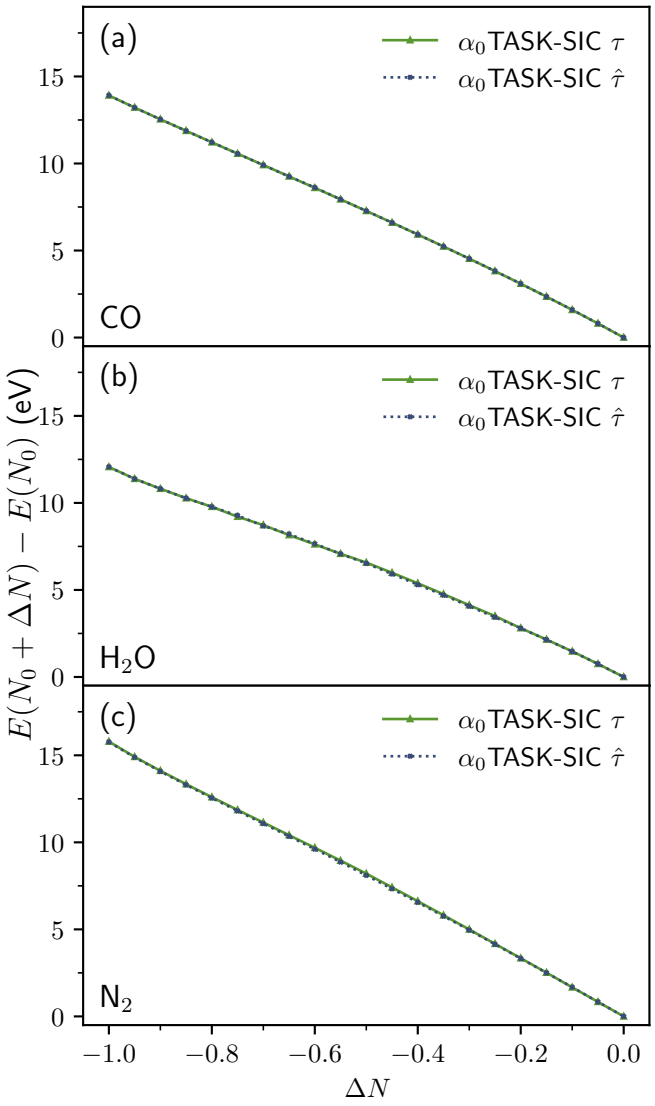

Figure B.5: Total energy difference to the neutral CO (panel (a)), H_2O (panel (b)), and N_2 (panel (c)) molecule as a function of the electron number change ΔN calculated with α_0TASK τ (without current-density correction) and with α_0TASK $\hat{\tau}$ (with current-density correction).

current-density correction are negligible for all model systems: CO, H_2O, and N_2, shown in panels (a), (b), and (c), respectively. Consequently, incorporating the current-density correction is not required to compute the energy curves of the test set.

Table B.2 additionally compares the ΔSCF values and the HOMO energies (corresponding to the highest occupied diagonal element of the Lagrange multiplier, i. e., $\lambda_{\mathrm{HOMO\,HOMO}}$). Nearly identical results are observed for both calculations, with a maximum deviation of 0.03 eV in the ΔSCF value for N_2, confirming our previous finding that the current-density correction has a negligible impact on our outcomes.

Table B.2: Comparison of calculated IPs for CO, H_2O, and N_2 as $\Delta\text{SCF} = E(N_0 - 1) - E(N_0)$ and HOMO eigenvalues of the neutral molecule (in eV) for α_0TASK τ without and α_0TASK-SIC $\hat{\tau}$ with current-density correction (with LSDA correlation).

	α_0**TASK-SIC** τ		α_0**TASK-SIC** $\hat{\tau}$	
	ΔSCF	ϵ_{HOMO}	ΔSCF	ϵ_{HOMO}
CO	13.91	−16.51	13.91	−16.51
H_2O	12.06	−18.13	12.07	−18.14
N_2	15.79	−18.01	15.76	−18.01

B.14 HOMO Energy Curves for CO, H_2O, and N_2 with and without Using the PZ-SIC

Figure B.6 shows the HOMO energy curves for the CO molecule using different (semi-)local xc approximations, with and without using the PZ-SIC. For the uncor-

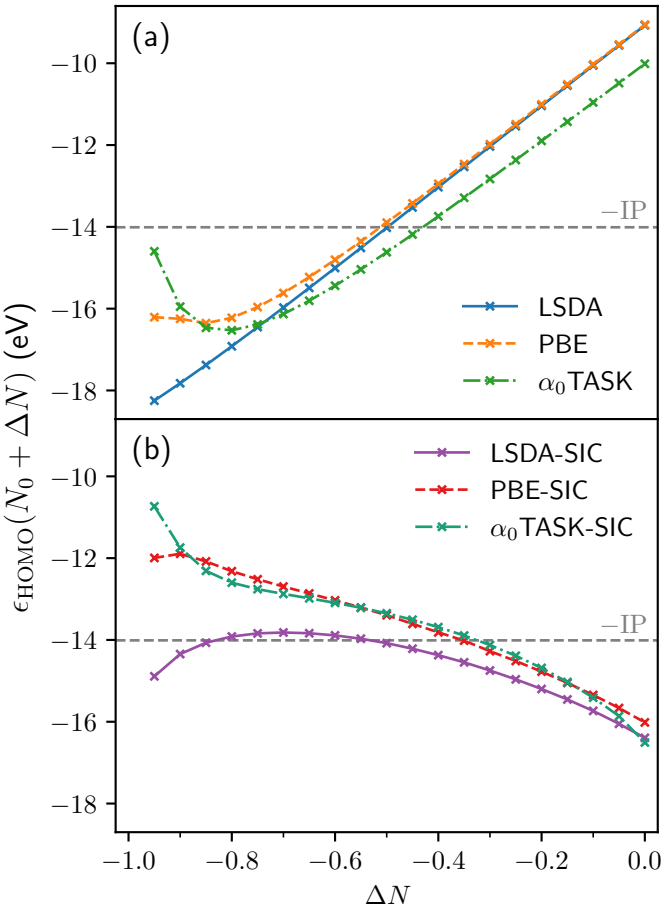

Figure B.6: HOMO energy curves for the CO molecule obtained using LSDA, PBE, and α_0TASK: panel (a) shows results without using the PZ-SIC, and panel (b) displays the results using the PZ-SIC. The dashed gray horizontal lines indicate the negative experimental IP.

rected functionals, the HOMO energy corresponds to the KS eigenvalue, whereas for the corrected functionals it is given by $\lambda'_{\mathrm{HOMO\,HOMO}} = \langle\varphi_{\mathrm{HOMO}}|\hat{H}_{\mathrm{HOMO}}|\varphi_{\mathrm{HOMO}}\rangle$, where $\hat{H}_{\mathrm{HOMO}}$ denotes the HOMO-dependent Hamiltonian.

Analogously to the energy curves presented in the main text, $\Delta N = 0$ in Fig. B.6 corresponds to the neutral CO molecule with N_0 electrons. The dashed gray horizontal line indicates the negative experimental IP. According to Janak's theorem and the straight-line condition for the total energy curve, the exact xc functional would yield a constant HOMO energy for $N_0-1 < N \leq N_0$. Since this does not apply to $\epsilon_{\mathrm{HOMO}}(N_0-1)$, which deviates significantly from the values in the range $]N_0 - 1, N_0]$, it is omitted from the graphs of the HOMO energy curves.

The curves for the CO molecule in Fig. B.6 exhibit the expected behavior for $\Delta N > -0.8$: while using (semi-)local functionals results in an increasing HOMO energy curve, the curves obtained using the PZ-SIC decrease. Generally, the increase in ϵ_{HOMO} for the uncorrected functionals is more pronounced than the decrease observed for the functionals employing the PZ-SIC, indicating a stronger deviation from the exact straight-line condition.

However, for $\Delta N < -0.8$, the HOMO energy curves exhibit a different behavior for some functionals. In particular, the curves for α_0TASK and PBE display a negative slope in this range, in contrast to the previously discussed range of $\Delta N > -0.8$, where the slope was strongly positive. A similar change in slope is also observed for the LSDA-SIC and PBE-SIC results: while the HOMO energy generally decreases with ΔN for these self-interaction corrected functionals, the slope becomes slightly positive for $\Delta N < -0.8$.

The results for the H_2O molecule are illustrated in Fig. B.7. For the uncorrected functionals in panel (a), the HOMO energy increases with a pronounced slope, deviating significantly from the horizontal line of the negative experimental IP. In contrast to the CO molecule, the slope for the curve obtained with the α_0TASK functional remains nearly unchanged near $N_0 - 1$. While generally closer to the experimental IP, the PZ-SIC results in panel (b) exhibit a noticeable slope change at approximately $\Delta N = -0.6$ for all three functionals considered. Furthermore, near the neutral H_2O molecule, the HOMO energy curves display a strongly negative slope.

Finally, the results for the N_2 molecule are shown in Fig. B.8. The HOMO energy curves for the (semi-)local functionals without using the PZ-SIC exhibit an almost linear behavior with a pronounced positive slope, leading to a significant deviation from the negative experimental IP. This is consistent with previous findings that the curvature of the corresponding energy curves in Fig. 7.3 for LSDA and PBE, as well as in Fig. 7.8 for α_0TASK, remains nearly unchanged.

In contrast, the HOMO energy curves obtained with the PZ-SIC are considerably closer to a horizontal line. Nevertheless, for all functionals considered, the absolute values of the HOMO energies systematically overestimate the experimental IP. Moreover, similar to the observations for H_2O, the PZ-SIC results exhibit a pronounced drop near $\Delta N = 0$.

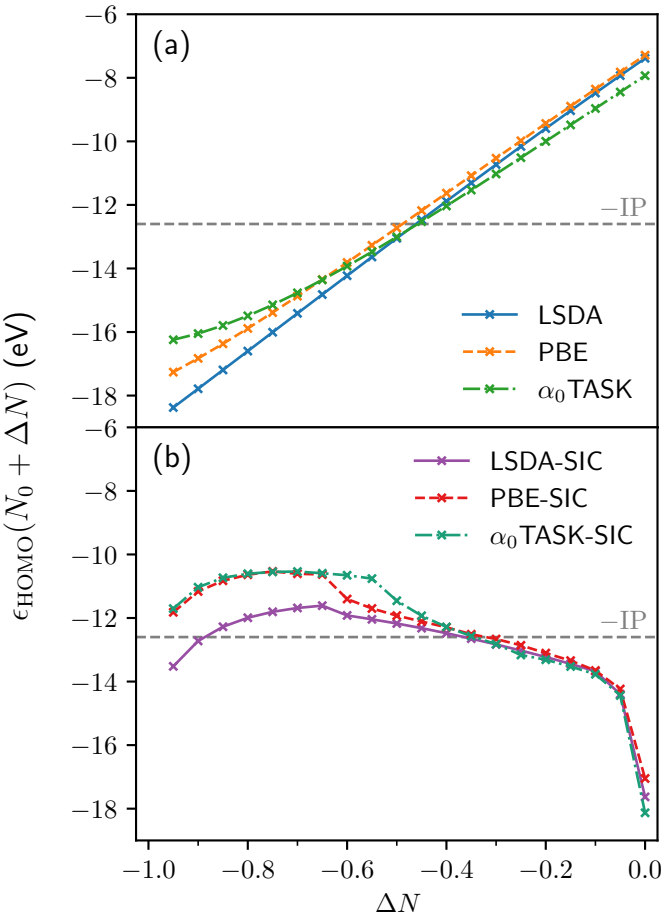

Figure B.7: HOMO energy curves for the H_2O molecule obtained using LSDA, PBE, and α_0TASK: panel (a) shows results without using the PZ-SIC, and panel (b) displays the results using the PZ-SIC. The dashed gray horizontal lines indicate the negative experimental IP.

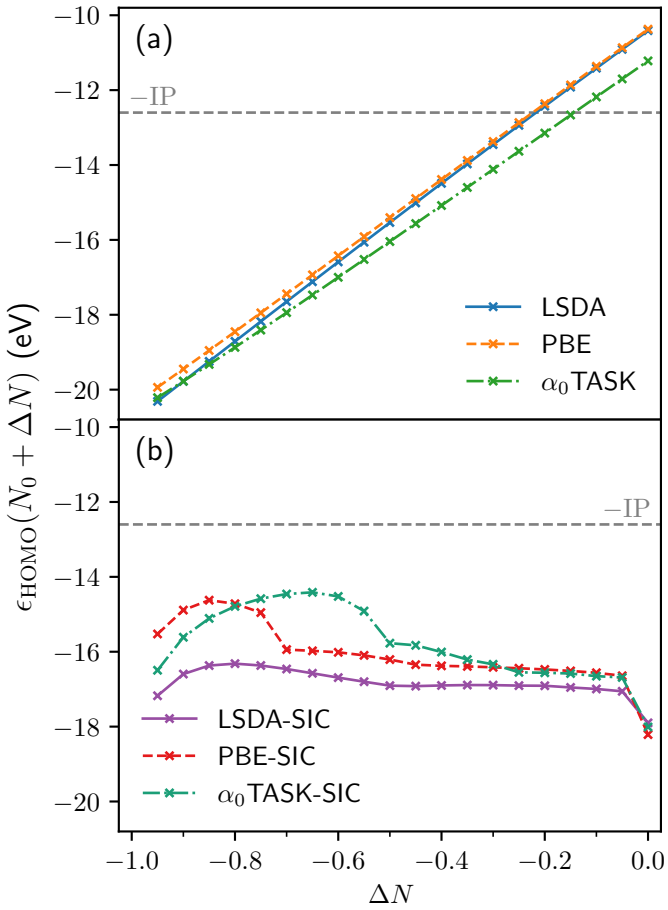

Figure B.8: HOMO energy curves for the N_2 molecule obtained using LSDA, PBE, and α_0TASK: panel (a) shows results without using the PZ-SIC, and panel (b) displays the results using the PZ-SIC. The dashed gray horizontal lines indicate the negative experimental IP.

B.15 Influence of Boundary Condition for Solving the Screened Poisson Equation

To assess the impact of the boundary condition used for solving the screened Poisson equation (see Eq. (8.13)), we compare calculations performed with and without using the monopole moment of $v^{(\gamma)}_{\text{Yukawa}}$ as the boundary condition. For this comparison, we compute the electronic ground state of the CO molecule (with a bond length of $2.132\,\text{a}_0$) using the uncorrected LDA. All numerical parameters are chosen as described in Section B.9, and the tolerance for solving both the Poisson and screened Poisson equations is set to 10^{-10} (see Ref. [Sch17] for details). Panel (a) of Fig. B.9 shows the difference between the Hartree potential (computed using a 9th-order multipole expansion boundary condition) and the Yukawa potential (with screening parameter $\gamma = 0$, so that it equals the Hartree potential) calculated with a zero-boundary condition. The results are plotted in the yz plane (with $x = 0$), parallel to the CO molecule's bond

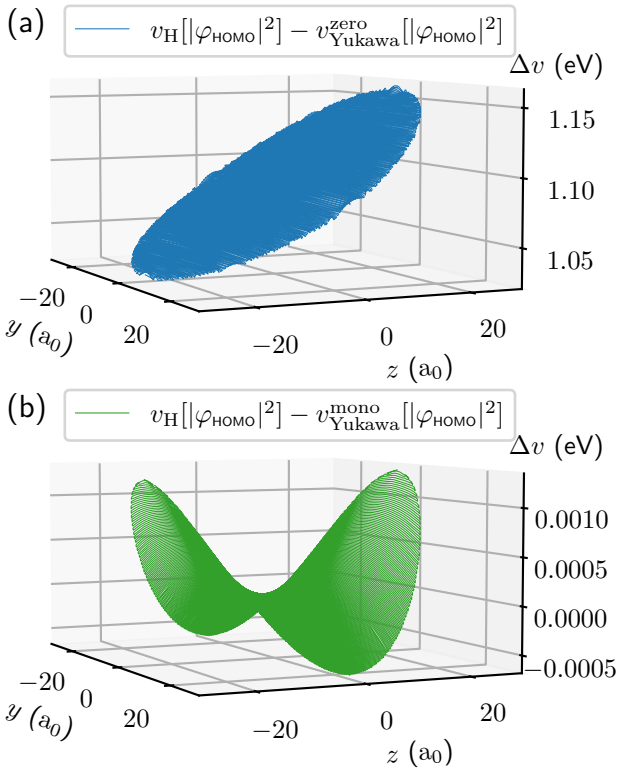

Figure B.9: Difference between the Hartree potential (computed using a 9th-order multipole expansion boundary condition) and the Yukawa potential (with screening parameter $\gamma = 0$) calculated using a zero-boundary condition in panel (a) and a monopole boundary condition in panel (b). Both potentials are evaluated on the HOMO ground-state density $|\varphi_{\text{HOMO}}|^2$ of the CO molecule, obtained with the LDA functional.

axis. Panel (b) shows the same difference but with the Yukawa potential calculated using the monopole moment as the boundary condition. A comparison of the two panels reveals that using the monopole moment as the boundary condition significantly reduces the error, lowering the maximum deviation from approximately 1.15 eV to about 0.001 eV. This is further confirmed by the corresponding energy values: $E_{\text{H}}[|\varphi_{\text{HOMO}}|^2] = 7.904\,\text{eV}$,

$E^{\text{zero}}_{\text{Yukawa}}[|\varphi_{\text{HOMO}}|^2] = 7.359\,\text{eV}$, and $E^{\text{mono}}_{\text{Yukawa}}[|\varphi_{\text{HOMO}}|^2] = 7.904\,\text{eV}$. While the difference between using the 9th-order multipole expansion and the monopole moment as the boundary condition is negligible, employing a zero-boundary condition introduces a deviation of 0.545 eV.

These results indicate that the monopole boundary condition is crucial for accurately calculating the Yukawa potential. Given that the Yukawa potential decays most slowly for $\gamma = 0$ and that the monopole boundary condition yields results comparable to those obtained using the 9th-order multipole expansion for the Hartree potential, we expect that using the monopole boundary condition with a real-space spherical grid of radius $25\,\text{a}_0$ is sufficient for accurately computing the Yukawa potential.

B.16 Derivation of the Long-Range LSDA Expression

The derivation of the long-range LDA exchange energy expression is based on Chapter 6 of Ref. [Par20] and Ref. [Rob+62]. For simplicity, the spin index σ is omitted throughout this section. The corresponding spin-dependent expressions can be obtained by applying the spin-scaling relations described in Section 3.6.3.

We begin by defining the (spin-independent) one-particle density matrix:

$$\rho(\mathbf{r}_1, \mathbf{r}_2) = 2 \sum_{i=1}^{N/2} \varphi_i(\mathbf{r}_1)\varphi_i^*(\mathbf{r}_2)\,. \tag{B.90}$$

Using this definition, the exact exchange energy using the long-range screening function

$$\mu^{\text{lr}(\gamma)}(|\mathbf{r}_1 - \mathbf{r}_2|) = 1 - e^{-\gamma|\mathbf{r}_1 - \mathbf{r}_2|} \tag{B.91}$$

can be written as

$$E_{\text{x}}^{\text{lr-exact}(\gamma)} = -\frac{e^2}{4} \iint \mu^{\text{lr}(\gamma)}(|\mathbf{r}_1 - \mathbf{r}_2|) \frac{|\rho(\mathbf{r}_1, \mathbf{r}_2)|^2}{|\mathbf{r}_1 - \mathbf{r}_2|}\, \mathrm{d}^3 r_1\, \mathrm{d}^3 r_2\,. \tag{B.92}$$

For the uniform electron gas with particle-in-a-box boundary conditions, the wave function satisfies $\psi(x = 0) = \psi(x = L) = 0$, where L is the box length. Consequently, it can be written as

$$\psi(k_x, k_y, k_z) = \frac{1}{\sqrt{L^3}} e^{\mathrm{i}(k_x x + k_y y + k_z z)} = \frac{1}{\sqrt{V}} e^{\mathrm{i}\mathbf{k}\cdot\mathbf{r}} \tag{B.93}$$

with $L^3 = V$ and

$$\mathbf{k} = \frac{2\pi}{L}\mathbf{n} \quad \text{with} \quad \mathbf{n} = \begin{pmatrix} n_x \\ n_y \\ n_z \end{pmatrix} \tag{B.94}$$

where $n_i \in \mathbb{Z}$. Inserting this into Eq. (B.90) leads to

$$\rho(\mathbf{r}_1, \mathbf{r}_2) = \frac{2}{V} \sum_{\mathbf{k} \in \text{ occ.}} e^{\mathrm{i}\mathbf{k}\cdot(\mathbf{r}_1 - \mathbf{r}_2)}\, \mathrm{d}^3 k\,. \tag{B.95}$$

For many occupied states, the sum can be replaced by an integral and $V = (2\pi)^3$

$$\rho(\mathbf{r}_1, \mathbf{r}_2) = \frac{1}{4\pi^3} \int e^{\mathrm{i}\mathbf{k}\cdot(\mathbf{r}_1 - \mathbf{r}_2)}\, \mathrm{d}^3 k = \frac{1}{4\pi^3} \int_0^{k_{\text{F}}} k^2 \int_0^{\pi} \int_0^{2\pi} e^{\mathrm{i}\mathbf{k}\cdot(\mathbf{r}_1 - \mathbf{r}_2)} \sin\vartheta\, \mathrm{d}k\, \mathrm{d}\vartheta\, \mathrm{d}\phi\,. \tag{B.96}$$

The Fermi wavevector k_F can be obtained by $\rho(\mathbf{r},\mathbf{r}) = n(\mathbf{r})$ and therefore

$$n(\mathbf{r}) = \frac{k_\mathrm{F}^3(\mathbf{r})}{3\pi^2} \quad \Leftrightarrow \quad k_\mathrm{F}(\mathbf{r}) = \left[3\pi^2 n(\mathbf{r})\right]^{1/3} . \tag{B.97}$$

The density $n(\mathbf{r})$ and the Fermi wave vector k_F are constant for homogeneous systems. For slightly inhomogeneous systems, one may approximate the local value of k_F at a point $\mathbf{r}$ by evaluating it at the midpoint between two spatial points, i. e., $\mathbf{r} = (\mathbf{r}_1 + \mathbf{r}_2)/2$. Therefore, we use the coordinates

$$\mathbf{r} = \frac{1}{2}(\mathbf{r}_1 + \mathbf{r}_2), \quad \mathbf{s} = \mathbf{r}_1 - \mathbf{r}_2 \tag{B.98}$$

for rewriting Eq. (B.96). Without loss of generality, we choose $\mathbf{s}$ to be parallel to the k_z axis. Then, the density matrix from Eq. (B.96) can be written in terms of $\mathbf{r}$ and $s = |\mathbf{s}|$ as

$$\begin{aligned} \rho(\mathbf{r}, s) =& \frac{1}{4\pi^3} \int_0^{k_\mathrm{F}} \int_0^{\pi} k^2 \sin\vartheta \, e^{iks\cos\vartheta} \, \mathrm{d}\vartheta \, \mathrm{d}k \int_0^{2\pi} \mathrm{d}\phi \\ =& 3n(\mathbf{r}) \left[\frac{\sin\left(t(\mathbf{r})\right) - t(\mathbf{r})\cos\left(t(\mathbf{r})\right)}{t^3(\mathbf{r})} \right] \end{aligned} \tag{B.99}$$

with $t = k_\mathrm{F}\, s$. Inserting this into Eq. (B.92) leads to

$$\begin{aligned} E_\mathrm{x}^{\text{lr-LDA}(\gamma)} =& -\pi e^2 \int_0^\infty s(1 - e^{-\gamma s}) \int \rho^2(\mathbf{r}, s) \, \mathrm{d}^3 r \, \mathrm{d}s \\ =& -9\pi e^2 \int_0^\infty \int \frac{1}{k_\mathrm{F}^2}(1 - e^{-\gamma s}) \frac{(\sin t - t\cos t)^2}{t^6} 9n^2(\mathbf{r}) \, \mathrm{d}^3 r \, \mathrm{d}s \, . \end{aligned} \tag{B.100}$$

This can be further rewritten using $s = t/k_\mathrm{F}$ and $\mathrm{d}s = \mathrm{d}t/k_\mathrm{F}$ with k_F from Eq. (B.97) to

$$\begin{aligned} E_\mathrm{x}^{\text{lr-LDA}(\gamma)} =& \underbrace{-\frac{3}{4}\left(\frac{3}{\pi}\right)^{1/3}}_{=A_\mathrm{x}} e^2 \int_0^\infty \int n^{4/3}(\mathbf{r}) \left(1 - e^{-\gamma\frac{t}{k_\mathrm{F}}}\right) \frac{4(\sin t - t\cos t)^2}{t^5} \, \mathrm{d}^3 r \, \mathrm{d}t \\ =& A_\mathrm{x} \int n^{4/3}(\mathbf{r}) 4 \int_0^\infty \left(1 - e^{-\gamma\frac{t}{k_\mathrm{F}}}\right) \frac{(\sin t - t\cos t)^2}{t^5} \, \mathrm{d}t \, \mathrm{d}^3 r \, , \end{aligned} \tag{B.101}$$

with $e^2 = 1$ for Hartree atomic units. The enhancement factor that modifies the LDA exchange energy to yield $E_\mathrm{x}^{\text{lr-LDA}}$ is thus defined as

$$\begin{aligned} F_\mathrm{x}^{\text{lr-LDA}(\gamma)} =& 4 \int_0^\infty \left(1 - e^{-\gamma\frac{t}{k_\mathrm{F}}}\right) \frac{(\sin t - t\cos t)^2}{t^5} \, \mathrm{d}t \\ =& \frac{\gamma\left[4k_\mathrm{F}^2\left(\gamma + 8k_\mathrm{F}\arctan\left(\frac{2k_\mathrm{F}}{\gamma}\right)\right) - \gamma\left(12k_\mathrm{F}^2 + \gamma^2\right)\ln\left(1 + \frac{4k_\mathrm{F}^2}{\gamma^2}\right)\right]}{24k_\mathrm{F}^4} \, . \end{aligned} \tag{B.102}$$

The integral in Eq. (B.102) can be evaluated using the computer algebra system `Mathematica` [WR] and closely resembles the expression derived in Ref. [Rob+62].

In the main text, the enhancement factor is expressed in terms of the Wigner-Seitz radius using

$$k_{\mathrm{F}}(\mathbf{r}) = \underbrace{\left(\frac{9\pi}{4}\right)^{1/3}}_{=:c_{\mathrm{x}}} \frac{1}{r_{\mathrm{s}}} \tag{B.103}$$

which yields

$$F_{\mathrm{x}}^{\text{lr-LDA}(\gamma)} = \frac{\gamma\left\{4\frac{c_{\mathrm{x}}^2}{r_{\mathrm{s}}^2}\left[\gamma + 8\frac{c_{\mathrm{x}}}{r_{\mathrm{s}}}\arctan\left(\frac{2c_{\mathrm{x}}}{\gamma r_{\mathrm{s}}}\right)\right] - \gamma\left(12\frac{c_{\mathrm{x}}^2}{r_{\mathrm{s}}^2} + \gamma^2\right)\ln\left(1 + \frac{4c_{\mathrm{x}}^2}{r_{\mathrm{s}}^2\gamma^2}\right)\right\}}{24\frac{c_{\mathrm{x}}^4}{r_{\mathrm{s}}^4}}. \tag{B.104}$$

B.17 Numerical Details of lrSIC Calculations

The grid parameters (size of the main and Hartree grid), as well as the PP parameters for CO, H_2O, and N_2, are adapted from our full PZ-SIC calculations, as described in Section B.9. For the calculation in Section 8.4, the convergence criteria for the outer loop was $\Delta_{\text{error}\sigma} = 1.0 \times 10^{-6}$ and the convergence threshold for the inner loop algorithms was $\max(\mathbf{G}_\sigma) = 5.0 \times 10^{-8}\,\mathrm{Ry}$.

Similarly to the LSDA-lrSIC calculation for the CO molecule described in Section 8.4.3, where two nearly degenerate ground states exhibited a strong deviation in their HOMO energies, we also observe this behavior for the H_2O molecule in calculations with screening parameters of $\gamma = 0.45\,\mathrm{a_0^{-1}}$ and $0.5\,\mathrm{a_0^{-1}}$. Specifically, starting our LSDA-lrSIC calculation with $\gamma = 0.45\,\mathrm{a_0^{-1}}$ either from an uncorrected LSDA ground-state calculation or from an LSDA-lrSIC calculation with $\gamma = 0.4\,\mathrm{a_0^{-1}}$ results in an energy difference of only 0.04 eV. In contrast, the HOMO energies differ significantly by 2.62 eV, with values of $-12.38\,\mathrm{eV}$ (starting from LSDA ground-state) and $-15.00\,\mathrm{eV}$ (starting from LSDA-lrSIC ground-state). For the LSDA-lrSIC calculation with $\gamma = 0.5\,\mathrm{a_0^{-1}}$, we find a HOMO energy of $-12.67\,\mathrm{eV}$ when starting from an uncorrected LSDA ground-state calculation, whereas starting from an LSDA-lrSIC calculation with $\gamma = 0.55\,\mathrm{a_0^{-1}}$ yields a HOMO energy of $-15.40\,\mathrm{eV}$. However, the difference in ground-state energy remains minimal at just 0.05 eV. In Section 8.4, the HOMO energies are generally presented for the calculations yielding the lower ground-state energies.

B.18 Attempts for Mitigating the Numerical Difficulties within the Screened LDA Potential

To mitigate numerical instabilities associated with the enhancement factor of the screened LSDA functional (see Section 8.4.3) and its derivative in the low-density limit, i.e., $n \to 0$ or $r_{\mathrm{s}} \to \infty$, we considered several approaches.

As described in Section 8.4.3, the individual terms F_1 and F_2 of the enhancement factor $F_{\mathrm{x}}^{\text{lr-LDA}(\gamma)}$ diverge in the low-density limit. However, the sum of F_1 and F_2 converges to a constant as $r_{\mathrm{s}} \to \infty$. To improve the numerical accuracy of the cancellation of these terms in the low-density limit, we reformulate the enhancement factor such that the cancellation of the individually diverging terms occurs at the lowest possible orders

in r_s and γ. This approach leads to

$$F_\mathrm{x}^{\text{lr-LDA}(\gamma)}(r_\mathrm{s}) = \underbrace{\frac{4}{3}\frac{\gamma r_\mathrm{s}}{c_\mathrm{x}}\arctan\left(\frac{2c_\mathrm{x}}{\gamma r_\mathrm{s}}\right)}_{=F_2}\underbrace{-\frac{1}{2}\frac{\gamma^2 r_\mathrm{s}^2}{c_\mathrm{x}^2}\ln\left[1+\frac{4c_\mathrm{x}^2}{r_\mathrm{s}^2\gamma^2}\right]}_{=F_3} \underbrace{+\frac{1}{6}\frac{\gamma^2 r_\mathrm{s}^2}{c_\mathrm{x}^2}\left(1-\frac{1}{4}\frac{\gamma^2 r_\mathrm{s}^2}{c_\mathrm{x}^2}\ln\left[1+\frac{4c_\mathrm{x}^2}{r_\mathrm{s}^2\gamma^2}\right]\right)}_{=F_1+F_4}, \tag{B.105}$$

and analogously for the derivative

$$\frac{\partial F_\mathrm{x}^{\text{lr-LDA}(\gamma)}}{\partial r_\mathrm{s}} = \underbrace{\frac{4}{3}\frac{\gamma}{c_\mathrm{x}}\arctan\left(\frac{2c_\mathrm{x}}{\gamma r_\mathrm{s}}\right)}_{=\partial_{r_\mathrm{s}}F_2}\underbrace{-\frac{\gamma^2 r_\mathrm{s}}{c_\mathrm{x}^2}\ln\left[1+\frac{4c_\mathrm{x}^2}{r_\mathrm{s}^2\gamma^2}\right]}_{=\partial_{r_\mathrm{s}}F_3} \underbrace{+\frac{1}{3}\frac{\gamma^2 r_\mathrm{s}}{c_\mathrm{x}^2}\left(2-\frac{1}{2}\frac{\gamma^2 r_\mathrm{s}^2}{c_\mathrm{x}^2}\ln\left[1+\frac{4c_\mathrm{x}^2}{r_\mathrm{s}^2\gamma^2}\right]\right)}_{=\partial_{r_\mathrm{s}}F_1+\partial_{r_\mathrm{s}}F_4}, \tag{B.106}$$

with the constant $c_\mathrm{x} = (9\pi/4)^{1/3}$. However, this rearrangement of the individual terms of the enhancement factor does not resolve the numerical instabilities.

An alternatively tested approach to improve the numerical accuracy for small densities involves using the series expansion

$$\ln(1+x) = \sum_{k=1}^{\infty}(-1)^{k+1}\frac{x^k}{k} \quad \text{with} \quad x \coloneqq \frac{4c_\mathrm{x}^2}{\gamma^2 r_\mathrm{s}^2}, \tag{B.107}$$

which is valid for $|x| \leq 1$. Applying Eq. (B.107), the sum $F_1 + F_4$ can be written as

$$F_1 + F_4 = \underbrace{\frac{1}{3}}_{=\lim_{r_\mathrm{s}\to\infty}(F_1+F_4)} + \frac{2}{3}\sum_{k=1}^{\infty}(-1)^k\frac{2^{2k}}{k+2}\left(\frac{c_\mathrm{x}}{r_\mathrm{s}\gamma}\right)^{2k} \quad \text{for} \quad \left|\frac{c_\mathrm{x}}{\gamma r_\mathrm{s}}\right| \leq \frac{1}{2}\,. \tag{B.108}$$

where the divergent terms of F_1 and F_4 vanish. Similarly, this approach can be applied to the derivative, resulting in

$$\partial_{r_\mathrm{s}}F_1 + \partial_{r_\mathrm{s}}F_4 = \frac{4}{3}\frac{1}{r_\mathrm{s}}\left[1 + 2\sum_{k=1}^{\infty}(-1)^k\frac{2^{2k}}{k+2}\left(\frac{c_\mathrm{x}}{\gamma r_\mathrm{s}}\right)^{2k}\right] \quad \text{for} \quad \left|\frac{c_\mathrm{x}}{\gamma r_\mathrm{s}}\right| \leq \frac{1}{2}\,. \tag{B.109}$$

However, implementing this approach for calculating $F_\mathrm{x}^{\text{lr-LDA}(\gamma)}$ and $\partial F_\mathrm{x}^{\text{lr-LDA}(\gamma)}/\partial r_\mathrm{s}$ and evaluating the first 50 terms of the series for $|c_\mathrm{x}/(\gamma r_\mathrm{s})| \leq 1/2$ did not improve the numerical stability of our lrSIC ground-state calculations.

B.19 HOMO Energy Curves for CO, H_2O, and N_2 Using LSDA-lrSIC

This section shows the HOMO energy curves for our test set consisting of CO, H_2O, and N_2 employing the LSDA-lrSIC functional. The figures in this section illustrate the curves for the γ values that correspond to those used in the total energy curves presented in Section 8.4.1. Since the HOMO energy exhibits a discontinuous jump at

$\Delta N = -1.0$, which is not relevant for assessing the piecewise linearity of the energy curve, the displayed range is limited to $\Delta N = -0.9$ to 0.0.

Figure B.10 illustrates the results for the CO molecule. The gray horizontal dashed

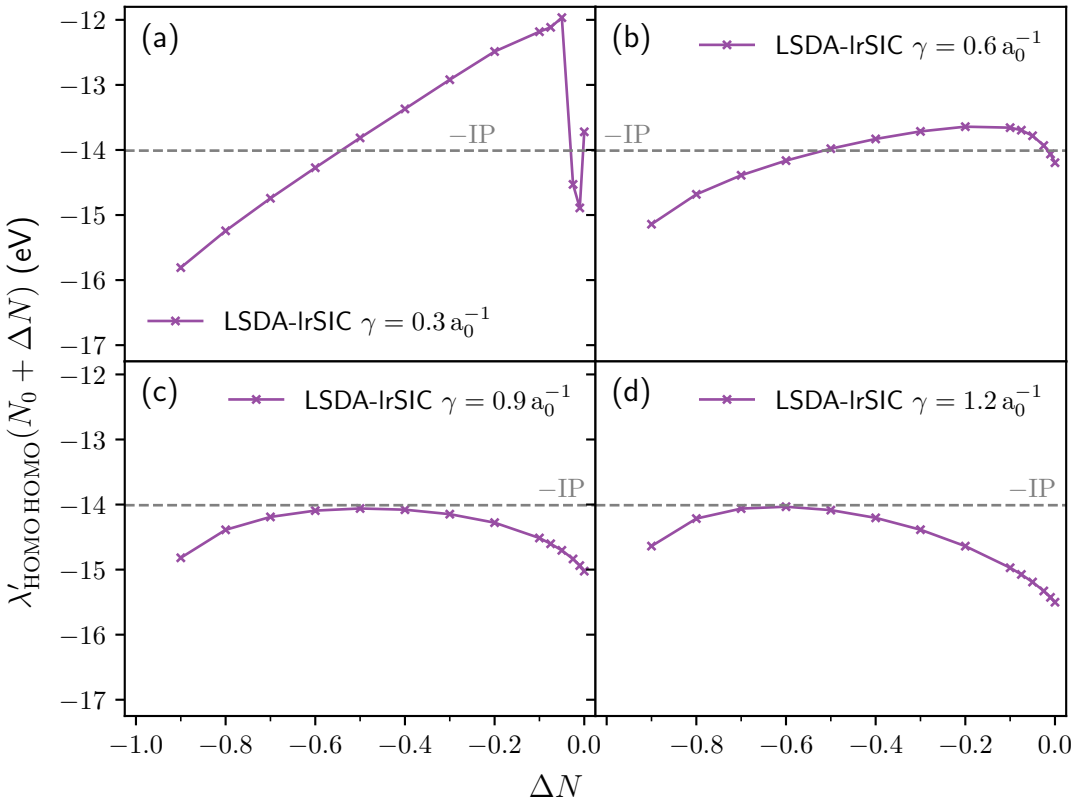

Figure B.10: HOMO energy curves for CO using sr-LSDA-lrSIC with different screening parameters: $\gamma = 0.3$ (panel (a)), 0.6 (panel (b)), 0.9 (panel (c)), and $1.2\,a_0^{-1}$ (panel (d)). The gray horizontal lines indicate the negative experimental IP.

lines indicate the negative value of the experimental IP. In order to improve the resolution of the HOMO energy variations near the neutral molecule at N_0, additional energy points are calculated beyond the interval of 0.1, specifically at $\Delta N = -0.075, -0.05, -0.025$, and -0.01. For the results of our LSDA-lrSIC calculation for the CO molecule with a screening parameter of $\gamma = 0.3\,a_0^{-1}$, shown in panel (a) of Fig. B.10, pronounced oscillations of the HOMO energy value near the neutral molecule ($\Delta N = 0$) are visible. These spurious oscillations appear due to numerical challenges in finding the energy-minimizing unitary transformation for small values of γ. This issue becomes particularly pronounced for particle numbers close to the neutral molecule, as discussed in detail in Section 8.4.3.

The HOMO energy curves for the other screening parameters shown in panels (b), (c), and (d) exhibit a change in slope. This behavior is consistent with the S-shaped energy curves presented in Section 8.4, as the HOMO energy corresponds to the derivative of the total energy with respect to the number of particles. The straight-line condition for the energy curve implies that the exact HOMO energy curve should be a horizontal line. This condition is most closely satisfied for $\gamma = 0.9\,a_0^{-1}$. The deviation of the HOMO energy from the ΔSCF value and/or the experimental IP at the neutral molecule

($\Delta N = 0$) for this γ arises due to the change in slope of the $\lambda'_{\mathrm{HOMO\,HOMO}}(N)$ curve near $\Delta N = 0$, as discussed in Section 8.7.

The results for the H_2O molecule using the LSDA-lrSIC functional are shown in Fig. B.11. Similar to the behavior observed for the CO molecule, numerical difficulties

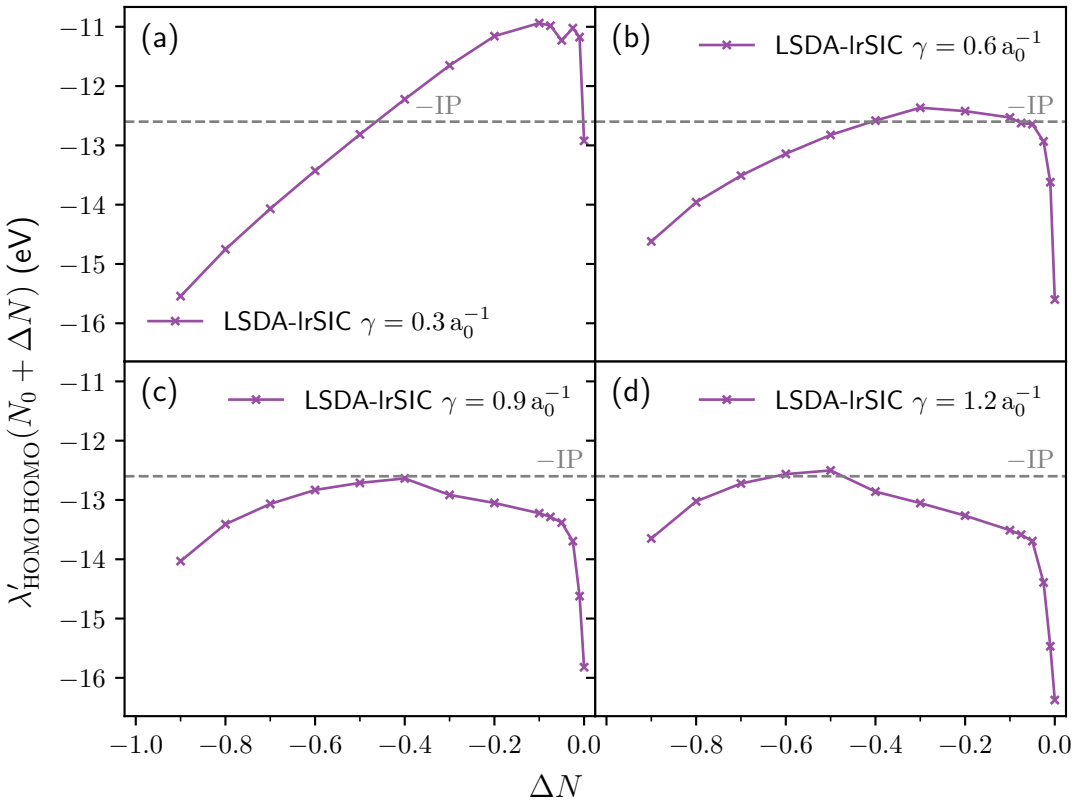

Figure B.11: HOMO energy curves for H_2O using sr-LSDA-lrSIC with different screening parameters: $\gamma = 0.3$ (panel (a)), 0.6 (panel (b)), 0.9 (panel (c)), and $1.2\,\mathrm{a}_0^{-1}$ (panel (d)). The gray horizontal lines indicate the negative experimental IP.

arise for $\gamma = 0.3\,\mathrm{a}_0^{-1}$ in panel (a), as the HOMO energy curve for H_2O exhibits small oscillations near $\Delta N = 0$. These spurious oscillations disappear for larger values of the screening parameter (see panels (b), (c), and (d)). As observed for CO, the $\lambda'_{\mathrm{HOMO\,HOMO}}(N)$ curves show a change in slope. However, for H_2O, this change in curvature – and the corresponding variation in the HOMO energy near $\Delta N = 0$ – is particularly pronounced, as the curve exhibits an abrupt drop in $\lambda'_{\mathrm{HOMO\,HOMO}}$ near the neutral molecule. While the values for $\gamma = 0.9\,\mathrm{a}_0^{-1}$ remain nearly horizontal in the range $\Delta N = -0.1$ to $\Delta N = -0.9$, closely fulfilling the straight-line condition, they show a drop near $\Delta N = 0$. As a result, $\lambda'_{\mathrm{HOMO\,HOMO}}(N_0)$ deviates strongly from the other HOMO energy values, as well as from the ΔSCF value and the negative experimental IP. Consequently, the screening parameter that best satisfies the straight-line condition and the IP theorem deviates more substantially for H_2O than for the other molecules, as discussed in Section 8.4.

Finally, Fig. B.12 illustrates our results using the LSDA-lrSIC approach for the N_2 molecule. For a screening parameter of $0.3\,\mathrm{a}_0^{-1}$, the HOMO energy curve shows a sharp drop near the neutral molecule, similar to the results for H_2O. For larger values of γ in panels (b), (c), and (d), this rapid decrease of $\lambda'_{\mathrm{HOMO\,HOMO}}$ shifts towards the positively

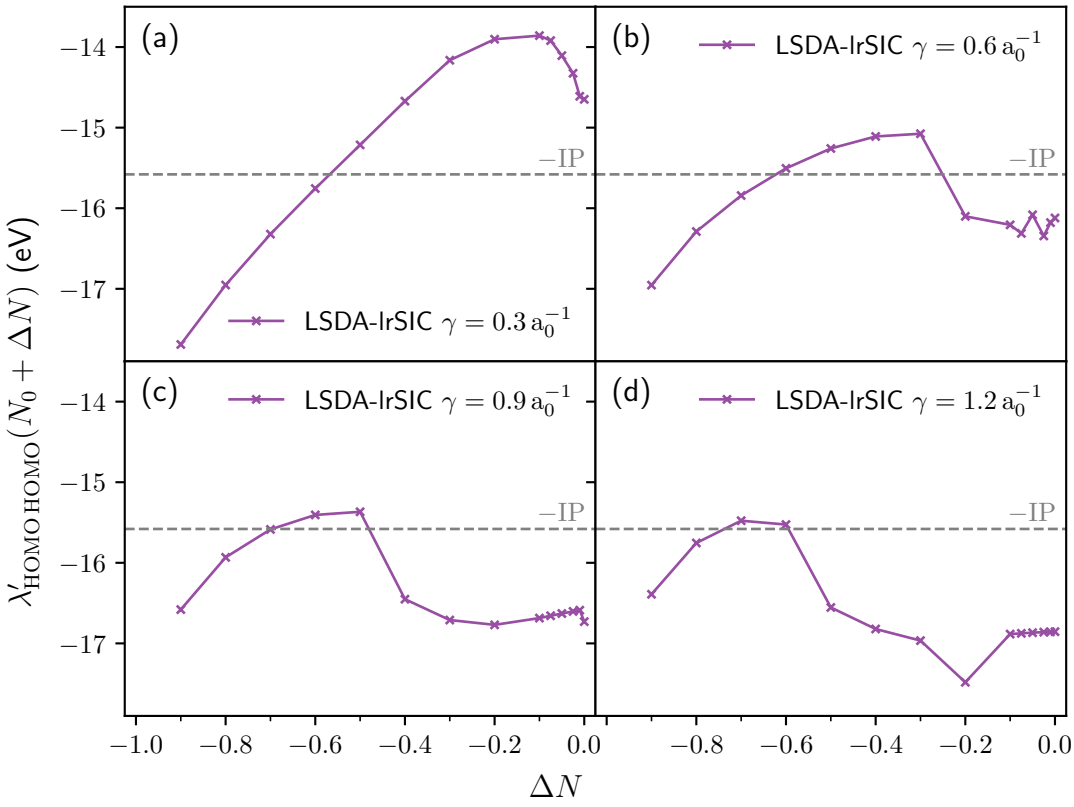

Figure B.12: HOMO energy curves for N_2 using sr-LSDA-lrSIC with different screening parameters: $\gamma = 0.3$ (panel (a)), 0.6 (panel (b)), 0.9 (panel (c)), and $1.2\,a_0^{-1}$ (panel (d)). The gray horizontal lines indicate the negative experimental IP.

charged molecule. This behavior is also evident in the total energy curves in Fig. 8.6, where the change in curvature similarly moves in the direction of the cation. The small oscillations near the neutral molecule for $\gamma = 0.6\,a_0^{-1}$, as well as the abrupt drop in HOMO energy observed for $\gamma = 1.2\,a_0^{-1}$ at $\Delta N = -0.2$, are likely due to numerical difficulties discussed in Section 8.4.3.

B.20 HOMO Energy Curves for CO, H_2O, and N_2 Using sr-LSDA-lrHcSIC

This section presents the HOMO energy curves corresponding to the sr-LSDA-lrHcSIC calculations discussed in Section 8.6. As the curves presented in this section, particularly for the H_2O molecule, exhibit a noticeable change in curvature near the neutral system, we include, in addition to the particle number steps of 0.1, HOMO energy values at $\Delta N = 0.01,\ 0.025,\ 0.05,\ 0.075$, where ΔN is the deviation in particle number from the neutral system. Since the HOMO energy exhibits a discontinuous jump at $\Delta N = -1.0$, which is not relevant for assessing the piecewise linearity of the energy curve, the displayed range is restricted to $\Delta N = -0.9$ to 0.0.

The results for the CO molecule using the sr-LSDA-lrHcSIC functional with the values of the range-separation parameter of $\gamma = 0.3,\ 0.6,\ 0.9$, and $1.2\,a_0^{-1}$ are shown in Fig. B.13. The dashed gray horizontal line indicates the negative experimental IP value. The curve for $\gamma = 0.3\,a_0^{-1}$ in panel (a) exhibits a predominantly positive slope, with

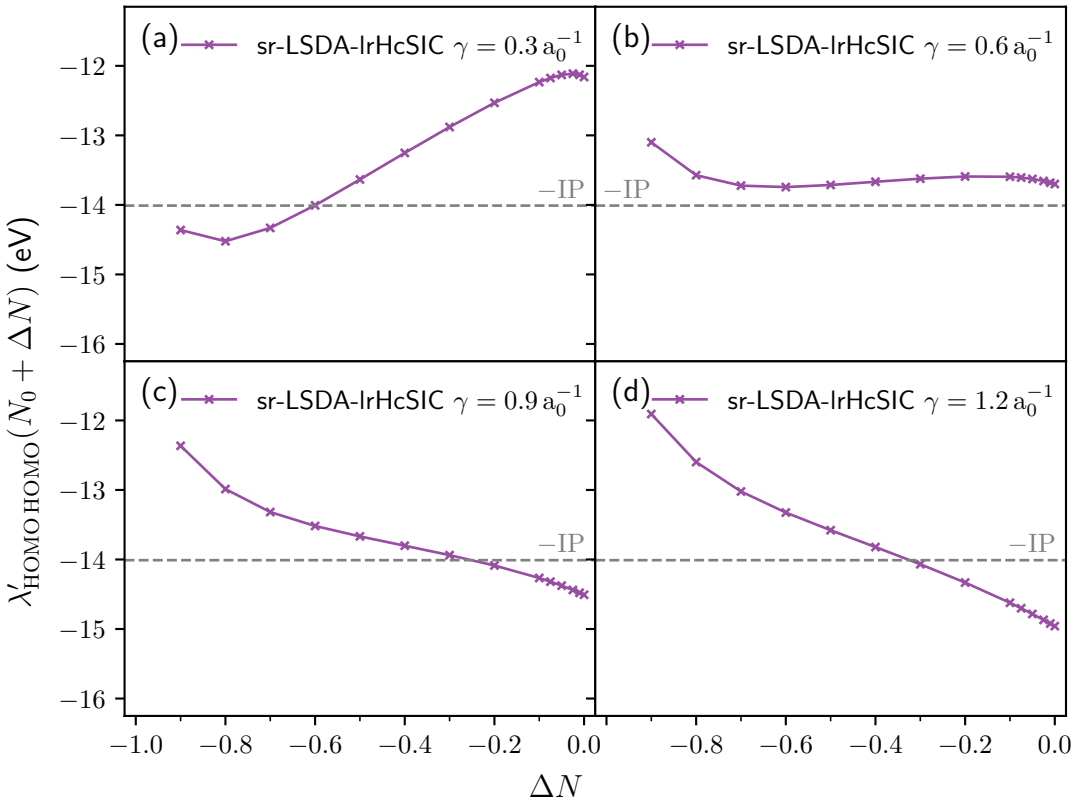

Figure B.13: HOMO energy curves for CO using LSDA-lrHcSIC with different screening parameters: $\gamma = 0.3$ (panel (a)), 0.6 (panel (b)), 0.9 (panel (c)), and $1.2\,a_0^{-1}$ (panel (d)). The gray horizontal lines indicate the negative experimental IP.

slight changes in curvature near the neutral CO molecule and its cation. Notably, the numerical difficulties observed for the LSDA-lrSIC functional near the neutral molecule, shown in panel (a) of Fig. B.10, do not occur in this calculation. The remaining curves in Fig. B.13 exhibit the expected trends: for $\gamma = 0.6\,a_0^{-1}$ in panel (b), which is close to the optimal value of $0.7\,a_0^{-1}$ for fulfilling the straight-line condition, the HOMO energy remains nearly constant across the considered range of ΔN, lying slightly above the negative value of the experimental IP. For the larger values of $\gamma = 0.9\,a_0^{-1}$ in panel (c) and $\gamma = 1.2\,a_0^{-1}$ in panel (d), the HOMO energy curves exhibit a negative slope, which corresponds to the concave shape of the total energy in Section 8.6.

The results for the H_2O molecule using the sr-LSDA-lrHcSIC functional are shown in Fig. B.14. Similarly to the results for CO, the $\lambda'_{\mathrm{HOMO\,HOMO}}(N)$ curve increases for smaller γ values in the range from $\Delta N = -0.9$ to -0.1 (see panels (a) and (b)), while for $\gamma = 1.2\,a_0^{-1}$ it exhibits a negative slope. However, all the curves shown in Fig. B.14 exhibit a pronounced drop near the neutral system. This drop in the HOMO energy, which also manifests as a change in curvature of the total energy curves discussed in Section 8.6, can lead to considerable differences between the HOMO energies of the neutral and positively charged molecule. As particularly evident in panel (c) for $\gamma = 0.9\,a_0^{-1}$, the HOMO energy remains nearly constant over the range $\Delta N = -0.9$ to -0.2, closely matching the negative of the experimental IP. For $\Delta N > -0.2$, however, it drops sharply, resulting in a substantial deviation from both the experimental IP and the ΔSCF value at $\Delta N = 0$.

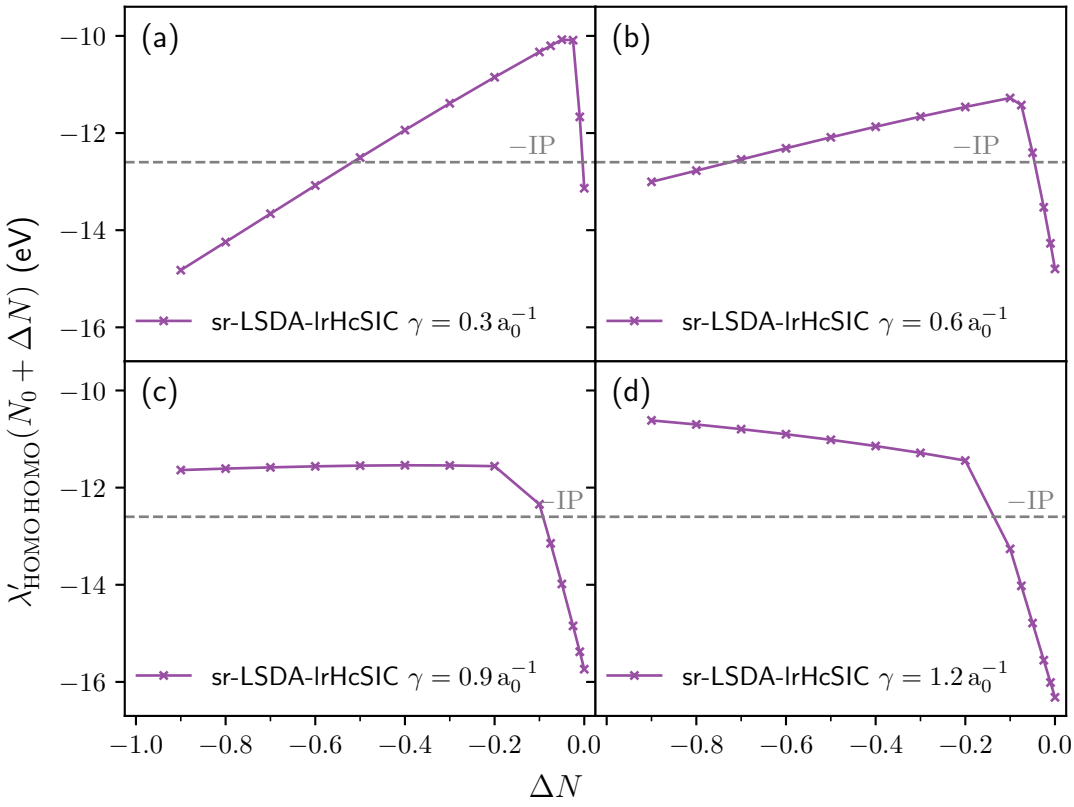

Figure B.14: HOMO energy curves for H_2O using LSDA-lrHcSIC with different screening parameters: $\gamma = 0.3$ (panel (a)), 0.6 (panel (b)), 0.9 (panel (c)), and $1.2\,a_0^{-1}$ (panel (d)). The gray horizontal lines indicate the negative experimental IP.

Finally, Fig. B.15 shows the curves for the N_2 molecule using the sr-LSDA-lrHcSIC functional. For $\gamma = 0.3\,a_0^{-1}$ in panel (a), a drop in the HOMO energy near the neutral system is observed, similar to the behavior seen for the CO molecule. Additionally, the S-shaped character of the total energy curves, discussed in Section 8.6, is also evident in Fig. B.15. For instance, for $\gamma = 0.6\,a_0^{-1}$ in panel (b), the slope of the curve changes abruptly from increasing to decreasing around $\Delta N = -0.5$, before transitioning back to an increasing trend. A similar behavior is apparent in the results shown in panels (c) and (d), corresponding to larger values of γ. However, in these cases, the change in slope occurs closer to the positively charged N_2 molecule.

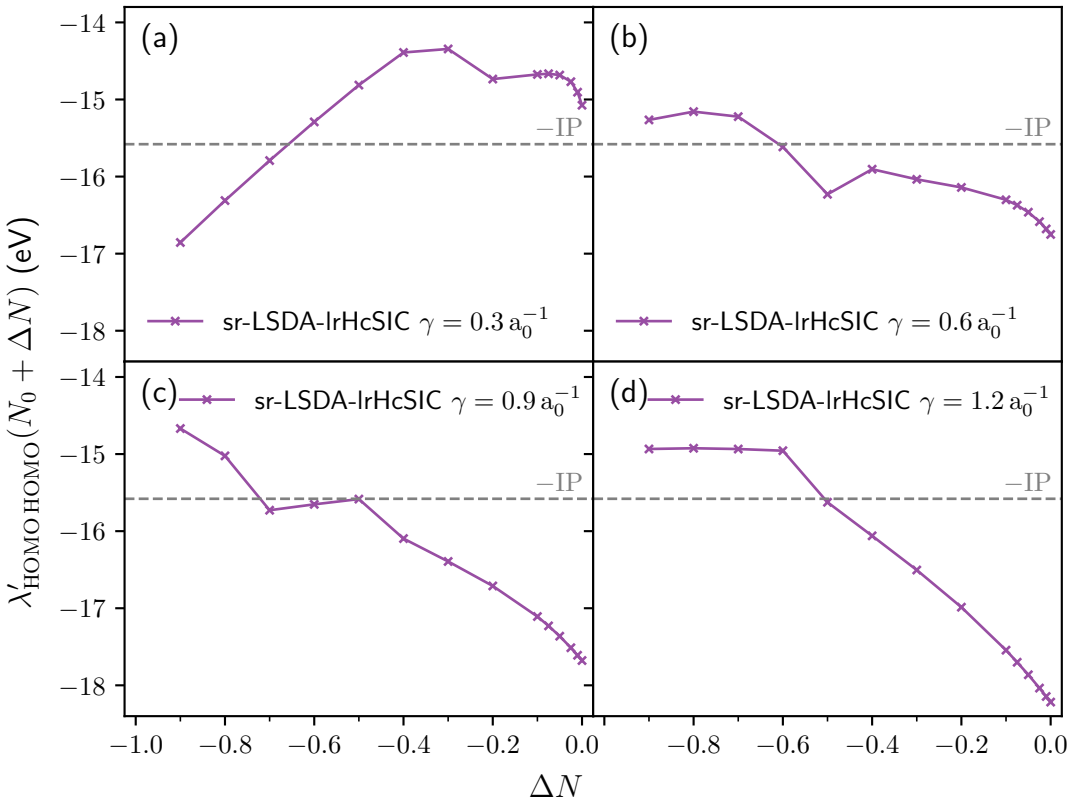

Figure B.15: HOMO energy curves for N_2 using LSDA-lrHcSIC with different screening parameters: $\gamma = 0.3$ (panel (a)), 0.6 (panel (b)), 0.9 (panel (c)), and $1.2\,\mathrm{a_0^{-1}}$ (panel (d)). The gray horizontal lines indicate the negative experimental IP.

List of Abbreviations

ADSIC	**a**verage **d**ensity **s**elf-**i**nteraction **c**orrection
CT	**c**harge **t**ransfer
DFA	**d**ensity **f**unctional **a**pproximation
DFT	**d**ensity **f**unctional **t**heory
EA	**e**lectron **a**ffinity
FLO	**F**ermi-**L**öwdin **o**rbital
FLO-SIC	**F**ermi-**L**öwdin **o**rbital **s**elf-**i**nteraction **c**orrection
FOBO	**Fo**ster-**Bo**ys
GKS	**g**eneralized **K**ohn-**S**ham
HK	**H**ohenberg-**K**ohn
HOMO	**h**ighest **o**ccupied **molecule orbital**
IP	**i**onization **p**otential
KLI	Approximation by **K**rieger, **L**i, and **I**afrate
KS	**K**ohn-**S**ham
LDA	local **d**ensity **a**pproximation
LSDA	local **s**pin-**d**ensity approximation
LSIC	local-**s**caling **s**elf-**i**nteraction **c**orrection
lrHcSIC	long-**r**ange **H**artree and **c**orrelation **s**elf-**i**nteraction **c**orrection
lrSIC	long-**r**ange **s**elf-**i**nteraction **c**orrection
NLCC	**n**on**l**inear **c**ore **c**orrection
OEP	**o**ptimized **e**ffective **p**otential
PP	**p**seudo**p**otential
PZ-SIC	**P**erdew-**Z**unger **s**elf-**i**nteraction **c**orrection
SIC	**s**elf-**i**nteraction **c**orrection
SIE	**s**elf-**i**nteraction **e**rror
TDDFT	**t**ime-**d**ependent **d**ensity **f**unctional **t**heory
TDGKS	**t**ime-**d**ependent **g**eneralized **K**ohn-**S**ham
TDKS	**t**ime-**d**ependent **K**ohn-**S**ham
TDLDA	**t**ime-**d**ependent **l**ocal **d**ensity **a**pproximation
xc	e**x**change-**c**orrelation

Bibliography

[AAK17] T. Aschebrock, R. Armiento, and S. Kümmel, "Orbital nodal surfaces: topological challenges for density functionals", Physical Review B **95**, 245118 (2017).

[AB85] C.-O. Almbladh and U. von Barth, "Exact results for the charge and spin densities, exchange-correlation potentials, and density-functional eigenvalues", Physical Review B **31**, 3231–3244 (1985).

[AEK09] T. Abrudan, J. Eriksson, and V. Koivunen, "Conjugate gradient algorithm for optimization under unitary matrix constraint", Signal Processing **89**, 1704–1714 (2009).

[AK13] R. Armiento and S. Kümmel, "Orbital localization, charge transfer, and band gaps in semilocal density-functional theory", Phys. Rev. Lett. **111**, 036402 (2013).

[AK19] T. Aschebrock and S. Kümmel, "Ultranonlocality and accurate band gaps from a meta-generalized gradient approximation", Physical Review Research **1**, 033082 (2019).

[AS14] J. Autschbach and M. Srebro, "Delocalization error and "functional tuning" in kohn–sham calculations of molecular properties", Accounts of Chemical Research **47**, 2592–2602 (2014).

[Asc+23] T. Aschebrock, T. Lebeda, M. Brütting, R. Richter, I. Schelter, and S. Kümmel, "Exact exchange-like electric response from a meta-generalized gradient approximation: a semilocal realization of ultranonlocality", The Journal of Chemical Physics **159**, 234107 (2023).

[Asc19] T. Aschebrock, "Ultranonlocality in density functional theory", PhD thesis (University of Bayreuth, Bayreuth, 2019).

[Bal+20] S. G. Balasubramani, G. P. Chen, S. Coriani, et al., "Turbomole: modular program suite for ab initio quantum-chemical and condensed-matter simulations", The Journal of Chemical Physics **152**, 184107 (2020).

[Bec02] A. D. Becke, "Current density in exchange-correlation functionals: application to atomic states", The Journal of Chemical Physics **117**, 6935–6938 (2002).

[Bec86] A. D. Becke, "Density functional calculations of molecular bond energies", The Journal of Chemical Physics **84**, 4524–4529 (1986).

[BF12] J. E. Bates and F. Furche, "Harnessing the meta-generalized gradient approximation for time-dependent density functional theory", The Journal of Chemical Physics **137**, 164105 (2012).

[BH72] U. v. Barth and L. Hedin, "A local exchange-correlation potential for the spin polarized case.", Journal of Physics C: Solid State Physics **5**, 1629–1642 (1972).

[Bha+20] P. Bhattarai, K. Wagle, C. Shahi, Y. Yamamoto, S. Romero, B. Santra, R. R. Zope, J. E. Peralta, K. A. Jackson, and J. P. Perdew, "A step in the direction of resolving the paradox of perdew–zunger self-interaction correction. ii. gauge consistency of the energy density at three levels of approximation", The Journal of Chemical Physics **152**, 214109 (2020).

[Bha+21] P. Bhattarai, B. Santra, K. Wagle, Y. Yamamoto, R. R. Zope, A. Ruzsinszky, K. A. Jackson, and J. P. Perdew, "Exploring and enhancing the accuracy of interior-scaled perdew–zunger self-interaction correction", The Journal of Chemical Physics **154**, 094105 (2021).

[BK18] R. Baer and L. Kronik, "Time-dependent generalized kohn–sham theory", The European Physical Journal B **91**, 170 (2018).

[BLL16] A. Bruner, D. LaMaster, and K. Lopata, "Accelerated broadband spectra using transition dipole decomposition and padé approximants", Journal of Chemical Theory and Computation **12**, 3741–3750 (2016).

[BO27] M. Born and R. Oppenheimer, "Zur quantentheorie der molekeln", Annalen der Physik **389**, 457–484 (1927).

[Bor+15] G. Borghi, C.-H. Park, N. L. Nguyen, A. Ferretti, and N. Marzari, "Variational minimization of orbital-density-dependent functionals", Physical Review B **91**, 155112 (2015).

[Bor+20] P. Borlido, J. Schmidt, A. W. Huran, F. Tran, M. A. L. Marques, and S. Botti, "Exchange-correlation functionals for band gaps of solids: benchmark, reparametrization and machine learning", npj Computational Materials **6**, 96 (2020).

[Boy60] S. F. Boys, "Construction of some molecular orbitals to be approximately invariant for changes from one molecule to another", Reviews of Modern Physics **32**, 296–299 (1960).

[Bra+16] J. G. Brandenburg, J. E. Bates, J. Sun, and J. P. Perdew, "Benchmark tests of a strongly constrained semilocal functional with a long-range dispersion correction", Physical Review B **94**, 115144 (2016).

[Bry+23] K. R. Bryenton, A. A. Adeleke, S. G. Dale, and E. R. Johnson, "Delocalization error: the greatest outstanding challenge in density-functional theory", WIREs Computational Molecular Science **13**, e1631 (2023).

[BS97] T. Bally and G. N. Sastry, "Incorrect dissociation behavior of radical ions in density functional calculations", The Journal of Physical Chemistry A **101**, 7923–7925 (1997).

[Bur+03] W. Burdick, Y. Saad, L. Kronik, I. Vasiliev, M. Jain, and J. R. Chelikowsky, "Parallel implementation of time-dependent density functional theory", Computer Physics Communications **156**, 22–42 (2003).

[CA80] D. M. Ceperley and B. J. Alder, "Ground state of the electron gas by a stochastic method", Physical Review Letters **45**, 566–569 (1980).

[Cal+00] F. Calvayrac, P.-G. Reinhard, E. Suraud, and C. Ullrich, "Nonlinear electron dynamics in metal clusters", Physics Reports **337**, 493–578 (2000).

[Cap06] K. Capelle, "A bird's-eye view of density-functional theory", Brazilian Journal of Physics **36**, 1318–1343 (2006).

[Car+15] J. Carmona-Espíndola, J. L. Gázquez, A. Vela, and S. B. Trickey, "Generalized gradient approximation exchange energy functional with correct asymptotic behavior of the corresponding potential", The Journal of Chemical Physics **142**, 054105 (2015).

[Cas+98] M. E. Casida, C. Jamorski, K. C. Casida, and D. R. Salahub, "Molecular excitation energies to high-lying bound states from time-dependent density-functional response theory: characterization and correction of the time-dependent local density approximation ionization threshold", The Journal of chemical physics **108**, 4439–4449 (1998).

[Cas95] M. E. Casida, "Time-dependent density functional response theory for molecules", in *Recent advances in density functional methods* (World Scientific, 1995), pp. 155–192.

[Che+03] J. R. Chelikowsky, L. Kronik, I. Vasiliev, M. Jain, and Y. Saad, "Using real space pseudopotentials for the electronic structure problem", in *Special volume, computational chemistry*, **10**, Handbook of Numerical Analysis (Elsevier, 2003), pp. 613–637.

[CJ98] G. I. Csonka and B. G. Johnson, "Inclusion of exact exchange for self-interaction corrected h 3 density functional potential energy surface", Theoretical Chemistry Accounts: Theory, Computation, and Modeling (Theoretica Chimica Acta) **99**, 158–165 (1998).

[CK57] B. C. Carlson and J. M. Keller, "Orthogonalization procedures and the localization of wannier functions", Physical Review **105**, 102–103 (1957).

[CMR04] A. Castro, M. A. L. Marques, and A. Rubio, "Propagators for the time-dependent kohn–sham equations", The Journal of Chemical Physics **121**, 3425–3433 (2004).

[CN47] J. Crank and P. Nicolson, "A practical method for numerical evaluation of solutions of partial differential equations of the heat-conduction type", Mathematical Proceedings of the Cambridge Philosophical Society **43**, 50–67 (1947).

[Coc+14] C. Cocchi, D. Prezzi, A. Ruini, E. Molinari, and C. A. Rozzi, "Ab initiosimulation of optical limiting: the case of metal-free phthalocyanine", Physical Review Letters **112**, 198303 (2014).

[Cor+19] V. Coropceanu, X.-K. Chen, T. Wang, Z. Zheng, and J.-L. Brédas, "Charge-transfer electronic states in organic solar cells", Nature Reviews Materials **4**, 689–707 (2019).

[CP82] L. A. Cole and J. P. Perdew, "Calculated electron affinities of the elements", Physical Review A **25**, 1265–1271 (1982).

[DG90] R. M. Dreizler and E. K. U. Gross, *Density functional theory, An approach to the quantum many-body problem* (Springer, Berlin, 1990), 302 pp.

[DH04] A. Dreuw and M. Head-Gordon, "Failure of time-dependent density functional theory for long-range charge-transfer excited states: the zincbacteriochlorin-bacteriochlorin and bacteriochlorophyll-spheroidene complexes", Journal of the American Chemical Society **126**, 4007–4016 (2004).

[Dun+17] D. Dundas, P. Mulholland, A. Wardlow, and A. de la Calle, "Probing the role of excited states in ionization of acetylene", Physical Chemistry Chemical Physics **19**, 19619–19630 (2017).

[Dun89] T. H. Dunning, "Gaussian basis sets for use in correlated molecular calculations. i. the atoms boron through neon and hydrogen", The Journal of Chemical Physics **90**, 1007–1023 (1989).

[DWH03] A. Dreuw, J. L. Weisman, and M. Head-Gordon, "Long-range charge-transfer excited states in time-dependent density functional theory require non-local exchange", The Journal of Chemical Physics **119**, 2943–2946 (2003).

[Eng09] E. Engel, "Relevance of core-valence interaction for electronic structure calculations with exact exchange", Physical Review B **80**, 161205 (2009).

[Faa+02] M. van Faassen, P. L. de Boeij, R. van Leeuwen, J. A. Berger, and J. G. Snijders, "Ultranonlocality in time-dependent current-density-functional theory: application to conjugated polymers", Physical Review Letters **88**, 186401 (2002).

[FB60] J. M. Foster and S. F. Boys, "Canonical configurational interaction procedure", Reviews of Modern Physics **32**, 300–302 (1960).

[FNM03] C. Fiolhais, F. Nogueira, and M. A. L. Marques, eds., *A primer in density functional theory*, Lecture notes in physics (Springer, New York, NY, 2003).

[Foc30] V. Fock, "Näherungsmethode zur lösung des quantenmechanischen mehrkörperproblems", Zeitschrift für Physik **61**, 126–148 (1930).

[Fuk16] J. I. Fuks, "Time-dependent density functional theory for charge-transfer dynamics: review of the causes of failure and success", The European Physical Journal B **89**, 236 (2016).

[Fur+20a] J. W. Furness, A. D. Kaplan, J. Ning, J. P. Perdew, and J. Sun, "Accurate and numerically efficient r^2scan meta-generalized gradient approximation", The Journal of Physical Chemistry Letters **11**, 8208–8215 (2020).

[Fur+20b] J. W. Furness, A. D. Kaplan, J. Ning, J. P. Perdew, and J. Sun, "Correction to "accurate and numerically efficient r^2scan meta-generalized gradient approximation"", The Journal of Physical Chemistry Letters **11**, 9248–9248 (2020).

[GB18] P. Gori-Giorgi and E. J. Baerends, "Asymptotic nodal planes in the electron density and the potential in the effective equation for the square root of the density", The European Physical Journal B **91**, 160 (2018).

[GGB02] M. Grüning, O. V. Gritsenko, and E. J. Baerends, "Exchange potential from the common energy denominator approximation for the kohn–sham green's function: application to (hyper)polarizabilities of molecular chains", The Journal of Chemical Physics **116**, 6435–6442 (2002).

[GGB16] P. Gori-Giorgi, T. Gál, and E. J. Baerends, "Asymptotic behaviour of the electron density and the kohn–sham potential in case of a kohn–sham homo nodal plane", Molecular Physics **114**, 1086–1097 (2016).

[Gis+99] S. J. A. van Gisbergen, P. R. T. Schipper, O. V. Gritsenko, E. J. Baerends, J. G. Snijders, B. Champagne, and B. Kirtman, "Electric field dependence of the exchange-correlation potential in molecular chains", Physical Review Letters **83**, 694–697 (1999).

[GKC04a] J. Gräfenstein, E. Kraka, and D. Cremer, "Effect of the self-interaction error for three-electron bonds: on the development of new exchange-correlation functionals", Phys. Chem. Chem. Phys. **6**, 1096–1112 (2004).

[GKC04b] J. Gräfenstein, E. Kraka, and D. Cremer, "The impact of the self-interaction error on the density functional theory description of dissociating radical cations: ionic and covalent dissociation limits", The Journal of Chemical Physics **120**, 524–539 (2004).

[GL76] O. Gunnarsson and B. I. Lundqvist, "Exchange and correlation in atoms, molecules, and solids by the spin-density-functional formalism", Physical Review B **13**, 4274–4298 (1976).

[GSS86] R. W. Godby, M. Schlüter, and L. J. Sham, "Accurate exchange-correlation potential for silicon and its discontinuity on addition of an electron", Physical Review Letters **56**, 2415–2418 (1986).

[GU97] S. Goedecker and C. J. Umrigar, "Critical assessment of the self-interaction-corrected–local-density-functional method and its algorithmic implementation", Physical Review A **55**, 1765–1771 (1997).

[Har28] D. R. Hartree, "The wave mechanics of an atom with a non-coulomb central field. part ii. some results and discussion", Mathematical Proceedings of the Cambridge Philosophical Society **24**, 111–132 (1928).

[HHL83] J. G. Harrison, R. A. Heaton, and C. C. Lin, "Self-interaction correction to the local density hartree-fock atomic calculations of excited and ground states", Journal of Physics B: Atomic and Molecular Physics **16**, 2079–2091 (1983).

[Hil12] J. G. Hill, "Gaussian basis sets for molecular applications", International Journal of Quantum Chemistry **113**, 21–34 (2012).

[HK12] D. Hofmann and S. Kümmel, "Self-interaction correction in a real-time kohn-sham scheme: access to difficult excitations in time-dependent density functional theory", The Journal of Chemical Physics **137**, 064117 (2012).

[HK20] F. Hofmann and S. Kümmel, "Molecular excitations from meta-generalized gradient approximations in the kohn–sham scheme", The Journal of Chemical Physics **153**, 114106 (2020).

[HK64] P. Hohenberg and W. Kohn, "Inhomogeneous electron gas", Physical Review **136**, B864–B871 (1964).

[HKK12] D. Hofmann, T. Körzdörfer, and S. Kümmel, "Kohn-sham self-interaction correction in real time", Physical Review Letters **108**, 146401 (2012).

[Hof+12] D. Hofmann, S. Klüpfel, P. Klüpfel, and S. Kümmel, "Using complex degrees of freedom in the kohn-sham self-interaction correction", Physical Review A **85**, 062514 (2012).

[HSC79] D. R. Hamann, M. Schlüter, and C. Chiang, "Norm-conserving pseudopotentials", Physical Review Letters **43**, 1494–1497 (1979).

[HSE03] J. Heyd, G. E. Scuseria, and M. Ernzerhof, "Hybrid functionals based on a screened coulomb potential", The Journal of Chemical Physics **118**, 8207–8215 (2003).

[HSK18] F. Hofmann, I. Schelter, and S. Kümmel, "Linear response time-dependent density functional theory without unoccupied states: the kohn-sham-sternheimer scheme revisited", The Journal of Chemical Physics **149**, 024105 (2018).

[Hub79] K. Huber, *Molecular spectra and molecular structure, Iv. constants of diatomic molecules* (Springer, New York, NY, 1979), 1729 pp.

[Jan78] J. F. Janak, "Proof that $\partial E/\partial n_i = \epsilon_i$ in density-functional theory", Physical Review B **18**, 7165–7168 (1978).

[JC33] H. M. James and A. S. Coolidge, "The ground state of the hydrogen molecule", The Journal of Chemical Physics **1**, 825–835 (1933).

[Jen12] F. Jensen, "Atomic orbital basis sets", WIREs Computational Molecular Science **3**, 273–295 (2012).

[Joh22] R. Johnson, *Nist computational chemistry comparison and benchmark database*, 2022.

[Jón11] H. Jónsson, "Simulation of surface processes", Proceedings of the National Academy of Sciences **108**, 944–949 (2011).

[Kar+11] A. Karolewski, T. Stein, R. Baer, and S. Kümmel, "Communication: tailoring the optical gap in light-harvesting molecules", The Journal of Chemical Physics **134**, 151101 (2011).

[KB82] L. Kleinman and D. M. Bylander, "Efficacious form for model pseudopotentials", Physical Review Letters **48**, 1425–1428 (1982).

[KBM23] P. Kovács, P. Blaha, and G. K. H. Madsen, "Origin of the success of mggas for bandgaps", The Journal of Chemical Physics **159**, 244118 (2023).

[Keh+20] J. Kehrer, R. Richter, J. M. Foerster, I. Schelter, and S. Kümmel, "Self-interaction correction, electrostatic, and structural influences on time-dependent density functional theory excitations of bacteriochlorophylls from the light-harvesting complex 2", The Journal of Chemical Physics **153**, 144114 (2020).

[KK08] S. Kümmel and L. Kronik, "Orbital-dependent density functionals: theory and applications", Reviews of Modern Physics **80**, 3–60 (2008).

[KK18] A. Kaiser and S. Kümmel, "Revealing the field-counteracting term in the exact kohn-sham correlation potential", Physical Review A **98**, 052505 (2018).

[KK20] L. Kronik and S. Kümmel, "Piecewise linearity, freedom from self-interaction, and a coulomb asymptotic potential: three related yet inequivalent properties of the exact density functional", Physical Chemistry Chemical Physics **22**, 16467–16481 (2020).

[KKJ11] S. Klüpfel, P. Klüpfel, and H. Jónsson, "Importance of complex orbitals in calculating the self-interaction-corrected ground state of atoms", Physical Review A **84**, 050501 (2011).

[KKJ12] S. Klüpfel, P. Klüpfel, and H. Jónsson, "The effect of the perdew-zunger self-interaction correction to density functionals on the energetics of small molecules", The Journal of Chemical Physics **137**, 124102 (2012).

[KKP04] S. Kümmel, L. Kronik, and J. P. Perdew, "Electrical response of molecular chains from density functional theory", Physical Review Letters **93**, 213002 (2004).

[KLI92a] J. B. Krieger, Y. Li, and G. J. Iafrate, "Construction and application of an accurate local spin-polarized kohn-sham potential with integer discontinuity: exchange-only theory", Physical Review A **45**, 101–126 (1992).

[KLI92b] J. B. Krieger, Y. Li, and G. J. Iafrate, "Systematic approximations to the optimized effective potential: application to orbital-density-functional theory", Physical Review A **46**, 5453–5458 (1992).

[Klü+13] P. Klüpfel, P. M. Dinh, P.-G. Reinhard, and E. Suraud, "Koopmans' condition in self-interaction-corrected density-functional theory", Physical Review A **88**, 052501 (2013).

[Koh99] W. Kohn, "Nobel lecture: electronic structure of matter—wave functions and density functionals", Reviews of Modern Physics **71**, 1253–1266 (1999).

[KPB99] S. Kurth, J. P. Perdew, and P. Blaha, "Molecular and solid-state tests of density functional approximations: lsd, ggas, and meta-ggas", International Journal of Quantum Chemistry **75**, 889–909 (1999).

[Kro+06] L. Kronik, A. Makmal, M. L. Tiago, M. M. G. Alemany, M. Jain, X. Huang, Y. Saad, and J. R. Chelikowsky, "Parsec – the pseudopotential algorithm for real-space electronic structure calculations: recent advances and novel applications to nano-structures", physica status solidi (b) **243**, 1063–1079 (2006).

[Kro+12] L. Kronik, T. Stein, S. Refaely-Abramson, and R. Baer, "Excitation gaps of finite-sized systems from optimally tuned range-separated hybrid functionals", Journal of Chemical Theory and Computation **8**, 1515–1531 (2012).

[Kru+20] J. Krumland, A. M. Valencia, S. Pittalis, C. A. Rozzi, and C. Cocchi, "Understanding real-time time-dependent density-functional theory simulations of ultrafast laser-induced dynamics in organic molecules", The Journal of Chemical Physics **153**, 054106 (2020).

[KS65] W. Kohn and L. J. Sham, "Self-consistent equations including exchange and correlation effects", Physical Review **140**, A1133–A1138 (1965).

[Küm04] S. Kümmel, "Damped gradient iteration and multigrid relaxation: tools for electronic structure calculations using orbital density-functionals", Journal of Computational Physics **201**, 333–343 (2004).

[Küm17] S. Kümmel, "Charge-transfer excitations: a challenge for time-dependent density functional theory that has been met", Advanced Energy Materials **7**, 1700440 (2017).

[Kur+11] N. Kuritz, T. Stein, R. Baer, and L. Kronik, "Charge-transfer-like $\pi \to \pi^*$ excitations in time-dependent density functional theory: a conundrum and its solution", Journal of Chemical Theory and Computation **7**, 2408–2415 (2011).

[LAK22] T. Lebeda, T. Aschebrock, and S. Kümmel, "First steps towards achieving both ultranonlocality and a reliable description of electronic binding in a meta-generalized gradient approximation", Physical Review Research **4**, 023061 (2022).

[LAK24] T. Lebeda, T. Aschebrock, and S. Kümmel, "Balancing the contributions to the gradient expansion: accurate binding and band gaps with a nonempirical meta-gga", Phys. Rev. Lett. **133**, 136402 (2024).

[LB07] E. Livshits and R. Baer, "A well-tempered density functional theory of electrons in molecules", Physical Chemistry Chemical Physics **9**, 2932 (2007).

[LB94] R. van Leeuwen and E. J. Baerends, "Exchange-correlation potential with correct asymptotic behavior", Physical Review A **49**, 2421–2431 (1994).

[Leb+23] T. Lebeda, T. Aschebrock, J. Sun, L. Leppert, and S. Kümmel, "Right band gaps for the right reason at low computational cost with a meta-gga", Physical Review Materials **7**, 093803 (2023).

[Lee01] R. van Leeuwen, "Key concepts in time-dependent density-functional theory", International Journal of Modern Physics B **15**, 1969–2023 (2001).

[Lee98] R. van Leeuwen, "Causality and symmetry in time-dependent density-functional theory", Physical Review Letters **80**, 1280–1283 (1998).

[Lei+97] T. Leininger, H. Stoll, H.-J. Werner, and A. Savin, "Combining long-range configuration interaction with short-range density functionals", Chemical Physics Letters **275**, 151–160 (1997).

[Lev79] M. Levy, "Universal variational functionals of electron densities, first-order density matrices, and natural spin-orbitals and solution of the v -representability problem", Proceedings of the National Academy of Sciences **76**, 6062–6065 (1979).

[Lev82] M. Levy, "Electron densities in search of hamiltonians", Physical Review A **26**, 1200–1208 (1982).

[LFC82] S. G. Louie, S. Froyen, and M. L. Cohen, "Nonlinear ionic pseudopotentials in spin-density-functional calculations", Physical Review B **26**, 1738–1742 (1982).

[LG11] K. Lopata and N. Govind, "Modeling fast electron dynamics with real-time time-dependent density functional theory: application to small molecules and chromophores", Journal of Chemical Theory and Computation **7**, 1344–1355 (2011).

[LHJ16] S. Lehtola, M. Head-Gordon, and H. Jónsson, "Complex orbitals, multiple local minima, and symmetry breaking in perdew–zunger self-interaction corrected density functional theory calculations", Journal of Chemical Theory and Computation **12**, 3195–3207 (2016).

[Loo+18] P.-F. Loos, A. Scemama, A. Blondel, Y. Garniron, M. Caffarel, and D. Jacquemin, "A mountaineering strategy to excited states: highly accurate reference energies and benchmarks", Journal of Chemical Theory and Computation **14**, 4360–4379 (2018).

[Löw50] P.-O. Löwdin, "On the non-orthogonality problem connected with the use of atomic wave functions in the theory of molecules and crystals", The Journal of Chemical Physics **18**, 365–375 (1950).

[LP75] D. Langreth and J. Perdew, "The exchange-correlation energy of a metallic surface", Solid State Communications **17**, 1425–1429 (1975).

[LPS84] M. Levy, J. P. Perdew, and V. Sahni, "Exact differential equation for the density and ionization energy of a many-particle system", Physical Review A **30**, 2745–2748 (1984).

[LSR02] C. Legrand, E. Suraud, and P.-G. Reinhard, "Comparison of self-interaction-corrections for metal clusters", Journal of Physics B: Atomic, Molecular and Optical Physics **35**, 1115–1128 (2002).

[LZ20] H. Li and W. Zhang, "Perovskite tandem solar cells: from fundamentals to commercial deployment", Chemical Reviews **120**, 9835–9950 (2020).

[Mai05] N. T. Maitra, "Undoing static correlation: long-range charge transfer in time-dependent density-functional theory", The Journal of Chemical Physics **122**, 234104 (2005).

[Mai17] N. T. Maitra, "Charge transfer in time-dependent density functional theory", Journal of Physics: Condensed Matter **29**, 423001 (2017).

[Mar03] M. Marques, "Octopus: a first-principles tool for excited electron–ion dynamics", Computer Physics Communications **151**, 60–78 (2003).

[May02] I. Mayer, "On löwdin's method of symmetric orthogonalization", International Journal of Quantum Chemistry **90**, 63–65 (2002).

[MB68] S.-k. Ma and K. A. Brueckner, "Correlation energy of an electron gas with a slowly varying high density", Physical Review **165**, 18–31 (1968).

[MBW02] N. T. Maitra, K. Burke, and C. Woodward, "Memory in time-dependent density functional theory", Physical Review Letters **89**, 023002 (2002).

[MCY06] P. Mori-Sánchez, A. J. Cohen, and W. Yang, "Many-electron self-interaction error in approximate density functionals", The Journal of Chemical Physics **125**, 201102 (2006).

[Mes+09] J. Messud, P. Dinh, P.-G. Reinhard, and E. Suraud, "On the exact treatment of time-dependent self-interaction correction", Annals of Physics **324**, 955–976 (2009).

[Mes+11] J. Messud, P. Dinh, P.-G. Reinhard, and E. Suraud, "The generalized sic-oep formalism and the generalized sic-slater approximation (stationary and time-dependent cases)", Annalen der Physik **523**, 270–290 (2011).

[MK06] M. Mundt and S. Kümmel, "Optimized effective potential in real time: problems and prospects in time-dependent density-functional theory", Physical Review A **74**, 022511 (2006).

[MK07] M. Mundt and S. Kümmel, "Photoelectron spectra of anionic sodium clusters from time-dependent density-functional theory in real time", Physical Review B **76**, 035413 (2007).

[MK22] D. Mester and M. Kállay, "Charge-transfer excitations within density functional theory: how accurate are the most recommended approaches?", Journal of Chemical Theory and Computation **18**, 1646–1662 (2022).

[MKK09] A. Makmal, S. Kümmel, and L. Kronik, "Fully numerical all-electron solutions of the optimized effective potential equation for diatomic molecules", Journal of Chemical Theory and Computation **5**, 1731–1740 (2009).

[MKK11] A. Makmal, S. Kümmel, and L. Kronik, "Fully numerical all-electron solutions of the optimized effective potential equation for diatomic molecules", Journal of Chemical Theory and Computation **7**, 2665–2665 (2011).

[MR80] R. A. Madden and V. Ramanathan, "Detecting climate change due to increasing carbon dioxide", Science **209**, 763–768 (1980).

[Mun+07] M. Mundt, S. Kümmel, R. van Leeuwen, and P.-G. Reinhard, "Violation of the zero-force theorem in the time-dependent krieger-li-iafrate approximation", Physical Review A **75**, 050501 (2007).

[NJO80] E. S. Nielsen, P. Jo/rgensen, and J. Oddershede, "Transition moments and dynamic polarizabilities in a second order polarization propagator approach", The Journal of Chemical Physics **73**, 6238–6246 (1980).

[OP79] G. L. Oliver and J. P. Perdew, "Spin-density gradient expansion for the kinetic energy", Physical Review A **20**, 397–403 (1979).

[Par20] W. Y. Parr Robert G., *Density-functional theory of atoms and molecules*, Oxford scholarship online (Oxford University Press, New York, 2020), 1342 pp.

[PB15] M. R. Pederson and T. Baruah, "Chapter eight - self-interaction corrections within the fermi-orbital-based formalism", in *Advances in atomic, molecular, and optical physics*, **64**, edited by E. Arimondo, C. C. Lin, and S. F. Yelin, Advances In Atomic, Molecular, and Optical Physics (Academic Press, 2015), pp. 153–180.

[PBE96] J. P. Perdew, K. Burke, and M. Ernzerhof, "Generalized gradient approximation made simple", Physical Review Letters **77**, 3865–3868 (1996).

[Ped15] M. R. Pederson, "Fermi orbital derivatives in self-interaction corrected density functional theory: applications to closed shell atoms", The Journal of Chemical Physics **142**, 064112 (2015).

[Per+15] J. P. Perdew, A. Ruzsinszky, J. Sun, and M. R. Pederson, "Chapter one - paradox of self-interaction correction: how can anything so right be so wrong?", in *Advances in atomic, molecular, and optical physics*, **64**, edited by E. Arimondo, C. C. Lin, and S. F. Yelin, Advances In Atomic, Molecular, and Optical Physics (Academic Press, 2015), pp. 1–14.

[Per+82] J. P. Perdew, R. G. Parr, M. Levy, and J. L. Balduz, "Density-functional theory for fractional particle number: derivative discontinuities of the energy", Physical Review Letters **49**, 1691–1694 (1982).

[Per+92] J. P. Perdew, J. A. Chevary, S. H. Vosko, K. A. Jackson, M. R. Pederson, D. J. Singh, and C. Fiolhais, "Atoms, molecules, solids, and surfaces: applications of the generalized gradient approximation for exchange and correlation", Physical Review B **46**, 6671–6687 (1992).

[Per+99] J. P. Perdew, S. Kurth, A. Zupan, and P. Blaha, "Accurate density functional with correct formal properties: a step beyond the generalized gradient approximation", Physical Review Letters **82**, 2544–2547 (1999).

[Per90] J. P. Perdew, "Size-consistency, self-interaction correction, and derivative discontinuity in density functional theory", in *Density functional theory of many-fermion systems*, **21**, edited by P.-O. Löwdin, Advances in Quantum Chemistry (Academic Press, 1990), pp. 113–134.

[PHL84] M. R. Pederson, R. A. Heaton, and C. C. Lin, "Local-density hartree–fock theory of electronic states of molecules with self-interaction correction", The Journal of Chemical Physics **80**, 1972–1975 (1984).

[PHL85] M. R. Pederson, R. A. Heaton, and C. C. Lin, "Density-functional theory with self-interaction correction: application to the lithium moleculea", The Journal of Chemical Physics **82**, 2688–2699 (1985).

[Pic89] W. E. Pickett, "Pseudopotential methods in condensed matter applications", Computer Physics Reports **9**, 115–197 (1989).

[PJJ00] M. Pecul, M. Jaszunski, and P. Jorgensen, "Singlet excitations and dipole polarizabilities of li2, li4 and li8 clusters", Molecular Physics **98**, 1455–1465 (2000).

[PL83] J. P. Perdew and M. Levy, "Physical content of the exact kohn-sham orbital energies: band gaps and derivative discontinuities", Physical Review Letters **51**, 1884–1887 (1983).

[PL97] J. P. Perdew and M. Levy, "Comment on "significance of the highest occupied kohn-sham eigenvalue"", Physical Review B **56**, 16021–16028 (1997).

[PM89] J. Pipek and P. G. Mezey, "A fast intrinsic localization procedure applicable for ab initio and semiempirical linear combination of atomic orbital wave functions", The Journal of Chemical Physics **90**, 4916–4926 (1989).

[PPL99] D. Porezag, M. R. Pederson, and A. Y. Liu, "Importance of nonlinear core corrections for density-functional based pseudopotential calculations", Physical Review B **60**, 14132–14139 (1999).

[Pre07] W. H. Press, *Numerical recipes the art of scientific computing, The art of scientific computing* (Cambridge University Press, 2007).

[PRP14] M. R. Pederson, A. Ruzsinszky, and J. P. Perdew, "Communication: self-interaction correction with unitary invariance in density functional theory", The Journal of Chemical Physics **140**, 121103 (2014).

[PW92] J. P. Perdew and Y. Wang, "Accurate and simple analytic representation of the electron-gas correlation energy", Physical Review B **45**, 13244–13249 (1992).

[PZ02] S. Patchkovskii and T. Ziegler, "Improving "difficult" reaction barriers with self-interaction corrected density functional theory", The Journal of Chemical Physics **116**, 7806–7813 (2002).

[PZ81] J. P. Perdew and A. Zunger, "Self-interaction correction to density-functional approximations for many-electron systems", Physical Review B **23**, 5048–5079 (1981).

[Rep+15] M. Repisky, L. Konecny, M. Kadek, S. Komorovsky, O. L. Malkin, V. G. Malkin, and K. Ruud, "Excitation energies from real-time propagation of the four-component dirac–kohn–sham equation", Journal of Chemical Theory and Computation **11**, 980–991 (2015).

[RG84] E. Runge and E. K. U. Gross, "Density-functional theory for time-dependent systems", Physical Review Letters **52**, 997–1000 (1984).

[Ric+23] R. Richter, T. Aschebrock, I. Schelter, and S. Kümmel, "Meta-generalized gradient approximations in time dependent generalized kohn–sham theory: importance of the current density correction", The Journal of Chemical Physics **159**, 124117 (2023).

[Rob+62] J. E. Robinson, F. Bassani, R. S. Knox, and J. R. Schrieffer, "Screening correction to the slater exchange potential", Physical Review Letters **9**, 215–217 (1962).

[Rom+21] S. Romero, Y. Yamamoto, T. Baruah, and R. R. Zope, "Local self-interaction correction method with a simple scaling factor", Physical Chemistry Chemical Physics **23**, 2406–2418 (2021).

[Rub+12] A. Rubio, M. A. Marques, F. M. Nogueira, and E. Gross, eds., *Fundamentals of time-dependent density functional theory*, Lecture Notes in Physics Ser. (Springer Berlin, 2012), 1572 pp.

[Ruz+06] A. Ruzsinszky, J. P. Perdew, G. I. Csonka, O. A. Vydrov, and G. E. Scuseria, "Spurious fractional charge on dissociated atoms: pervasive and resilient self-interaction error of common density functionals", The Journal of Chemical Physics **125**, 194112 (2006).

[Ruz+07] A. Ruzsinszky, J. P. Perdew, G. I. Csonka, O. A. Vydrov, and G. E. Scuseria, "Density functionals that are one- and two- are not always many-electron self-interaction-free, as shown for h_2^+, he_2^+, lih^+, and ne_2^+", The Journal of Chemical Physics **126**, 104102 (2007).

[Sav20] A. Savin, "Models and corrections: range separation for electronic interaction—lessons from density functional theory", The Journal of Chemical Physics **153**, 160901 (2020).

[Sch+07] K. L. Schuchardt, B. T. Didier, T. Elsethagen, L. Sun, V. Gurumoorthi, J. Chase, J. Li, and T. L. Windus, "Basis set exchange: a community database for computational sciences", Journal of chemical information and modeling **47**, 1045–1052 (2007).

[Sch+14a] T. Schmidt, E. Kraisler, L. Kronik, and S. Kümmel, "One-electron self-interaction and the asymptotics of the kohn–sham potential: an impaired relation", Phys. Chem. Chem. Phys. **16**, 14357–14367 (2014).

[Sch+14b] T. Schmidt, E. Kraisler, A. Makmal, L. Kronik, and S. Kümmel, "A self-interaction-free local hybrid functional: accurate binding energies vis-à-vis accurate ionization potentials from kohn-sham eigenvalues", The Journal of Chemical Physics **140**, 18A510 (2014).

[Sch+19] I. Schelter, J. M. Foerster, A. T. Gardiner, A. W. Roszak, R. J. Cogdell, G. M. Ullmann, T. B. de Queiroz, and S. Kümmel, "Assessing density functional theory in real-time and real-space as a tool for studying bacteriochlorophylls and the light-harvesting complex 2", The Journal of Chemical Physics **151**, 134114 (2019).

[Sch+20] S. Schwalbe, L. Fiedler, J. Kraus, J. Kortus, K. Trepte, and S. Lehtola, "Pyflosic: python-based fermi–löwdin orbital self-interaction correction", The Journal of Chemical Physics **153**, 084104 (2020).

[Sch17] I. Schelter, "Excitation dynamics in molecular systems from efficient grid-based real-time density functional theory", PhD thesis (University of Bayreuth, Bayreuth, 2017).

[Sch26] E. Schrödinger, "An undulatory theory of the mechanics of atoms and molecules", Phys. Rev. **28**, 1049–1070 (1926).

[Sei+96] A. Seidl, A. Görling, P. Vogl, J. A. Majewski, and M. Levy, "Generalized kohn-sham schemes and the band-gap problem", Physical Review B **53**, 3764–3774 (1996).

[SH53] R. T. Sharp and G. K. Horton, "A variational approach to the unipotential many-electron problem", Physical Review **90**, 317–317 (1953).

[Sha+14] Y. Shao, Z. Gan, E. Epifanovsky, et al., "Advances in molecular quantum chemistry contained in the q-chem 4 program package", Molecular Physics **113**, 184–215 (2014).

[SK16] T. Schmidt and S. Kümmel, "One- and many-electron self-interaction error in local and global hybrid functionals", Physical Review B **93**, 165120 (2016).

[SK18] I. Schelter and S. Kümmel, "Accurate evaluation of real-time density functional theory providing access to challenging electron dynamics", Journal of Chemical Theory and Computation **14**, 1910–1927 (2018).

[SKB09] T. Stein, L. Kronik, and R. Baer, "Reliable prediction of charge transfer excitations in molecular complexes using time-dependent density functional theory", Journal of the American Chemical Society **131**, 2818–2820 (2009).

[SRP15] J. Sun, A. Ruzsinszky, and J. P. Perdew, "Strongly constrained and appropriately normed semilocal density functional", Physical Review Letters **115**, 036402 (2015).

[SS83] L. J. Sham and M. Schlüter, "Density-functional theory of the energy gap", Physical Review Letters **51**, 1888–1891 (1983).

[SŞS12] J. Strümpfer, M. Şener, and K. Schulten, "How quantum coherence assists photosynthetic light-harvesting", The Journal of Physical Chemistry Letters **3**, 536–542 (2012).

[Ste+10] T. Stein, H. Eisenberg, L. Kronik, and R. Baer, "Fundamental gaps in finite systems from eigenvalues of a generalized kohn-sham method", Physical Review Letters **105**, 266802 (2010).

[Tao+03] J. Tao, J. P. Perdew, V. N. Staroverov, and G. E. Scuseria, "Climbing the density functional ladder: nonempirical meta–generalized gradient approximation designed for molecules and solids", Physical Review Letters **91**, 146401 (2003).

[Tao05] J. Tao, "Explicit inclusion of paramagnetic current density in the exchange-correlation functionals of current-density functional theory", Physical Review B **71**, 205107 (2005).

[TCS04] J. Toulouse, F. Colonna, and A. Savin, "Short-range exchange and correlation energy density functionals: beyond the local-density approximation", The Journal of Chemical Physics **122**, 014110 (2004).

[TKH03] T. Tsuneda, M. Kamiya, and K. Hirao, "Regional self-interaction correction of density functional theory", Journal of Computational Chemistry **24**, 1592–1598 (2003).

[TM91] N. Troullier and J. L. Martins, "Efficient pseudopotentials for plane-wave calculations", Physical Review B **43**, 1993–2006 (1991).

[Toz+99] D. J. Tozer, R. D. Amos, N. C. Handy, B. O. Roos, and L. Serrano-Andres, "Does density functional theory contribute to the understanding of excited states of unsaturated organic compounds?", Molecular Physics **97**, 859–868 (1999).

[Toz03] D. J. Tozer, "Relationship between long-range charge-transfer excitation energy error and integer discontinuity in kohn–sham theory", The Journal of Chemical Physics **119**, 12697–12699 (2003).

[TS76] J. D. Talman and W. F. Shadwick, "Optimized effective atomic central potential", Physical Review A **14**, 36–40 (1976).

[UGG95] C. A. Ullrich, U. J. Gossmann, and E. K. U. Gross, "Time-dependent optimized effective potential", Physical Review Letters **74**, 872–875 (1995).

[Ull16] C. A. Ullrich, *Time-dependent density-functional theory, Concepts and applications*, Oxford graduate texts (Oxford University Press, Oxford, 2016), 526 pp.

[Val+12] Á. Valdés, J. Brillet, M. Grätzel, et al., "Solar hydrogen production with semiconductor metal oxides: new directions in experiment and theory", Phys. Chem. Chem. Phys. **14**, 49–70 (2012).

[Vig08] G. Vignale, "Real-time resolution of the causality paradox of time-dependent density-functional theory", Physical Review A **77**, 062511 (2008).

[VS04] O. A. Vydrov and G. E. Scuseria, "Effect of the perdew–zunger self-interaction correction on the thermochemical performance of approximate density functionals", The Journal of Chemical Physics **121**, 8187–8193 (2004).

[VS05] O. A. Vydrov and G. E. Scuseria, "Ionization potentials and electron affinities in the perdew–zunger self-interaction corrected density-functional theory", The Journal of Chemical Physics **122**, 184107 (2005).

[VS06] O. A. Vydrov and G. E. Scuseria, "A simple method to selectively scale down the self-interaction correction", The Journal of Chemical Physics **124**, 191101 (2006).

[VSP07] O. A. Vydrov, G. E. Scuseria, and J. P. Perdew, "Tests of functionals for systems with fractional electron number", The Journal of Chemical Physics **126**, 154109 (2007).

[Vyd+06] O. A. Vydrov, G. E. Scuseria, J. P. Perdew, A. Ruzsinszky, and G. I. Csonka, "Scaling down the perdew-zunger self-interaction correction in many-electron regions", The Journal of Chemical Physics **124**, 094108 (2006).

[VZ07] A. Vlček and S. Záliš, "Modeling of charge-transfer transitions and excited states in d6 transition metal complexes by dft techniques", Coordination Chemistry Reviews **251**, 258–287 (2007).

[WAY03] Q. Wu, P. W. Ayers, and W. Yang, "Density-functional theory calculations with correct long-range potentials", The Journal of Chemical Physics **119**, 2978–2990 (2003).

[Wil+13] A. Willand, Y. O. Kvashnin, L. Genovese, Á. Vázquez-Mayagoitia, A. K. Deb, A. Sadeghi, T. Deutsch, and S. Goedecker, "Norm-conserving pseudopotentials with chemical accuracy compared to all-electron calculations", The Journal of Chemical Physics **138**, 104109 (2013).

[WJP22] K. P. K. Withanage, K. A. Jackson, and M. R. Pederson, "Complex fermi–löwdin orbital self-interaction correction", The Journal of Chemical Physics **156**, 231103 (2022).

[WR] W. R. Inc., *Mathematica, Version 13.3*, Champaign, IL, 2023.

[WU08] H. O. Wijewardane and C. A. Ullrich, "Real-time electron dynamics with exact-exchange time-dependent density-functional theory", Physical Review Letters **100**, 056404 (2008).

[Yam+19] Y. Yamamoto, C. M. Diaz, L. Basurto, K. A. Jackson, T. Baruah, and R. R. Zope, "Fermi-löwdin orbital self-interaction correction using the strongly constrained and appropriately normed meta-gga functional", The Journal of Chemical Physics **151**, 154105 (2019).

[Yam+20] Y. Yamamoto, S. Romero, T. Baruah, and R. R. Zope, "Improvements in the orbitalwise scaling down of perdew–zunger self-interaction correction in many-electron regions", The Journal of Chemical Physics **152**, 174112 (2020).

[Yam+23] Y. Yamamoto, T. Baruah, P.-H. Chang, S. Romero, and R. R. Zope, "Self-consistent implementation of locally scaled self-interaction-correction method", The Journal of Chemical Physics **158**, 064114 (2023).

[Yan+16] Z.-h. Yang, H. Peng, J. Sun, and J. P. Perdew, "More realistic band gaps from meta-generalized gradient approximations: only in a generalized kohn-sham scheme", Phys. Rev. B **93**, 205205 (2016).

[YCM12] W. Yang, A. J. Cohen, and P. Mori-Sánchez, "Derivative discontinuity, bandgap and lowest unoccupied molecular orbital in density functional theory", The Journal of Chemical Physics **136**, 204111 (2012).

[YK17] Y. Yao and Y. Kanai, "Plane-wave pseudopotential implementation and performance of scan meta-gga exchange-correlation functional for extended systems", The Journal of Chemical Physics **146**, 224105 (2017).

[YPP17] Z.-h. Yang, M. R. Pederson, and J. P. Perdew, "Full self-consistency in the fermi-orbital self-interaction correction", Physical Review A **95**, 052505 (2017).

[YTH04] T. Yanai, D. P. Tew, and N. C. Handy, "A new hybrid exchange–correlation functional using the coulomb-attenuating method (cam-b3lyp)", Chemical Physics Letters **393**, 51–57 (2004).

[YZA00] W. Yang, Y. Zhang, and P. W. Ayers, "Degenerate ground states and a fractional number of electrons in density and reduced density matrix functional theory", Physical Review Letters **84**, 5172–5175 (2000).

[Zop+19] R. R. Zope, Y. Yamamoto, C. M. Diaz, T. Baruah, J. E. Peralta, K. A. Jackson, B. Santra, and J. P. Perdew, "A step in the direction of resolving the paradox of perdew-zunger self-interaction correction", The Journal of Chemical Physics **151**, 214108 (2019).

[ZY98] Y. Zhang and W. Yang, "A challenge for density functionals: self-interaction error increases for systems with a noninteger number of electrons", The Journal of Chemical Physics **109**, 2604–2608 (1998).

[ZYB24] R. R. Zope, Y. Yamamoto, and T. Baruah, "How well do one-electron self-interaction-correction methods perform for systems with fractional electrons?", The Journal of Chemical Physics **160**, 084102 (2024).

Auxiliary Tools

Grammarly, provided by the University of Bayreuth Graduate School, was used as an auxiliary tool for grammar and style checking.

Danksagung

An dieser Stelle bedanke ich mich bei allen beteiligten Personen, die mich während der Zeit der Anfertigung dieser Arbeit unterstützt haben. Besonders bedanken möchte ich mich bei ...

- **Stephan Kümmel**, der mich während meines Studiums und schlussendlich auch als Doktorvater über viele Jahre betreut hat. Neben der fachlichen Expertise und der Begeisterung für die Physik, die auch für mich immer eine Motivationsquelle war, gilt mein besonderer Dank auch seiner menschlichen Art und persönlichen Unterstützung in schwierigen Zeiten, die so nicht selbstverständlich war.

- **allen ehemaligen und aktuellen Mitglieder des Lehrstuhls Theoretische Physik IV** für eine großartige Atmosphäre und viele spannende physikalische Diskussionen. Dazu gehören **Ingo Schelter**, der mich mit als eine der ersten Personen am Lehrstuhl willkommen geheißen hat und mich immer gut gelaunt bei technischen, fachlichen oder auch mal persönlichen Fragen unterstützt hat, **Benedikt Billmaier**, **Moritz Brütting**, **Sophie Meißner** und **Thomas Trepl**, die sich die Zeit genommen haben Teile dieses Manuskripts Korrektur zu lesen, sowie **Markus Hilt** und **Bettina Müller**, die mich technisch sowie administrativ unterstützt haben. Außerdem war es mir eine Freude die letzten Jahre mein Büro mit **Benedikt** zu teilen.

- **allen meinen Freunden**. Nicht nur die, die ich neu in Bayreuth kennengelernt habe, haben mir eine unvergessliche Zeit beschert – auch meine alten Schulfreunde, mit denen ich bis heute in Kontakt bin, haben einen wichtigen Platz.

- meinen beiden Großmüttern **Ingeborg Richter** und **Inge Schörner**, die mich immer mit all ihren Möglichkeiten unterstützt haben.

- meinen Eltern **Susanne** und **Thomas**, die mir alles ermöglicht haben und immer an meiner Seite waren, sowie bei meinem Bruder **Ronan** für seine Unterstützung.

Eidesstattliche Versicherung

Hiermit versichere ich an Eides statt, dass ich die vorliegende Arbeit selbstständig verfasst und keine anderen als die von mir angegebenen Quellen und Hilfsmittel verwendet habe.

Weiterhin erkläre ich, dass ich die Hilfe von gewerblichen Promotionsberatern bzw. -vermittlern oder ähnlichen Dienstleistern weder bisher in Anspruch genommen habe, noch künftig in Anspruch nehmen werde.

Zusätzlich erkläre ich hiermit, dass ich keinerlei frühere Promotionsversuche unternommen habe.

Bayreuth, den